Thermally Driven Technologies for Atmospheric Water Capture to Provide Decentralized Drinking Water

by

Anjali Mulchandani

A Dissertation Presented in Partial Fulfillment
of the Requirements for the Degree
Doctor of Philosophy

Approved December 2019 by the
Graduate Supervisory Committee:

Paul Westerhoff, Chair
Bruce Rittmann
Pedro Alvarez
Pierre Herckes

ARIZONA STATE UNIVERSITY

May 2020

ABSTRACT

Limited access to clean water due to natural or municipal disasters, drought, or contaminated wells is driving demand for point-of-use and humanitarian drinking water technologies. Atmospheric water capture (AWC) can provide water off the centralized grid by capturing water vapor in ambient air and condensing it to a liquid. The overarching goal of this dissertation was to define geographic and thermodynamic design boundary conditions for AWC and develop nanotechnology-enabled AWC technologies to produce clean drinking water.

Widespread application of AWC is currently limited because water production, energy requirement, best technology, and water quality are not parameterized. I developed a geospatial climatic model for classical passive solar desiccant-driven AWC, where water vapor is adsorbed onto a desiccant bed at night, desorbed by solar heat during the day, and condensed. I concluded passive systems can capture 0.25–8 $L/m^2/day$ as a function of material properties and climate, and are limited because they only operate one adsorption-desorption-condensation cycle per day. I developed a thermodynamic model for large-scale AWC systems and concluded that the thermodynamic limit for energy to saturate and condense water vapor can vary up to 2-fold as a function of climate and mode of saturation.

Thermodynamic and geospatial models indicate opportunity space to develop AWC technologies for arid regions where solar radiation is abundant. I synthesized photothermal desiccants by optimizing surface loading of carbon black nanoparticles on micron-sized silica gel desiccants (CB-SiO_2). Surface temperature of CB-SiO_2 increased to 60^oC under solar radiation and water vapor desorption rate was 4-fold faster than bare

silica. CB-SiO_2 could operate >10 AWC cycles per day to produce 2.5 L/m^2/day at 40% relative humidity, 3-fold more water than a conventional passive system.

Models and bench-scale experiments were paired with pilot-scale experiments operating electrical desiccant and compressor dehumidifiers outdoors in a semi-arid climate to benchmark temporal water production, water quality and energy efficiency. Water quality varied temporally, e.g, dissolved organic carbon concentration was 3 – 12 mg/L in the summer and <1 mg/L in the winter. Collected water from desiccant systems met all Environmental Protection Agency standards, while compressor systems may require further purification for metals and turbidity.

To the scientists who came before me, Mom and Dad, I walk in your footsteps.

To the curious minds, young and old, past present and future,

who marvel at the wonders of the world and yearn to discover.

You are my inspiration.

ACKNOWLEDGEMENTS

- A huge thank you to my advisor, Dr. Paul Westerhoff, for giving me an opportunity to pursue a research topic of my choosing, challenging me continuously, never wavering as I both struggled and succeeded, providing me freedom to pursue my passion for teaching and education, and ultimately helping me reach my full potential. Your impact is boundless.
- Committee members, Dr. Bruce Rittmann, Dr. Pierre Herckes and Dr. Pedro Alvarez. Bruce, for inspiring me to come to ASU, teaching me the value of fundamental knowledge, and giving me an opportunity to develop an idea from a class project into a research proposal. Pierre, for providing valuable insight every Friday meeting and teaching me the value of having an in-depth understanding of data quality and instrumentation. Pedro, for giving me a network and platform within NEWT to discuss ideas, guiding me towards impactful and sustainable nanotechnology research, and teaching me how to be an effective leader.
- Dr. Shaily Mahendra, my undergraduate research advisor at UCLA, for helping me grow when I was a nascent researcher, teaching me how to think about solving grand research challenges, and encouraging me to pursue a PhD.
- Wonderful undergraduate students who I have had the privilege to work with, Justin Edberg, Shannon Malinda, Kaley Yazzie, Adam Tran, Emma Westerhoff, Nathaniel Fink, Perivaldo Fernandez, and Bader Al-Muha, whose curiosity and enthusiasm inspire me every day.

- Friends from the lab, around Arizona, and in other far places, Heather Tugaoen, Ariel Atkinson, Sergi Garcia-Segura, Xiangyu Bi, Daniella Saetta, Natalia Fischer, Juliana Levi, Emmy Pruitt, Omar Alrehaili, Naushita Sharma, Onur Apul, Mariana Lanzarini-Lopes, Justin Kidd, Yuqiang Bi, Ana Barrios, Tara Nietzold, Jorge Loyo, Abi Gomez-Morales, Neil Tugaoen, Apoorva Pasricha, Mina Mohammad, Anmy Vu, Joey Yan, and members of the Changing Hands Modern Fiction Book Club. Your friendship has kept me smiling.
- Most importantly, my family. Dr. Ashok Mulchandani, Dr. Priti Mulchandani, and (future Dr.) Divya Mulchandani. You are my first teachers and forever cheerleaders. Thank you for encouraging my curiosity, teaching me the value of hard work, and supporting my aspirations. I am eternally grateful.
- This research was funded by the National Science Foundation Graduate Research Fellowship, National Science Foundation Engineering Research Center on Nanotechnology Enabled Water Treatment, Arizona State University Ira A. Fulton Engineering Dean's Fellowship, and PepsiCo Beverage Manufacturing Plant Water Efficiency Challenge Grant.

TABLE OF CONTENTS

Page

CHAPTER Page

CHAPTER Page

CHAPTER Page

APPENDIX Page

LIST OF TABLES

Table Page

LIST OF FIGURES

Figure Page

Figure Page

Figure Page

Figure Page

Figure Page

Figure Page

INTRODUCTION

Hurricane Maria was a category 5 hurricane that left Puerto Rico without access to running water and a stable electrical grid for more than three months. School children in Flint, Michigan could not rely upon municipally treated tap water because of leaching of lead from water distribution pipes. Thirty percent of the Navajo Nation does not have running water in their homes, but instead haul water from unregulated wells that may be contaminated with fecal coliform and uranium. I seek to explore a strategy to provide limited volumes of high-quality water in these and other circumstances that can be used by anyone, in any location, at any time.

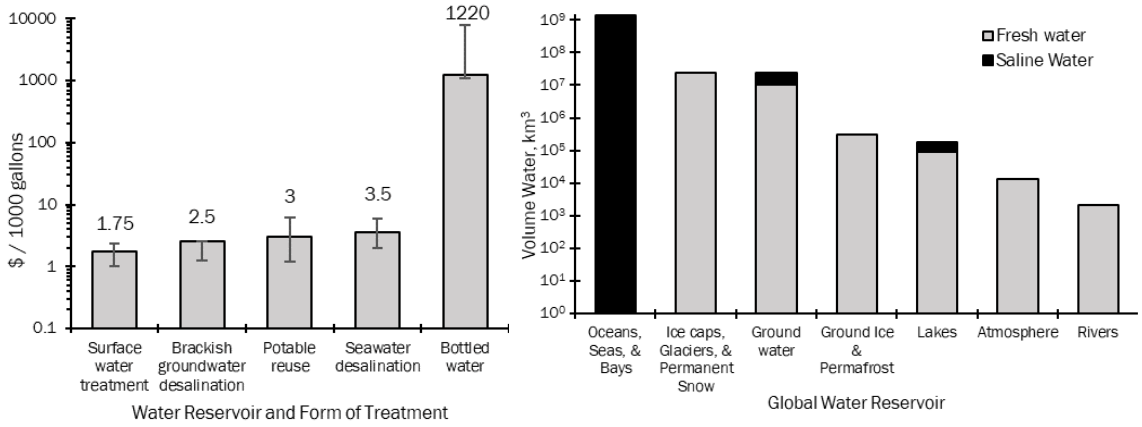

Figure 1-1 a) Cost per kilogallon for treating various sources of water. b) Volume of water stored in global water reservoirs.

When liquid water sources such as lakes, rivers, or groundwater are inaccessible or contaminated, communities often rely upon bottled or transported water for weeks to months. Figure 1-1a shows bottled water costs 2 to 3 orders of magnitude more than conventional surface water treatment, desalination of brackish or seawater, and potable wastewater reuse. Technologies capable of providing the flexibility of bottled water

without the infrastructure required for centralized municipal potable water would be of great economic and societal value.

Figure 1-1b shows the volume of water stored in different global water reservoirs. The atmosphere contains 12,900 km^3 of water, six times more than the volume stored in rivers. The universal presence and accessibility of water in the atmosphere provides the opportunity for added resilience to water stressed communities. Atmospheric water capture (AWC) does not require fixed physical infrastructure such as pipelines and does not produce large concentrated waste streams associated with contaminant or salt removal from liquid water supplies. The technical challenge of AWC lies in the high thermodynamic energy requirement to convert water vapor to liquid water.

The field of AWC has been recently growing in academic research and commercial sectors. *Academic research* has focused on development of desiccant materials with high vapor sorption capacities for "passive AWC" – the desiccants are saturated with water vapor at night, and water vapor is desorbed and condensed during the day using solar thermal energy. Passive AWC systems have not been reported to produce more than 2 L water/day, but they operate completely off the electrical grid. Simultaneously, the *commercial sector* has pushed "active AWC" – compressor systems with refrigerants continuously harvest water vapor during all hours of the day and require electrical energy or gas. Small active AWC systems produce 7 L water/day, while larger units can produce up to 5000 L/day, with energy efficiencies ranging from 0.15 – 0.63 kWh/L in tested conditions (likely the favorable condition of high relative humidity).

Despite research and development on novel desiccant materials, AWC system configurations, and units for in-home use, several barriers remain. Specifically, it is

unknown what level of success each AWC technology will have in different climatic regions, whether solar energy can offset electrical energy costs, and the quality of water produced.

1.1 Dissertation Organization

The overarching goal of my dissertation is to define geographic and thermodynamic design boundary conditions for AWC and develop nano-enabled AWC technologies to produce clean drinking water. This dissertation is organized into chapters guided by research questions.

Chapter 2 contains a literature review of AWC principles and technologies and identifies barriers and opportunities for technology progression. The body of the dissertation (Chapters 3, 4, 5 and 6) is guided by the 4 research questions addressed in **Table 1-1**. Chapter 7 is an engineering education tool that expands upon the broader impacts of my dissertation work. The synthesis chapter (Chapter 8) summarizes answers to research questions and provides reflection on scope of this body of work. The final chapter (Chapter 9) summarizes this work and provides recommendations for future work. The appendix contains a research paper I published on resource recovery from sewage sludges as part of my masters-in-passing research.

Table 1-1 Organization of dissertation chapters and resulting publications

Chapter 3 Research Question 1: What is the maximum volume of water that can be captured from the atmosphere through climatic regions of the U.S. for passive direct solar desiccants? Submitted, in review: Mulchandani, A. and Westerhoff, P. Geospatial climatic factors influence water production of solar desiccant-driven atmospheric water capture devices.
Chapter 4 Research Question 2: To what extent does coating solar-light active photothermal nanomaterials on desiccant surfaces improve vapor desorption efficiency? In preparation: Mulchandani, A., Malinda, S., Edberg, J., Westerhoff, P. Sunlight driven atmospheric water capture capacity is enhanced by photothermal nanomaterial enabled desiccants.
Chapter 5 Research Question 3: How do dehumidification devices that use either condensers or desiccants impact rate of water capture, energy efficiency and water quality when operated in outdoor environments? In preparation: Mulchandani, A., Edberg, J., Herckes, P., Westerhoff, P. Seasonal atmospheric water capture yield and water quality using electric-powered desiccant and compressor dehumidifiers.
Chapter 6 Research Question 4: What is the minimum energy requirement for AWC as a function of scale, climate and thermodynamic process of condensation? In preparation: Mulchandani, A. and Westerhoff, P. Thermodynamic boundaries guide development of operation envelopes for atmospheric water capture.
Chapter 7 Objective: Develop and test a hands-on engineering education tool to effectively teach nanotechnology and sorption fundamentals and applications for water and air treatment. Published: Mulchandani, A., Atkinson, A., Garcia-Segura, S., Westerhoff, P. "Nanoblocks": A playful method to learn about nanotechnology-enabled water and air treatment. *Journal of Chemical Education*, **2019**, *4*, 708-713.
Appendix Objective: Review and proof-of-concept of novel thermo-chemical processes for recovery of metals and energy from sewage sludges. Published: Mulchandani, A. and Westerhoff, P. Recovery opportunities for metals and energy from sewage sludges. *Bioresource Technology*, **2016**, *2015*, 215-226.

BACKGROUND

2.1. How Much Water is Available in the Air to Capture?

The atmosphere contains 12,900 km^3 of water vapor, which recirculates every 9 days through natural evaporation and precipitation processes. (**Figure 2-1**) This quantity is 6-fold more than the amount of water stored in global rivers and 14% of the freshwater stored in lakes and rivers, combined (Shiklomanov, 1992). The atmosphere's universal presence and abundance of water suggests that it can be used as a source of drinking water anywhere a liquid water source is not available.

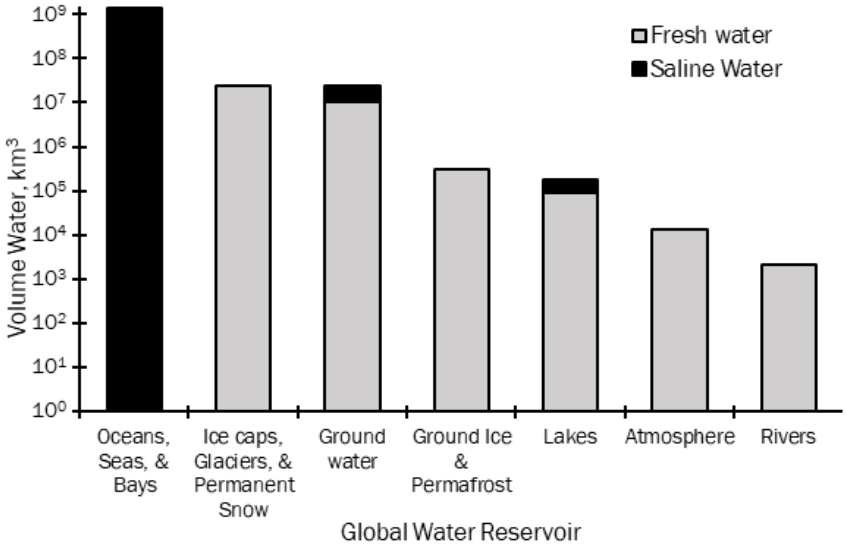

Figure 2-1 Volume of water stored in global water reservoirs

While the total volume of water in the atmosphere globally is 12,900 km^3, the density of vapor in the air can vary regionally, from 2 g/m^3 in an arid region to 25 g/m^3 in a humid region. Vapor density (ρ_{vapor}) is defined in **Equation 1** as a function of vapor pressure (e [Pa]), air temperature (T_{air} [K]) and the vapor gas constant (R_v = 461 J/kg/K). Water vapor will condense if the vapor density is equal to the saturation vapor density

($\rho_{vapor,sat}$). Relative humidity (RH) is a ratio of these two variables and defines how close air is to saturation. RH (**Equation 2**) is typically written as a ratio of the vapor pressure to the saturation vapor pressure (e_s), where e can be related to ρ_{vapor} through **Equation 1**, e_s is given by the Clausius Clapeyron equation (**Equation 3**), temperature T_o is 273 K and vapor pressure $e_{s,0}$ is 611 Pa (Margulis, 2017). Fog and dew are air that is completely saturated; fog droplets are suspended in the air, while dew is found on a cool surface.

$$\rho_{vapor} = \frac{e}{R_v T_{air}} \quad (1)$$

$$RH = \frac{\rho_{vapor}}{\rho_{vapor,sat}} = \frac{e}{e_s} \quad (2)$$

$$e_s = e_{s,0} \exp\left[\frac{L_v}{R_v}\left(\frac{1}{T_0} - \frac{1}{T_{air}}\right)\right] \quad (3)$$

2.2. How Much Energy is Required to Condense Water Vapor?

Figure 2-2 shows the water phase diagram as a function of temperature and saturated vapor pressure. Vapor can transition to a liquid if i) air is cooled and/or ii) pressure is increased. The energy required for a phase change of water can be calculated through the Gibbs Free Energy equation (**Equation 4**).

$$\Delta G^o = \Delta H^o - T\Delta S^o \quad (4)$$

At a temperature (T) of 25°C, the Gibbs free energy (ΔG^o) of phase change from vapor to liquid is -8.6 kJ/mol, the enthalpy of condensation (i.e. ΔH^o or L_v) is -44.1 kJ/mol , and the change in entropy (ΔS^o) is -0.12 kJ/mol. The phase change reaction at 25°C is exothermic and not spontaneous. To condense 1 L of water, the minimum thermodynamic energy required for the phase change is 2450 kJ, or 0.68 kWh.

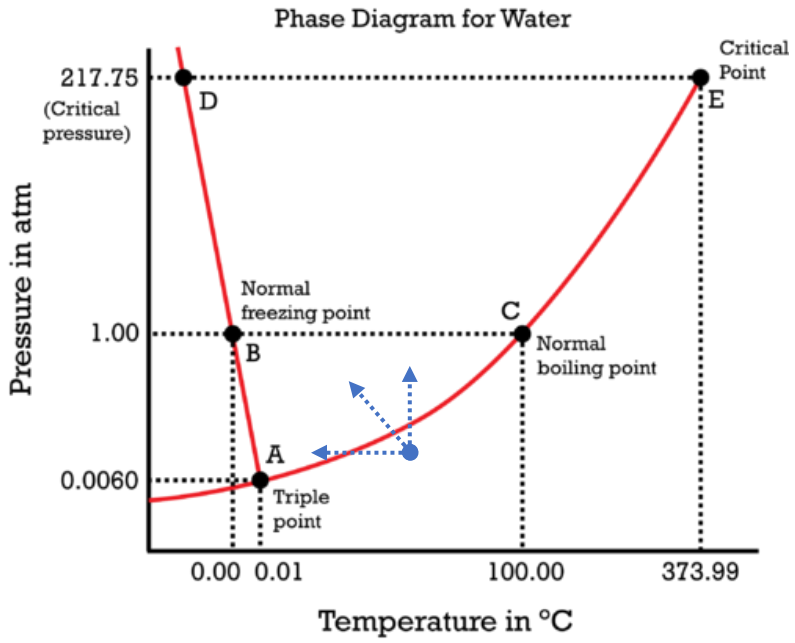

Figure 2-2 Phase diagram of water. The blue dot is an arbitrary starting point for AWC. Directional arrows signify change in thermodynamic property to achieve saturation of water vapor.

2.3. What Are the Modes of Atmospheric Water Capture?

2.3.1. Fog Collection

The AWC field has been inspired by the Namib desert beetle and other flora and fauna (e.g., cactus) which can capture fog and dew aerosol droplets on their surfaces (Andrews, Eccles, Schofield, & Badyal, 2011; Ju et al., 2012; Malik, Clement, Gethin, Krawszik, & Parker, 2014). The desert beetle's black back consists of alternating non-waxy hydrophilic and waxy hydrophobic regions. The hydrophilic bumps act as seeding points for fog droplets to bind and grow. The droplet continues to grow until the capillary force holding the droplet to the hydrophilic surface is overcome. Then, the droplet detaches and rolls down the hydrophobic troughs into the beetle's mouth (K. C. Park et al., 2016; Parker & Lawrence, 2001).

Several polymeric materials have been synthesized to “biomimic” the desert beetle. These studies have attempted various modes for synthesis of surfaces with alternating hydrophilic and hydrophobic regions, such as dewetting (Thickett, Neto, & Harris, 2011), plasma deposition (Garrod et al., 2007), inkjet printing (Lianbin Zhang, Wu, Hedhili, Yang, & Wang, 2015), eletrospinning (Dong et al., 2012; Lalia, Anand, Varanasi, & Hashaikeh, 2013), and femtosecond laser (Lu et al., 2019; Yin et al., 2017). If the surface is oriented perpendicular to the flow of aerosols, droplets will nucleate on the hydrophilic surfaces, grow, and easily roll down due to gravity due to low contact angle hysteresis.

Companies such as FogQuest and Aqualonis have developed large nets that stand 5 – 8 m^2 high and several meters across, perpendicular to the wind, and collect water in a trough below the net. Nets such as these have been operated in fog-rich areas such as the west coast of South America (Chile, Peru) and coastal regions of Africa (Morocco, Tanzania, South Africa). Aerosol droplet capture onto fog nets can be an effective way to produce water in regions with limited rainfall or groundwater. Water production rate can be as high as 2000 L/day (528 gallons/day) using 600 m^2 of nets. Research in this area continues to be active as new materials fabrication techniques continue to be published.

Aerosol capture has several disadvantages. It can only be used where there is heavy fog, e.g. coastal regions. These regions could potentially perform seawater desalination at a price cheaper than fog nets ($2.5 / kgal for desalination, $1000 - $15,000 capital investment for fog net). Patents and companies in this field are sparse in

comparison to the quantity of published research papers, suggesting low potential for commercial growth.

2.3.2. Cooling to Dew Point

Air can reach vapor saturation when temperature is decreased, which lowers the saturation vapor pressure and increases RH. The dew point temperature is the temperature to which air needs to be cooled to reach saturated conditions. Dew point temperature (T_d) can be calculated by a modified Clausius-Clapeyron equation (**Equation 5**).

$$T_d = \left[\frac{1}{T_0} - \frac{R_v}{L_v}\ln\left(\frac{e}{e_{s0}}\right)\right]^{-1} \quad (5)$$

Dew point, air temperature, and relative humidity are correlated through **Equations 2,3 and 5**. **Figure 2-3** shows dew point temperature as a function of air temperature and relative humidity. The blue box shows the region in which dew point temperature is below freezing (i.e. frost will form on the condensing surface, which is not ideal for atmospheric water capture). For RH<30%, air temperature must be at least greater than 20^{o}C. For RH 60%, air temperatures only need to be >8^{o}C for condensation to occur without freezing. This indicates that in more humid climates, or regions where night time RH is >60%, cooling to dew point can be a good method to capture water from the air. Conversely, in drier climates (e.g. RH 10%), air temperature must also be warm enough (e.g. >35^{o}C) such that the dew point temperature is above freezing.

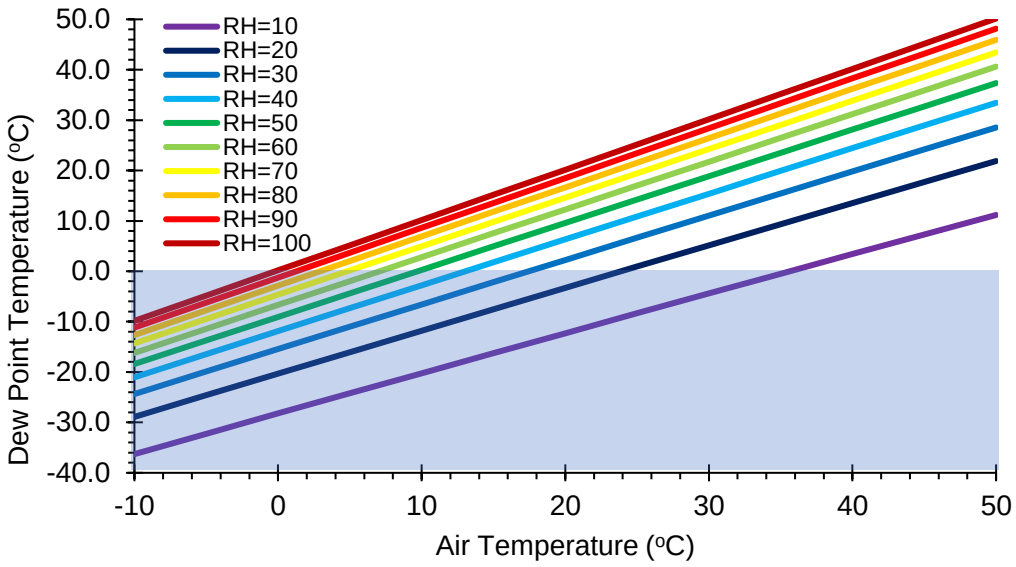

Figure 2-3 Dew point temperature as a function of air temperature and relative humidity, calculated by the Clausius-Clapeyron equation (Equation 5). The blue box shows the region in which dew point temperature is below freezing.

Refrigerants are typically used to cool and condense air. The cold gaseous refrigerant flows through copper coils. Heat from the air is transferred to the refrigerant and the water condenses on the coils. The hot refrigerant goes through a vapor compression refrigeration cycle. In this cycle, the mixed liquid and vapor phase refrigerant in the evaporator becomes a low-pressure gas due to extraction of latent heat from hot air. The gas phase refrigerant cycles first to the compressor, where its temperature and pressure are increased, and next to a condenser, where the heat is transferred to air/water and the refrigerant condenses to a liquid. The liquid refrigerant passes through an expansion valve, where the pressure is decreased and a portion of the refrigerant becomes vapor, before cycling back into the evaporator. A commonly used refrigerant for condensation of water vapor is R410A, which is a blend of R32 (difluoromethane) and R125 (pentafluroethane). R410A is a hydrofluorocarbon, so it is

safer for the environment in comparison to chlorofluorocarbons (e.g. R12 Freon, CCl_2F_2. It also has a high enthalpy of vaporization (276 kJ/kg), indicating good heat transfer properties, and high vapor pressure.

Refrigerant compressor systems for atmospheric water capture are widely used and resemble conventional home electrical dehumidifiers. Patents on these devices date to the 1990s, and are owned by companies such as Ecoloblue and Water-Gen (5259203, 1993; US 2010/0266742 A1, 2010; 5,701,749, 1997; US 2014/0053580 A1, 2014; US 2011/0048039 A1, 2011; 5,669,221, 1997; US 6,945,063 B2, 2005; 6,343,479, 2002; 5301516, 1994; 5106512, 1992; US 2008/0314062 A1, 2008). In most configurations, air is drawn over condensing coils, where it cools to dew point. Then, the liquid water passes through a series of filters (e.g. mineral, sediment, carbon, membrane) and either a UV bulb or ozone for disinfection.

Water production rate of dew point cooling systems is both a function of the quantity of water in the air (**Equation 1**) and the heat transfer properties of the refrigerant. Bagheri (2018) tested 3 commercial atmospheric water harvesting units (names not provided) that were rated with water generation capacity of 30 L/day and 1500 W power requirement in an environmental chamber under various climatic conditions. Climate can have a severe impact on rate of water capture: in cold and humid simulated climates, water capture rate was 0.05 L/hr using 6.23 kWh/L, while in warm and humid simulated climates, water capture rate increased to 0.65 L/hr at 1.02 kWh/L.. (Bagheri, 2018). **Table 2-1** contains a summary of commercial atmospheric water capture units. Most companies report the upper limit of water capture capacity (i.e. measurements taken at RH = 80%), which can range from 7 L/day to 5000 L/day depending on the size

Table 2-1 Commercial atmospheric water capture machines for drinking water

Company	Machine name	Capacity	Power	kWh/L	$/L from kWh	Features	Notes
Drinkable air	Chameleon 8	up to 38 L/day	765 W	0.48	0.05	Compressor system; Ozone purification (adds 70 ppm oxygen to water) every 15 mins; air filter, mineral filter, and 5µm carbon block filter	Working temp 70-100F (21-38C); Working RH 35-100; **"Recommended for indoor use only"**
Atmospheric water solutions	Aquaboy Pro II	7.5-19 L/day	970 W (Heating 500W, generating power 470W)	0.63	0.07	Compressor system; 7 stage EZ-filter: HEPA, UV, sediment filter, activated carbon/coconut shell, UF membrane, carbon filter #2, UV #2; microcomputer and sensors	T 55-90 F, RH 28-90; **"Not designed for outdoor use"**
Akvo	Akvo 55K	150 L/day	2100 W	0.34	0.04	Compressor system; nano carbon filter	Ideal T=25-32C, RH=70-75; Can also operate in T=18-45C, RH=35-40
	Akvo 110k	300 L/day	3300 W	0.26	0.03	Compressor system, Ozonator, 5µm sediment filter, nano carbon filter, UV	Ideal T=25-32C, RH=70-75; Can also operate in T=18-45C, RH=35-40
	Akvo 180k	500 L/day	4000 W	0.19	0.02		
	Akvo 365k	1000 L/day	8200 W	0.20	0.02		
Genaq	Stratus	50 L/day	700 W	0.34	0.04	Compressor system; carbon filter + "purifyer"	for residential, office, hotels, hospitals
		200 L/day	2450 W	0.29	0.03		
	Nimbus	500 L/day	4.1 kW	0.20	0.02		"remote supply units"; options for solar panel power or diesel power
		4500 L/day	40 kW	0.21	0.02		
	Cumulus	50 L/day	700 W	0.34	0.04		emergency response unit; options for solar panel (AC power) and diesel
		500 L/day	4.1 kW	0.20	0.02		
		5000 L/day	50 kW	0.24	0.03		
Water Gen	GEN-350	up to 900 L/day	5.6 kW; 0.33 kWh/L; 3.3 L/kWh	0.15	0.02	Patented technology (plastic heat exchanger); sediment filter, activated carbon, UV, mineralization	2-4 cents/L based on 8c/kWh,also a large scale option available
Skywater	30	100 L/day				Compressor system; ozone, carbon filter	RH 40-100, T 21C-32C; xPrize winner; Skywater300 used by military, 1 gal fuel = 10-14 gallons water/hr
	75	250 L/day					
	150	500 L/day	4.2 kW	0.20	0.02		
	300	1000 L/day	7-10 kW/hr	0.24	0.03		
	ESU-20	3400 L/day	30 kWh/hr	0.21	0.02		
H2O machine		10-115 L/day	1500 W	0.31	0.13	Compressor system; "various purification measures"	$0.08/gallon

of the unit. Energy efficiency of these systems ranges from 0.15 – 0.63 kWh/L. This upper end value is the same as the enthalpy of condensation. This implies that systems that are able to condense water vapor with less energy than the enthalpy of condensation are reusing heat or energy within the compressor system.

Compressor systems are the ideal water capture technology for regions where relative humidity is very high (i.e. >60%) because the energy requirement to operate refrigerants to decrease the air temperature and saturated vapor pressure can be supplied by generators or diesel power. The energy cost of these systems is already at or below the minimum thermodynamic energy of condensation. There could be an opportunity to improve the energy efficiency of these systems even further by developing refrigerants with enhanced heat transfer properties or designing heat sinks that improve waste heat capture and reuse.

2.3.3. Desiccants

Desiccants sorb water vapor from the air due to a pressure differential between the air (i.e. RH) and the desiccant surface. Desiccants continue to sorb water until they reach equilibrium with the surrounding air. Once the desiccants are saturated, they can be regenerated by heating, which increases the vapor pressure at the desiccant surface and causes the water vapor molecule to desorb. The amount of water adsorbed from the air and the temperature requirement for desorption depends on the type of desiccant used (American Society of Heating Refrigerating and Air-Conditioning Engineers, 2013).

2.3.3.1. Solid Desiccants

Solid desiccants *adsorb* water vapor onto their surface by physical adsorption mechanisms (i.e. van der Waals), and the desiccant does not change state. The affinity of

a desiccant to water vapor is illustrated by its water vapor sorption isotherm (Zheng, Ge, & Wang, 2014). In a Type I (i.e. Langmuir) isotherm, water vapor sorption capacity and relative humidity are linearly correlated until the material begins to reach its maximum sorption capacity. These materials are typically microporous, and the maximum sorption capacity is a function of the surface area and pore volume. Type IV materials are mesoporous and have an isotherm similar to Type I for lower RH, indicating monolayer saturation, followed by a large step increase in sorption capacity at mid-range RH, indicating capillary condensation, i.e. water vapor phase changes into a liquid-like state inside the pores of the desiccant. Type V materials also have capillary condensation at mid-high RH, but have very low sorption capacities at low RH. Type VI materials exhibit step-wise multi-layer adsorption. Desiccants are not usually Type II (nonporous and microporous materials), or Type III (hydrophobic, weak adsorbate-adsorbent interaction) (Burtch, Jasuja, & Walton, 2014).

Common solid sorbents include silica and zeolite. Silica gel adsorbs water though hydrogen binding to surface silanol groups (W. Wang et al., 2013). The pore size of the silica can impact the sorption capacity and isotherm; average pore diameter of 2 nm will result in a Type I isotherm with maximum sorption capacity 0.35 – 0.4 g water / g material, while pore diameter of 10 nm (mesoporous silica MCM-41) results in Type V isotherm (i.e. very low sorption capacity at lower RH) with capillary condensation occurring at 80% RH (Branton, Hall, Treguer, & Sing, 1995; Tashiro, Kubo, Katsumi, Meguro, & Komeya, 2004). This trend follows micropore filling theory – micropores (<2 nm) have higher adsorption affinity than mesopores (2 – 50 nm) and macropores (> 50 nm) (Dawoud & Aristov, 2003). This explains why desorption activation energy

increases from 26 kJ/mol to 35 kJ/mol as pore size decreases from 10 nm to 2 nm (X. Li, Li, Xia, & Xi, 2007; W. Wang et al., 2013). Silica gel can be regenerated at 90^{o}C, but the time is not reported. At 140^{o}C, 95% of the water can be evacuated from the silica in 5 minutes (Ng et al., 2001).

Zeolites, also known as molecular sieves, are aluminosilicates of alkali or alkali earth elements (e.g. potassium, sodium, calcium). A high Al/Si ratio, implying large aluminum content of zeolite, increases its adsorption capacity due to the large number of hydrophilic active sites. There are a variety of zeolites with varying pore sizes, such as Zeolite 4A (sodium) with 0.4 nm pores, 5A (calcium) with 0.5 nm pores, and 13X (sodium) with 0.85 nm pores (Cohen, 2003). Zeolites exhibit Type I isotherms and are excellent moisture sorbents at lower RH but reach their maximum sorption capacity of 0.25 g water / g material at RH 20%. They require very high temperatures (150 – 250 ^{o}C) for desorption because it is difficult to break the water-aluminum bond (Permyakova et al., 2017; W. Wang et al., 2013; Zheng et al., 2014).

A new class of solid desiccants are metal organic frameworks (MOFs), composed of metal ions linked by organic ligands in porous, cage-like structures. The variety of metals, ligands and frameworks that can be designed lend MOFs a high level of tunability for a desired application. MOFs can sorb water i) by chemisorption, where water is adsorbed onto the metallic clusters following Type I isotherm, ii) reversibly, through monolayer or multilayer sorption, or iii) irreversibly, through capillary condensation (Type IV, V, VI) (Canivet, Fateeva, Guo, Coasne, & Farrusseng, 2014).

CPO-27 (Co_2(2,5-dihydroxyterephthalate)) and HKUST-1 (Cu_3(1,3,5-benzenetricarboxyate)$_2$) sorb water by chemisorption, where a water molecule is

coordinated with a metal atom. Water vapor uptake increases linearly (i.e. Type I) until the molar equivalent of water uptake is greater than the molar equivalent of metal coordination sites on the MOF, which causes the material to become unstable and decompose. Therefore, they are not ideal for water capture (Canivet et al., 2014; Küsgens et al., 2009).

UiO-66 (Zr_6O_6(1,3,5-benzenetricarboxyate)$_{12}$) and MOF-801 ($Zr_6O_4(OH)_4$(fumarate)$_6$) adsorb water reversibly over at least 5 cycles and have high water stability. MOF-801 is ideal for low RH conditions, with sorption capacity of 0.2 g water/g material at RH 10%, and UiO-66 sorbs 0.5 g water/g material at 50% RH. Both materials have been used for water capture and adsorption heat pump applications (Fathieh et al., 2018; Furukawa et al., 2014; H. Kim et al., 2018a; H. Kim, Yang, et al., 2017; Schoenecker, Carson, Jasuja, Flemming, & Walton, 2012).

MIL101-(Cr) has a very large step increase in sorption capacity at mid-RH (either Type V or Type VI), indicating sorption by capillary condensation into the MOF's pores. MIL-101(Cr) has a very high surface area (>3000 m^2/g), which leads to the highest sorption capacity of all MOFs at 1.4 g water / g material at >70% RH, but the hydrophobicity of its organic linkers can limit water sorption at lower RH (0.1 g water / g material at <30% RH). MIL101(Cr) exhibits a large desorption hysteresis loop because of strong interactions between the water vapor molecules and the pores of the MOF (Akiyama et al., 2012; Khutia, Rammelberg, Schmidt, Henninger, & Janiak, 2013; Seo et al., 2012; Xian et al., 2015; Yan et al., 2015). The MIL family of MOFs also contains MIL-100(Fe) with surface area 1900 m^2/g and MIL-100(Al) with surface area 1800 m^2/g. MIL-101(Fe) can uptake 0.7 g water / g material at RH > 50% with a smaller desorption

hysteresis loop than MIL-101(Cr), and it does not contain chromium, which could be seen as problematic in a drinking water application (Jeremias, Khutia, Henninger, & Janiak, 2012; S. Wang, Li, Zhao, & Li, 2015).

The advantage of MOFs is that the regeneration temperature is typically below the boiling temperature of water. Some MOFs can be regenerated at 80^{o}C (Khutia et al., 2013; Seo et al., 2012). However, few studies have shown that when cycling between adsorption and desorption multiple times, desorption is performed 140^{o}C (Jeremias et al., 2012; Jeremias, Lozan, Henninger, & Janiak, 2013).

System configurations for solid desiccants include rotating honeycomb wheel, packed bed, and fluidized bed. The most common configuration is the rotating honeycomb, where desiccants are encapsulated within a wheel that rotates between an adsorption zone open to air, and a desorption zone where heat is applied and desorbed water vapor is directed towards a condenser. The wheel is considered an optimal configuration because of high space efficiency, dehumidification efficiency, ability to adsorb and desorb simultaneously, and use low- grade heat sources (W. Wang et al., 2013). Electrical power and solar heat and power have been implemented to drive desorption of water vapor from the desiccant and operation of the wheel (Ahmed, Kattab, & Fouad, 2005; US 2018/0043295 A1, 2018; Ge, Li, Wang, & Dai, 2008; La, Dai, Li, Wang, & Ge, 2010; Misha, Mat, Ruslan, & Sopian, 2012; W. Wang et al., 2013). Friesen (2018) produce up to 5 L water per day using solar operated desiccant wheel configuration (US 2018/0043295 A1, 2018).

Desiccants can be packed into a vertical bed, with moist air flowing from bottom to top for a period of time (e.g. 20-30 mins), followed by flow of dry hot air to desorb the

vapor (Hamed, 2002). Pesaran found that in a packed bed, there is a dynamic hysteresis that was not predicted by models of packed beds (Pesaran & Mills, 1987a, 1987b). Awad (2008) and Hamed (2010) suggest that in a packed bed, adsorption efficiency can be limited due to concentration gradient or pressure drops across the bed because the bottom layers adsorb moisture faster than the top layers. A radial flow packed bed can fix the pressure drop issue by flowing air from a hollow inside cylinder outwards, decreasing the distance air has to travel through the bed as well as the energy required to blow air over the bed (Awad, Ramzy K, Hamed, & Bekheit, 2008). Fluidized beds can also fix issues faced by a packed bed. The bed can be fluidized with humid air during adsorption such that each desiccant can get access to the humid air stream. Desorption with hot air is performed after adsorption is complete (Chiang, Chen, Chiang, & Chen, 2016; Hamed, Abd El Rahman, & El-Eman, 2010).

Solid desiccants have also been used in a thin-layer bed for "passive" atmospheric water capture. In this configuration, water vapor is adsorbed onto the desiccants at night, when RH is high, and desorbed from the desiccants during the day using solar thermal heat (Fathieh et al., 2018; H. Kim et al., 2018a; H. Kim, Yang, et al., 2017). Kim (2017,2018) used MOF-801 in a copper foam coated with graphite or pyromark paint and produced 0.25 L H_2O/kg MOF, or 0.2 L water/m^2 desiccant with bed thickness 5 mm in one adsorption cycle at 20% RH (H. Kim et al., 2018a; H. Kim, Yang, et al., 2017).

2.3.3.2. Liquid Desiccants

Liquid desiccants *absorb* water vapor and undergo a chemical change from solid to liquid phase to form a saturated solution. Examples of liquid desiccants include triethylene glycol, calcium chloride, lithium chloride, and lithium bromide. Since

triethylene glycol has a low vapor pressure, some of the desiccant can evaporate into the air when heated during desorption, which is both dangerous for drinking water applications and causes loss of the desiccant (Fumo & Goswami, 2002). Lithium chloride is an excellent sorbent; 1 molecule of LiCl can hold 2 molecules of water vapor before hydrating to the liquid phase. Then, it can continue to absorb water as a liquid. At 90% RH, LiCl can hold 26 molecules of water (American Society of Heating Refrigerating and Air-Conditioning Engineers, 2013). A downside of LiCl is that it can be corrosive. Calcium chloride is not as good a drying agent as lithium chloride, 1 molecule of $CaCl_2$ can hydrate 6 molecules of water. However, $CaCl_2$ is safer, cheaper and abundant (Kallenberger & Fröba, 2018).

When used in dehumidification, liquid desiccants are sprayed over a humid stream of air. In a packed bed absorption tower, a desiccant is sprayed and trickles over a high surface area material, where it comes into contact with the air to be dehumidified. The saturated desiccant, now in a liquid phase, is regenerated by heating. The vapor is cooled by condensation on a cool surface (e.g. refrigerant or cool process air) and the desiccant is returned to be reused. (Fumo & Goswami, 2002; Gido, Friedler, & Broday, 2016; Jain & Bansal, 2007; Martin & Goswami, 1999; Öberg & Goswami, 1998)

Liquid desiccants have also been studied for passive solar-driven atmospheric water capture. Calcium chloride is saturated into a cloth that can be positioned as a corrugated bed or tiered flat sheets. In a similar manner as the passive desiccant AWC system, the desiccants are saturated at night, and water is recovered during the daytime using solar thermal heat (Gad, Hamed, & El-Sharkawy, 2001; Mohamed, William, & Fatouh, 2017; William, Mohamed, & Fatouh, 2015). Li (2018) studied copper chloride,

copper sulfate and magnesium sulfate salts coated with carbon nanotubes for passive solar atmospheric water capture (R. Li, Shi, Shi, Alsaedi, & Wang, 2018). Calcium chloride and CNT were incorporated into a hydrogel and tested for water sorption at 60-70% RH. Under normal solar irradiation, 0.3 g water/ g material was recovered, and under a magnifying glass, 0.52 g water / g material was recovered (R. Li, Shi, Alsaedi, et al., 2018).

2.4. Conclusions

The atmosphere is a promising resource reservoir to provide decentralized drinking water at various scales, from household scale (1 – 10 L/day) to large community scale (up to 5000 L/day). The last two decades have seen two largely separate research directions. On the one hand, the commercial sector has established and patented compressor systems with refrigerants for active AWC, in which water vapor is cooled to dew point to condense. On the other hand, academic research has developed high performance desiccants for passive solar AWC.

While each approach has been tested with ideal conditions, many issues about practical application have not been resolved. For example, the level of success each AWC technology will have in different climatic regions is unknown. Likewise, it is unclear if solar can provide enough energy to operate systems with > 2L/day production. Furthermore, the quality of water produced has not been broached. To overcome these knowledge gaps, there is critical need to develop models to predict AWC production in various climatic regions, technologies to improve water yield and cost, as well as study AWC water quality.

GEOSPATIAL CLIMATIC FACTORS INFLUENCE WATER PRODUCTION OF SOLAR DESICCANT-DRIVEN ATMOSPHERIC WATER CAPTURE DEVICES

This chapter has been submitted and is under review for publication as:

Mulchandani, A. and Westerhoff, P. Geospatial Climatic Factors Influence Water Production of Solar Desiccant-Driven Atmospheric Water Capture Devices. *Submitted to Environmental Science and Technology*. Jan 2020.

3.1 Abstract

Atmospheric water capture (AWC) can provide clean drinking water in locations not connected to the centralized water grid for disaster relief, rural, military, and other applications. The atmosphere contains 14% of the equivalent freshwater volume stored in lakes and rivers and is universally accessible without pipelines or dams. A growing number of solar-based materials and devices to capture water vapor off the electrical grid have been reported, all of which assume varying relative humidity, solar irradiance, and desiccant materials (e.g., silica gel, zeolite, metal organic frameworks). This work uses Monte Carlo simulations and geospatial mapping to integrate material and system parameters from literature with United States spatial and temporal climate data to pinpoint key driving parameters for solar desiccant driven AWC and forecast AWC potential ($L/m^2/day$). Solar irradiance provides energy to desorb water vapor adsorbed to desiccants and determines maximum AWC capacity with respect to location and season; 4–8 L/m^2 system footprint/day can be captured across the United States in spring and summer, while capacity lowers to 0–5 $L/m^2/day$ in fall and winter. Desiccants can be designed with Langmuir specific surface area > 1500 m^2/g and Langmuir constant (k_L) > 0.1 to adsorb water vapor and meet these maximum potentials.

3.2 Keywords

Water vapor adsorption, solar desorption, atmospheric water harvesting, relative humidity, drinking water, off-grid, geographic information system mapping (GIS)

3.3 Introduction

Water scarcity is a global issue that impacts 4 billion people each year. (Damania et al., 2017) Freshwater scarcity has led to unconventional water supplies (e.g., oceans, brackish groundwater, and wastewater reuse) that require advanced treatment to remove salts and pollutants prior to use. (E. Jones, Qadir, Vliet, Smakhtin, & Kang, 2019) These solutions are adequate for large municipal treatment systems. (Larsen, Hoffmann, Luthi, Truffer, & Maurer, 2016) However, small water systems, military units, humanitarian aid units, rural communities, or communities without access to water and electrical grids after a natural or municipal disaster may face financial or operational challenges that limit ability to implement and maintain the required infrastructure. (Foster et al., 2018; Thomas, 2016; United States Environmental Protection Agency, 2016, 2019) Atmospheric water capture (AWC) is an emerging technology that can provide a localized or point-of-use solution to freshwater scarcity. The atmosphere contains 12,900 km^3, or 3.4 quadrillion gallons of water vapor, is universally present, and can provide water off the municipal water grid. (Shiklomanov, 1992)

AWC devices that pull water from the air can be grouped as: 1) dew collectors, 2) condensation by cooling to dew point temperature, and 3) moisture capture by a sorbent (i.e., desiccant). (Wahlgren, 2001) Dew collectors capture water aerosols rather than water vapor, and thus only function when relative humidity (RH) $\geq$ 100%. (Ang et al., 2019; D. Chen et al., 2018; Lalia et al., 2013; D. Li, Huang, Han, & Guo, 2018; K. C.

Park et al., 2016; Parker & Lawrence, 2001) Many electrical plug-in commercial systems (e.g., WaterGen, AquaBoy®) operate by condensing water vapor onto refrigerant coils, but these can only operate when $RH \geq 30\%$. (7,272,947 B2, 2007; US 2010/0266742 A1, 2010; 5,669,221, 1997; US 6,945,063 B2, 2005; 6,343,479, 2002; US 7.043.934 B2, 2006; US 2008/0314062 A1, 2008; 5,701,749, 1997; Wahlgren, 2001) In the Midwest and Eastern United States (U.S.), average year-round *RH* varies between 60 and 100%, so dew collection systems cannot be universally applied, while in the Southwestern U.S., *RH* is often < 30%, rendering both dew and condensation systems non-functional (**Figure 3-S1**). Desiccant systems operate by sorption of water vapor to bring it closer to saturation, desorption induced by heat or pressure, and condensation by cooling the saturated vapor. (American Society of Heating Refrigerating and Air-Conditioning Engineers, 2013; Cohen, 2003; Gido et al., 2016; Zheng et al., 2014) Desiccants can be either liquid or solid. Liquid desiccants (i.e., saturated salts) are not advantageous because there are three thermodynamically-intensive water phase changes occurring, including: 1) sorption of water to form the saturated salt solution (i.e., liquid), 2) heating the saturated salt to release the liquid water into the vapor phase, and then 3) condensing the vapor back to a liquid. In addition, salts may carry over into the clean liquid water stream, and salt particle agglomeration limits adsorption. (Abualhamayel & Gandhidasan, 1997; B. Chen, Zhao, & Yang, 2019; Gad et al., 2001; Gido et al., 2016; Jain & Bansal, 2007; Kallenberger & Fröba, 2018; R. Li, Shi, Alsaedi, et al., 2018; R. Li, Shi, Shi, et al., 2018; R. Li, Shi, Wu, Hong, & Wang, 2019; Mohamed et al., 2017; William et al., 2015)

In solid desiccant systems, water vapor molecules adsorb onto desiccant surfaces by physical adsorption mechanisms (i.e., van der Waals), and neither the desiccant nor

water vapor change state. (Cohen, 2003) Solid desiccants can be used in solar-driven water capture systems to provide drinking water off both the water and electrical grid. (Ahmed et al., 2005; H. Kim et al., 2018a; H. Kim, Yang, et al., 2017; Rieth, Yang, Wang, & Dincă, 2017) Examples of solid desiccants include silica gel, zeolite, and metal organic frameworks (MOFs). Solid desiccants are stable, durable, and safe over 5–40 regeneration cycles and up to 10,000–100,000 hours. (American Society of Heating Refrigerating and Air-Conditioning Engineers, 2013; Henninger, Munz, Ratzsch, & Schossig, 2011; Jeremias et al., 2012, 2013; Khutia et al., 2013; S.-I. Kim et al., 2016; Seo et al., 2012; C. Wang et al., 2019) For these reasons, this paper focuses on solid desiccants' suitability to generate potable drinking water.

In solar desiccant AWC devices, desiccants are layered in a packed bed and exposed to open outdoor environment at night. During the day, the saturated desiccant bed is exposed to solar radiation to drive desorption. (H. Kim et al., 2018a; Lapotin, Kim, Rao, & Wang, 2019a) Recent experimental and modeling studies have shown desiccants with sorption capacity up to 1.6 g water / g desiccant at ideal conditions (i.e., *RH* > 60%), and 0.4 g water / g desiccant in arid conditions (i.e., *RH* 20%). (H. Kim, Yang, et al., 2017; Lapotin et al., 2019a) However, desiccant behavior and operation as a function of geographic climatic variability are not yet studied.

Climate varies with geography, season, and time of day. In arid climates, vapor density (ρ_{vapor}, **Equation 1**) varies from 4 to 14 g/m^3 over the year, whereas ρ_{vapor} ranges from 14 to 22 g/m^3 in humid gulf coast regions **(Figure 3-1 a-b**). *RH* (**Equation 2**), which describes water saturation of the air (**Equation 3**), varies diurnally and inverse to temperature (**Figure 3-1 c-f**).

$$\rho_{vapor} = \frac{e}{R_v T_{air}} \tag{1}$$

$$RH = \frac{e}{e_s} * 100 \tag{2}$$

$$e_s = e_{s0} \exp\left(\frac{L_v}{R_v}\left[\frac{1}{T_0} - \frac{1}{T_{air}}\right]\right), \tag{3}$$

where e is vapor pressure (Pa), e_s is saturated vapor pressure (Pa) at temperature T_{air} (K), e_{s0} is saturated vapor pressure (611 Pa) at temperature T_o (273 K), R_v is the vapor gas constant (461 J/kg-K), and L_v is latent heat of vaporization (2250 kJ/kg).

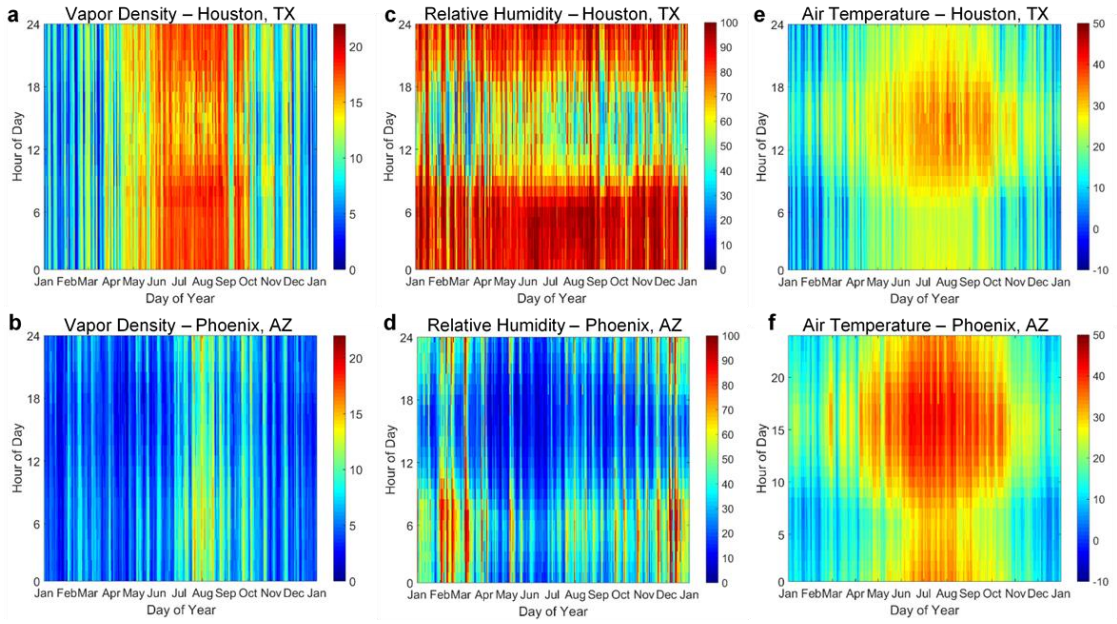

Figure 3-1 Vapor density, g vapor / m^3 air (left), relative humidity, % (middle) and temperature, °C (right) over the course of a typical meteorological year in a humid region (Houston, TX) (top) and an arid region (Phoenix, AZ) (bottom). X-axis represents day of year, from January 1 to December 31; y-axis represents hour of day, where 0 is midnight and 12 is noon. Data obtained from National Solar Radiation Database Typical Meteorological year 3 files. (National Renewable Energy Laboratory, n.d.)

Diurnal fluctuations are more pronounced in humid climates than arid climates. Solar radiation intensity drives solar-AWC systems and also exhibits geospatial and temporal variation, from 0.08 kWh/day in northern U.S. latitudes in the winter to 8 kWh/day in the southwestern U.S. in the spring and summer. (National Renewable Energy Laboratory, n.d.) This indicates that AWC potential, both adsorption potential as a function *RH* and ρ_{vapor} and desorption potential as a function of available solar radiation, will vary by geographic location, climate, season, and time of day.

The aim of this paper is to identify the relationship between atmospheric parameters (e.g. *RH*, solar radiation availability) and solid desiccant material properties to quantify geospatial and temporal water production potentials. We use first principles of adsorption/desorption on desiccants with Monte Carlo simulations and sensitivity analysis to define an operational envelope (i.e., boundary conditions). This is coupled with year-round atmospheric data to quantify and map geographic and seasonal potential of solar-driven AWC using solid desiccants across the U.S. This analysis answers three research questions: 1) What is the impact of geospatial climatic and seasonal factors on the water volume that can be captured using existing desiccants? 2) Which material, system, and climate parameters most impact AWC potential? 3) What is the maximum AWC potential based on available solar irradiance for desorption? Geospatial analysis is presented for the U.S., but the method can be applied to any region in the world.

3.4 Conceptual System and Thermodynamic Modeling Approach

To normalize water production to standard, scalable areal units, our analysis assumes a solid desiccant-based device with a 1 m^2 footprint and a total system volume of 1 m^3 (**Figure 3-2**). The 1 m^2 footprint correlates to units of solar radiation (W/m^2) and

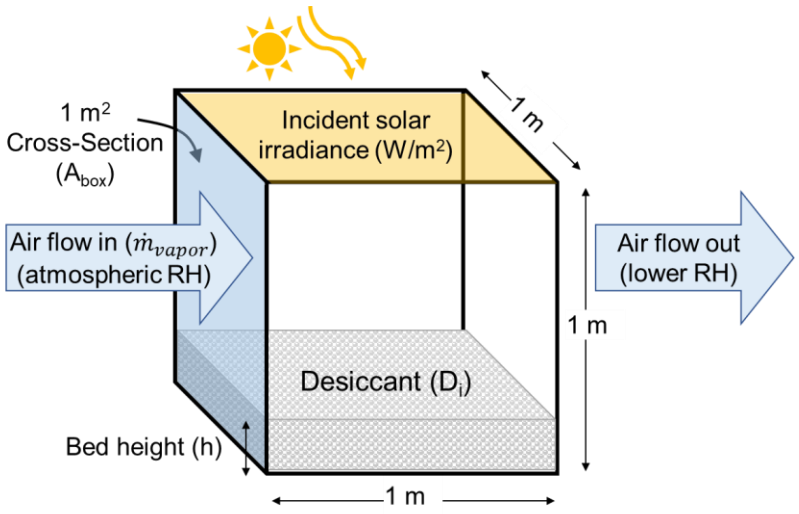

Figure 3-2 The system control volume (CV) for water capture is 1 m^3, with 1 m^2 footprint. The desiccant bed sits at the bottom of the CV with bed height *(h*). There is a constant linear direction of air flow through 1 m^2 cross-sectional area of the CV.

can be scaled for larger footprints for point-of-use or larger operation. The device contains a desiccant bed with height (*h*). Moist air moves via wind or fans over the desiccant bed through a 1 m^2 cross-sectional area (A_{box}).

Most solar desiccant-based systems are assumed to operate in diurnal cycles, adsorbing water vapor at night and desorbing it during the day. Saturated water vapor condenses on a cool surface (e.g., floor or walls of the AWC system) through dew point condensation. (H. Kim et al., 2018a) The units of AWC are L/m^2/day, referring to volume of water captured over the system footprint for 1 adsorption/desorption cycle per day.

3.4.1 Water Vapor Adsorption onto Desiccants

Desiccant water vapor holding capacity at a specified temperature is modeled with an adsorption isotherm relating the *RH* and the desiccant's sorption capacity (*q*, kg water vapor / kg desiccant). (Furukawa et al., 2014) Adsorption isotherms exhibit varying shapes according to the properties of the material; water sorbing materials typically

exhibit Type I or Type V isotherms. (Zheng et al., 2014) Type I isotherms are typical for hydrophilic materials (e.g., silica gel, zeolite, and some MOFs) and demonstrate a constant increase in vapor sorption capacity with *RH* until reaching a maximum sorption capacity. (Burtch et al., 2014; H. Kim et al., 2018a; H. Kim, Yang, et al., 2017; J. H. Kim et al., 2003; X. Li et al., 2007) Type V isotherms are typical for high surface area MOFs (e.g. MIL-101(Cr), MIL-100(Fe)), where sorption capacity is lower at lower *RH*. These MOFs exhibit a drastic step increase in sorption at an intermediate pressure ratio between *RH* at 40–60%, followed again by a slower step increase in sorption capacity for *RH* at 60–100%. (Akiyama et al., 2012; Canivet et al., 2014; S.-I. Kim et al., 2016; Qi, Hay, & Rood, 1998; Yan et al., 2015) Herein, we studied Type I materials using a Langmuir isotherm (**Equation 4**), representing commonly-deployed microporous materials with strong adsorbate-adsorbent interactions and reversible water sorption.

$$q = \frac{q_{max} k_L C_e}{1 + k_L C_e} \tag{4}$$

where q (g adsorbate / g adsorbent) is the adsorbent material's sorption capacity for an adsorbate at concentration C_e (g adsorbate / volume), q_{max} (g adsorbate / g adsorbent) is the adsorbent's maximum sorption capacity for the adsorbate, and k_L (volume / g adsorbate) is the Langmuir sorption constant.

While alternative isotherm theories can predict water sorption capacity for a wider material class, we chose a Langmuir sorption isotherm because it will match or overestimate water sorption capacity of Type V materials at lower *RH*, providing a more optimistic estimate for vapor sorption capacity at both low and high *RH*.

The water adsorption Langmuir isotherm is given by **Equation 5**,

$$q_{D_i} = \left[SSA_{D_i} * SSD_{D_i} * \frac{1}{N_A} * \left(\frac{0.018\ kg\ H_2O}{mol}\right)\right]\left[\frac{k_L RH}{1 + (k_L RH)}\right] \quad (5)$$

where q_{D_i} (kg vapor / kg D_i) is the desiccant (D_i) sorption capacity, k_L is the Langmuir constant (i.e., the slope of the step increase in vapor sorption capacity with *RH*) and becomes unitless, and C_e is the equilibrium concentration of the adsorbate (i.e., water vapor) and is denoted as *RH*. Here, q_{max} is the maximum desiccant sorption capacity to form a water vapor monolayer and is calculated as a function of SSA_{D_i}, which is the desiccant specific surface area (m^2/ kg D_i), SSD_{D_i}, which is the desiccant's specific site density (molecules/nm^2), and Avogadro's number N_A (6.02*10^{23} molecules). SSD_{D_i} denotes the number of hydroxyl sites available on the desiccant surface for water vapor molecule sorption, with a maximum potential of 12.8 molecules/nm^2 (i.e., the maximum packing density of water molecules (diameter 2.8Å) per nm^2 site). Together, SSA_{D_i} and SSD_{D_i} represent the number of sorption sites available per gram of desiccant. **Equations 6–8** define additional desiccant characteristics (volume V_{D_i} (m^3), mass m_{D_i} (kg), diameter d_{D_i} (mm), density ρ_{D_i} (kg/m^3)) to determine the water mass that will be adsorbed by a specific desiccant, D_i. **Equation 9** calculates the number of desiccants (N_{D_i}) contained within the system volume, using a packing density of spheres (0.64) and height of desiccant bed *h* (mm). (Lapotin et al., 2019a) The water volume adsorbed within a system containing N_{D_i} of a specific desiccant D_i is given by **Equation 11** (L water / m^2).

$$V_{D_i} = \frac{\pi d_{D_i}^3}{6} \quad (6)$$

$$m_{D_i} = \rho_{D_i} * V_{D_i} \quad (7)$$

$$Water\ adsorbed\ by\ 1\ desiccant\ = q_{D_i} * m_{D_i} \quad (8)$$

$$N_{D_i} = 0.64 * \frac{(1\ m^2 footprint) * h}{V_{D\,i}} \quad (9)$$

$$Mass\ of\ desiccants\ in\ system\ \left[\frac{kg\ D_i}{m^2}\right] = m_{D_i} * N_{D_i} \quad (10)$$

$$Volume\ water\ adsorbed\ in\ system = N_{D_i} * water\ adsorbed\ by\ 1\ desiccant \quad (11)$$

3.4.2 Water Vapor Desorption from Desiccants

Water vapor desorption from desiccant surfaces requires energy from either 1) reversal of pressure differential from a vacuum or 2) heating the desiccant to its peak desorption temperature to overcome the water vapor desorption activation energy ($E_{des_{D_i}}$). (American Society of Heating Refrigerating and Air-Conditioning Engineers, 2013; Redhead, 1962; Xian et al., 2015) Practical desiccant use for AWC, particularly off the electrical grid, indicates the latter is more favorable for desorption. (H. Kim et al., 2018a; R. Li, Shi, Shi, et al., 2018) **Equation 12** calculates $Q_{des_{D_i}}$ (kJ/m^2), the energy required to desorb all water vapor adsorbed to the desiccants contained in the 1 m^3 system volume.

$$Q_{des_{D_i}} = E_{des_{D_i}} * q_{D_i} * mass\ of\ desiccants\ in\ system * \left(\frac{mol}{0.018\ kg\ H_2O}\right) \quad (12)$$

where $E_{des_{D_i}}$ is the activation energy of desorption (kJ/mol).

If $Q_{des_{D_i}}$ is completely available, all of the water adsorbed on to the desiccants (**Equation 11**) will be desorbed. When using solar energy for desorption, only a portion of the adsorbed water will desorb if the available energy is less than $Q_{des_{D_i}}$, calculated by **Equation 13**.

$$Volume\ water\ desorbed\ from\ desiccants\ by\ solar\ thermal\ energy \quad (13)$$

$$= \frac{Solar\ energy\ available}{Energy\ required\ for\ desorption} * Volume\ H_2O\ adsorbed\ to\ D_i\ in\ system$$

Therefore, the AWC is dictated by desorption potential.

3.4.3 Monte Carlo Simulations and Sensitivity Analysis to Determine Operational Envelope of Solar Desiccant Based AWC

Monte Carlo simulations and sensitivity analysis were performed to understand the water capture operational envelope for desiccant parameters and the water volume captured by desiccants within the system volume. Monte Carlo simulations used a random number generator to vary the material, climate, and system parameters (**Table 3-1**) over a defined distribution shape to calculate all possible outputs for **Equations 6–12** and their likelihood. The independent variables ranges were based on literature data and material manufacturer specifications. This analysis used a triangular distribution because it is a common method for when limited data exist to perform a statistical analysis to fit to a specified probability distribution. (Landis, Miller, & Theis, 2007; Miller, Landis, & Theis, 2006; Song, Qin, Suh, & Keller, 2017; Weber & Clavin, 2012; Zaimes, Soratana, Harden, Landis, & Khanna, 2015) A probability distribution of 100,000 values was created based on provided minimum, peak, and maximum values.

A sensitivity analysis was conducted to understand the effect of individual independent variables. All independent variables (**Table 3-1**) were initially set to their "peak" (i.e., mode) to calculate the "most likely" outcome for water volume adsorbed by the system desiccants volume (**Equation 11**). Additionally, each parameter was individually varied to its minimum and maximum value while keeping all other variables

at their peak. This identified the magnitude of each variable's impact on the final outcome.

Table 3-1 Independent variables and range of values for Monte Carlo simulations and Sensitivity Analysis for water vapor adsorption and desorption onto desiccants

Indep. variable	Units	Values in distribution			Reference
		Min	Peak	Max	
Desiccant diameter (d_{D_i})	mm	1	3	5	(Ahn & Lee, 2004; Dawoud & Aristov, 2003; Kallenberger & Fröba, 2018; Seo et al., 2012)
Desiccant bulk density (ρ_{D_i})	kg/m^3	300	600	800	(Ahn & Lee, 2004; Kallenberger & Fröba, 2018; Seo et al., 2012)
Specific surface area (SSA_{D_i})	m^2/g	100	600	6000	(Ahn & Lee, 2004; Akiyama et al., 2012; American Society of Heating Refrigerating and Air-Conditioning Engineers, 2013; Burtch et al., 2014; Dawoud & Aristov, 2003; Furukawa et al., 2014; Seo et al., 2012)
Specific site density (SSD_{D_i})	sites /m^2	5x10^{18}	10x10^{18}	12.8x10^{18}	(Pfeifer, Freude, & Hunger, 1985)
Langmuir constant (k_L)	---	0.01	0.1	1	Calculated mathematically from isotherms
Bed depth (h)	mm	1	5	10	(Lapotin et al., 2019a)
RH		1	50	100	---
Activation energy of desorption ($E_{des_{D_i}}$),	kJ/mol	2	35	80	(X. Li et al., 2007; Redhead, 1962; S. Wang et al., 2015; Zhou et al., 2014)
Desiccant sorption capacity, (q_{D_i}),	kgH_2O / kgD_i	0.019	0.55	2.5	Calculated from adsorption
Mass of desiccants in the system	kgD_i / m^2	0.2	1.9	4.9	Calculated from adsorption

3.4.4 Geospatial Mapping of Solar Desiccant Based AWC

Geospatial and climatic models and maps were generated using data from National Renewable Energy Laboratory's (NREL) National Solar Radiation Database (NSRDB) Typical Meteorological Year 3 (TMY3) files. (National Renewable Energy Laboratory, n.d.) The database contains one year of hourly meteorological and solar irradiance data that best represents the median weather conditions at 1020 locations across the U.S. over several years. Because climate varies seasonally, we calculated the average night-time *RH* and ρ_{vapor} and day-time solar irradiance at each location for four seasons. Water capture and solar desorption potential were calculated at each data point using the seasonal averages. Then, data was spatially joined with U.S. county boundaries in ArcGIS to display the average in each county and within a 120-km surrounding radius of the county boundary.

We first mapped AWC potential across the U.S. by two commonly available and well-characterized materials (silica gel and zeolite) and one MOF that has one of the highest reported water sorption capacities (MOF MIL-101(Cr)). Adsorption capacity of silica and zeolite, both Type I materials, was calculated by **Equation 5** with material parameters (SSA_{D_i}, SSD_{D_i}, k_L) from literature (**Table 3-S1**) and seasonal average night-time *RH* inputs from NSRDB. MIL-101(Cr) adsorption capacity was obtained directly from isotherm data at the specified *RH* (**Figure 3-S2**). (S.-I. Kim et al., 2016; Seo et al., 2012) Total water sorption capacity by these desiccants in the system volume was calculated with **Equations 6–11,** with material parameters (i.e. d_{D_i}, ρ_{D_i}) from literature and *h* of 10mm, which the sensitivity analysis identified as the optimal value. We assumed the desiccant bed adsorbs water vapor and reaches saturation overnight,

therefore wind speed of vapor over the desiccants and adsorption kinetics are not considered. This assumption is valid because saturation typically occurs within 10 minutes to 4 hours. (Dawoud & Aristov, 2003; Hao et al., 2015; H. Kim, Yang, et al., 2017; Rieth et al., 2017; Tan et al., 2019; Yan et al., 2015) **Equation 12** was applied to calculate the total energy required for desorption. Daytime solar radiation intensity (kW/m^2) obtained from weather station data was summed over the daylight hours to calculate kWh/m^2, or kJ/m^2, of solar energy available for thermal desorption per day (1 kW = 1 kJ/s). If the available solar radiation energy was greater than $Q_{des_{D_i}}$, we assumed complete desorption of the water adsorbed that was calculated from **Equation 11**. Else, **Equation 13** was applied to calculate partial desorption.

Viewing the problem from another angle—where solar energy rather than desiccant mass limits AWC yield—the maximum solar desiccant based AWC potential can be calculated by the maximum water volume that could be desorbed by available solar thermal energy. **Equation 14** was applied to calculate and map geospatial AWC potential as a function of available solar energy and $E_{des_{D_i}}$ of 65 kJ/mol, which is the $E_{des_{D_i}}$ of MOF MIL-101(Cr).

$$Maximum\ volume\ water\ desorbed\ = \frac{Available\ solar\ energy}{E_{des_{D_i}}\ * \left(\frac{1mol}{0.018\ kg\ water}\right)} \tag{14}$$

Finally, **Equation 15** was applied to calculate and map the maximum volume available to capture in the atmosphere as a function of the water vapor mass passing through the scalable system volume over a 12-hour night. The 12-hour time frame represents the night-time adsorption phase of the solar desiccant AWC system. The wind

speed, v_{air}, was set to 1 m/s (i.e., 2.2 mph), representing "light air" flow the Beaufort scale. While average night-time wind speed at the NSRDB locations was 2–5 m/s, we chose a lower wind speed as a conservative estimate for this calculation.

$$\dot{m}_{vapor} = \rho_{vapor}\, v_{air}\, A_{box} \tag{15}$$

3.5 Results and Discussion

3.5.1 Geospatial Climatic and Seasonal Factors Affecting Volume Captured by Desiccants

Figure 3-3 and **Figure 3-S3** show seasonal variations in AWC by three commonly-studied desiccants (MOF MIL-101(Cr), silica, and zeolite). The maximum water production (3.1 L/m^2/day) occurs for MOF MIL-101(Cr). In the summer and spring, highest water production from MOF MIL-101(Cr) occurs along the west coast and in the midwestern and eastern half of the U.S. In the fall, highest water production occurs in the southeastern U.S. In the winter, highest production is only in Florida. Zeolite has a near constant annual production rate of 0.94 L/m^2/day year-around across the U.S. Silica gel's maximum water production (1.3 L/m^2/day) follows the same geospatial trend as MOF MIL-101(Cr) in the spring and summer. In the fall and winter, this value occurs throughout the U.S. barring the arid southwestern region. MOF MIL-101(Cr) is advantageous in regions where *RH* > 40%. As indicated by the adsorption isotherms of MOF MIL-101(Cr), zeolite, and silica gel, the latter two desiccants are more favorable in arid regions (i.e., *RH* < 40%). **Figure 3-3 d–f** shows a spring *RH* of 10–40% in the arid southwest results in AWC potential of 0.94 L/m^2/day for Zeolite, 0.84–1.3 L/m^2/day for silica gel, and 0.28–0.45 L/m^2/day for MOF MIL-101(Cr). This indicates AWC desiccant material selection should consider the region and season.

In the system volume posed in this model, the solar thermal heat required to drive desorption can be limited when the amount of available solar energy is insufficient to overcome the minimum thermodynamic requirement. For example, MOF MIL-101(Cr) is capable of capturing 3 L/m^2/day in the northern latitudes of the U.S. (e.g., Washington, North Dakota) in the winter. However, available solar radiation only permits 35% desorption (**Figure 3-3c)**. MOF MIL-101(Cr) requires a maximum of $1.1x10^4$ kJ/m^2 (3.1 kWh/m^2) for desorption, while zeolite requires $4.7x10^3$ kJ/m^2 (1.3 kWh/m^2), and silica gel requires $3.4x10^3$ kJ/m^2 (0.95 kWh/m^2). The solar constant is 1367 W/m^2, and solar panels typically assume solar irradiance as 1000 W/m^2 for 6 hours of daylight (i.e., 6 kWh/m^2). However, weather station data indicates that actual solar irradiance can be much lower than this theoretical value. Solar irradiance varies across the U.S. in the winter from 0.08 kWh/m^2 in the northern latitudes to 4.7 kWh/m^2 in the southern latitudes. Across the 1020 U.S. NSRDB data locations, 83% do not have enough solar irradiance in the winter to achieve complete desorption of MOF MIL-101(Cr) (**Figure 3-S4**). Only 7.4% and 6.9% of locations cannot achieve complete desorption of zeolite (**Figure 3-S6**) and silica gel (**Figure 3-S5**), respectively. Still, the total amount of water collected by the MOF, even with limited sunlight, can be up to double that of zeolite or silica in many regions due to its high adsorption capacity.

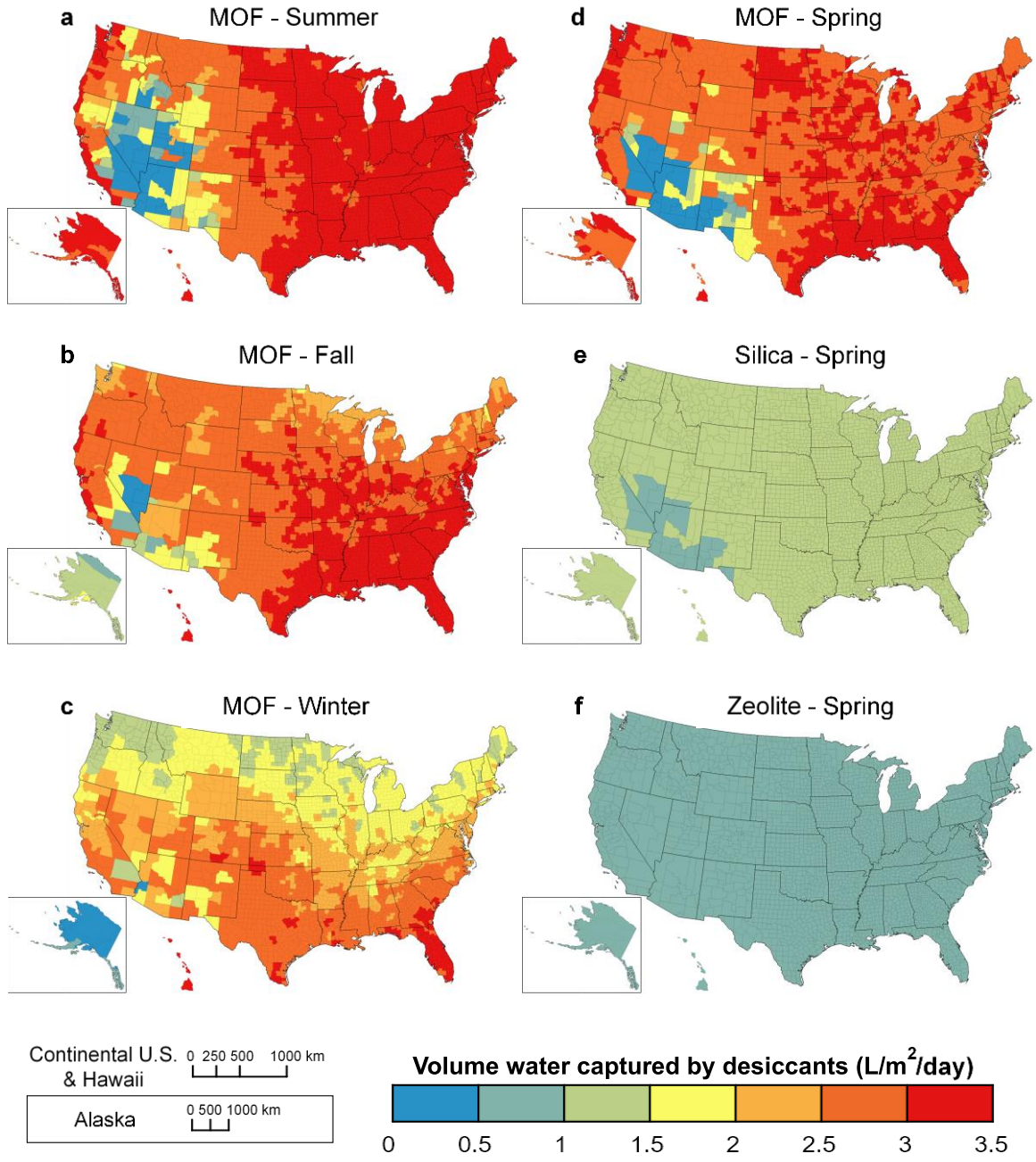

Figure 3-3 Geospatial atmospheric water capture potential for existing desiccants ($L/m^2/day$). a) MOF MIL-101(Cr) in summer, b) MOF MIL-101(Cr) in fall, c) MOF MIL-101(Cr) in winter, d) MOF MIL-101(Cr) in spring, e) silica gel in spring, f) zeolite in spring.

3.5.2 Material, System and Climate Parameters Having Greatest Effect on AWC Potential

Data shown in **Figure 3-3** and **Figure 3-S3** are based on representative, but singular, adsorbent materials. The literature reports many desiccants developed and tested for lab-scale and pilot-scale AWC, but the results are system and site specific. (Ahmed et al., 2005; Akiyama et al., 2012; American Society of Heating Refrigerating and Air-Conditioning Engineers, 2013; Branton et al., 1995; Burtch et al., 2014; Cadiau et al., 2015; Canivet et al., 2014; B. Chen et al., 2019; Dawoud & Aristov, 2003; Fathieh et al., 2018; Furukawa et al., 2014; Hall, Tsang, Casey, Khan, & Yang, 2012; Hao et al., 2015; Heidari, Roshandel, & Vakiloroaya, 2019; Henninger et al., 2011; Jeremias et al., 2012, 2013; Jia, Dai, Wu, & Wang, 2006; Khutia et al., 2013; H. Kim et al., 2018a; H. Kim, Yang, et al., 2017; S.-I. Kim et al., 2016; Küsgens et al., 2009; Lapotin et al., 2019a; Ng et al., 2001; Rieth et al., 2017; 2012; Seo et al., 2012; Tan et al., 2019; Tashiro et al., 2004; Wahlgren, 2001; C. Wang et al., 2019; W. Wang et al., 2013; Yan et al., 2015; S.-Y. Zhang et al., 2018) To better understand the material properties and operational parameters that maximize water production, Monte Carlo simulations were run to predict distribution frequency of water volume adsorbed (**Equation 11**) by many materials property, *RH*, and desiccant bed height (*h*) combinations (**Table 3-1**). **Figure 3-4a** shows cumulative distribution function for 100,000 trials, where the y-axis reports the number of trials yielding daily water capture volumes indicated on the x-axis. Independent variable combinations indicated 54% of material, *RH*, and *h* combinations yielded less than 1 L/m^2/day of water adsorbed in the system volume, consistent with results from materials such as silica and zeolite. This leaves 45,000 combinations that could yield

more than 1 L/m^2/day, which is marginally enough water to serve as an individual's drinking water supply; 45% of combinations yielded 1–5 L/m^2/day, and 0.4% yielded > 5 L/m^2/day.

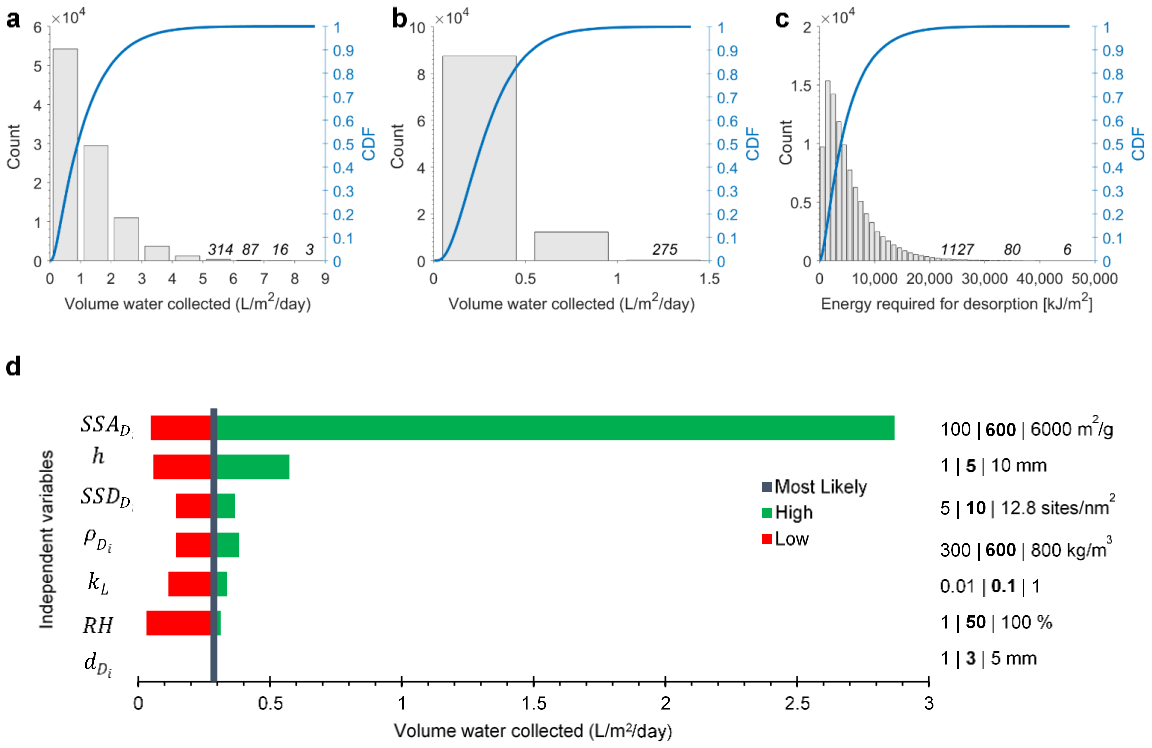

Figure 3-4 a) Cumulative distribution of volume of water collected by AWC system, calculated by Monte Carlo simulations over 100,000 trials. The primary y-axis (grey bars) indicates how many trials yielded a value between the boundaries indicated by the x-axis values. The secondary y-axis (blue line) shows a cumulative distribution function (CDF). b) Monte Carlo simulations using triangular distribution of SSA ranging from 100 to 1000 m^2/g, peak at 500 m^2/g, all other variables remain unchanged from Table 3-1. c) Cumulative distribution of minimum energy for desorption of water vapor from desiccants contained in system volume [kJ/m^2], calculated by Monte Carlo simulations using triangular distribution over 100,000 trials. d) Sensitivity analysis on independent variables that impact volume of water adsorbed by desiccants in a 1 m^2 footprint system. Centerline of tornado plot depicts most likely outcome if independent variables are set to "peak" value in Table 3-1. Low (red) and high (green) outcomes occur when single parameters are varied to their minimum and maximum value, respectively. Values on right represent *low* | *peak* | *high (units)* for each variable.

While the Monte Carlo simulations show the range and potential of water capture, they do not reflect the influence of individual material and system parameters. As such, a sensitivity analysis was performed to complement the probability distribution, and a tornado plot (**Figure 3-4d**) shows the results. The "most likely" outcome of 0.29 L/m^2/day of water adsorbed to the desiccants in the system volume occurs when all independent variables are set to their peak values listed in **Table 3-1**. The tornado plot width shows the final volume collected as each variable is modified to its lowest and highest possible values. Desiccant SSA_{D_i} has the greatest effect on water volume adsorption. When SSA_{D_i} is 6000 m^2/g (e.g., a MOF attached to graphene oxide (MIL-101(Cr)@GO)), 2.9 L/m^2/day could be adsorbed. For the lower end, SSA_{D_i} of 100 m^2/g only yields 0.05 L/m^2/day. While MIL-101(Cr)@GO has a Type V isotherm (as opposed to the Type I Langmuir isotherm used for this model) and would likely have a lower than projected water capture potential at lower *RH* (<40%), this analysis shows that designing Type I materials with very high SSA_{D_i} can further maximize AWC potential. Bed depth (*h*) linearly increases water production due to the linear relationship between N_{D_i} and '*volume water adsorbed in system'* (**Equations 9 and 11**). Bed depth (*h*) could be increased beyond 10 mm to increase water capture potential, but solar radiation availability may become a limiting factor for desorption.

Interestingly, high k_L and *RH* have little impact on net water adsorption. The Langmuir adsorption isotherm equation contains the term $\left[\frac{k_L RH}{1+(k_L RH)}\right]$, which only varies from 0.83 for the "peak" k_L and *RH* values to 0.91 or 0.98 for the highest k_L and *RH* values, respectively, thus reducing effect on the overall adsorption isotherm and

subsequent water volume adsorbed. However, decreasing *RH* to 10% can decrease $\left[\frac{k_L RH}{1+(k_L RH)}\right]$ to 0.5, which has a larger impact on the desiccant adsorption isotherm and subsequently the water volume adsorbed (0.17 L/m^2/day). This implies that if performing AWC in an arid region, traditional desiccant materials (i.e., those with parameters in the range of the "peak" of the triangular distribution indicated in **Table 3-1**) will have limited function and capacity, as seen in **Figure 3-S2**. To overcome the limitations posed by low *RH*, arid regions could use desiccants with high SSA_{D_i}, SSD_{D_i}, and k_L (i.e., steeper isotherm slope, which indicates higher adsorption capacity at low *RH*). Existing materials that fit these criterion are zeolites, UiO-66, MOF-801, and H_2N-MIL-125. (Burtch et al., 2014; Canivet et al., 2014; Fathieh et al., 2018; Jeremias et al., 2013; Schoenecker et al., 2012)

Because SSA_{D_i} has such a large effect on adsorption, it overshadows the impact of other variables. Therefore, a second Monte Carlo simulation sequence was conducted excluding high SSA_{D_i} materials. SSA_{D_i} ranged between 100 and 1000 m^2/g, with 600 m^2/g remaining the peak of the triangular distribution. **Figure 3-4b** shows the maximum water adsorption capacity for this class of desiccants is 1.4 L/m^2/day. The 275 material combinations that produce >1 L/m^2/day all have SSA_{D_i} greater than 560 m^2/g, bed height thicker than 6 mm, and SSD_{D_i} equal to or larger than 9.0x10^{18} sites/nm^2. The other independent variables did not have a large impact on the outcome. This analysis assumes no limitation posed by available solar irradiance.

High SSA_{D_i} materials such as MOFs seem to be ideal for increasing water adsorption capacity in a solar desiccant AWC system. MOFs were discovered and since

have been tailored in lab settings over the last 20 years, but producing large scale batches cheaply and efficiently makes them cost-prohibitive. For comparison, the average price of MOF from Sigma Aldrich, a commercial chemical producer, is >200 times higher than silica or zeolite. A MOF-based system producing 8 L/m^2/day, the highest value calculated from Monte Carlo simulations, requires 4 kg of high SSA_{D_i} MOF. At \$15/g, the system would cost \$60,000. In comparison, 5 systems containing 4kg SiO_2 each to capture a total of 8 L/m^2/day would have a material cost of \$1400, more than 40 times less than MOF. However, a larger system may require higher capital costs for framing, controls, etc. A formal technoeconomic analysis would be necessary. If material synthesis cost and large-scale production issues are alleviated, high SSA_{D_i} materials could perhaps replace conventional materials such as silica and zeolite.

A final Monte Carlo simulation sequence was performed on **Equation 12** with desiccant properties from **Table 3-1** to determine the range of potential desorption energy requirements. While E_{des} values were found in literature, q_{D_i} and '*mass of desiccants in the system*' were obtained from the first Monte Carlo simulation. **Figure 3-4c** shows resulting cumulative distribution frequency for the minimum energy required to desorb water vapor from desiccants contained in the system volume. The energy required for desorption varied from 9 kJ/m^2 to 45,000 kJ/m^2 (0.0025–12.5 kWh/m^2).

Using the standard value for solar irradiance (1000 W/m^2), 1 hour of constant irradiation under peak sunlight could overcome a minimum theoretical energy of desorption of 3600 kJ/m^2 (1 kWh/m^2), 2 hours of radiation could overcome 7200 kJ/m^2 (2 kWh/m^2), etc. Six hours of peak sunlight could provide 21,600 kJ/m^2 (6 kWh/m^2), enough thermal energy to completely desorb 99% of the values predicted in **Figure 3-4c**.

Therefore, using a theoretical constant for solar irradiance indicates the available solar thermal energy should not be a limitation for solar desiccant based AWC, even if the highest-adsorbing desiccant is used.

However, the geospatial analysis in the prior section showed that solar irradiance can be limiting in the winter, particularly in northern latitudes. In Alaska, 0.15–0.75 kWh/m^2 of solar radiation is available per day in the winter, which can desorb only 3.5%–35% of material combinations predicted in the Monte Carlo desorption analysis. At northern latitudes (40– 49°N), solar irradiance is 1.05–2.5 kWh/m^2, which can achieve complete desorption of 50–85% of material combinations. However, it is very likely that freezing temperatures and snow or other precipitation will occur during the majority of the winter in these latitudes, rendering solar AWC unlikely. Across the continental U.S., available solar irradiance can still be a limiting factor in the fall and spring, with 72–95% of material combinations achieving complete desorption in the fall and 50–99% of material combinations achieving complete desorption in the spring, depending on geographic location.

The theoretical energy of desorption, $Q_{des_{D_i}}$ is most affected by q_{D_i}, the desiccant sorption capacity. Therefore, it follows that desiccant SSA_{D_i} will have a large impact on the energy required for desorption because $Q_{des_{D_i}}$ is linearly correlated with SSA_{D_i} through the sorption capacity equation (**Equation 5**). Achieving complete desorption requires balancing desiccant material properties and AWC operation location, choosing a material with a high enough SSA_{D_i} but operating in a location with enough solar irradiance to overcome $E_{des_{D_i}}$.

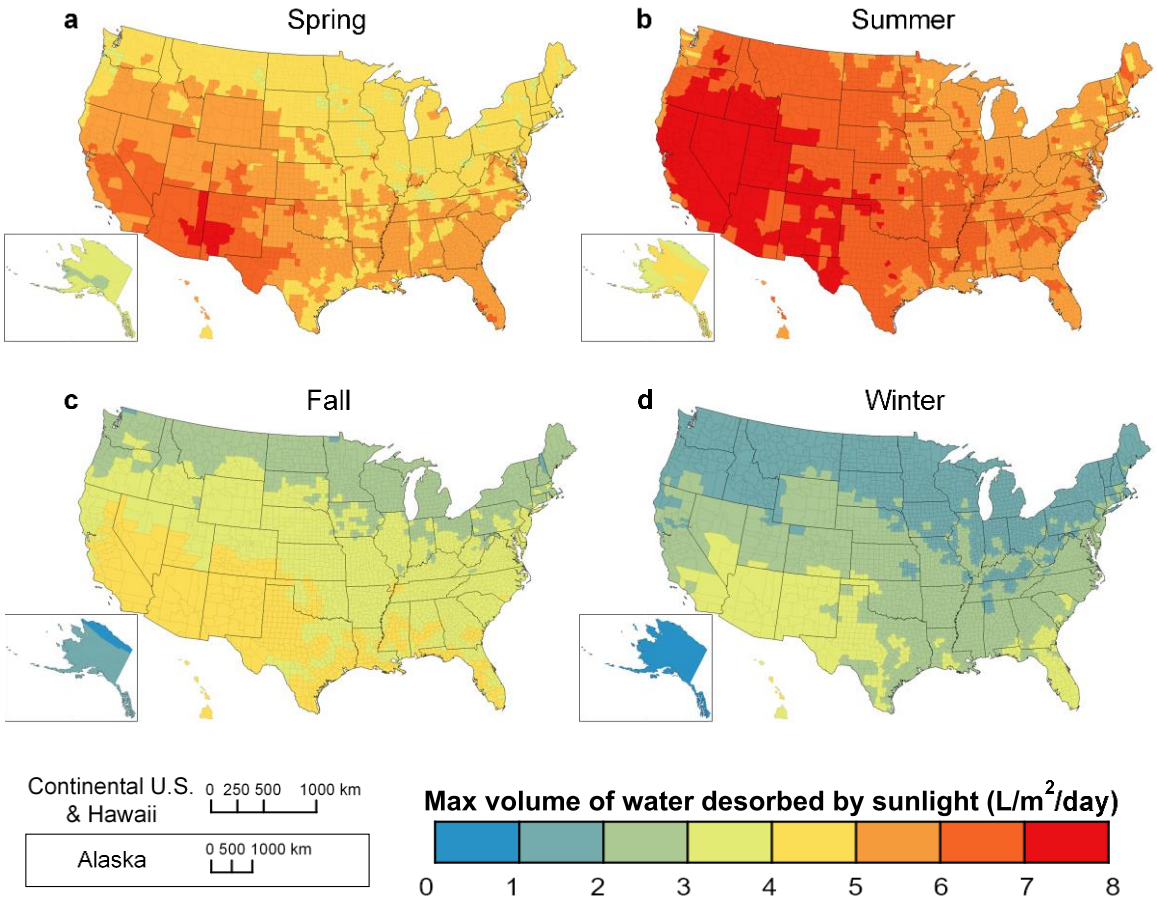

Figure 3-5 Water volume captured as a function of solar energy available for desorption when E_{des} = 65 kJ/mol in a) spring, b) summer, c) fall, and d) winter.

3.5.3 Maximum AWC Potential Based on Solar Irradiance Available for Desorption

The geospatial mapping analysis and Monte Carlo simulations both showed that AWC potential is often driven by the amount of available solar thermal energy. Even if an ideal, high SSA_{D_i} is utilized to maximize water adsorption, solar radiation to overcome the minimum thermodynamic requirement for desorption becomes the limiting factor. **Figure 3-5** shows AWC potential calculated by **Equation 14** as a function of desorption rather than adsorption. When using $E_{des_{D_i}}$ of 65 kJ/mol (i.e., MOF MIL-101(Cr)), AWC

potential varies from 0.50 to 8 L/m^2/day as a function of geography and season. This range matches the probability range predicted by Monte Carlo simulations on adsorption. Solar desorption calculations show AWC potential is highest in the summer, with water production 7–8 L/m^2/day in the western U.S. and 4–6 L/m^2/day in the eastern U.S. Spring AWC potential as a function of solar radiation is slightly lower than summer and varies across the country between 3 and 8 L/m^2/day. Distinct striations in AWC potential can be seen in the fall and winter as a function of latitude and available solar radiation. AWC potential in the fall is 2–4 L/m^2/day in the majority of the country, barring the southwest, which produces up to 5.2 L/m^2/day. Meanwhile, wintertime AWC potential is limited to 0–4.7 L/m^2/day as a function of latitude.

This analysis shows that the ideal way to choose a solar AWC desiccant for a specific geographic location is to first look at solar desorption potential rather than the material's adsorption characteristics. Desorption potential can then be coupled with *RH* to determine desiccant selection criteria; e.g., high k_L for arid climates, high SSA_{D_i} for the humid southeast where water vapor and solar radiation are abundant, and mid-range SSA_{D_i} for northern latitudes where a high-range SSA_{D_i} will not be able to desorb to its complete sorption capacity.

3.6 Outlook of Solar Desiccant Based AWC Systems

Conventional solar desiccant based AWC systems operate with desiccants passively adsorbing water vapor to reach saturation overnight and desorbing water vapor using solar thermal heat during the day. In this diurnal cycling mode, accounting for wind speed and water vapor movement over the desiccant bed has not been necessary because saturation conditions are always achieved. When considering the true mass of water

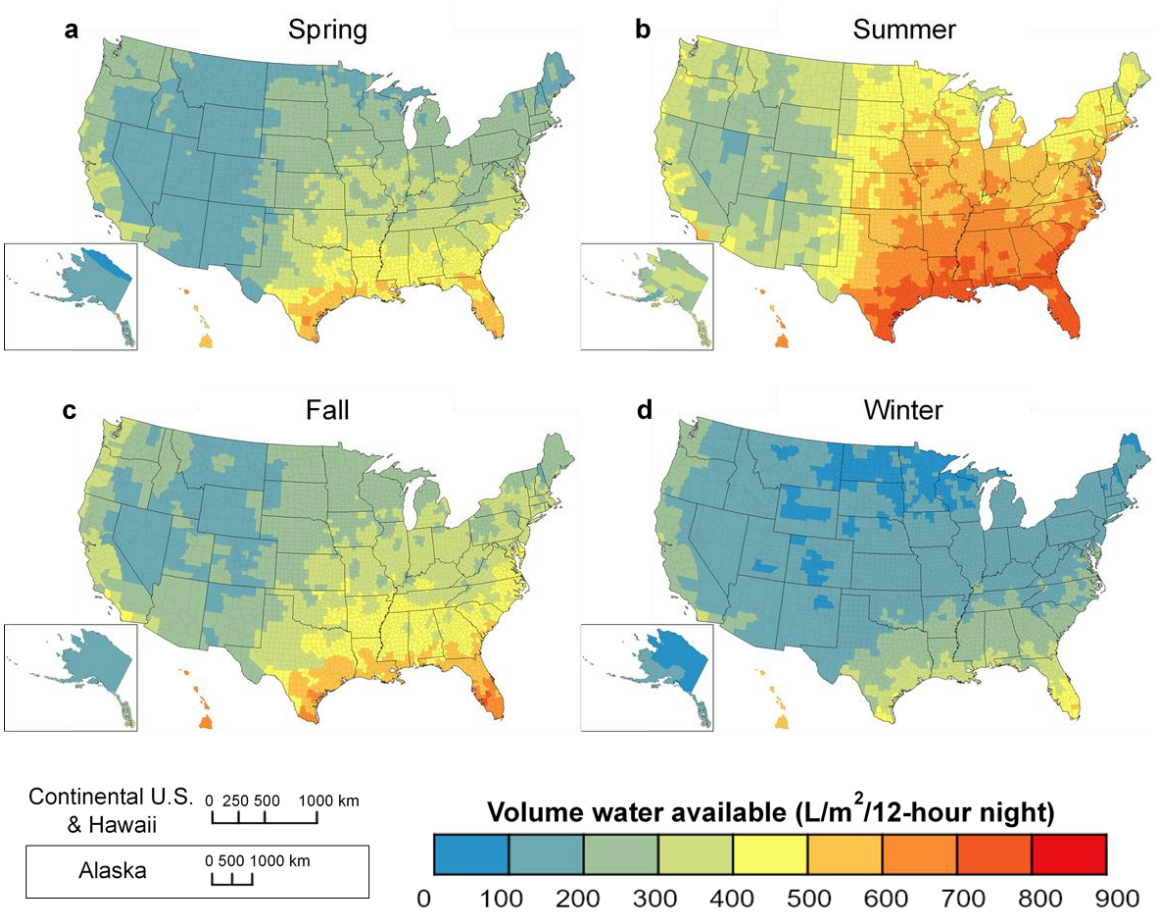

Figure 3-6 Upper boundary of water volume available in the atmosphere passing through the system volume (Figure 2) every night (L/m^2/12-hour night) in a) spring, b) summer, c) fall, and d) winter.

passing through the system volume over a 12-hour night-time period (**Equation 15**), solar desiccant based systems capture 0.1–20% of the available water vapor in the air, where the water volume captured is equivalent to the solar desorption potential. **Figure 3-6** shows the upper boundary of available water in the air across the U.S. in different seasons. Overlapping these maps with solar desorption potential maps (**Figure 3-5**) shows regions where solar desiccant based AWC has highest utilization potential, such as in the southern U.S. in the fall and winter and universally across the country in the spring

and summer. Particular emphasis should be given to the southeastern U.S. (i.e., humid gulf coast region), which is susceptible to natural disasters (e.g., Hurricane Harvey in Houston, TX and Hurricane Maria in Puerto Rico), causing limited access to liquid water supplies and a stable electric grid. In these regions, there is ample water vapor and sunlight to perform solar desiccant driven AWC to provide an alternative water supply until municipal water supply is restored.

Current research on solar desiccant AWC has focused on materials development and water vapor adsorption isotherm testing in controlled environments, with forays between bench and outdoor pilot scale testing of choice materials. Our modeling analysis shows there is potential to increase AWC from < 1 L/m^2/day obtained in current systems to up to 8 L/m^2/day as a function of both material parameters and geographic location. While optimizing high SSA_{D_i} has merits for particular applications, such as humid regions with abundant sunshine, research should focus on developing materials with 1) high Langmuir constant k_L values (>0.1) to achieve a steeper adsorption isotherm slope and maximize AWC in arid regions and 2) low E_{des} to minimize $Q_{des_{D_i}}$ and maximize desorption potential. In regions and seasons where there is not enough solar radiation to produce larger water volumes, alternative off-grid energy sources such as wind and geothermal could be harnessed to power desorption of water vapor from desiccants.

3.7 Acknowledgements

This work was funded through the National Science Foundation Nanosystems Engineering Research Center on Nanotechnology Enabled Water Treatment (EEC-1449500) and National Science Foundation Graduate Research Fellowship. We thank Dr. Cody Friesen and Zero Mass Water at Arizona State University for valuable discussion

on the scope of this project. Laurel Passantino at Arizona State University provided technical editing.

3.8 Nomenclature

Table 3-2 Nomenclature

Symbol	Definition	Units / Value
A_{box}	Cross-sectional area of system control volume	1 m^2
C_e	Equilibrium concentration of adsorbate	g adsorbate / volume
d_{D_i}	Diameter of desiccant D_i	mm
D_i	Desiccant	—
e	Vapor pressure	Pa
e_s	Saturated vapor pressure	Pa
e_{s0}	Saturated vapor pressure	611 Pa
$E_{des_{D_i}}$	Activation energy of desorption	kJ/mol
h	Height of desiccant bed	mm
k_L	Langmuir constant	unitless
L_v	Latent heat of vaporization	2250000 J/kg
m_{D_i}	Mass of desiccant D_i	kg
$\dot{m}_{vapor}$	Mass flow rate of water vapor through system	L/m^2/day
N_A	Avogadro's number	6.02E23
N_{D_i}	Number of desiccants in system	—
q	Sorption capacity	g adsorbate / g adsorbent
q_{max}	Maximum sorption capacity	g adsorbate / g adsorbent
q_{D_i}	Desiccant sorption capacity	g vapor / g desiccant
$Q_{des_{D_i}}$	Energy of desorption for desiccants D_i in system	kJ/m^2
RH	Relative humidity	%
R_v	Vapor gas constant	461 J/kgK
SSA_{D_i}	Desiccant specific surface area	m^2 / kg desiccant
SSD_{D_i}	Desiccant specific site density	molecules / nm^2
T_{air}	Air temperature	K
T_o	Air temperature	273 K
v_{air}	Wind speed	m/s
V_{D_i}	Volume of 1 desiccant D_i	m^3
ρ_{D_i}	Bulk density of desiccant D_i	kg/m^3
ρ_{vapor}	Vapor density	g/m^3

3.9 Supplemental Information

Table SI 3-1 Properties of three model desiccants used for geospatial AWC analysis. Silica gel and zeolite properties obtained from literature to calculate Langmuir sorption isotherm. MOF MIL-101(Cr) adsorption isotherm data was used directly from literature.

	Silica	**Zeolite**	**MOF MIL-101(Cr)**
Diameter (mm)	3	3	3
Bulk Density (kg/m^3)	750 (Cohen, 2003; Lee, Weng, Tseng, & Wang, 2015)	650 (Cohen, 2003; Lee et al., 2015; Seo et al., 2012)	N/A
Specific surface area (m^2/g)	830 (Cohen, 2003; X. Li et al., 2007; Ng et al., 2001; Zheng et al., 2014)	600 (Cohen, 2003; J. H. Kim et al., 2003)	N/A
Specific site density ($sites/nm^2$)	12.8	12.8	N/A
k_L	0.05 (calculated)	0.8 (calculated)	N/A
Bed depth (mm)	10 (Lapotin et al., 2019a)	10 (Lapotin et al., 2019a)	10
Total desiccant mass in 1 m^2 footprint system (kg)	4.8	4.16	2.24
Activation energy of desorption (kJ/mol)	35 (X. Li et al., 2007)	70 (Fan, Panezai, Sun, Bai, & Wu, 2014)	65 (S. Wang et al., 2015; Zhou et al., 2014)

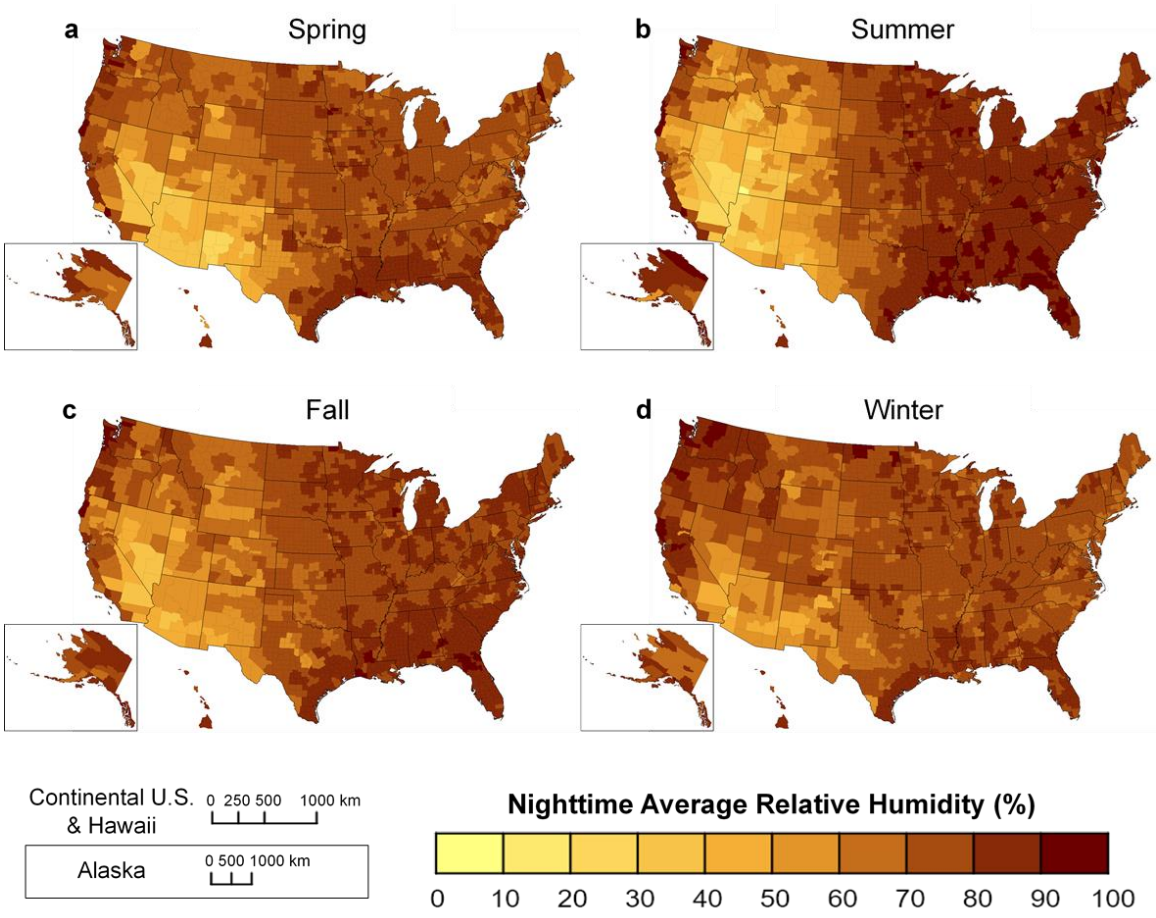

Figure SI 3-1 Relative humidity in a) spring, b) summer, c) fall, and d) winter.

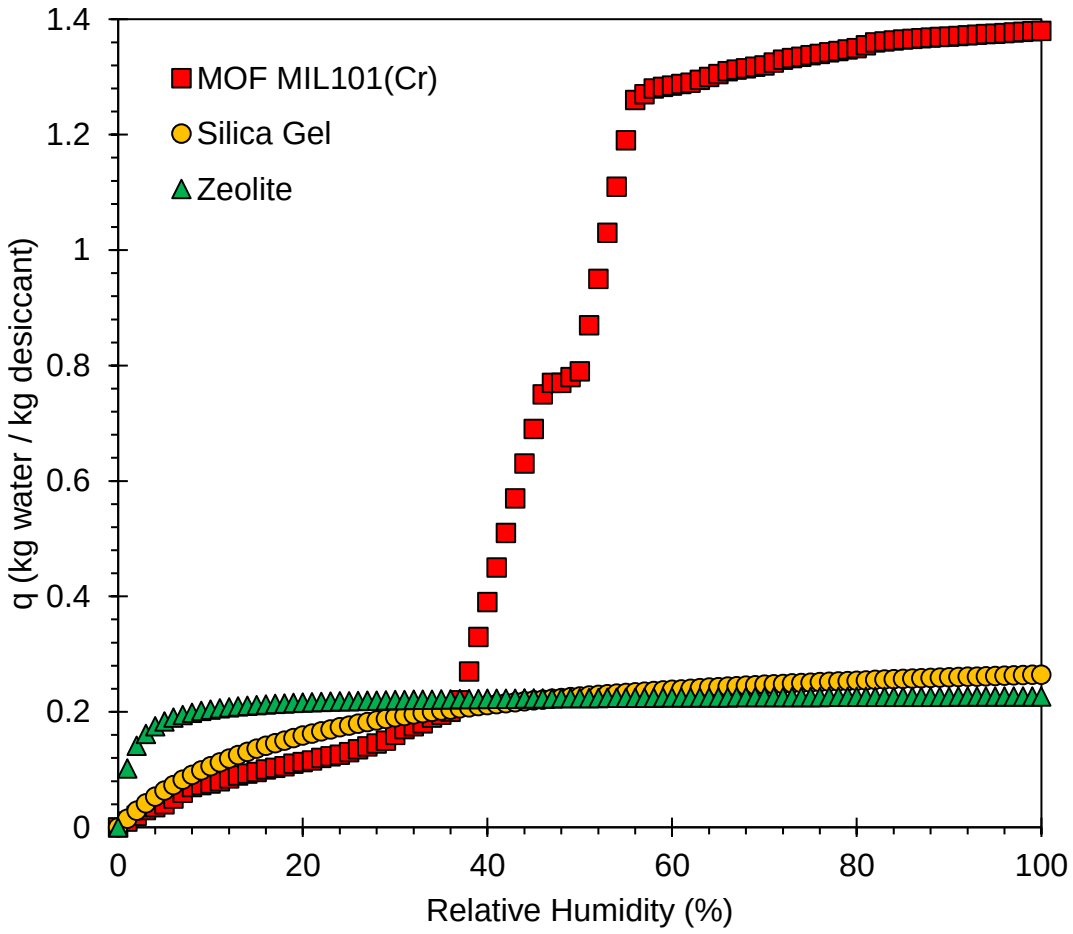

Figure SI 3-2 SiO_2 (Dawoud & Aristov, 2003; Lee et al., 2015; X. Li et al., 2007; Zheng et al., 2014), Zeolite (Lee et al., 2015; Zheng et al., 2014), and MOF MIL-101(Cr) (Akiyama et al., 2012; S.-I. Kim et al., 2016; Seo et al., 2012; Yan et al., 2015) isotherms

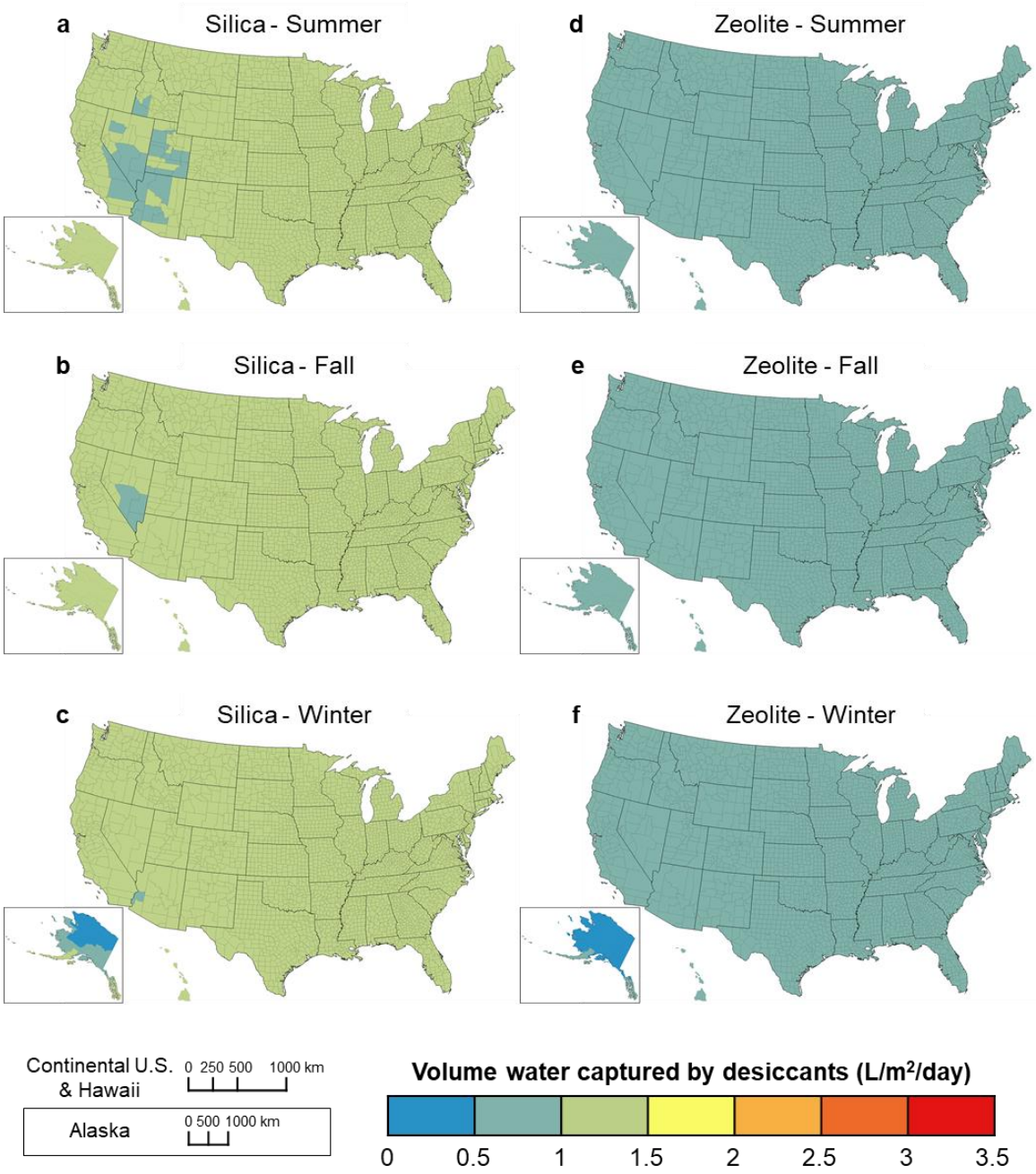

Figure SI 3-3 Water volume captured by silica gel in the a) summer, b) fall, and c) winter. Water volume captured by zeolite in d) summer, e) fall, and f) winter.

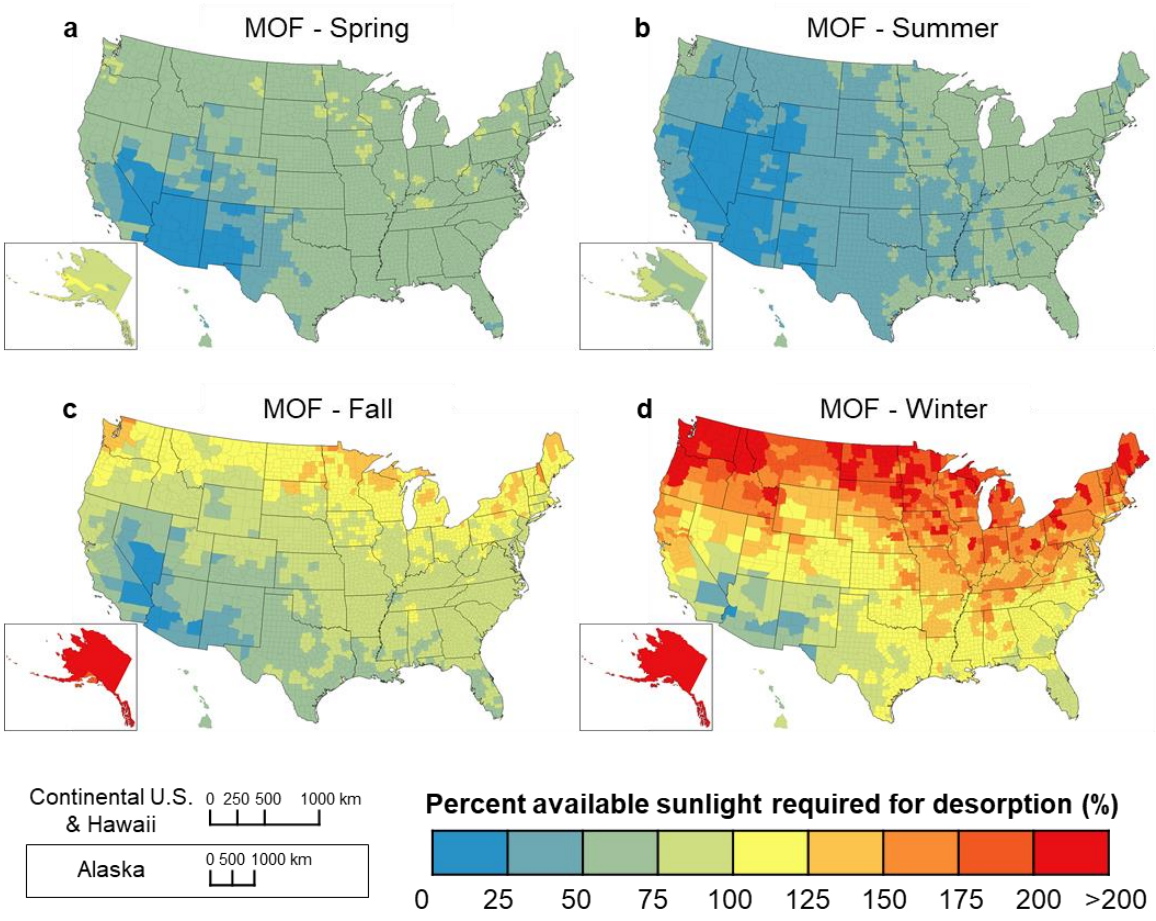

Figure SI 3-4 Percent of sunlight required to achieve desorption for MOF in a) spring, b) summer, c) fall, and d) winter.

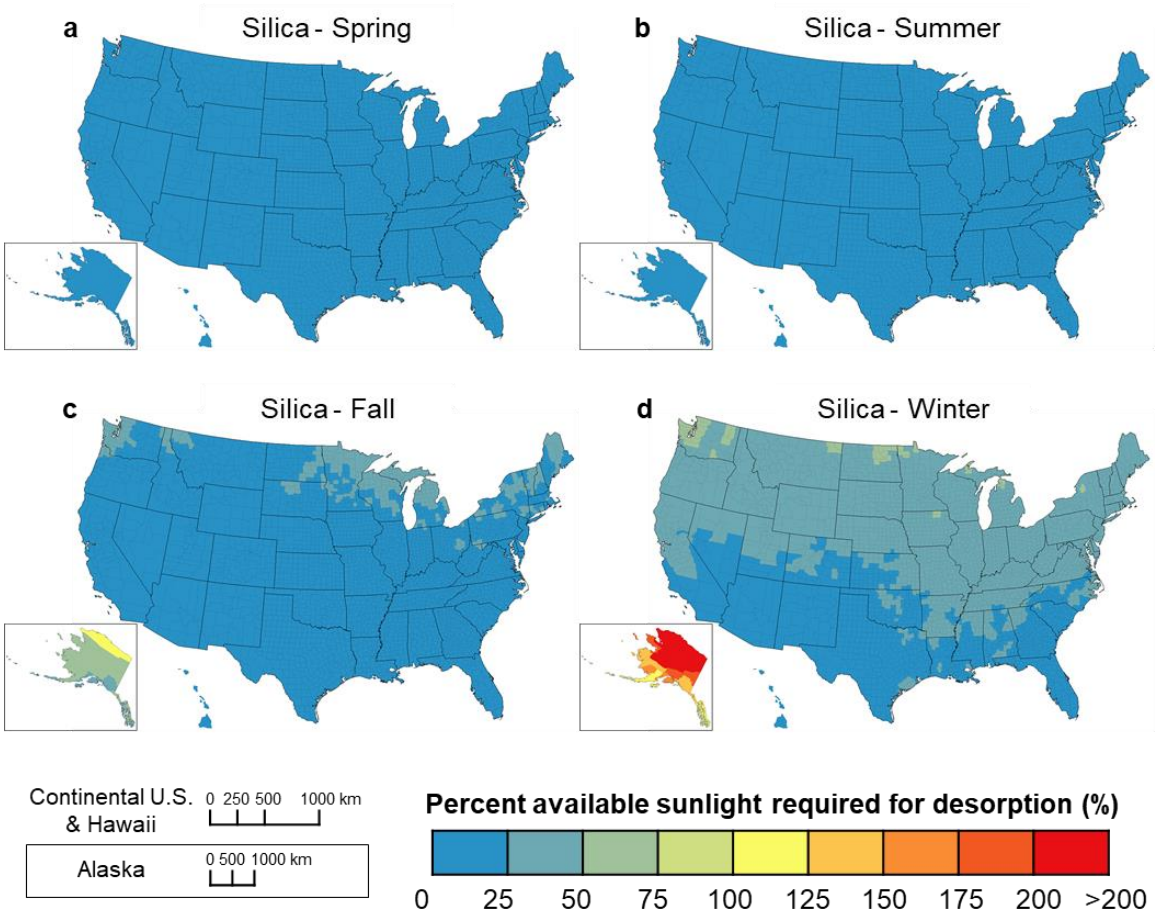

Figure SI 3-5 Percent of sunlight required to achieve desorption for silica in a) spring, b) summer, c) fall, and d) winter.

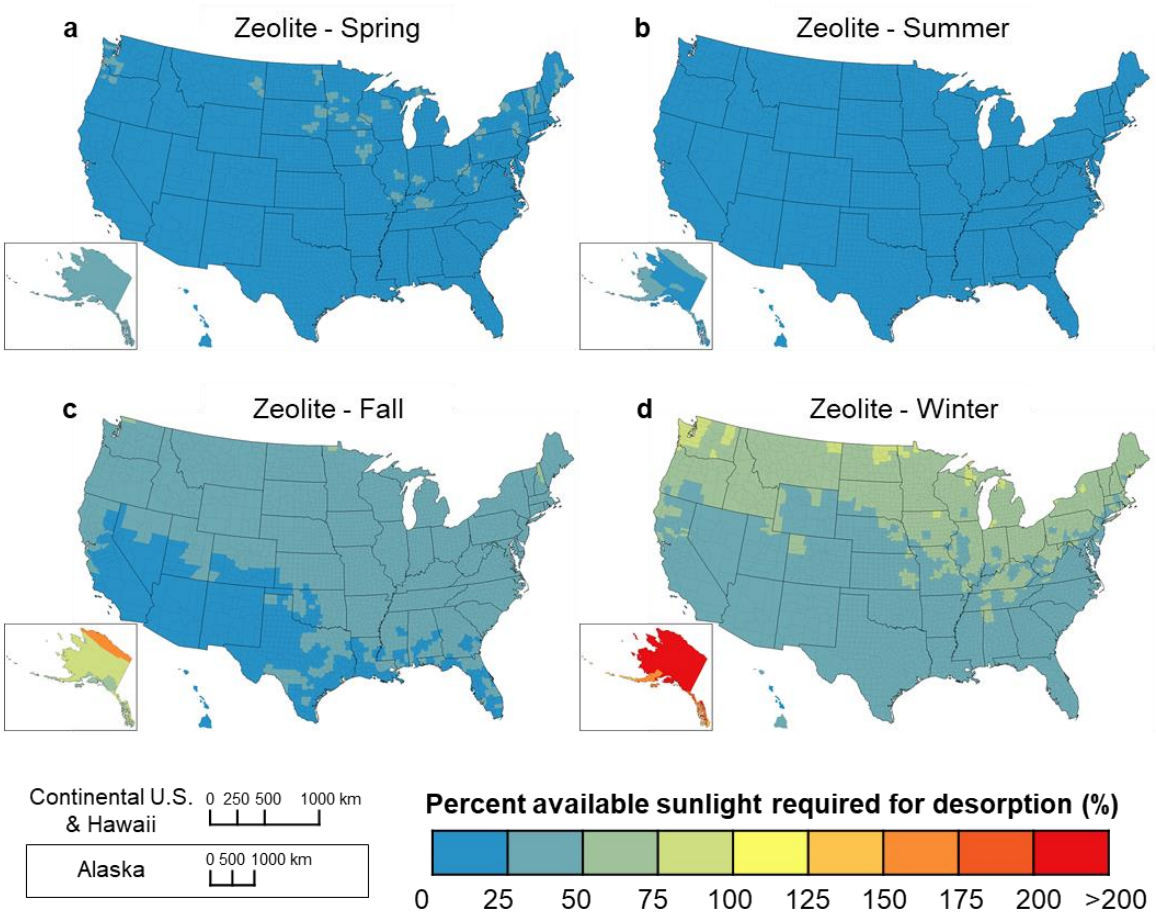

Figure SI 3-6 Percent of sunlight required to achieve desorption for zeolite in a) spring, b) summer, c) fall, and d) winter.

SUNLIGHT DRIVEN ATMOSPHERIC WATER CAPTURE CAPACITY IS ENHANCED BY PHOTOTHERMAL NANOMATERIAL ENABLED DESICCANTS

This chapter is a manuscript draft in preparation for submission as:

> Mulchandani, A., Malinda, S., Edberg, J., and Westerhoff, P. Sunlight driven atmospheric water capture capacity is enhanced by photothermal nanomaterial enabled desiccants. *In prep for submission to Environmental Science: Nanotechnology*.

4.1 Introduction

Removing salts and pollutants from unconventional water supplies (e.g., oceans, brackish groundwater, wastewater, stormwater) and distributing clean water within a municipality can be energy intensive, costly and produces large amounts of waste residual (Alspach & Juby, 2018; Stratton et al., 2017). Atmospheric water capture (AWC) is an emerging method of decentralized water production, whereby very low salt content water is removed from air without producing concentrated waste streams to dispose. As a hydrologic reservoir, the atmosphere contains 12,900 km^3 of water, ~14% of the volume of freshwater stored in lakes and rivers combined. (Shiklomanov, 1992) Its universal presence suggests that it can be used in a variety of locations from rural homes, to military locations and disaster relief scenarios. Amongst the most interesting applications for AWC are to enable an off-grid water source (i.e., away from both the municipal water and electricity grids).

Devices which pull water from the air can be grouped as: 1) dew collectors, 2) dew point condensation dehumidifiers, and 3) relative humidity (RH) capture by

adsorption / desorption cycling (i.e. desiccants). Dew collection is only relevant for fully saturated air such as fog, where RH is >100%. Dehumidifying condensation systems often utilize compressors which use refrigerants to directly cool humid air to below the dew point temperature. This process is only effective for higher RH (at least >30-40%) and is energy intensive (0.5 – 2 kWh / L water produced).

Desiccant-based AWC can use liquid desiccants (e.g. $CaCl_2$), solid desiccants (e.g. silica gel, zeolites, metal organic frameworks (MOFs)), or super moisture-adsorbent gels (SMAGs). The quantity of water captured by desiccant-based AWC is a function of RH, wherein the vapor pressure differential between the air and the desiccant surface acts as a driving force for sorption. Heat is applied to drive desorption of vapor from the desiccant onto a cool surface, where clean water condenses and can be collected. Liquid desiccants react with water vapor to form a complexed hydrate (e.g. $CaCl_2 \cdot H_2O$) that continues to absorb water to produce saturated salt solutions. Eventually the salt and water must be separated by heat to obtain fresh water and regenerate the desiccant for reuse (Gido et al., 2016; R. Li, Shi, Shi, et al., 2018). Liquid desiccants can produce large volumes of water (up to 2 g H_2O/ g desiccant), but the AWC process requires three phase changes, from water vapor to liquid salt, to saturated water vapor, to re-condensed and low-salt liquid water. In contrast, solid desiccant systems only undergo one phase change. First, water vapor adsorbs to solid desiccants and it does not change state on the surface (Cohen, 2003). Second, nearly saturated water vapor is desorbed from the desiccant using heat. Third, liquid water is condensed from the high RH air on a cool surface. Due to the ineffectiveness of dew collectors and dew point condensation in a wide range of climates, (H. Kim et al., 2018b; H. Kim, Yang, et al., 2017; Lapotin, Kim, Rao, & Wang, 2019b)

and the complexity and multiple changes of state required for salt-based desiccants, this paper focuses on solid desiccants for AWC.

Desiccant-based AWC systems are often reported to adsorb water vapor at night, when RH is high, and utilize solar heating during the daytime to desorb vapor, which can then be condensed to produce drinkable water (US 2018/0043295 A1, 2018; H. Kim et al., 2018a). Much of the existing literature focuses on materials that achieve high water vapor adsorption capacity (e.g. 1.2 g H_2O / g MOF MIL101(Cr) at 80% RH (Akiyama et al., 2012; Khutia et al., 2013; Yan et al., 2015)). Less attention has been given to the energy and rate of water vapor desorption, which can limit the overall water production of AWC systems that rely upon solar heating. The temperature required to heat the desiccants for desorption (>90^{o}C for SiO_2, >150^{o}C for zeolite, >85^{o}C for MOFs) is a limiting step in AWC. Sufficient solar heating of the desiccant bed to temperatures required for release of sorbed water vapor can take many hours of sunlight, which limits the AWC system to just one adsorption-desorption-condensation cycle per day. Thus, in systems with large masses of super-efficient water sorption capacities (e.g. >1g water / g sorbent) solar heating may limit water capture potential of AWC systems.

Given that available solar thermal energy may be a limiting factor to AWC potential, there is a need to develop novel desiccant materials that either require less thermal heat input or can maximize the available solar thermal energy to achieve complete desorption. Broadband light absorbing photothermal nanomaterials can absorb photons from incident solar radiation and superheat. Photothermal nanoparticles such as gold and carbon black have been applied to heat membranes in nanophotonics enabled solar membrane distillation (Dongare et al., 2017) and inactivate microbes in solution and

on surfaces (Loeb, Li, & Kim, 2018). In this work, we apply solar-light active photothermal nanomaterials (gold, carbon black) on silica desiccant surfaces with the aim of providing localized sources of heat, increasing desiccant surface temperature rapidly, and improving kinetics of water vapor desorption and desiccant regeneration. Faster desiccant regeneration can lead to operation of two or more AWC cycles per day.

Gold nanoparticles (AuNPs) are both plasmonic and photothermal – when light at the surface plasmonic resonance (SPR) wavelength hits the nanoparticle (NP), the electrons in the NP's conduction band are excited and begin to oscillate, creating a hot electron distribution. The electron oscillation decays by transferring the generated heat to the surrounding media (Averitt, Westcott, & Halas, 1999; Govorov & Richardson, 2007; Qiu & Wei, 2014; Richardson, Carlson, Tandler, Hernandez, & Govorov, 2009; Roper, Ahn, & Hoepfner, 2007; P. Wang, 2018). The size and shape of a NP can have a large impact on the SPR wavelength(s), and correspondingly, the SPR induced photothermal heating (Jiang, Cheng, Shao, Ruan, & Wang, 2013). Gold nanorods (AuNR) have two SPR peaks (520nm, 790 nm), indicating they can use more photons from the solar spectrum than gold nanocubes (AuNC, SPR peak 534 nm) to generate heat (Loeb et al., 2018; Nguyen et al., 2016). To contrast narrow spectral properties of gold nanoparticles, we compared them to a lower cost and broadband spectrum absorbing commercially available carbon black (CB) nanoparticles. (Dongare et al., 2017; Han, Meng, Wu, Zhang, & Zhu, 2011; Jiang et al., 2013; Loeb et al., 2018; Neumann et al., 2013)

The goal of this paper is to understand material properties that can maximize the net volume of water that desiccants can capture during the day. The net water production is a function of the water capacity during one adsorption-desorption cycle multiplied by

the number of cycles performed per day. The number of cycles that can be operated per day depends upon the rates of water vapor adsorption and desorption via solar photothermal heating capacity of desiccants. Photothermal nanomaterials (AuNC, AuNR, CB) were chemically attached to micron-sized silica gel desiccants to increase desiccant surface temperature under sunlight, increase rate of water vapor desorption, and facilitate multiple cycles of water capture throughout a 12-hour day period. Material characterizations of nano-enabled desiccants were related to their photothermal properties under simulated one-sun solar radiation. Atmospheric water capture experiments were performed in in multiple realistic environmental conditions (40%, 60 and 80% RH) to determine optimal use-case for photothermal nano-enabled desiccants (PNED).

4.2 Materials and Methods

4.2.1 Chemicals

Silica gel desiccants (high purity grade, pore size 40Å, 70-230 mesh particle size (63 – 210 µm), (3-Aminopropyl) triethoxysilane (APTES), hexadecyltrimethylammonium bromide (CTAB), gold (III) chloride hydrate ($HAuCl_4$), sodium borohydride ($NaBH_4$), ascorbic acid, silver nitrate ($AgNO_3$) and ethanol were acquired from Sigma Aldrich. ACS grade hydrochloric acid (HCl) was obtained from VWR. Ultrapure water (18.2 MΩ cm, Barnstead GenPure xCAD Plus) was used to make all solutions.

4.2.2 Synthesis of Photothermal Nanomaterial Enabled Desiccants (PNED)

Silica gel desiccants (SiO_2) with pore size 40 Å and mesh particle size 70-230 (63-210 µm) were selected because they had the highest reported surface area among commercial silica gel desiccants (500 m^2/g). Surface area is a driving property in

maximizing water vapor adsorption. SiO_2 was washed with ultrapure water and separated using centrifugation (5000 RPM, 30 min) two times and washed and centrifuged once with ethanol. Washed SiO_2 (20 g) was silanized with 2.14 mmol APTES per gram SiO_2 via reflux condensation in 400 mL ethanol for 12 hours at 80^{o}C. SiO_2-APTES was washed with ethanol and collected after vacuum filtration using 0.45 μm Nylon filter, then dried at 80^{o}C overnight.

Gold nanocubes and nanorods (AuNC and AuNR) were synthesized using a seeded-growth method and capped with CTAB (details provided in S.I.). The gold nanocube solution is a bright red color with concentration 25 mg/L and surface plasmonic resonance peak at 534 nm. The final gold nanorod solution is a deep purple color with concentration 82 mg/L and has two surface plasmonic resonance peaks at 520 nm and 790 nm. Carbon black nanoparticles (CB) were purchased in powder form (Emperor 2000 was obtained from Cabot Corporation) and used without further purification.

For preliminary photonic and photothermal experiments, six different mass loadings of NPs (0.1 – 10 w/w% NP/SiO_2) were prepared for each NP. To facilitate statistical analysis of results, each sample was synthesized in triplicate. Varying volumes of premade 25 ppm AuNC or 80 ppm AuNR solution were added to 0.2 g premade SiO_2-APTES in Qorpak 500 mL wide mouth amber bottles to result in mass loadings of 0.1 – 7 w/w% AuNP-SiO_2. Nanopure water was added to each bottle such that the final volume of solution in each bottle was 400 mL. To synthesize CB-SiO_2-APTES, various masses of commercial CB were added to 0.2 g SiO_2-APTES and 400 mL water in Qorpak 500 mL wide mouth amber bottles to result in mass loadings of 0.1 – 10 w/w% CB-SiO_2. Secondary water capture experiments required production of 1 g 5w/w%NP-SiO_2-APTES

in triplicate. For this, 1 g of premade SiO_2-APTES was added to either 625 mL of AuNC (2 L of 25 ppm AuNC were pre-concentrated by centrifuging and resuspending in 625 mL water), 625 mL 80 ppm AuNR solution, or 50 mg CB and 625 mL water in Qoropak 1250 mL wide mouth amber bottles.

The bottles were placed on a rotating shaker table (350 RPM) overnight. After mixing the SiO_2-APTES with NPs overnight, the desiccants were allowed to settle for 2 hours, then the supernatant was removed. The jars with wet desiccants were placed in an oven at 105^oC overnight to dry. Dry desiccants were collected and stored in glass vials at room temperature for use. **Figure 4-1** shows different colors of the desiccants which varied depending on mass loading from various shades of greys for the carbon black on SiO_2-APTES (CB-SiO_2), pinks for gold nanocubes on SiO_2-APTES (AuNC-SiO_2), and blues for gold nanorods (AuNR-SiO_2).

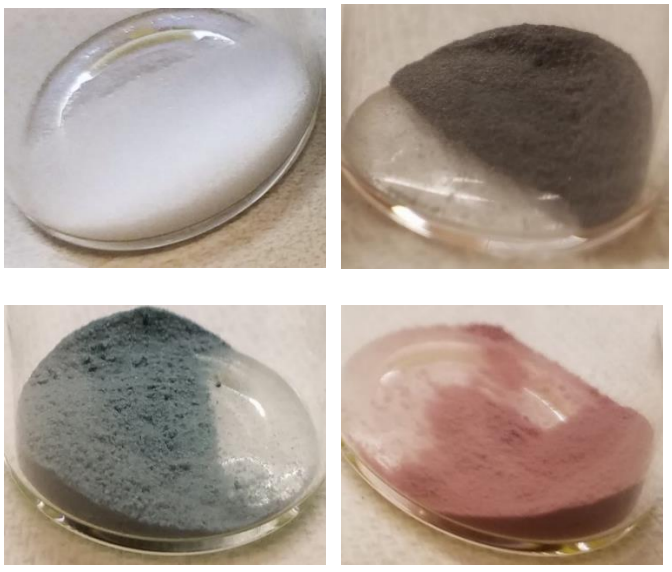

Figure 4-1 a) Bare SiO_2 desiccants. **b)** 5 w/w% carbon black coated SiO_2 desiccants. **c)** 5 w/w% Gold nanorod coated SiO_2 desiccants. **d)** 5 w/w% gold nanocube coated desiccants.

The SiO_2 desiccants have an average spherical diameter of 136 μm, which equates to 5.8×10^{-8} m^2 of external surface area onto which the APTES and NPs can attach. Pores in the SiO_2 are 4 nm (40 Å), while AuNR are 20 nm x 60 nm, AuNC have unit length 60 nm, and CB nanoparticles have diameter 180 nm. Therefore, NPs will only attach to the surface of the desiccant and not within the pores. Nanoparticle dimensions were used to calculate surface loadings of 0 – 300% (0 – 7 w/w% for AuNC, 0 – 1 w/w% for AuNR, 0 – 5 w/w% for CB).

4.2.3 UV-Visible Light Absorption by PNED

Diffuse reflectance spectra of the desiccants were measured using Perkin Elmer Lambda 18 UV-Vis Spectrometer with 150 mm integrating sphere. Diffuse reflectance measures the portion of incident light in a spectrometer that entered the voids of the powders, scattered, and was not absorbed. The Kubelka Munk function (F(R)) (**Equation 1**) converts reflectance measurements (R) to a ratio of absorption (K) to scattering (s) coefficients, assuming a uniform, infinitely thick layer of material that either absorbs or scatters radiation. (Hecht, 1976)

$$F(R) = \frac{(1-R)^2}{2R} = K/s \quad (1)$$

K/s values above unity indicate absorption is more dominant than scattering, K/s values equal to 1 indicate equivalent absorption and scattering, and K/s values less than unity mean scattering is dominant.

4.2.4 PNED Heating Under Simulated Solar Irradiation

Desiccant (0.03 g) was mounted onto a glass microscope slide (Fisherbrand, thickness 1 mm) using 25 mm x 25 mm square of Scotch double-sided tape. The slide

was placed perpendicular to the horizontal path of light from Newport 1000 W Hg/Xe lamp at a distance where radiation intensity was 1000 W/m^2 (1 Sun). An infrared temperature sensor (Omega, OS-MINIUSB) was placed directly above the sample, and sample temperature was recorded at 1 second intervals. Samples were irradiated until stable maximum temperature was reached, following which the light source was covered to allow samples to cool. Heating experiments for each desiccant were performed in triplicate.

4.2.5 Water Vapor Adsorption onto PNED in Controlled Humidity Enclosure

Adsorption experiments were performed in a 0.16 m^3 polycarbonate enclosure. (**Figure 4-S1a**) The enclosure contained 2 balances (Ohaus Pioneer PX224AM, readability 0.0001 g), ultrasonic humidifier with hose attachment (Electro-Tech Systems model 5462), circulation fan (Vornado Flippi V6), and combined humidity and temperature meter (Omega RH820U). The humidifier tube attachment was placed above the fan to evenly distribute humid air throughout the chamber. Humidity and temperature were monitored and logged by the meter every second. Experiments were performed at ambient temperature (20 – 22^{o}C) and RH was maintained at either 40%, 60% or 80% (+/- 2%) by manually adjusting the humidifier throughout the duration of the experiment. One gram of 5 w/w% NP-SiO_2 dry desiccant (removed from oven at 105^{o}C immediately before experiment) was placed on a balance in an open glass petri dish, and weight increase due to water vapor adsorption was recorded by Ohaus serial port data collection software every 5 seconds.

4.2.6 Water Vapor Desorption off PNED Under Simulated Solar Irradiation

Water vapor desorption testing was performed in ambient lab environment (RH 25%, Temperature 20^{o}C). (**Figure 4-S1b**) After saturating the desiccant in the humidity-controlled enclosure, the glass petri dish containing saturated desiccant was placed on a balance beneath a vertical beam from Newport 1000 W Hg/Xe lamp with A.M. 1.5G filter at a distance where radiation intensity was equivalent to 1 Sun (1000 W/m^2). Mass loss over time due to water vapor desorption was recorded at 5 second intervals from the balance by Ohaus serial port data collection software.

4.2.7 Statistical Analysis

Two-tailed t-tests were performed on results obtained by triplicates of desiccant samples to determine statistical similarity. Triplicate results of 2 independent samples (e.g. virgin SiO_2 desiccant vs 5w/w%CB-SiO_2) were compared, with the null hypothesis stating that the obtained results are statistically different. The analysis had 4 degrees of freedom, α=0.05 and t_{crit} = 2.132. Equation 2 was used to calculate t-value (t_{obs}) of the data set, where X_1 is the average of triplicate data from Sample 1, X_2 is the average of triplicate data from Sample 2, var_1 is the variance of data from Sample 1, var_2 is the variance of data from sample 2, n_1 is the number of data points obtained for sample 1 (i.e. 3), and n_2 is the number of data points obtained for sample 2. If $t_{obs} > t_{crit}$, i.e. p-value <0.05, the null hypothesis was valid and the samples were determined to be statistically different, while if p-value was >0.05, the t-test failed and results were deemed statistically similar.

$$t_{obs} = \frac{X_1 - X_2}{\sqrt{\left(\frac{var_1}{n_1}\right) + \left(\frac{var_2}{n_2}\right)}} \quad (2)$$

4.3 Results and Discussion

4.3.1 Photonic Characterization of NPs and PNEDs

AuNC, AuNR and CB nanoparticles exhibit light absorption properties in both water and on the desiccant surface. In water, the AuNR show surface plasmonic resonance (SPR) peaks at 520 nm and 790 nm and gold nanocubes peak at 534 nm. Carbon black exhibits broad absorption through the visible and near-IR wavelength spectra. (**Figure 4-S2a**). **Figure 4-2** shows the Kubelka Munk transformation of diffuse reflectance for the SiO_2 desiccants with and without a 1 w/w% and 5 w/w% mass loading of nanoparticles on their surface. As anticipated, the spectral similarity of the NPs in water to Kubelka-Munk transformation of NP-SiO_2 shows that the light absorption properties of the nanomaterial are maintained once attached to SiO_2. Comparing the 1 and 5 w/w% loading of NPs shows that increased surface loading of the NPs leads to increased light absorption. However, above 5 w/w%, absorption plateaus at an "absorption maxima", indicating any further loading of NPs will not lead to additional enhancement of light absorption. (**Figure 4-S3**) Therefore, atmospheric water capture analysis was performed on 5 w/w% PNEDs.

It was hypothesized that the magnitude of light absorption by the nanoparticles in solution would be maintained once the nanoparticles were attached to the SiO_2, and accordingly light absorption would follow the trend CB-SiO_2 > AuNR-SiO_2 > AuNC-SiO_2. However, integrated area of Kubelka Munk absorbance of 5 w/w% CB-SiO_2 from 300 nm to 800 nm is equivalent to that of 5 w/w% AuNC-SiO_2 and 1.5x higher than AuNR-SiO_2. Higher absorbance by AuNC-SiO_2 compared to AuNR-SiO_2 was not because a higher density of NPs was attached to the SiO_2. Based on the size and density

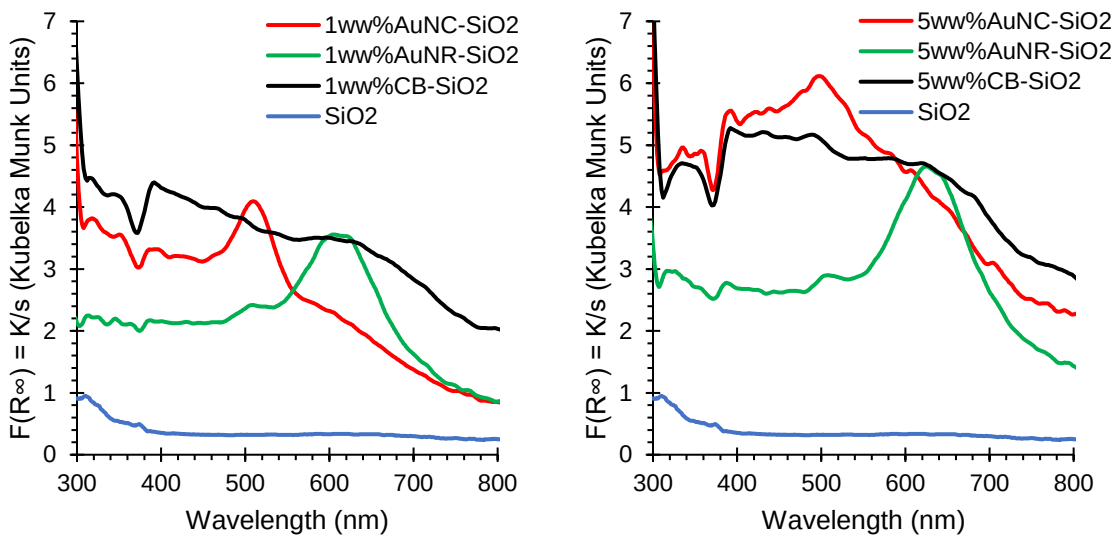

Figure 4-2 Kubelka Munk Transformation of Diffuse Reflectance on 1 w/w% NP-SiO_2 (left) and 5 w/w% NP-SiO_2 (right).

of the nanoparticles, a 5 w/w% loading of AuNC should cover 260% of the available surface area on the bare SiO_2 desiccant. A 5 w/w% loading of AuNR corresponds to 1666% of the SiO_2 surface area. Instead, it is likely that the combination of the arrangement of nanorods on the SiO_2 substrate surface and the incident direction of light interacting with the nanoparticles led to a damping or suppression of the plasmonic resonance and higher light scattering. (Linden, Kuhl, & Giessen, 2001; Sönnichsen et al., 2002)

Interestingly, the plasmonic resonance peaks of gold nanoparticles (both cubes and rods) exhibit a blue-shift from measurements in water vs air. The SPR peaks for AuNR in solution are at 520 nm and 790 nm, while the SPR peaks for AuNR-SiO_2 are at 505 nm and 625 nm. The SPR peak for AuNC in solution is at 534 nm and shifts to 500 nm for AuNC-SiO_2. The refractive index (RI) of water (1.33) is higher than that of air (1.0), (Mock, Smith, & Schultz, 2003) which causes the nanoparticle extinction spectrum

to shift when the particles are transferred from a water matrix to air. This is important because solar irradiance is higher at the blue-shifted wavelengths (1.40 W/m^2 at 625 nm, 1.56 W/m^2 at 505 nm) compared with the anticipated absorption wavelengths (1.09 W/m^2 at 790 nm, 1.53 W/m^2 at 534 nm and 520 nm). Therefore, light absorption and corresponding heat production by AuNP-SiO_2 under exposure to solar irradiation in air should be more pronounced.

4.3.2 Photothermal Characterization of PNED Under Simulated Solar Irradiation

Attachment of photothermal NPs to the surface of desiccants increased the desiccant surface temperature under simulated solar irradiation. For each of the three classes of NPs, higher NP surface loading increased the rate and maximum temperature. For example, **Figure 4-3a** shows carbon black loading of 1 w/w% achieves similar surface temperature as 2.5, 5 and 10 w/w%. **Figures 4-3b and 4-3c** and **Table 4-1** show for the same mass loading of NP, carbon black heats 2 times faster than AuNC and 4 times faster than AuNR to reach their steady-state temperatures. Maximum surface temperature achieved by 5 w/w% CB-SiO_2 is 59^{o}C, 5 w/w% AuNC-SiO_2 is 40.7^{o}C, 5 w/w% AuNR-SiO_2 is 31.4^{o}C and bare SiO_2 is 28.2^{o}C. We hypothesize AuNC-SiO_2 heats less than CB-SiO_2, even though the integrated Kubelka-Munk absorbance are near equal, because of heat losses in the energy conversion from electron oscillation due to SPR to heat.

4.3.3 Water Vapor Adsorption onto Desiccants Under Variable Humidity Conditions

Water capture experiments were performed on 5w/w% PNEDs because they had optimal heating rates and maximum surface temperatures. Maximum capacities and rates of water adsorption were determined at three RH values (40, 60, 80%) for the bare SiO_2

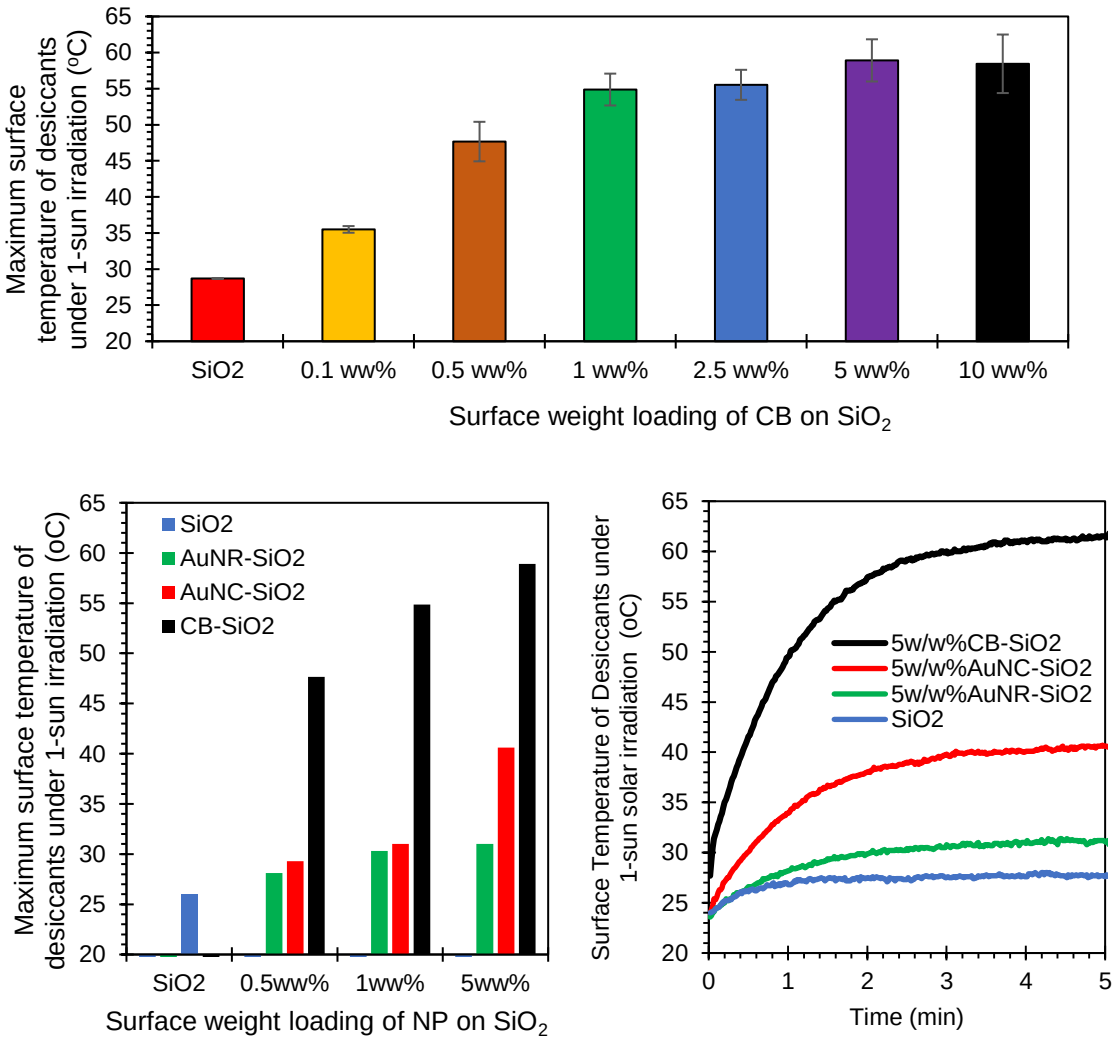

Figure 4-3 Dry desiccant surface temperature under 1-sun solar irradiation. 0.03 g of sample are loaded onto a glass slide and placed perpendicular to the beam path. a) Maximum surface temperature of various surface loadings of carbon black on SiO_2 desiccants. b) Maximum surface temperature of various surface loadings of NPs on SiO_2. c) Rate of surface temperature change by 5 w/w% NP-SiO_2.

Table 4-1 Heating rate and maximum surface temperature of 0.03 g desiccant sample attached onto a glass slide and placed perpendicular to the beam path of 1-sun irradiation

Loading (w/w% NP-SiO_2)	Carbon Black		Gold Nanocube		Gold Nanorod	
	Heating Rate (^oC/min)	Max Temp (^oC)	Heating Rate (^oC/min)	Max Temp (^oC)	Heating Rate (^oC/min)	Max Temp (^oC)
0	2.3	28.2	2.3	28.2	2.3	28.2
0.25	12.5	47.6	2.4	28.8	2.2	28.5
0.5	12.3	49.4	3.0	29.5	2.6	30.2
1	14.5	52.7	4.2	31.2	3.5	30.4
2.5	15.5	52.9	6.9	35.8	4.4	31.9
5	18.8	59.0	9.5	40.7	4.3	31.4
7	--	--	7.7	38	5.3	33.6
10	19.2	58.1	--	--	--	--

Table 4-2 Adsorption and desorption capacities and rates of desiccants

	40% RH				60% RH				80% RH			
	SiO_2	5w/w% CB-SiO_2	5w/w% AuNC-SiO_2	5w/w% AuNR-SiO_2	SiO_2	5w/w% CB-SiO_2	5w/w% AuNC-SiO_2	5w/w% AuNR-SiO_2	SiO_2	5w/w% CB-SiO_2	5w/w% AuNC-SiO_2	5w/w% AuNR-SiO_2
ADSORPTION AT SPECIFIED RELATIVE HUMIDITY												
Maximum capacity (gH_2O/ g)	0.067 ± 0.0033	0.049 ± 0.0084	0.045 ± 0.0036	0.049 ± 0.0039	0.201 ± 0.0152	0.119 ± 0.0083	0.116 ± 0.0156	0.101 ± 0.0059	0.495 ± 0.0284	0.421 ± 0.0643	0.352 ± 0.0250	0.212 ± 0.0341
Rate (mgH_2O/ min)	5 ± 0.7	4 ± 0.4	4 ± 0.2	3 ± 0.8	9 ± 0.4	5 ± 0.1	5 ± 0.1	4 ± 0.4	8 ± 0.5	6 ± 0.6	6 ± 0.6	5 ± 0.6
Time to Equilib (hrs)	0.75	0.75	0.75	0.75	1	1	1	1	8	8	8	6
DESORPTION UNDER 1-SUN												
Harvested water (gH_2O/ g)	0.041 ± 0.0056	0.045 ± 0.0052	0.043 ±0.0054	0.046 ± 0.0016	0.165 ± 0.0052	0.116 ± 0.0110	0.096 ± 0.0212	0.086 ± 0.0095	0.458 ± 0.0237	0.401 ± 0.0630	0.343 ± 0.0290	0.202 ± 0.202
Residual water (gH_2O/ g)	0.026 ± 0.0027	0.004 ± 0.0034	0.002 ± 0.0018	0.003 ± 0.0025	0.036 ± 0.0119	0.003 ± 0.0028	0.020 ± 0.0102	0.015 ± 0.0096	0.037 ± 0.0075	0.020 ± 0.0027	0.009 ± 0.0063	0.010 ± 0.0035
Rate (gH_2O/ min)	-0.003 ± 0.0001	-0.005 ±0.0004	-0.004 ± 0.0006	-0.004 ± 0.0005	-0.007 ± 0.0000	-0.014 ± 0.0008	-0.011 ± 0.0030	-0.009 ± 0.0014	-0.013 ± 0.0015	-0.023 ± 0.0036	-0.021 ± 0.0032	-0.015 ± 0.0015
Time to equilib (min)	30 ± 5	23 ± 2.8	27 ± 2.9	27 ± 2.9	45 ± 0	17 ± 2.9	20 ± 0	20 ± 0	60 ± 0	27 ± 2.9	25 ± 0	25 ± 0
Surface Temp (^oC)	40 ± 6.9	66 ± 2.1	58 ± 3.3	55 ± 2.1	38 ±0.7	58 ± 2.5	50 ± 1.2	49 ± 1.7	43 ± 1.2	66 ± 2.9	57 ± 4.4	59 ± 2.9

and the 5w/w% PNEDs. Adsorption experiments were run for 15 minutes – 1 hour past achieving saturation to confirm maximum adsorption capacity. **Figure 4-4a** shows representative data, wherein at 40% RH all desiccants were saturated with water vapor within 45 minutes. The time required to achieve water vapor saturation increased with increased RH. At 60% RH, all desiccants reached their maximum sorption capacity within 1 hour (**Figure 4-4b**), and at 80% RH, all desiccants reached maximum sorption capacity in 8 hours (**Figure 4-4c**).

Table 4-2 shows maximum adsorption capacities for all experiments, which at 40% RH ranged 0.045 (±0.0036) to 0.067 (±0.0033) g H_2O/g desiccant. The bare SiO_2 desiccant adsorbed more water ($p<0.03$) than either of the three NP enabled desiccants. Among the three NP enabled desiccants the maximum water adsorption capacities were statistically similar ($p>0.25$).

A similar trend was seen for adsorption experiments at 60% RH. Silica gel desiccants adsorb 0.201 (±0.0152) g H_2O / g desiccant within 1 hour, which is nearly double the capacity of all PNEDs ($p<0.003$). At 80% RH, the time required for water vapor saturation of the desiccants increases to 6-8 hours. Maximum sorption capacities of SiO_2 and 5w/w% CB-SiO_2 are statistically similar (0.495 ± 0.0284 vs 0.421 ± 0.0643 g vapor / g desiccant, $p=0.143$), as are the sorption capacities of 5 w/w% CB-SiO_2 and 5w/w% AuNC-SiO_2 (0.352 ± 0.0250 g vapor / g desiccant, $p=0.185$).

Two factors may be leading to lower adsorption of NP-enabled desiccants compared with virgin desiccants. First, the APTES coating may be limiting access to the desiccant pores. Second, NPs may be hindering access to the desiccant pores. **Table 4-3** shows BET surface area analysis shows virgin SiO_2 desiccant has specific surface area of

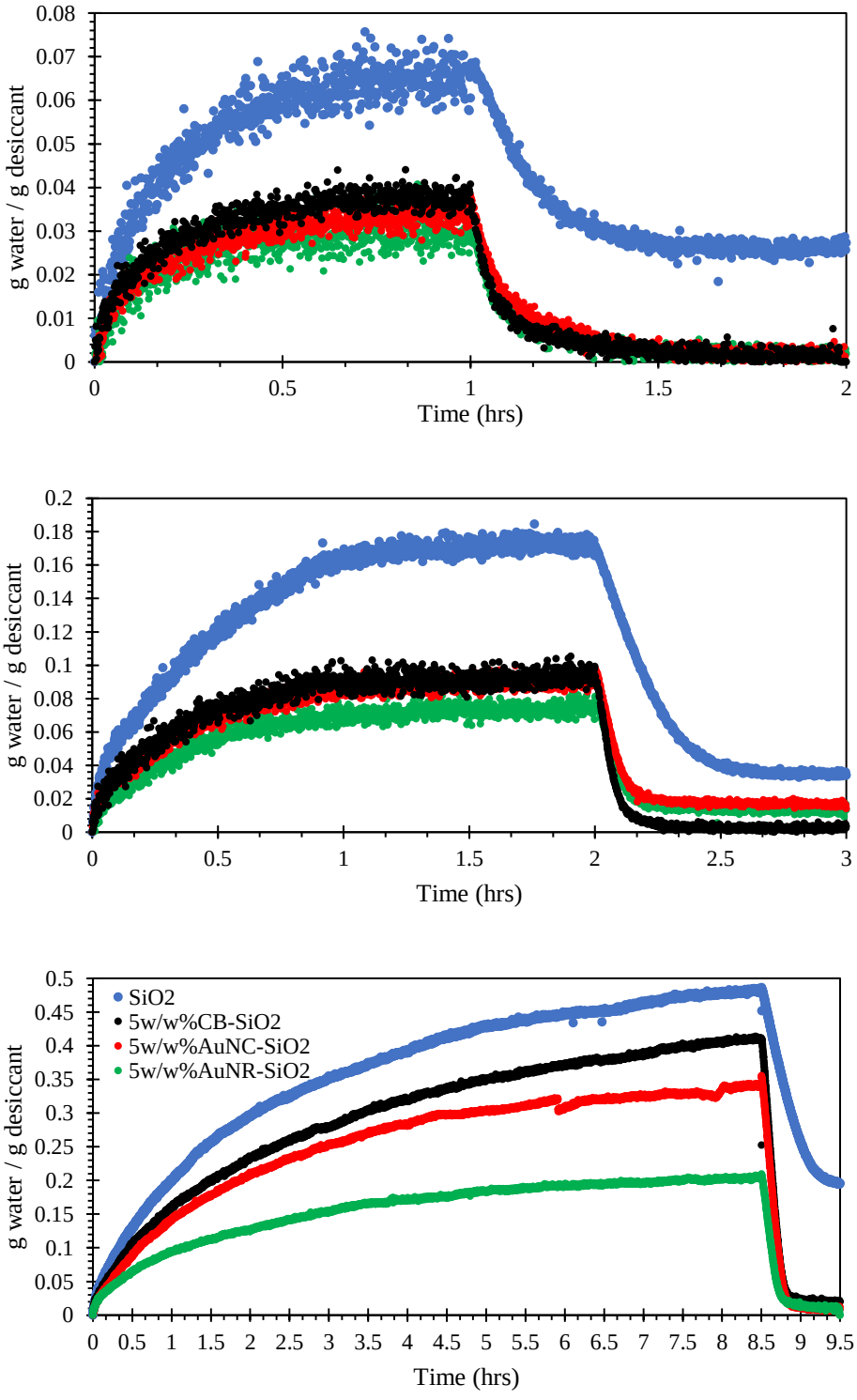

Figure 4-4 Water vapor adsorption under controlled humidity conditions and desorption under 1-sun irradiation over time. **a)** Adsorption experiments performed at RH = 40%, **b)** 60%, **c)** 80%.

Table 4-3 BET surface area of desiccants

Material	BET Surface Area (m^2/g)	Error
SiO_2	460	3.3511
SiO_2-APTES	290	2.5850
5w/w%CB-SiO_2	300	0.6488
5w/w%AuNC-SiO_2	280	0.9580
5w/w%AuNR-SiO_2	248	0.6726

460 g/m^2. Addition of the APTES linker on the surface of SiO_2 decreases surface area by 37% to 290 g/m^3. Attachment of carbon black nanoparticles and gold nanocubes to SiO_2-APTES does not impact the surface area beyond the decrease from APTES attachment. However, gold nanorod attachment to SiO_2-APTES resulted in a 46% decrease in surface area from the bare silica desiccant. Decrease in surface area limits availability of surface sites where water vapor can adsorb.

4.3.4 Water Vapor Desorption from Desiccants Under Simulated Solar Irradiation

After saturation, desorption rates were monitored for up to 1 hour under 1-sun simulated solar irradiation. **Figure 4-4a** shows one adsorption-desorption cycle for selected desiccants. **Table 4-2** summarizes desorption rates for each material and initial RH. Faster desorption rates of PNEDs are attributed to higher surface temperatures of desiccants. Notably, CB-SiO_2 achieves nearly double the desorption rate and surface temperature 20-30^oC higher than virgin SiO_2 for all RH. The linear regression coefficient of determination R^2 comparing rate of desorption to surface temperature for the 4 desiccants was 0.8102, 0.8592 and 0.6060 for 40%, 60% and 80% RH, respectively. The higher variability of results obtained from 80% RH desorption experiments was likely due to multi-layer desorption, with water vapor leaving the surface of the desiccant faster than water vapor bound in the pores.

Aside from desorption rates, we observed differences in the amount of water available for harvesting by the different desiccants. Higher RH lead to larger masses of water vapor on the desiccants, but because of pore blockage there was less total mass adsorbed by the PNEDs. However, PNEDs achieve near complete water desorption during the heating cycle whereas 40% of the water vapor failed to desorb from the virgin SiO_2 because it could not heat up to a high enough temperature. Considering these factors together, we compared the mass of "harvestable" water as the total water mass desorbed from the desiccant. (**Figure 4-5a**) Surprisingly, accounting for only the mass of water vapor desorbed from the desiccants for one cycle of adsorption and desorption, SiO_2 has higher water capture capacity compared to all PNEDs at 60% RH and AuNP-SiO_2 at 80% RH. One combination yielded similar water (SiO_2 has equal capacity to 5w/w% CB-SiO_2 at 80% RH). However, water harvested by SiO_2 and PNEDs in one cycle was statistically equal at 40% RH.

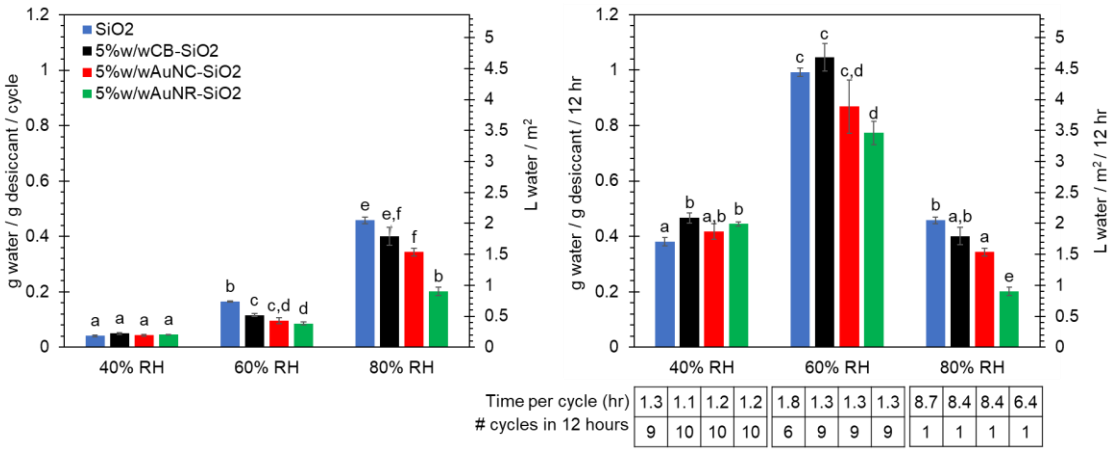

Figure 4-5 a) Volume water captured per gram desiccant for one cycle of adsorption and desorption. b) Volume water captured per gram desiccant for multiple cycles over 12 hours. Time per cycle accounts for adsorption and desorption time combined.

4.3.5 Desiccant Cycling Between Adsorption and Desorption over 12 hours

Considering that the volume of water captured by virgin SiO_2 and PNEDs at 40% RH was statistically equal and PNEDs had faster desorption rate, we hypothesized PNEDs could perform more adsorption and desorption cycles over a 12-hour daylight period to yield a higher volume of water collected. Accordingly, repetitive adsorption and desorption cycles were conducted over a 12-hour period to obtain data to estimate net water harvest capacity and evaluate material stability. Based on preliminary estimates and experimental monitoring, as soon as the desiccant achieved saturation it was subjected to a desorption cycle. **Figure 4-6** shows representative data for SiO_2 and the best performing PNED (5w/w%CB-SiO_2) at 40% RH. As illustrated by near identical rates and extents of water vapor adsorption and desorption, both bare and nano-enabled desiccants performed consistently over multiple cycles. The PNED (5w/w%CB-SiO_2) achieved 11 complete adsorption/desorption cycles within 12 hours, with complete desorption in each cycle, yielding a harvestable mass of water of 0.562 g water/g desiccant. In parallel experiments, the SiO_2 desiccant only achieved 9 cycles within 12 hours due to slower rate of desorption and incomplete desorption of adsorbed water due to lack of heating to as high a temperature as PNED. The total volume of water produced by SiO_2 desiccants cycling at 40% RH was 0.460 g water/ g desiccant. Thus, the net water harvesting capacity of the best performing desiccant was 25% greater than the virgin SiO_2 during a 12-hour period. There is still room for the PNED to achieve even greater improvements in water harvesting to overcome pore blockage caused by APTES (**Table 4-3**). This is the focus of ongoing research.

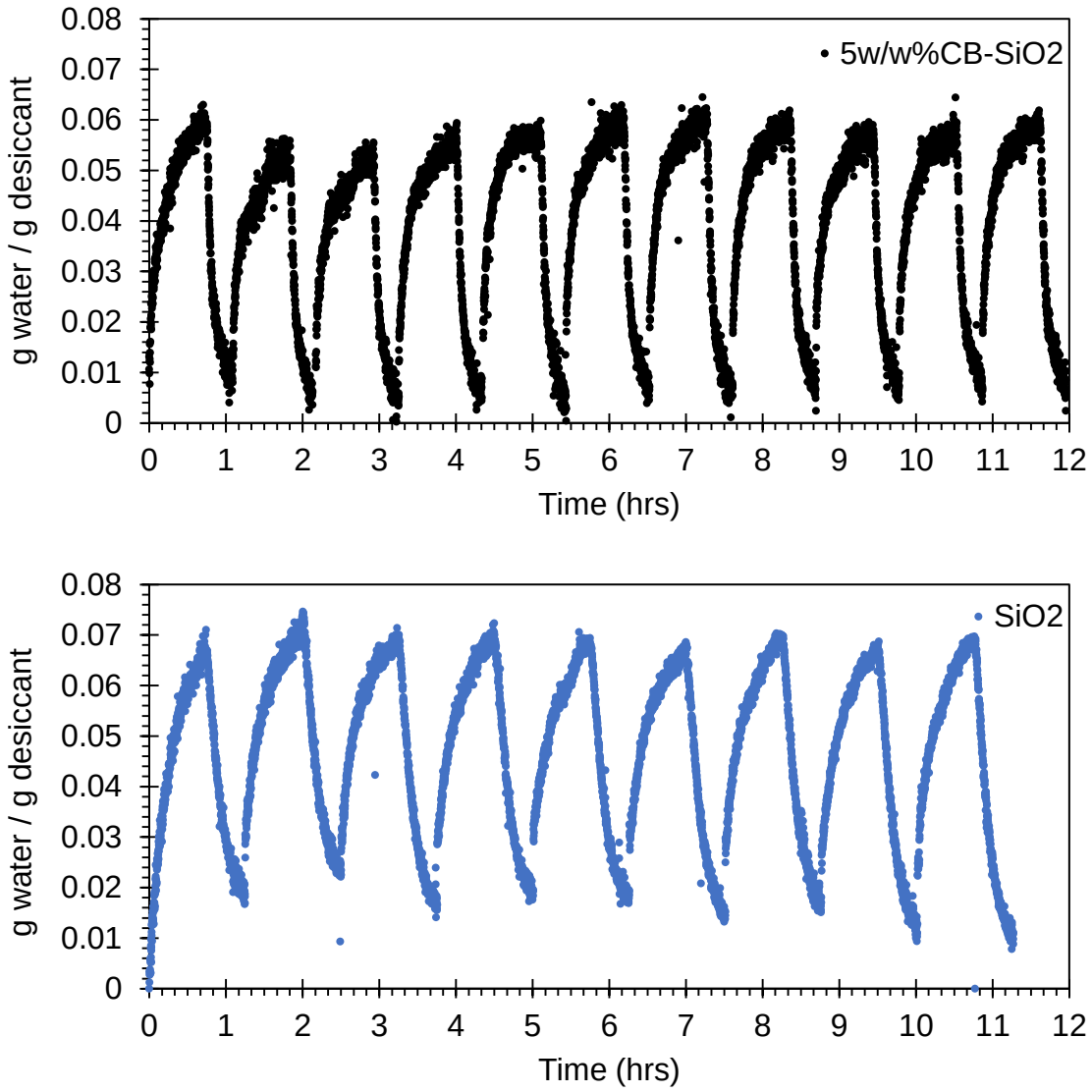

Figure 4-6 Experimental cycling of desiccants between adsorption at 40% RH and desorption under solar simulator. a) 5w/w%CB-SiO_2 desiccants, adsorption performed for 45 minutes and desorption performed for 20 minutes over 12 hours. b) SiO_2 desiccants, adsorption performed for 45 minutes and desorption performed for 30 minutes over 12 hours.

4.3.6 Theoretical Atmospheric Water Capture Potential by Desiccants Cycled in Large Scale System

Figure 4-5b illustrates the volume of water harvested over 12 hours by all desiccants under variable humidity conditions. The primary y-axis shows mass of water captured per gram of desiccant over 12 hours. The secondary y-axis represents the volume of water harvested by a 10 mm thick layer of desiccants spread over a 1 m^2 footprint (i.e. 4.5 kg of desiccant). These values represent a typical system configuration for passive AWC. At 40% RH there is statistically significant added benefit to using a nano-enabled desiccant, with 2.1 (+/- 0.16) L/m^2 water harvested by 5w/w%CB-SiO_2 compared to 1.7 (+/- 0.14) L/m^2 by virgin SiO_2 ($p=0.035$). PNED are able to produce more water over 12 hours because overall cycle time is shorter and therefore more cycles can be performed (**Table 4-4**). At mid- and high- RH conditions, all desiccants achieve similar water capture results. At 60% RH, even though all PNEDs can perform 3 more cycles than bare SiO_2, the total volume of water collected is statistically similar (5w/w%CB-SiO_2 = 4.7 +/- 0.44 L/m^2, SiO_2 = 4.4 +/- 0.14 L/m^2, $p = 0.422$). Bare SiO_2 can adsorb 40% more water than PNED, but also retains 40% of the adsorbed water vapor during desorption, leading to a net even production of water by bare and nano-enabled desiccants. At 80% RH, total time of adsorption is 6 hours for 5w/w%AuNR-SiO_2 and 8 hours for all other desiccants, therefore more than one adsorption and desorption cycle cannot be performed over a 12-hour period. Water harvesting potential is then dictated by the capacity of a single cycle.

Table 4-4 Time required per 1 adsorption and desorption cycle by desiccant under controlled humidity condition and theoretical number of adsorption and desorption cycles that could be performed in a 12-hour period

RH (%)	Material	Time per cycle (hr)	Number of cycles in 12 hours
40	SiO_2	1.3	9
	5w/w%CB-SiO_2	1.1	10
	5w/w%AuNC-SiO_2	1.2	10
	5w/w%AuNR-SiO_2	1.2	10
60	SiO_2	1.8	6
	5w/w%CB-SiO_2	1.3	9
	5w/w%AuNC-SiO_2	1.3	9
	5w/w%AuNR-SiO_2	1.3	9
80	SiO_2	8.7	1
	5w/w%CB-SiO_2	8.4	1
	5w/w%AuNC-SiO_2	8.4	1
	5w/w%AuNR-SiO_2	6.4	1

4.4 Conclusions and Future Outlook

Silica desiccants coated with photothermal carbon black nanoparticles can be used in arid climates with abundant solar radiation (i.e. Phoenix, AZ) to capture water vapor from the air. These desiccants progress the state of science on solid desiccants for atmospheric water capture, proving multiple cycles (>10) of adsorption and desorption can be performed within a 12-hour daylight period. A 5 w/w% CB-SiO_2 desiccant can capture 0.562 g water/g desiccant at 40% RH over 12 hours, an order of magnitude more than silica gel operated for only one cycle. Condensation of the desorbed water can be performed if desiccants were contained within a device where cool air can be transferred to the warm, saturated water vapor to bring it to below dew point temperature. An example of such a device could mimic an electrical dehumidifier, where desiccants are contained within a rotating wheel that passes from an adsorption zone open to ambient

air, a desorption zone where heat is applied, and a condensation zone where heat transfer occurs to cool and condense the water.

4.5 Acknowledgements

This work was funded through the National Science Foundation Nanosystems Engineering Research Center on Nanotechnology Enabled Water Treatment (EEC-1449500) and National Science Foundation Graduate Research Fellowship. We thank Dr. Stephanie Loeb and Dr. Jaehong Kim for valuable insight in synthesis, characterization and attachment of gold nanoparticles. Kaley Yazzie and Emma Westerhoff contributed to water capture and desiccant heating lab experiments.

4.6 Supplementary Information

4.6.1 Gold Nanoparticle Synthesis Methods

Gold nanocubes and nanorods were synthesized using a seeded-growth technique according to (Loeb et al., 2018). The gold nanocube seed was synthesized by mixing 0.1 M CTAB (7.5 mL) with 0.01 M $HAuCl_4$ (0.25 mL) and ice-cold, freshly prepared 0.01 M $NaBH_4$ (0.6 mL), then was kept in an oven at 27^{o}C for 1 hour. To make the growth solution, 0.1 M CTAB (524.8 mL), 0.01 M $HAuCl_4$ (65.6 mL), and 0.1 M ascorbic acid (311.6 mL) were added to 3280 mL of ultrapure water. The seed was diluted 1:10 in water, then 1.64 mL of the diluted seed solution was added to the growth mixture.

Gold nanorod seed solution consisted of 0.1 M CTAB (9.75 mL) mixed with 0.01 M $HAuCl_4$ (0.25 mL) and ice-cold, freshly prepared 0.01 M $NaBH_4$ (0.6 mL), and was kept in an oven at 27^{o}C for 2 hours. To make the growth solution, 0.12 mL of the gold nanorod seed was added to 0.1 M CTAB (3800 mL), 0.01 M $HAuCl_4$ (190 mL), 0.01 M $AgNO_3$ (38 mL), 0.1 M HCl (76 mL), and 0.1 M ascorbic acid (30.4 mL).

The nanocube and nanorod solutions were stirred on a magnetic stir plate for 5 minutes, then stored overnight at 27°C. Finally, the growth solutions were centrifuged washed (13,000 RPM for 2 hours) two times with ultrapure water to isolate the nanoparticles and remove unincorporated solvents. The final gold nanocube solution is a bright red color (at 25 mg/L) and surface plasmonic resonance peak at 534 nm. The final gold nanorod solution is a deep purple color (at 82 mg/L) and has two surface plasmonic resonance peaks at 520 nm and 790 nm.

4.6.2 Supplemental Figures

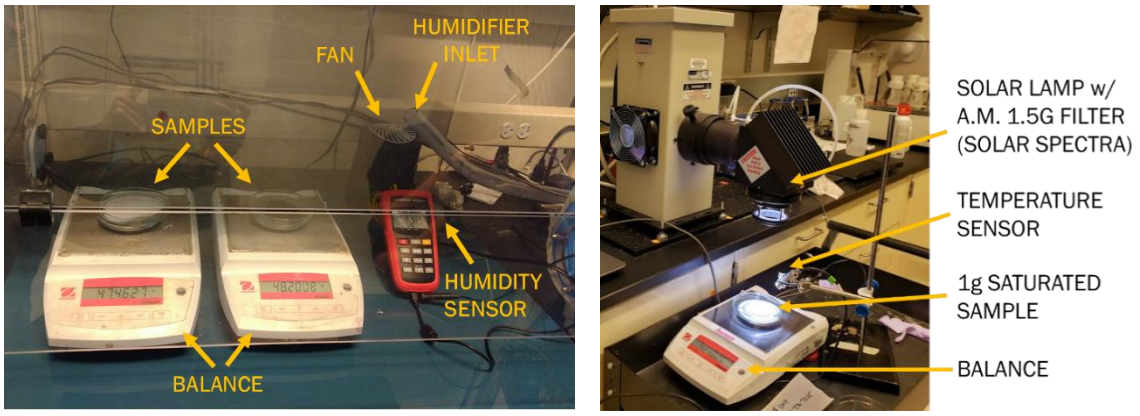

Figure SI 4-1 a) Testing set up for water vapor adsorption. Hood contains two balances with data loggers, desiccant samples in open glass petri dishes, humidity sensor, fan, and humidifier with setpoint either RH 40%, 60%, or 80%. b) Testing set up for photothermal desorption of water vapor. Petri dish containing saturated desiccant sample placed on balance with data logger underneath 1-sun simulated solar irradiation.

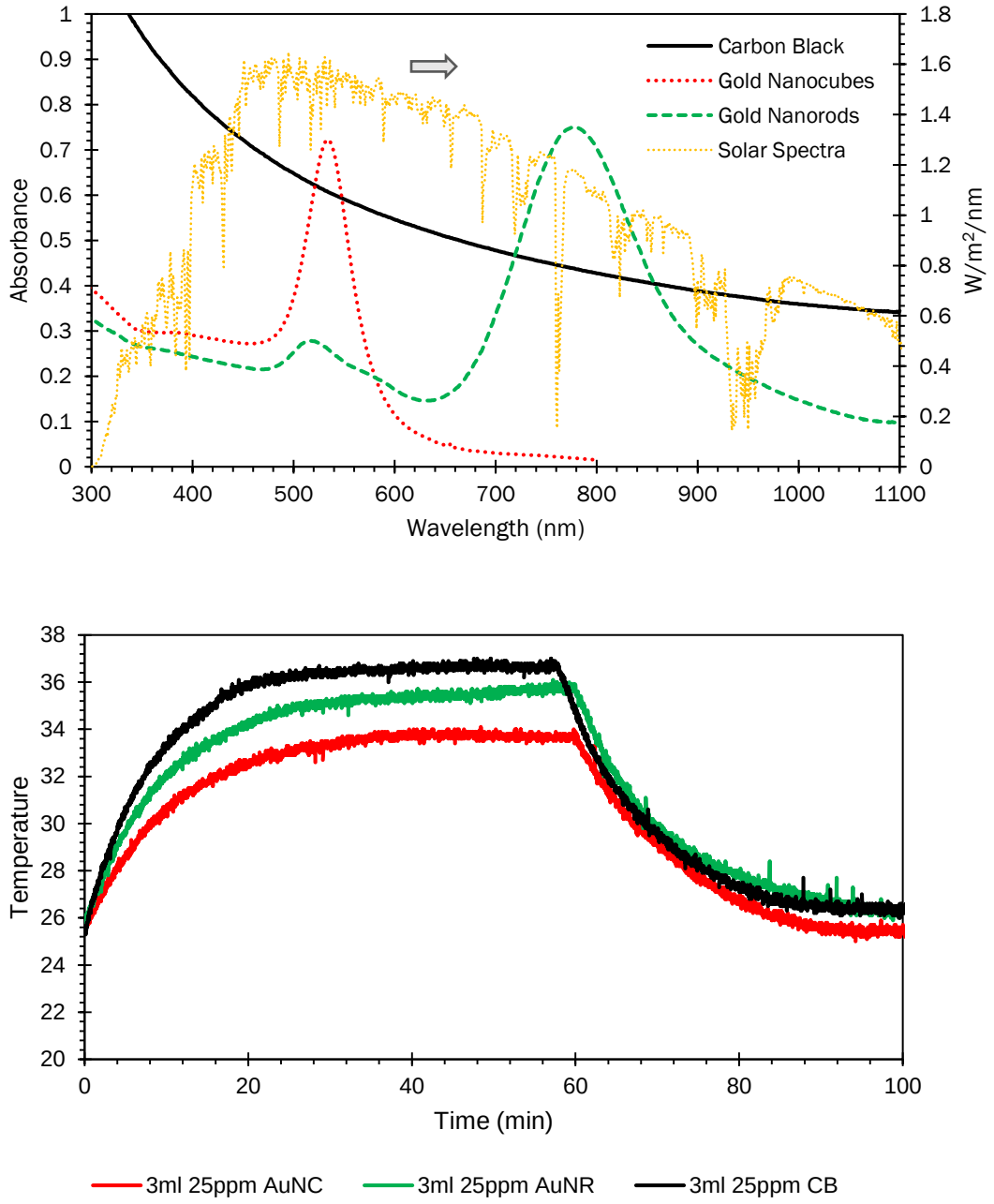

Figure SI 4-2 a) UV-Vis absorption spectra of photothermal nanoparticles (primary y-axis) superimposed over solar irradiation spectrum (secondary y-axis). **b)** Rate of heating and cooling of 3mL of 25ppm nanoparticles in water in quartz cuvette exposed to 1-sun solar irradiation. Sample temperature at time=0s was 25.7^{o}C (ambient).

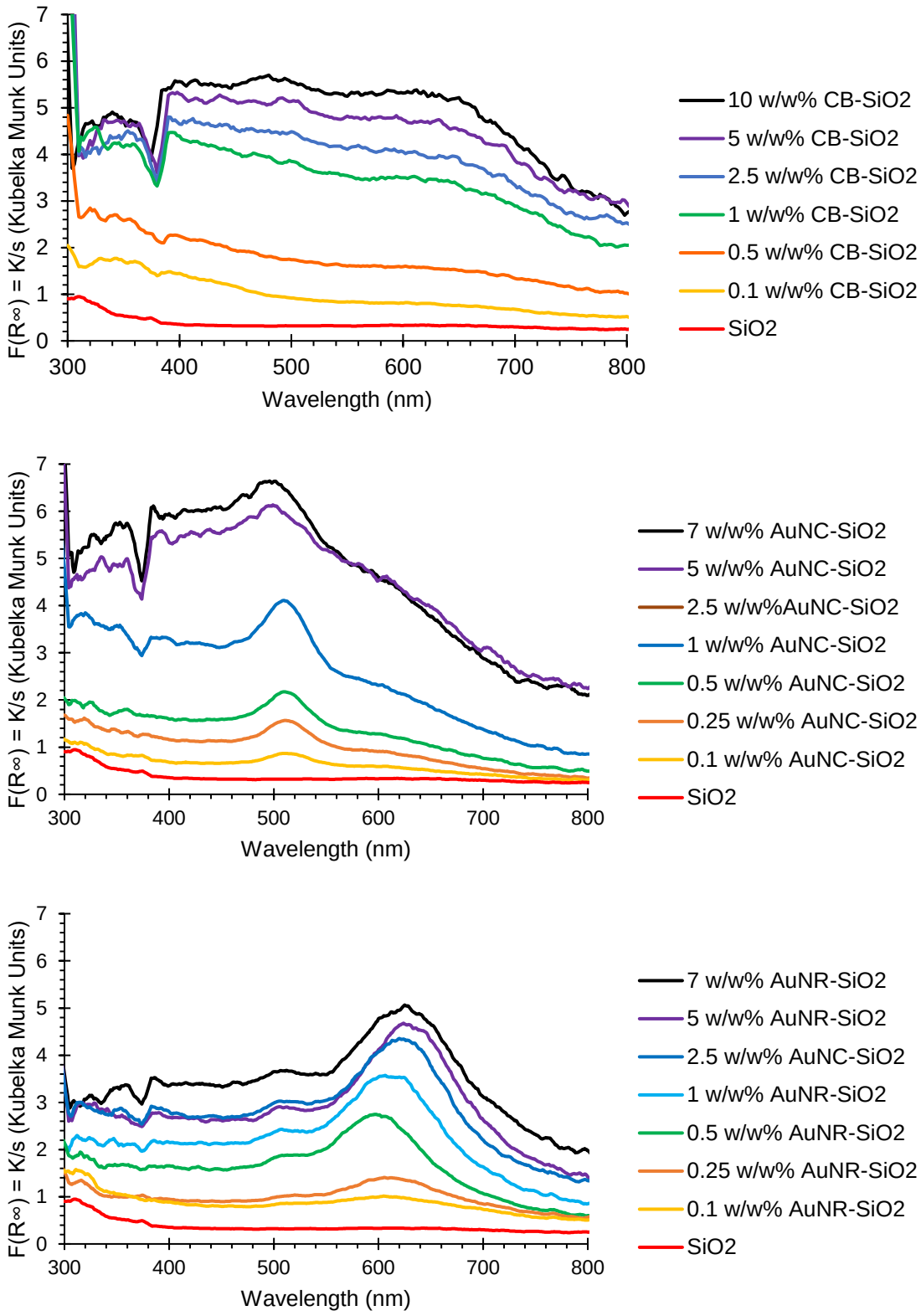

Figure SI 4-3 Kubelka-Munk Transformation of Diffuse Reflectance on PNEDs. A) CB-SiO_2. B) AuNC-SiO_2. C) AuNR-SiO_2.

SEASONAL ATMOSPHERIC WATER CAPTURE YIELD AND WATER QUALITY USING ELECTRIC-POWERED DESICCANT AND COMPRESSOR DEHUMIDIFIERS

This chapter is a manuscript draft in preparation for submission as:

> Mulchandani, A., Edberg, J., Herckes, P., and Westerhoff, P. Seasonal atmospheric water capture yield and water quality using electric-powered desiccant and compressor dehumidifiers. *In prep for submission to Water Research.*

5.1 Introduction

Natural and municipal water disasters, such as hurricanes, floods, and damaged infrastructure impact drinking water supply globally. In the face of these disasters, the immediate emergency response is to transport bottled water at a cost of >$1/gallon. Bottled water is not a sustainable water supply – in addition to the per gallon cost, there is an added cost of transportation, resulting greenhouse gas emissions, and plastic waste production.(EPA, 2011; T. Wang, Kim, & Whelton, 2019) There is a need for an alternative supply of safe, clean drinking water during emergency relief. The atmosphere is a freshwater reservoir that contains 12,900 km^3 of water, 6x more than the volume of rivers.(Shiklomanov, 1992) The atmosphere is universally present and can be accessed as a source of drinking water in any location by dehumidification processes.

Dehumidification is the process of separating water vapor from moist air, resulting in a separate dry air stream as well as a liquid water byproduct. Electrical and passive dehumidifiers are typically used in an indoor environment (e.g. basement, warehouse) to alleviate moisture conditions.(Energy Star, n.d.) Water is usually discarded

or considered as greywater (non-potable reuse). However, there has been increased commercialization of indoor and outdoor dehumidifiers to capture and store drinking water. (7,272,947 B2, 2007; 5259203, 1993; 5,701,749, 1997; US 2010/0266742 A1, 2010; US 2014/0053580 A1, 2014; US 2011/0048039 A1, 2011; 5,669,221, 1997; 6,343,479, 2002; 5301516, 1994; US 7.043.934 B2, 2006; 5106512, 1992) (**Table 5-1**)

Two primary modes of dehumidification are a) dew point condensation (using a refrigerant coupled with a compressor or thermo-electric cooling) and b) moisture removal by a sorbent (i.e. desiccant).(American Society of Heating Refrigerating and Air-Conditioning Engineers, 2016a, 2016b) In a dew point condensation system, water vapor is brought to saturation by decreasing the air temperature, which decreases saturation vapor pressure and increases relative humidity (RH). In a sorbent system, water vapor is first sorbed onto a desiccant. Heat is then applied to the saturated desiccant to desorb the concentrated vapor, then cold air is exchanged with the warm saturated vapor to cool it by dew point condensation.

Dehumidification systems have been benchmarked in ideal conditions (RH > 60%, T = 18.3^{o}C) (10 CFR Appendix X1 to Subpart B of Part 430 - Uniform Test Method for Measuring the Energy Consumption of Dehumidifiers, 2017), and it is unknown how they will operate in more arid climates. Additionally, all dehumidification systems for drinking water application treat the captured water through several stages, including filtration (e.g. activated carbon, zeolite, ion exchange, membrane) and disinfection by UV germicidal lamps or ozone.(7,272,947 B2, 2007; 5259203, 1993; 5,701,749, 1997; US 2010/0266742 A1, 2010; US 2014/0053580 A1, 2014; US 2011/0048039 A1, 2011; 5,669,221, 1997; 6,343,479, 2002; 5301516, 1994; US

7.043.934 B2, 2006; 5106512, 1992) The quality of the initial captured untreated water has not been reported.

The aim of this paper is to benchmark atmospheric water capture water yield, energy usage, and water quality to determine impact of dehumidification processes on rate of water capture, energy efficiency and water quality. Commercial electrical dehumidifiers were operated outdoors for 1 year in a semi-arid climate (Tempe, AZ). Electric dehumidifiers were used in this study because they use the same mechanisms and machinery as commercial AWC machines at 10% of the cost. Electrical dehumidifiers do not have water filtration systems, so AWC water quality could be accurately characterized.

5.2 Technical Background

5.2.1 Atmospheric Parameters and Key Equations

Two key parameters are often used to describe the water quantity of air. Specific humidity (SH) defines water quantity on a mass basis (g water vapor / kg air), calculated by **Equation 1**. A more commonly used metric for water vapor concentration is relative humidity (RH), calculated by **Equation 2**. RH is the ratio of SH to saturated SH and defines how water saturated the air is. RH is inversely related to air temperature through the Clausius-Clapeyron relationship (**Equation 3**), therefore RH is typically higher at night and lower during the day. AWC is a function of both SH and RH: water vapor will condense when fully saturated (i.e. RH = 100%), and the quantity of water available in the air to saturate is given by SH.

$$SH = \frac{R_d}{R_v}\frac{e}{p} \quad (1)$$

Table 5-1 Commercial atmospheric water capture machines for drinking water.

Company	Machine name	Capacity	Power	kWh/L	$/L from kWh	Features	Notes
Drinkable air	Chameleon 8	up to 38 L/day	765 W	0.48	0.05	Compressor system; Ozone purification (adds 70 ppm oxygen to water) every 15 mins; air filter, mineral filter, and 5µm carbon block filter	Working temp 70-100F (21-38C); Working RH 35-100; **"Recommended for indoor use only"**
Atmospheric water solutions	Aquaboy Pro II	7.5-19 L/day	970 W (Heating 500W, generating power 470W)	0.63	0.07	Compressor system; 7 stage EZ-filter: HEPA, UV, sediment filter, activated carbon/coconut shell, UF membrane, carbon filter #2, UV #2; microcomputer and sensors	T 55-90 F, RH 28-90; **"Not designed for outdoor use"**
Akvo	Akvo 55K	150 L/day	2100 W	0.34	0.04	Compressor system; nano carbon filter	Ideal T=25-32C, RH=70-75; Can also operate in T=18-45C, RH=35-40
	Akvo 110k	300 L/day	3300 W	0.26	0.03	Compressor system, Ozonator, 5µm sediment filter, nano carbon filter, UV	Ideal T=25-32C, RH=70-75; Can also operate in T=18-45C, RH=35-40
	Akvo 180k	500 L/day	4000 W	0.19	0.02		
	Akvo 365k	1000 L/day	8200 W	0.20	0.02		
Genaq	Stratus	50 L/day	700 W	0.34	0.04	Compressor system; carbon filter + "purifyer"	for residential, office, hotels, hospitals
		200 L/day	2450 W	0.29	0.03		
	Nimbus	500 L/day	4.1 kW	0.20	0.02		"remote supply units"; options for solar panel power or diesel power
		4500 L/day	40 kW	0.21	0.02		
	Cumulus	50 L/day	700 W	0.34	0.04		emergency response unit; options for solar panel (AC power) and diesel
		500 L/day	4.1 kW	0.20	0.02		
		5000 L/day	50 kW	0.24	0.03		
Water Gen	GEN-350	up to 900 L/day	5.6 kW; 0.33 kWh/L; 3.3 L/kWh	0.15	0.02	Patented technology (plastic heat exchanger); sediment filter, activated carbon, UV, mineralization	2-4 cents/L based on 8c/kWh,also a large scale option available
Skywater	30	100 L/day				Compressor system; ozone, carbon filter	RH 40-100, T 21C-32C; xPrize winner; Skywater300 used by military, 1 gal fuel = 10-14 gallons water/hr
	75	250 L/day					
	150	500 L/day	4.2 kW	0.20	0.02		
	300	1000 L/day	7-10 kW/hr	0.24	0.03		
	ESU-20	3400 L/day	30 kWh/hr	0.21	0.02		
H2O machine		10-115 L/day	1500 W	0.31	0.13	Compressor system; "various purification measures"	$0.08/gallon

$$RH = \frac{e}{e_s} = \frac{SH}{saturated\ SH} \quad (2)$$

$$e_s = e_{s0} \exp\left(\frac{L_v}{R_v}\left(\frac{1}{T_o} - \frac{1}{T}\right)\right) \quad (3)$$

5.2.2 Compressor Dehumidifiers

Compressor systems bring vapor to saturation by decreasing air temperature, which decreases saturation vapor pressure and increases RH. In a compressor system, heat from the air is transferred to a cold refrigerant, and the water condenses on the coils. The hot refrigerant goes through a vapor compression refrigeration cycle to cool and recirculate back to the condenser coils. **(Figure 5-1a**) Air needs to be cooled to dew point temperature in order to condense. Dew point temperature can be calculated by a modified Clausius-Clapeyron equation. (**Equation 4**) **Figure 5-2** shows dew point temperature as a function of air temperature and RH. The blue box shows the region in which dew point temperature is below freezing, i.e. frost will form on the condensing surface, which is not ideal for AWC. For RH<30%, air temperature must be at least greater than 20^{o}C. For RH 60%, air temperatures only need to be >8^{o}C for condensation to occur without freezing. The energy required to operate a compressor system is a function of the temperature change required for condensation. ENERGY STAR (U.S. government-backed energy efficiency program) certified commercial compressor dehumidifiers have reported productivity of 20 – 50 pints/day (10 – 24 L/day) with integrated energy factor 1.57 – 3.3 L/kWh (0.30 – 0.63 kWh/L) at test conditions (RH > 60%). (Carmichael, 2020)

$$T_d = \left[\frac{1}{T_0} - \frac{R_v}{L_v}\ln\left(\frac{e}{e_{s0}}\right)\right]^{-1} \quad (4)$$

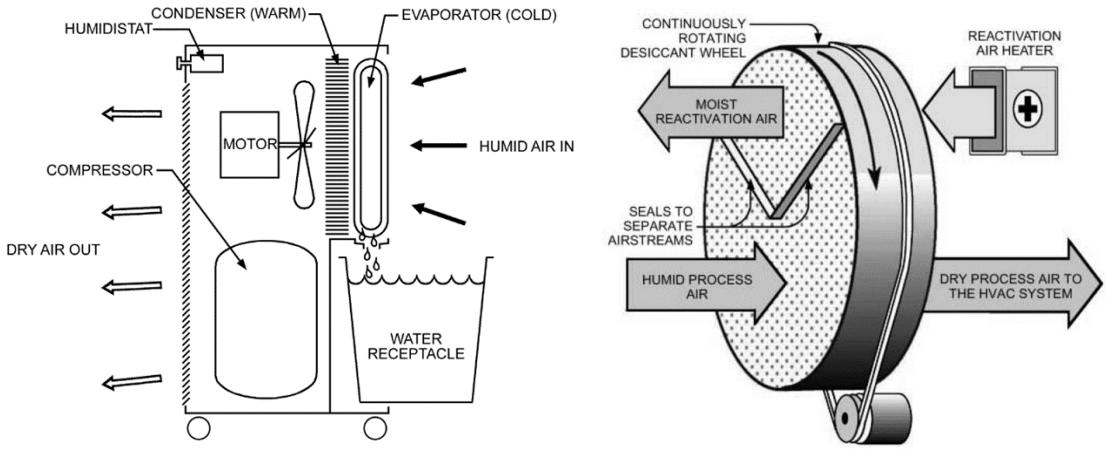

Figure 5-1 a) Operation process of a compressor dehumidifier. (American Society of Heating Refrigerating and Air-Conditioning Engineers, 2016b), **b)** Operation process of a rotary desiccant dehumidifier.(American Society of Heating Refrigerating and Air-Conditioning Engineers, 2016a)

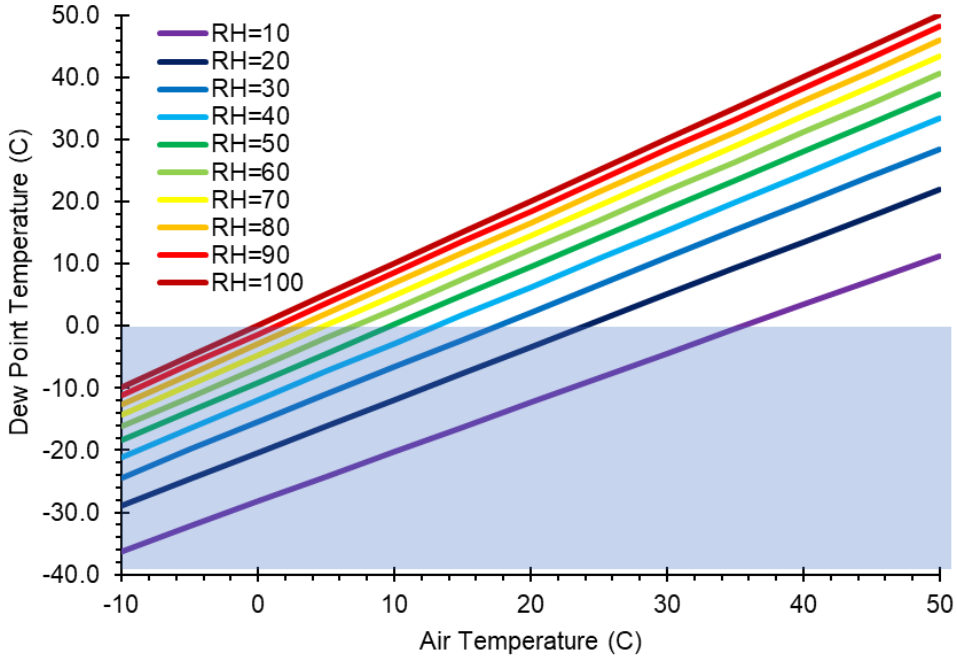

Figure 5-2 Dew point temperature as a function of air temperature and relative humidity, calculated by the Clausius-Clapeyron equation. Shaded blue region indicates conditions at which dew point is below freezing.

5.2.3 Desiccant Dehumidifiers

A rotary desiccant dehumidifier consists of a wheel containing a supported matrix structure (e.g. mesh, paper, fibers) impregnated with desiccants. The desiccant wheel has a diameter of 15 inches and thickness of 1 inch and is loaded with ~20 grams of desiccant. Moist air is pulled by a fan through an air filter and over the open area of the desiccant bed ($5/6^{th}$ of wheel area). The wheel rotates between this adsorption zone, and a desorption zone where a heater increases surface temperature of the desiccants to enable release of the water vapor into a condensation chamber. The water vapor condenses by heat exchange with cool process air. (**Figure 5-1b**) The wheel rotates at 1.33 RPM, so desiccants are exposed to incoming air for 37.5 seconds and heat for 7.5 seconds in each rotation. Electrical desiccant dehumidifiers commonly contain zeolite as the sorbent, which sorbs 0.25 g water vapor / g material at all RHs between 20% and 100%. For RH 0-20%, sorption capacity logarithmically increases from 0 to 0.25 g/g. This means that productivity of desiccant dehumidifiers should be the same for all RH > 20%, but is expected to decrease if RH < 20%. Commercial desiccant dehumidifiers have reported productivity of 15 – 21 pints/day (7-10 L/day) using 0.50 – 0.56 L/kWh (1.8 – 2 kWh/L) at test conditions (RH=60%) and are not ENERGY STAR certified.

5.3 Materials and Methods

Two desiccant dehumidifiers (Ecoseb DD322EA Simple (**D1**), Evadry EDV 4000 (**D2**)) and one compressor dehumidifier (Frigidaire FFAD7033R1A (**C1**)) were purchased in 2018. These dehumidifiers were chosen due to differences in energy efficiencies. The reported energy efficiency of **D1** is 10 L/day using 0.74 kWh (1.78 kWh/L) and air flow rate of 179 CFM (5.1 m^3/min). The reported efficiency of **D2** is 7

L/day using 0.615 kWh of power (2.1 kWh/L) and air flow rate of 114 CFM (3.2 m^3/min). These two desiccant dehumidifier models were chosen to compare energy efficiency as a function of air flow rate. The reported efficiency of **C1** is 33 L/day using 0.75 kWh (0.54 kWh/L) and air flow rate 182 CFM (5.2 m^3/min). it was chosen because it is Energy Star certified as an energy efficient dehumidifier (Energy factor 1.8 L/kWh or 0.55 kWh/L at 60% RH and 18.3^{o}C) and has similar flow rate as **D1**. **C1** also has energy efficiency similar to commercial atmospheric water capture machines (0.3 – 0.63 kWh/L).

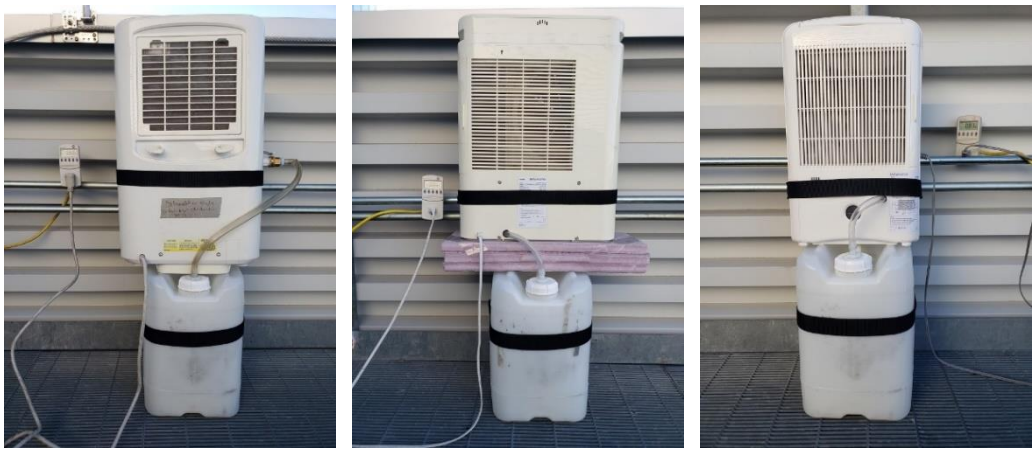

Figure 5-3 C1, D1 and D2 electric dehumidifiers placed above 5-gallon collection container (left to right)

Outdoor experiments were performed on the rooftop of a 7-story building in Tempe, AZ, USA (33°25'04.4"N 111°55'42.6"W). Dehumidifiers were operated outdoors for 1 year, 3 days per week, for 2 – 15 hours at a time during both the day and night. Operation times and hours were varied to determine if there was an impact of atmospheric conditions and operation length on productivity, energy efficiency and water quality. Dehumidifiers were plugged into energy usage monitors (Kill-A-Watt) which

were connected to the power outlets. Water was collected into 5-gallon storage containers attached to the dehumidifier water exit port by a ½ inch diameter tubing. (**Figure 5-3)**

After each run, the volume of water collected and energy usage (kWh) were recorded and basic water quality parameters (pH, conductivity, turbidity) were measured. Two times per week, samples were collected, acidified with either nitric or hydrochloric acid, and stored at 4^{o}C for monthly analysis of metals and organic carbon, respectively. One **D2** and one **C1** sample from November 2019 were sent to Eurofins Analytical lab for analysis of total organic carbon, aldehydes, carboxylic acids, volatile organic compounds, semi-volatile organic compounds, and HPC plate-count.

Metals analysis was performed on ThermoFisher XSeries2 ICP-MS. Analyzed metals were EPA primary regulated elements (As, Ba, Be, Cd, Cr, Cu, Pb, Sb, Se, Tl), secondary regulated elements (Ag, Al, Fe, Mn, Zn), as well as other commonly occurring transition metals (B, Ca, Co, K, Mg, Mo, Na, Ni, Si, Sr, Ti and V). Dissolved organic carbon (DOC) analysis was performed on Shimadzu TOC-VCSH. DOC samples were filtered with ashed Whatman glass microfiber GF/F filters prior to analysis.

5.4 Results and Discussion

5.4.1 Correlation Between Humidity and Quantity of Water Collected

Figure 5-4a shows water production rates (L/hr) from the 3 dehumidifiers operated side-by-side. The relative humidity range over the operation period is superimposed (blue lines, secondary y-axi). Water production rate for both **D1** (red) and **D2** (blue) was consistently 0.2 – 0.35 L/hr throughout the fall, winter and early spring but decreased to 0.1 – 0.15 L/hr in the summer. **C1** (green) productivity significantly varied

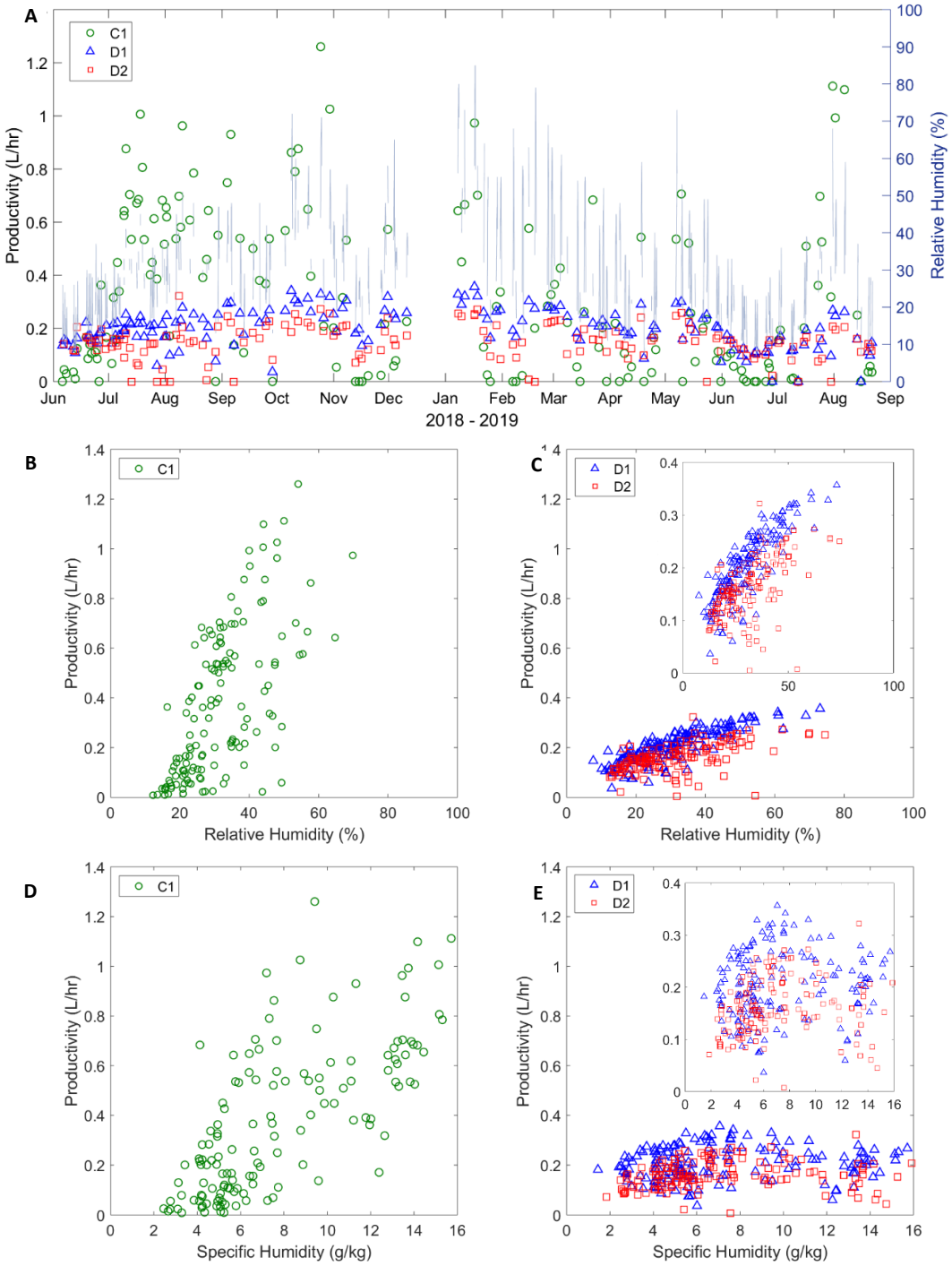

Figure 5-4 a) Productivity (L/hr)) of **C1** (green)**, D1** (blue) and **D2** (red) compressor and desiccant electrical dehumidifiers over 2018/2019. Black lines are range of relative humidity over each operation period. **b)** Productivity as a function of RH for compressor dehumidifier. **c)** Productivity as a function of RH for desiccant dehumidifiers. **d)** Productivity as a function of SH for compressor dehumidifier. **e)** Productivity as a function of SH for desiccant dehumidifiers.

between 0 – 1.2 L/hr. Accordingly, **D1** and **D2** can produce 2.4 – 8.4 L water / 24-hour day, while **C1** can produce 0 – 28 L / 24-hour day.

Productivity of desiccant systems is more strongly a function of RH than SH. **Figure 5-4c** inset and linear regression analysis show moderately strong correlation between productivity and average RH over the length of the run, with R^2 of 0.691 for **D1** and 0.213 for **D2**. In comparison, there is a much weaker correlation between productivity and average SH (**Figure 5-4e**), with R^2 of 0.0122 for **D1** and 0.000922 for **D2**. Desiccant water production is more strongly correlated to RH because of desiccant operation is governed by vapor pressure differential (i.e. RH) between the desiccant surface and air, and not the volume of water vapor available in the air (i.e. SH).

Figure 5-4b and d show productivity of compressor systems is a function of both average RH and SH. Multiple linear regression analysis comparing water production as a function of both average RH and SH over 159 observations returns adjusted R^2 of 0.822 with p-value < 10^{-31} for constants in **Equation 5**. Compressor productivity is positively correlated with RH for RH > 30%. Air closer to saturation will condense more readily than less saturated air. Compressor productivity is also positively correlated with SH, the available water in the air. At a constant air flow rate, air with higher water vapor mass will produce a larger volume of liquid water. Since RH and SH are not independent of one another (**Equations 1 and 2**), linear regression analysis on each atmospheric parameter was conducted as well. The R^2 for productivity vs RH was 0.488 with p-value 10^{-25} and R^2 for productivity vs SH was 0.548 with p-value 10^{-29}, proving that productivity of **C1** is more strongly predicted by both the vapor saturation of the air and vapor mass of the air together.

$$Productivity\ of\ C1\ \left(\frac{L}{hr}\right) = 0.0141\ RH + 0.0514\ SH - 0.467 \quad (5)$$

For RH < 20%, compressor systems are less effective than desiccant systems, as well as in some conditions where RH is between 20 – 50%. At lower RH, the dew point temperature is below or near freezing, rendering the compressor systems inoperable. (**Figure 5-2**) At RH > 20%, compressor systems can be up to 5x more productive than desiccant systems.

5.4.2 Energy Factor and Efficiency

Figure 5-5 relates energy factor to produce water (L/kWh) to RH or SH for the three devices. Device manufacturer reported energy factors (~0.5 L/kWh for **D1** and **D2**, 1.85 L/kWh for **C1**) are slightly higher than our observed data (0.05 – 0.5 L/kWh for **D1** and **D2**, 0 – 1.8 L/kWh for **C1**). This is primarily because device manufacturer reported energy factors are for RH >60%, and most of our observations occur for RH < 60%. Linear regression analysis shows very weak correlation between energy factor and RH or SH for **D1** and **D2** ($R^2 < 0.2$). It was hypothesized that energy factor would remain constant for RH > 30% because zeolite desiccants would uptake the same volume of water for RH 30 – 100%. However, productivity and energy factor data show that the desiccants in **D1** and **D2** produce a larger volume of water at higher energy factor with higher RH, albeit with only a mild correlation.

For dehumidifier **C1**, energy factor is linked to both RH and SH, similar to productivity results. When water vapor is closer to saturation, and when the water vapor quantity of air is higher, less heat needs to be transferred to the refrigerant to cool the vapor the volume of water that can be collected per energy spent increases. Multiple

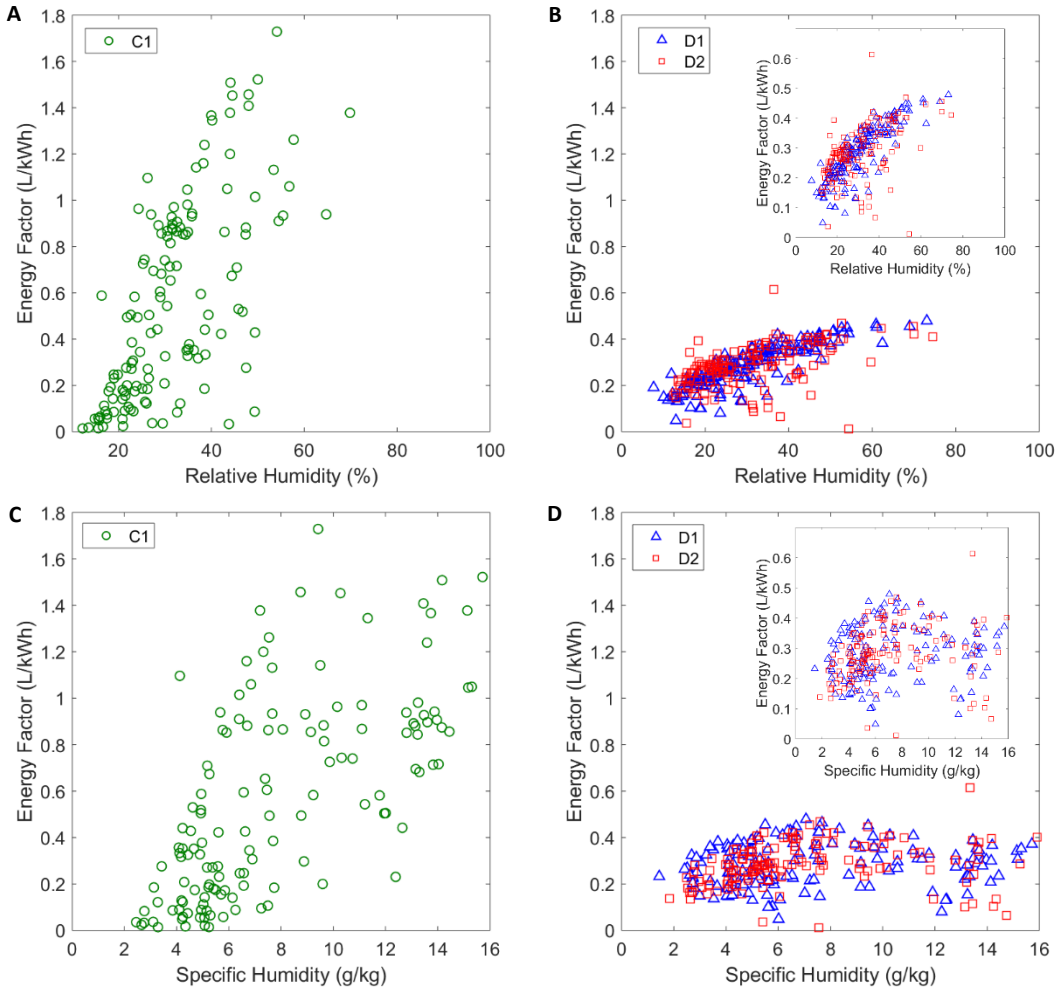

Figure 5-5 Energy factor (L/kWh) as a function of **a, b)** RH and **c, d)** SH for **C1** (green)**, D1** (blue) and **D2** (red) compressor and desiccant electrical dehumidifiers.

linear regression comparing energy factor to RH and SH produces regression **Equation 6**, with adjusted R^2 0.793.

$$EF\ of\ C1\ \left(\frac{L}{kWh}\right) = 0.0213\ RH + 0.0681\ SH - 0.641 \qquad (6)$$

Figure 5-6 shows efficiency of AWC vs RH and SH. Efficiency is productivity normalized to the amount of water available in the air that passes through the dehumidifier, calculated by **Equation 7**.

$$Efficiency = \frac{volume\ water\ produced}{volume\ water\ processed} = \frac{volume\ water\ produced}{SH * \rho_{air} * dehumidifier\ flow\ rate}$$

$$= \frac{\left[\frac{L}{hr}\right] * \left[\frac{hr}{min}\right] * \left[\frac{kg}{L}\right]}{\left[\frac{kg\ H_2O}{kg\ air}\right] * \left[\frac{kg\ air}{m^3}\right] * \left[\frac{m^3}{min}\right]} \quad (7)$$

Efficiency of desiccant systems decreases with SH. At higher SH, more water is passing through the system, but the desiccant has a fixed capacity, and any additional water not sorbed to the desiccant is lost. This can be exhibited by productivity and efficiency differences between **D1** and **D2**. **D1** has a higher device manufacturer reported productivity (10 L/day vs 7 L/day) and a higher air flow rate 179 CFM vs 114 CFM). While higher air flow rate leads to higher productivity, efficiency of the system decreases because there is also a larger volume of uncaptured water vapor. Desiccant systems could increase efficiency and productivity simultaneously by increasing the loading of desiccants contained within the wheel. This may however decrease the energy factor, as more energy would need to be spent to heat the desiccants in the desorption zone.

Efficiency of compressor systems increases with RH. As the water vapor gets closer to saturation, water can be more easily condensed. There is less competition for condensation sites on the refrigerant coils at higher RH, leading to higher efficiency.

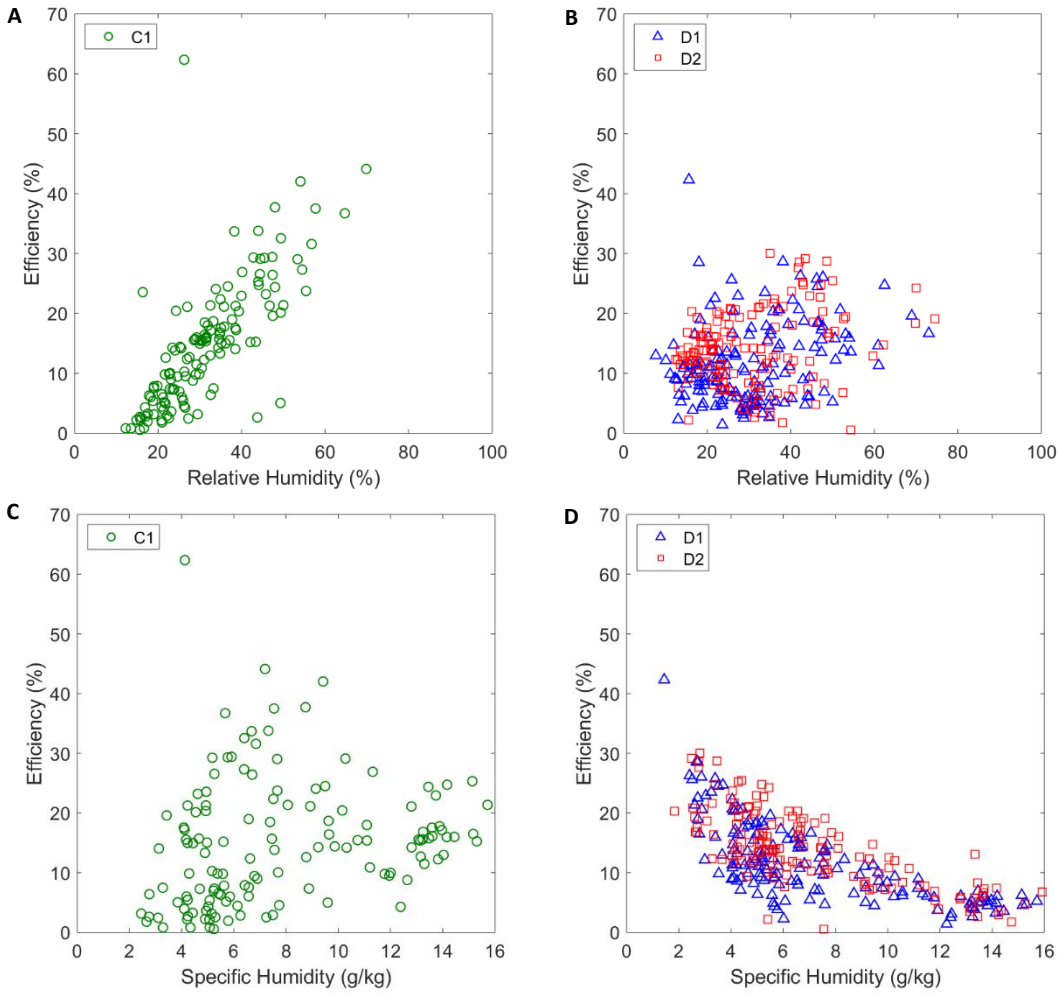

Figure 5-6 Efficiency of **C1** (green)**, D1** (blue) and **D2** (red) compressor and desiccant electrical dehumidifiers as a function of **a, b)** RH and **c, d)** SH.

5.4.3 Cost of Water Production

Using an electricity cost of $0.10 / kWh, the desiccant systems will cost $0.20 - $1.00 / L ($0.75 - $3.80 / gallon). The compressor system will cost $0.05 - $2.00 / L ($0.20 - $7.60 / gallon). The compressor system is cost competitive with bottled water (>$1.22 / gallon) in humid conditions. However, in dry conditions, a desiccant system is more cost and energy favorable.

5.4.4 Water Quality

The collected waters from both the desiccant and compressor dehumidifiers have pH levels of 6 – 7.5, and are similar to tap waters (6.5 – 8). (**Figure 5-7a**) **Figure 5-7b** shows similar conductivity of most water samples from compressor (15 – 80 μS/cm) and desiccant (15 – 60 μS/cm) dehumidifiers. However, the compressor system has several outliers with maximum conductivity of 180 μS/cm. These values are all on the lower end of the conductivity range of tap water (50 – 500 μS/cm). Salts and other charged ions are not as likely to be present in the vapor phase or associated with water vapor molecules compared to liquid water. However, conductivity of water from dehumidifiers is 3 orders of magnitude greater than distilled water (0.05 μS/cm), therefore it is not completely devoid of charged ions.

Dust particles associated with water vapor molecules can dissolve into condensed water. Water from the compressor system was visibly brown and turbid, and **Figure 5-7c** shows maximum turbidity peaking at 190 Nephelometric Turbidity Unit (NTU) and median value of 6 NTU. Conversely, in the desiccant system, water has a median turbidity of 0.22 NTU and maximum turbidity of 2 NTU. Turbidity is regulated by the US EPA Primary Drinking Water Standards at 1 NTU for systems that use conventional or direct filtration, and turbidity must be <0.3 NTU in at least 95% of samples taken per month. Turbidity of collected water from the compressor system is similar to rainwater, which ranges 0.5 – 35 NTU. (Mendez et al., 2011; Vialle et al., 2011; Yaziz, Gunting, Sapari, & Ghazali, 1989) Dust and other particulate matter that passes through the air filter of the compressor can potentially collect on refrigerant coils and become associated with the condensed collected water. Conversely, lack of turbidity in desiccant samples is

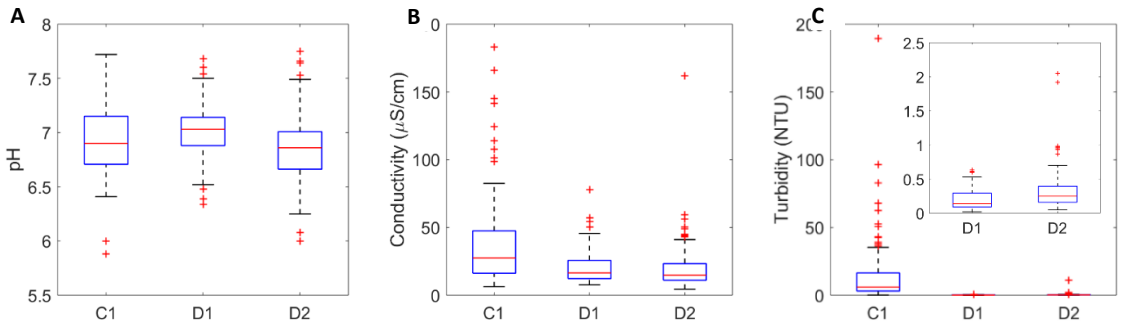

Figure 5-7 a) pH, **b)** Conductivity (uS/cm), and **c)** Turbidity (NTU) of water collected from compressor (**C1**) and desiccant (**D1, D2**) systems. Central mark of box represents the median value, bottom and top edges are 25th and 75th percentiles, respectively; whiskers extend to extremes not considered outliers. Outliers are points greater than (Q1 + 1.5(Q3 – Q1)) and less than (Q1 – 1.5(Q3-Q1)), where Q is quartile.

two-fold: a) dust is trapped in by the wheel matrix, and b) when water vapor is desorbed from the wheel matrix, the dust no longer associates with the free water vapor.

Figure 5-8 shows dissolved organic carbon (DOC) concentration in collected waters. DOC of compressor water is higher in the summer months, with median value 6.3 mg/L and maximum value 12 mg/L. Similar trends are seen with DOC of desiccant system water, with summer-time median value 3.5 – 6.4 mg/L. DOC decreases in the winter to 1 mg/L for all systems. DOC of collected waters from dehumidifiers are similar to or lower than DOCs of fog and rainwater. Fog, cloud and rainwater DOC (or TOC) concentration can range 2 – 40 mg C/L (Boris, Napolitano, Herckes, Clements, & Collett, 2018; Ervens et al., 2013; P. Herckes, Marcotte, Wang, & Collett, 2015; Pierre Herckes et al., 2002; Pierre Herckes, Valsaraj, & Collett, 2013; Mendez et al., 2011; Vialle et al., 2011) Particulate organic matter can enter fog (i.e. supersaturated water vapor) through either nucleation scavenging, where particles act as cloud condensation nuclei, or

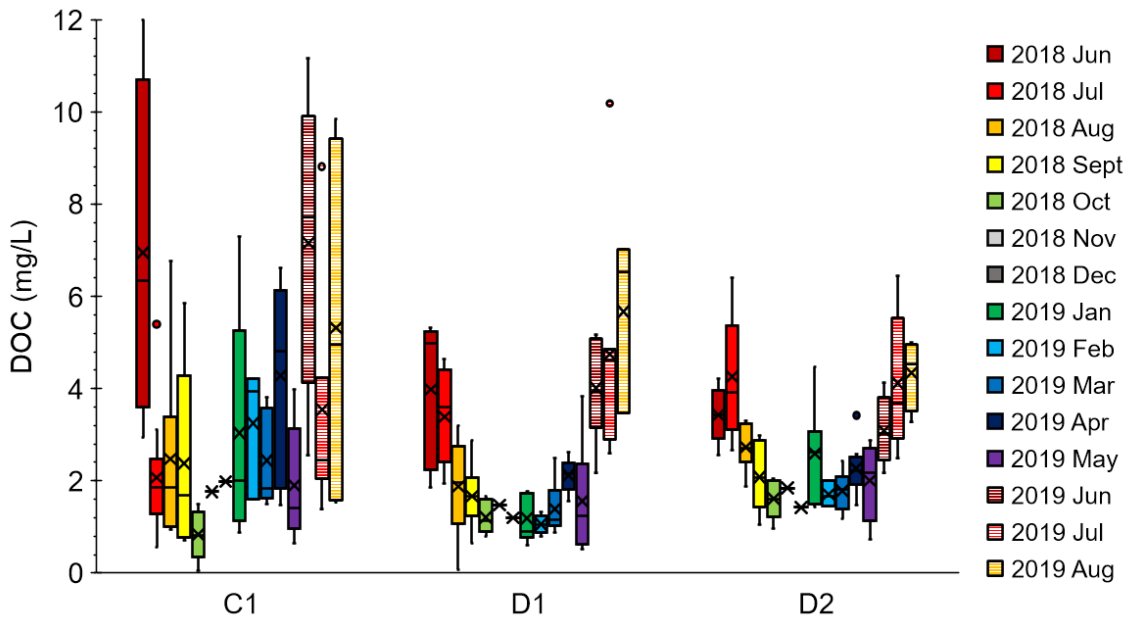

Figure 5-8 Dissolved organic carbon concentration in compressor (C1) and desiccant (D1, D2) waters. Central mark of box represents the median value, bottom and top edges are 25th and 75th percentiles, respectively; whiskers extend to extremes not considered outliers. Outliers are points greater than (Q1 + 1.5(Q3 – Q1)) and less than (Q1 – 1.5(Q3-Q1)), where Q is quartile.

collision with droplets. Similarly, in atmospheric water capture, particles entering the dehumidification system could attach to the refrigerant coil or desiccant wheel and act as nuclei where water vapor condenses or can interact with water vapor or condensate already collected in the system. Organic matter in fog is typically small chain carboxylic acids (e.g. formic acid, acetic acid), dicarboxylic acids (e.g. oxalic acid), aldehydes (e.g. formaldehyde), and dicarbonyls (e.g. glyoxal, methylglyoxal). Aldehydes and carboxylic acids are significant contributors or organic carbon because of their high solubility. Soluble compounds include oxidation products of VOCs that are emitted from anthropogenic or biogenic sources, such as fossil fuel emissions, oxidation of hydrocarbons such as methane, and biomass combustion. (Boris et al., 2018; Ervens et

al., 2013; P. Herckes et al., 2015; Pierre Herckes et al., 2002, 2013) While organic carbon is not regulated by US EPA drinking water standards, DOC/TOC are useful indicators of organic carbon loading in collected waters as a function of location and season and may be important parameters to consider during disinfection so as to not form toxic disinfection byproducts.

Of the 27 metals analyzed, 20 were detected above 1 ppb in **C1**, and 18 above 1 ppb in **D1** and **D2**. **Figure 5-9** shows unfiltered **C1** water samples from June 2018 contained up to 1000 ppb of aluminum and iron (median values 270 ppb, EPA secondary MCL 200 ppb and 300 ppb, respectively), up to 950 ppb of copper (median value 170 ppb, EPA primary MCLG 1300 ppb, secondary MCL 1000 ppb), and up to 50 ppb manganese (median value 25 ppb, EPA secondary MCL 50 ppb). Copper concentration decreased to below 140 ppb after one month of operation. Copper may have leached from condenser coils into the water samples. Water samples collected from both desiccant dehumidifiers had metal concentrations at least one order of magnitude lower than MCLs for all metals except antimony.

Median concentrations for aluminum in **C1** remained above MCL throughout the year. While median concentrations for iron were below the MCL, several samples every month showed concentrations near or above the MCL. Median values for concentration of manganese remained below half the MCL throughout the year, but some samples measured at near or above the MCL. Filtration by 0.45 μm filter resulted in removal of >90% of iron, >60% of aluminum, >40% of manganese and copper. Concentrations of aluminum and iron in the **C1** samples are very strongly correlated, with $R^2 = 0.928$, while correlation between manganese with iron or aluminum separately have R^2 of 0.798 and

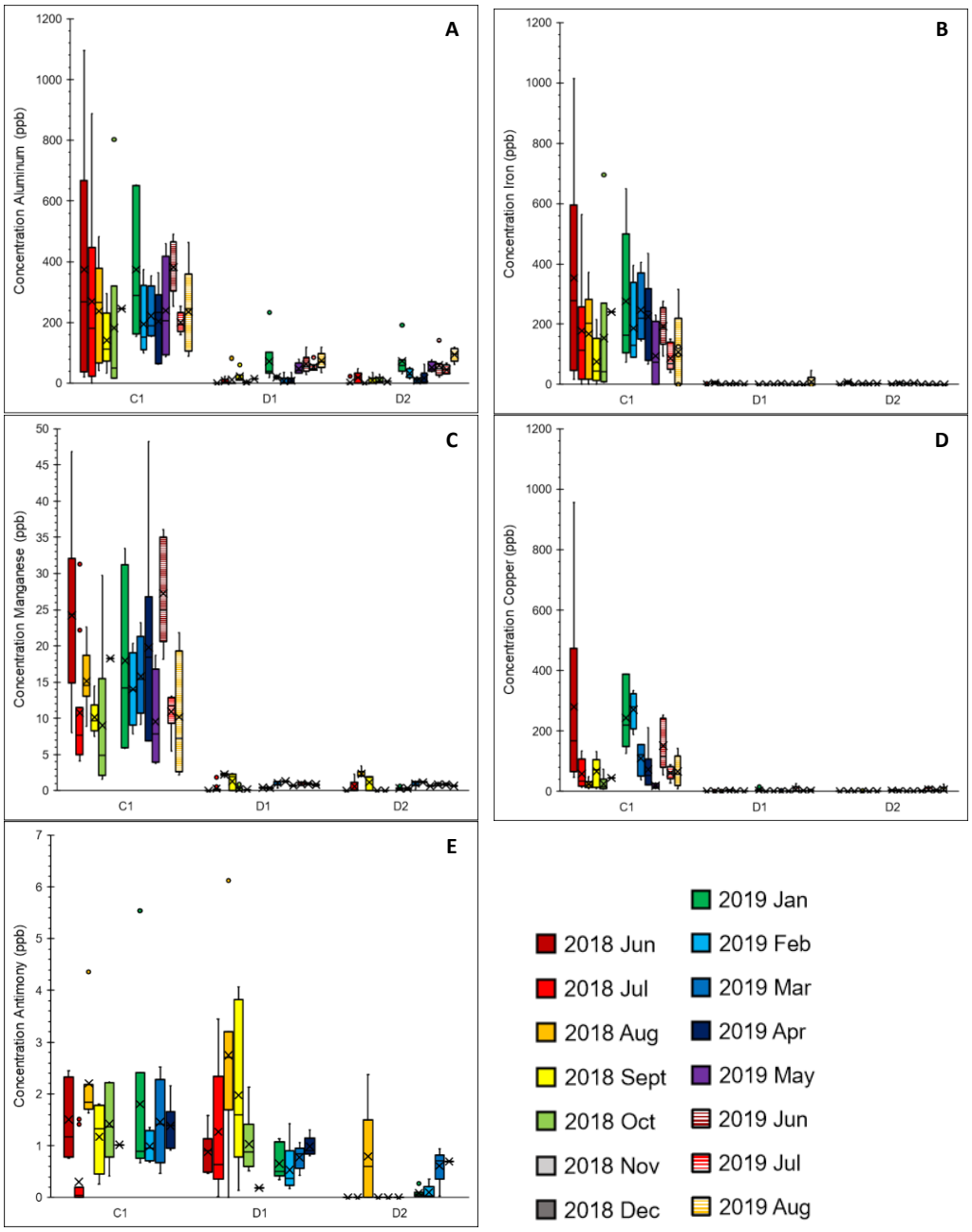

Figure 5-9 a) Concentration of aluminum in water collected from compressor (C1) and desiccant (D1, D2) dehumidifiers. The EPA secondary MCL of aluminum is 50-200 ppb. b) Concentration of iron, secondary MCL 300 ppb. c) Concentration of manganese, secondary MCL 50 ppb. d) Concentration of copper, Primary MCLG 1300 ppb, secondary MCL 1000 ppb. e) Concentration of antimony, primary MCL 6 ppb. Central mark of box represents the median value, bottom and top edges are 25th and 75th percentiles, respectively; whiskers extend to extremes not considered outliers. Outliers are points greater than (Q1 + 1.5(Q3 – Q1)) and less than (Q1 – 1.5(Q3-Q1)), where Q is quartile.

0.778. Aluminum, manganese and iron are primarily associated with dust and have bn associated with atmospheric deposition in rainwater collection tanks (Huston, Chan, Gardner, Shaw, & Chapman, 2009), therefore multiple linear regression correlating turbidity with aluminum, iron and manganese was performed. Regression over 69 observations results in **Equation 8**, with p-values for constants < 10^{-3} and adjusted R^2 of 0.774. However, the intercept of the multiple linear regression has p-value of 0.289, indicating turbidity is not completely explained by the 3 metals.

$$Turbidity\ of\ C1\ (NTU) = 0.438\ [Mn] + 0.0784\ [Fe] - 0.0489[Al] + 1.253 \quad (8)$$

Curiously, water collected from all 3 dehumidifiers had antimony concentration close to the Primary MCL value of 6 ppb. (**Figure 5-9e**) Antimony is a polymerization agent for terephthalic acid and ethylene glycol in the formation of polyethylene terephthalate (PET). Previous research has shown when PET is exposed to long durations of heat, antimony can leach. Antimony in the dehumidifier water samples is hypothesized to have come from microplastics leaching from the plastic dehumidifier holding container.

Heterotrophic plate count (HPC) analysis was performed on water samples collected over a 24 hour time period in November 2019. Water from **D1** had 620 CFU/mL, while water from **C1** had >5700 CFU/mL. Bacteria colony concentration is higher in compressor units due to airborne microbes associated with dust particles. The drinking water recommended limit for microbes is 100 – 500 CFU/mL, therefore water from both desiccant and compressor systems would need to be treated prior to consumption.

5.5 Implications of Water Quality on Treatment

Water collected from desiccant systems showed low conductivity and turbidity and metal concentrations well below MCLs. However, this water had DOC 1 – 6 mg/L due to presence of aldehydes and carboxylic acids in the atmosphere, and CFU is above safe drinking water limits. Water collected from desiccant systems should be treated via activated carbon to remove organic compounds and disinfected by either UV or ozone. In addition, given the very low conductivity, water may be recharged through a mineral block to add beneficial elements into the water (e.g. Ca^{2+}, Mg^{2+}, Li^{+}).

Water treatment modules for compressor systems will need to be more robust than desiccant systems. Water collected from compressor systems had high conductivity, turbidity, concentrations of aluminum, iron and manganese near or well above the secondary MCL, DOC up to 12 mg/L, and HPC result of >5700 CFU/mL. This water needs to be treated by filtration (membrane or sand) to remove dust particles, metals and microbes, activated carbon to remove soluble organics, and disinfection by UV or ozone to inactivate microbes.

THERMODYNAMIC BOUNDARIES GUIDE SELECTION OF WATER VAPOR SATURATION PROCESS FOR ATMOSPHERIC WATER CAPTURE

This chapter is a manuscript draft in preparation for submission as:

> Mulchandani, A., Edberg, J., and Westerhoff, P. Thermodynamic boundaries guide selection of water vapor saturation process for atmospheric water capture. *In prep for submission to Energy and Environmental Science.*

6.1 Introduction

Atmospheric water capture (AWC) processes capture water vapor present in ambient air and condense the vapor to a liquid. AWC processes have the potential to serve as a decentralized source of water, separate from or in addition to the municipal water grid. While the atmosphere as a global freshwater reservoir contains 12,900 km^3 of water vapor, vapor density (i.e. specific humidity) and vapor saturation (i.e. relative humidity) vary spatially and temporally from 1 – 30 g vapor/m^3 air and 0 – 100% RH, respectively. The variability in vapor density and RH can impact the maximum potential volume of water captured over a given period of time and the energy required for condensation. AWC technology selection must be a function of the location of implementation to accurately determine the quantity of water that could be supplied and the energy required for vapor condensation.

Water vapor can condense and become a liquid if it is fully saturated, i.e. when the vapor pressure (e) is equal to or greater than the saturated vapor pressure (e_s) so RH is ≥100%. The vapor pressure is related to the vapor density of air by the ideal gas law, **Equation 1**,

$$e = \rho_v R_v T \quad (1)$$

where R_v is the vapor gas constant 461 J/kg-K and T is temperature.

Water vapor saturation is calculated by the Clausius-Clapeyron equation, **Equation 2**

$$e_s = e_{s0} \exp\left[\frac{L_v}{R_v}\left(\frac{1}{T_0} - \frac{1}{T}\right)\right] \quad (2)$$

where L_v is latent heat of vaporization (2250 kJ/kg), and e_{s0} is vapor pressure (611 Pa) at T_o (273 K), and e_s is exponentially related to T. Once water vapor becomes saturated, it must surpass the liquid-vapor equilibrium to phase change into a liquid. **Figure 6-**1 and **Figure 6-2** show four modes exist to saturate water vapor, in correlation with the ideal gas law (**Equation 1**):

i) Isobaric process, where temperature is reduced to the dew point (T_d) at constant pressure and volume is decreased (orange line)

ii) Isothermal process, where pressure is increased at constant temperature and volume is decreased (blue line)

iii) Coupled isobaric and isothermal processes, where first temperature is reduced to a mid-point temperature (T_2) between T and T_d at constant pressure with change in volume, then pressure is increased at constant temperature T_2 (green line)

iv) Coupled isochoric and isothermal processes, where first temperature is reduced to T_d at constant volume while pressure is also decreased, then pressure is increased at constant temperature T_d while volume is also decreased (purple line)

The phase change energy as a function of thermodynamic process and starting climate variables has not been quantified, therefore the thermodynamic limit of AWC is also unknown.

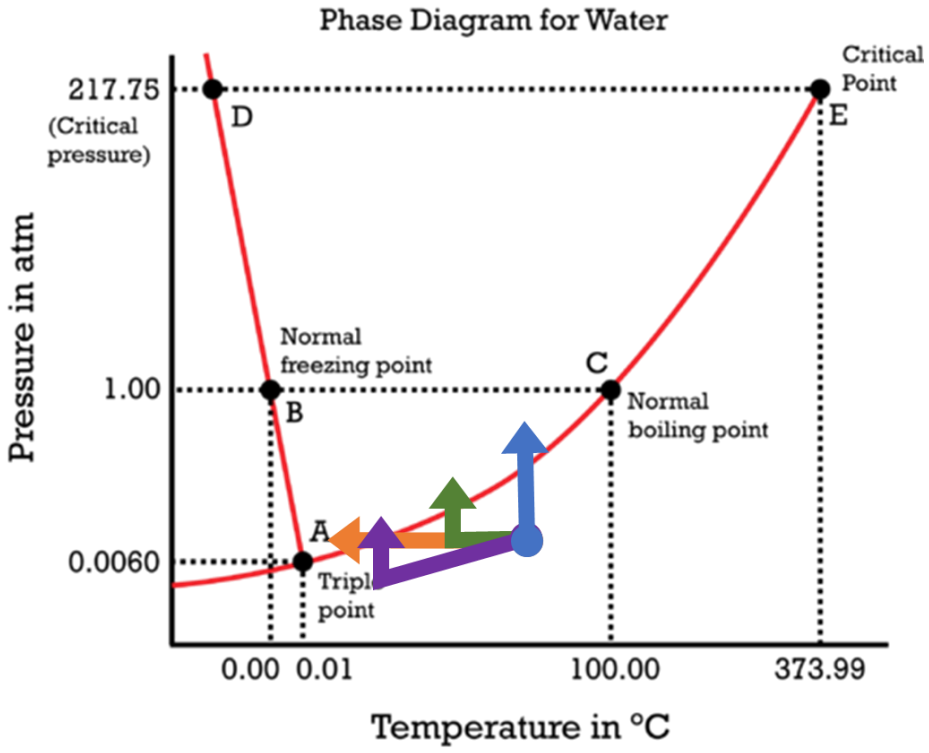

Figure 6-1 Phase diagram of water. The blue dot is an arbitrary starting point for AWC. Directional arrows signify change in thermodynamic property to achieve saturation of water vapor.

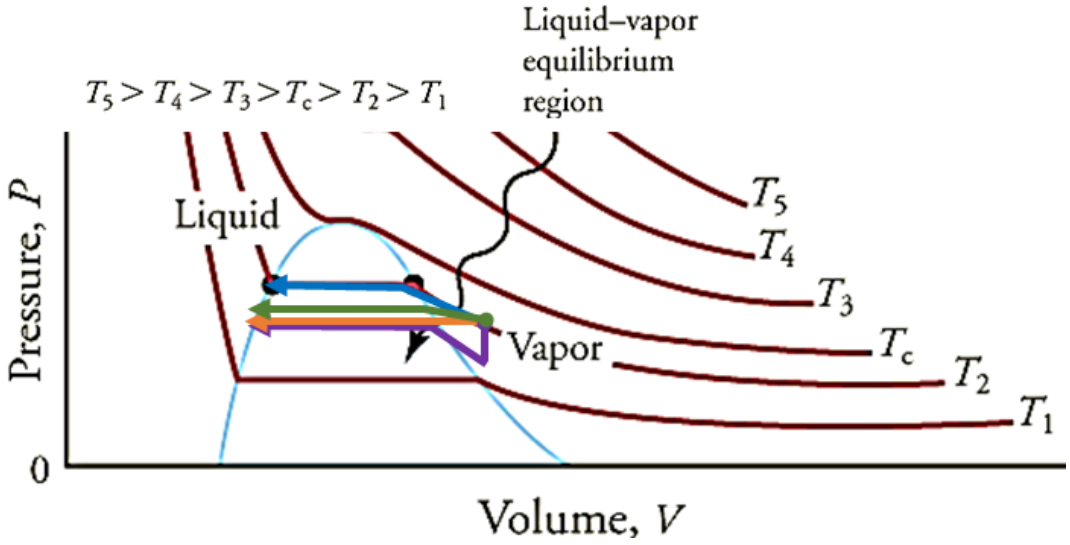

Figure 6-2 Pressure volume diagram showing liquid-vapor equilibrium region. Each curve represents an isotherm. The green dot is an arbitrary starting point for AWC. Directional arrows signify change in thermodynamic property to achieve saturation of water vapor.

AWC can assist industries that utilize large volumes of municipally treated water (e.g. beverage plants) offset their reliance upon liquid water sources. Optimally, beverage plants could produce 100,000 to 1,000,000 L of water / year from the ambient atmosphere or from air drying processes or HVAC systems. In these scenarios, it would be optimal to utilize renewable energy sources (e.g solar PV, wind) to sustainably provide energy for vapor condensation.

The relationship between productivity, climate and energy has been evaluated for individual technologies in separate experimental and theoretical studies, but an overarching understanding of the relationship between these parameters and a comparison across technologies is lacking (Bui, Kum Ja, Gordon, Ng, & Chua, 2017; He et al., 2016; H. Kim, Rao, et al., 2017; Koronaki, Christodoulaki, Papaefthimiou, & Rogdakis, 2013; La, Li, Dai, Ge, & Wang, 2012; Lin, Huang, Wang, & Chua, 2018; She, Yin, & Zhang, 2014; L. Wang, Li, & Zhao, 2010; L. Z. Zhang, Zhu, Deng, & Hua, 2005). There is a need to quantify the energy requirement for AWC as a function of climate, thermodynamic process of condensation, and scale (i.e. volume of production). The goal of this paper is to calculate the minimum energy requirement for AWC and define operational envelopes (i.e. boundary conditions) for technology selection as a function of region. We determine i) the impact of climate on energy required to condense water vapor via various thermodynamic processes, ii) energy requirement as a function of scale, and iii) feasibility and cost of application of electric and renewable power sources (solar PV, wind) for AWC.

6.2 Methods

6.2.1 Conceptual Approach

Energy is the capacity to do work or transfer heat. The first law of thermodynamics states that energy can neither be created nor destroyed, and instead can be transferred through interaction of heat (Q), work (W) and internal energy (U) (**Equation 3**).

$$\Delta U_{system} = Q + W \quad (3)$$

Work is a transfer of energy by a means that does not require temperature change, e.g. changing volume, and is calculated with **Equation 4,**

$$W = -\int_{V_i}^{V_2} e\, dV \quad (4)$$

where *e* is vapor pressure and W has units [J/mol] (Feinberg, Ramon, & Hoek, 2013; Yip & Elimelech, 2012; Yip, Vermaas, Nijmeijer, & Elimelech, 2014). Heat is the flow of energy between two bodies at two different temperatures and is calculated with **Equation 5**,

$$Q = mc\Delta T \quad (5)$$

where m is the mass of the substance in the system, *c* is the heat capacity of water vapor at constant volume (c_v = 26.28 J/mol-K) or constant pressure (c_p = 34.74 J/mol-K), ΔT is the temperature difference, and Q has units [J/mol]. Condensation of water vapor by cooling requires energy in the form of heat transfer, while condensation by applying pressure or decreasing volume requires energy in the form of mechanical work. The total energy required to reach phase change equilibrium is given by **Equation 6**.

$$Energy\ to\ reach\ phase\ change\ equilibrium = Q + W \quad (6)$$

Once water vapor reaches the liquid-vapor equilibrium region, the phase change can occur. The energy required for a phase change of water can be calculated through Gibbs Free Energy equation (**Equation 7**).

$$\Delta G^o = \Delta H^o - T\Delta S^o \quad (7)$$

At 25°C, the ΔG^o of the phase change of vapor to liquid is -8.6 kJ/mol, ΔH^o is the latent heat of condensation and equal to -44.1 kJ/mol, and ΔS^o is the change in entropy and equal to -0.12 kJ/mol. The total energy required to condense water is the sum of energy required to reach phase change equilibrium and the energy of the phase change itself (**Equation 8**).

$$Energy_{vapor \rightarrow liquid} = (Energy\ to\ reach\ phase\ change\ equlibrium) + (Energy\ of\ phase\ change\ ) \quad (8)$$

6.2.2 Deterministic Model

A deterministic MATLAB model was created to calculate energy to saturate water vapor as a function of starting atmospheric parameters. Energy was calculated as a function of work and heat for the 4 thermodynamic processes. Input parameters to the model were a matrix of RH (0-100%) and T (0-50°C). Initial e, e_s and volume (V) were determined by **Equation 1** and **2.** Finally, total energy required for condensation was calculated via **Equation 8**. Energy (work and heat) for each thermodynamic process were calculated as follows:

6.2.2.1 Isobaric Process

In an isobaric (constant pressure) system, water vapor is condensed by decreasing temperature and volume. Work performed by the system to saturate one mole of vapor is

given by **Equation 9** as a function of the change in volume (V) at constant vapor pressure (e).

$$W = e\left(V_{initial} - V_{final}\right) \quad (9)$$

The final volume of the system was calculated at T_d at constant pressure using the ideal gas law. Heat is transferred from the vapor to the surrounding due to the temperature change, described by **Equation 5**.

6.2.2.2 Isothermal Process

In an isothermal (constant temperature) system, water vapor is condensed by increasing pressure and volume. Work performed on the system is given by **Equation 10** as a function of the change in volume at a constant temperature.

$$W = -nRT\ ln\left(\frac{V_{final}}{V_{initial}}\right) = -nRT \ln\left(\frac{e}{e_s}\right) = -nRT \ln\left(\frac{RH}{100}\right) \quad (10)$$

The final volume of the system was calculated at saturated vapor pressure at constant temperature. Because temperature is constant, the volume fraction in **Equation 10** equates to the relative humidity pressure fraction and work is very simply a function of starting T and RH. The first law of thermodynamics states that energy can neither be created not destroyed. In an isothermal process, internal energy equals 0, therefore work performed on the system is equivalent to heat transferred from the system to the surroundings. However, this heat transfer does not require an additional energy input.

6.2.2.3 Coupled isobaric and isothermal process

The goal of the coupled isobaric and isothermal process is to decrease work required for saturation. First, vapor is cooled via an isobaric process to a temperature T_2 which is the midpoint between T and T_d. Isobaric work was calculated by **Equation 9**, where V_{final} was determined from the ideal gas law using T_2 at constant pressure. Heat

transferred from the system to the surroundings during the isobaric process was calculated by **Equation 5**. After the isobaric process, an isothermal process is applied to continue bringing the vapor to saturation. Work for the isothermal process was calculated from **Equation 10** at T_d, where e_s at T_d was determined from **Equation 2**.

Coupled isochoric and isothermal process

The coupled isochoric and isothermal process further decreases work required for saturation. In this coupled process, the system is first cooled to T_d through an isochoric (constant volume) process. As volume did not change, no work was done on or by the system. The heat energy required for cooling at constant volume was calculated by **Equation 5**. Next, the cooled water vapor is condensed through an isothermal process. Work performed on the system to increase pressure and decrease volume was calculated by **Equation 10**, where the final volume of the system was calculated at saturated vapor pressure at T_d.

6.3 Results and Discussion

6.3.1 Energy as Work to Bring Water Vapor to Saturation

Figure 6-3 shows work required to bring vapor to saturation for **a)** isobaric, **b)** isothermal, **c)** coupled isobaric and isothermal, and **d)** coupled isochoric and isothermal processes. For all four thermodynamic processes, the energy as work required to bring vapor to saturation decreases as RH increases. The closer vapor in ambient air is to saturation, the less energy will be required to bring it to saturation. Work has a lower dependence on starting temperature. The difference in energy requirement between arid and humid climates varies 4-fold for isobaric (**Figure 6-3a**), coupled isobaric and isothermal (**Figure 6-3c**), and coupled isochoric and isothermal (**Figure 6-3d**) processes.

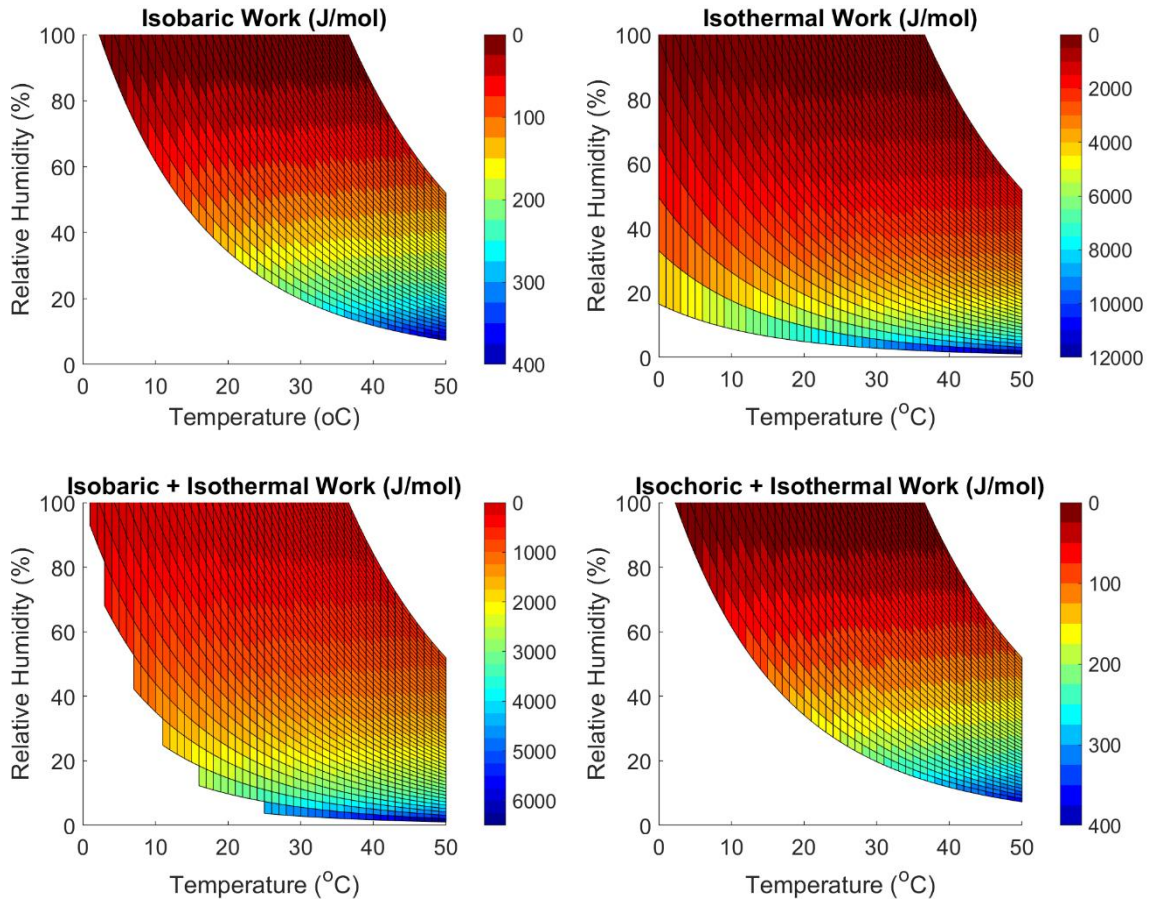

Figure 6-3 Energy as work (J/mol) to bring water vapor to saturation as a function of temperature and relative humidity for **a)** isobaric, **b)** isothermal, **c)** coupled isobaric and isothermal, and **d)** coupled isochoric and isothermal processes.

Additionally, these processes cannot proceed if T_d is below 0°C, as frost will form. In comparison, a direct isothermal process can have 10x energy difference for saturation between low and high RH but can perform work at all temperature and pressure conditions. This is because only mechanical work is being performed.

Figure 6-3a and 6-3d show isobaric and coupled isochoric and isothermal processes require the least amount of work to saturate water vapor. In both processes, water vapor is brought to T_d, either by decreasing temperature at constant pressure or decreasing temperature at constant volume. For humid climates (RH >80%), work energy

required for condensation is < 50 J/mol. For moderate climates (RH = 60%), work energy is < 100 J/mol. In arid climes (RH < 30%) work energy required is 200 – 400 kJ/mol. In comparison, a coupled isobaric and isothermal process (**Figure 6-3c**) requires 8-10 times more energy and an isothermal process (**Figure 6-3b**) requires 15-18 times more energy. These two processes require increase in pressure to bring vapor to saturation, which is very work energy intensive.

6.3.2 Energy as Heat to Bring Water Vapor to Saturation

In isobaric and isochoric processes, heat must be transferred from the water vapor in the system to the surrounding. **Figure 6-4** shows energy as heat for **a)** isobaric, **b)** coupled isobaric and isothermal, and **c)** coupled isochoric and isothermal processes. Similar to energy as work, RH is the dominant factor in determining energy as heat required for saturation. The coupled isobaric and isothermal process is most energy efficient because the system only cools to the midpoint between the starting and dew point temperatures. For humid climates (RH = 80%), heat energy requirement is <100 J/mol, while for moderate climates (RH = 60%), heat energy for saturation is <200 J/mol and for arid climates (RH <30%) heat energy is 400 – 1000 J/mol. Meanwhile, the isobaric system and the coupled isochoric and isothermal systems both cool water vapor down to dew point, the former through constant pressure and the latter through constant volume. The constant volume process requires less heat energy because c_v is 25% smaller than c_p. The heat energy requirement for the coupled isochoric and isothermal process is 1.5 times higher than the coupled isobaric and isothermal process at all conditions, while the isobaric process requires 2 times more heat to bring vapor to saturation.

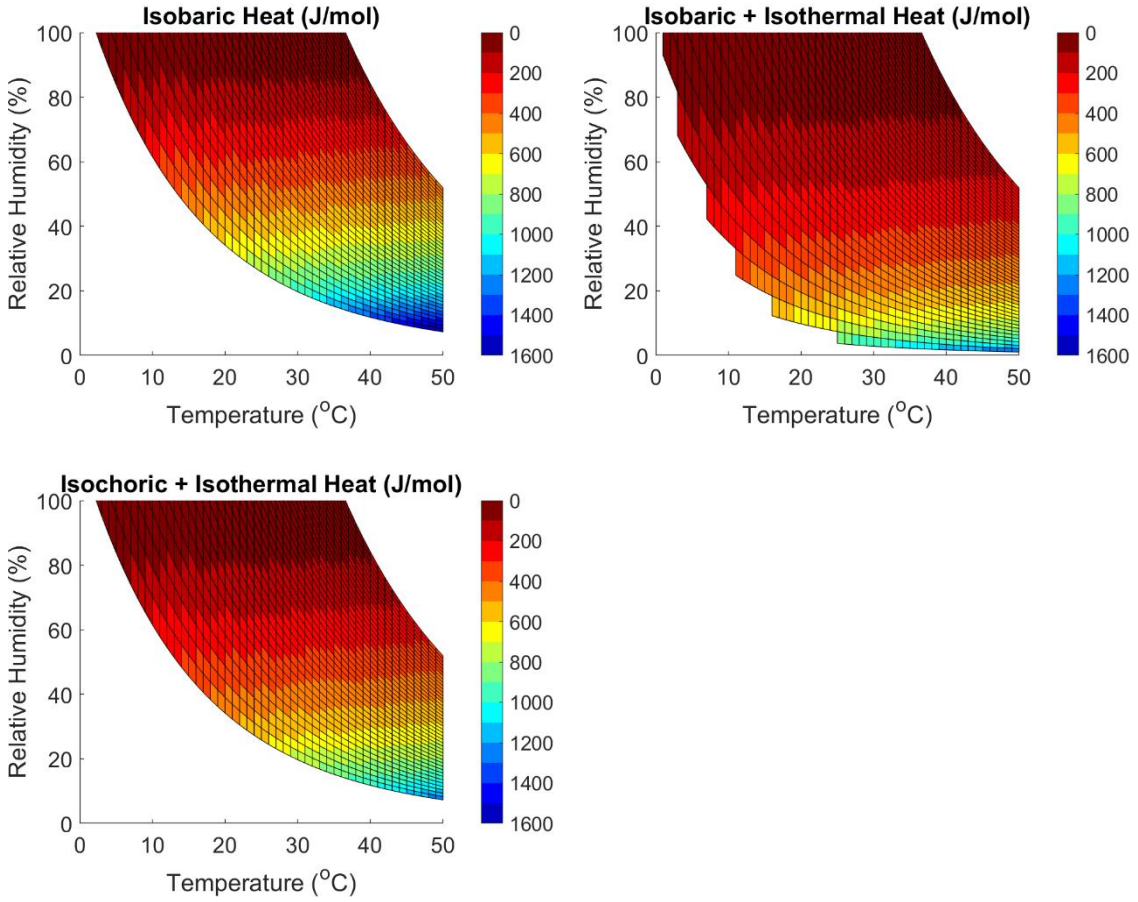

Figure 6-4 Energy as heat (J/mol) to bring water vapor to saturation as a function of temperature and relative humidity for **a)** isobaric, **b)** coupled isobaric and isothermal, and **c)** coupled isochoric and isothermal processes.

6.3.3 Total Energy to Bring Vapor to Saturation

Figure 6-5 shows the total energy required to bring water vapor to saturation as a function of starting temperature and relative humidity for the 4 thermodynamic processes. Total energy is a combination of work energy and heat energy. The most energy efficient process is dew point condensation, whether by isochoric or isobaric means. The coupled isochoric and isothermal process is 20% more energy efficient than the isobaric process. For humid climates (RH > 80%), the coupled process requires < 170 J/mol to bring vapor to saturation.

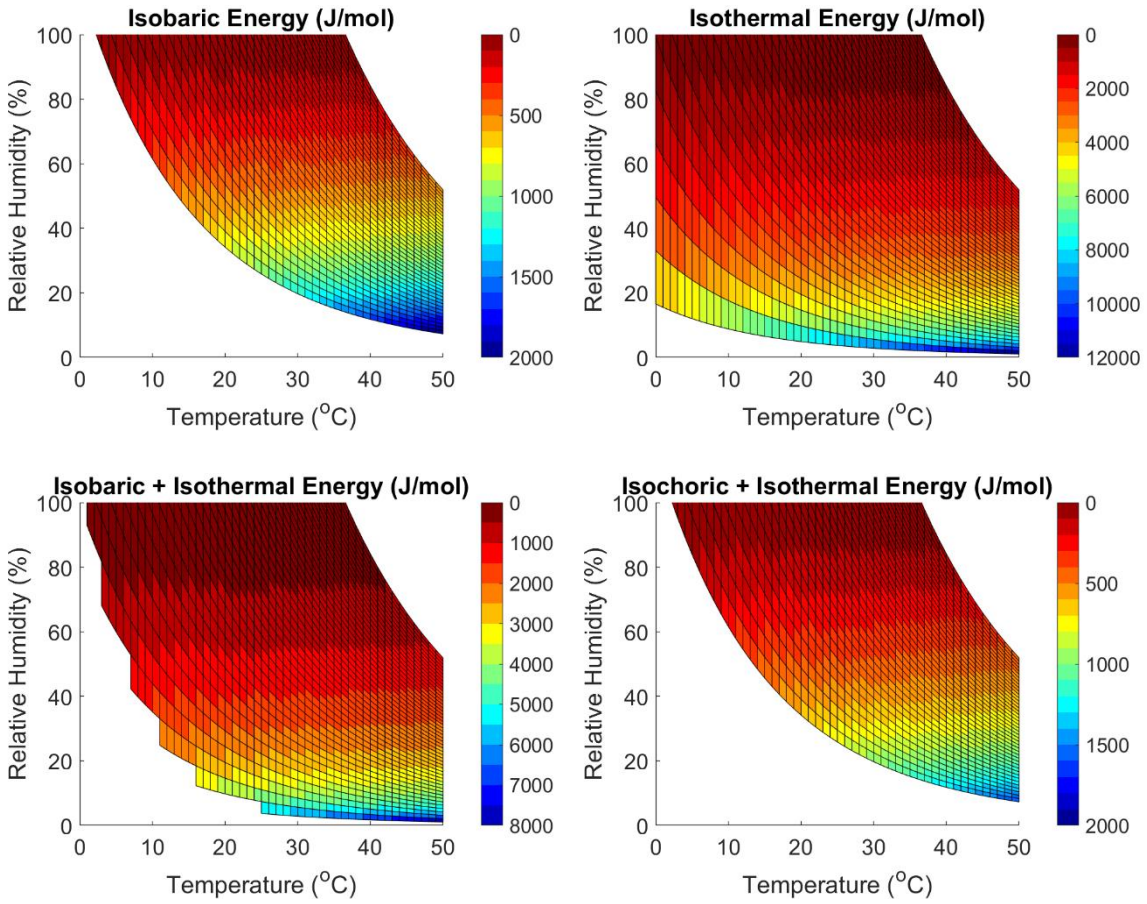

Figure 6-5 Total energy (J/mol) required to bring water vapor to saturation (work and heat) as a function of temperature and relative humidity for **a)** isobaric, **b)** isothermal, **c)** coupled isobaric and isothermal, and **d)** coupled isochoric and isothermal processes.

While the coupled isochoric and isothermal process is most ideal, particularly in humid climates, it is unable to perform in conditions where T_d is below freezing. This occurs for RH<30% and T>20°C, and RH>30% and T<20°C. **Figure 6-6a** shows coupled isobaric and isothermal, and pure isothermal processes can perform in these regions where the coupled isochoric and isothermal process is limited. The coupled isobaric and isothermal process can be used at RH <30% and T > 10°C. **Figure 6-6b** shows in this arid region, this coupled process requires 1800 – 5600 J/mol. While the energy requirement for the isothermal process (**Figure 6-5b**) is 4 times higher than the coupled

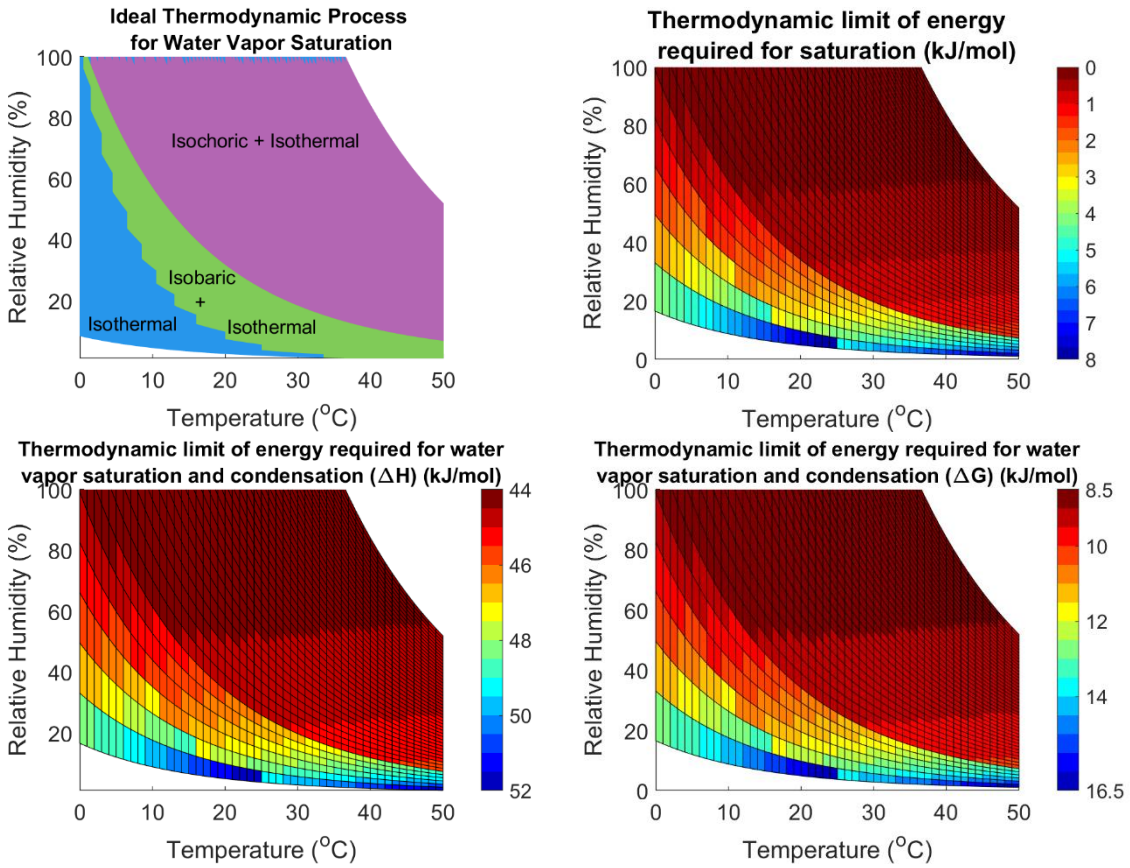

Figure 6-6 a) Ideal thermodynamic process for water vapor saturation as a function of temperature and relative humidity; **b)** Thermodynamic limit of energy (work + heat, kJ/mol) required for saturation for the process shown in (a) as a function of temperature and relative humidity; **c)** Thermodynamic limit of energy required for saturation and latent heat of condensation (ΔH^o); **d)** Thermodynamic limit of energy required for saturation and Gibbs free energy of phase change (ΔG^o).

isochoric and isothermal process, it is the only process able to saturate water vapor when air temperature is <20°C and for RH 10 – 100%. The isothermal process is most favorable at low temperature and high RH conditions, where energy to saturate water vapor is < 1000 J/mol.

6.3.4 Total Energy to Condense Water Vapor

Once water vapor reaches saturation, it will only condense if the latent heat of condensation is removed. The latent heat of condensation at 25°C is 44.1 kJ/mol water.

Figure 6-6c shows the total amount of energy required for saturation and condensation, combining the energy of the ideal thermodynamic process with the latent heat of condensation. If heat recovery were to be employed in an AWC device, the minimum thermodynamic energy cost of AWC could reach the theoretical limit posed by Gibbs free energy (**Figure 6-6d**). Therefore, **Figure 6-6c and 6-6d** together are the upper and lower bounds on the minimum energy requirement for AWC for saturation and condensation combined. The energy required for AWC as a function of ΔG^0 is 8.6 kJ/mol – 16.5 kJ/mol, and as a function of ΔH^0 is 44.1 kJ/mol – 52 kJ/mol.

In the ideal coupled isochoric and isothermal process, where vapor is cooled to dew point at constant temperature followed by isothermal compression to saturation, the total energy requirement in a humid climate (RH = 80%) is only <0.4% of the latent heat of condensation and <2% of the Gibbs free energy between the liquid and vapor states. The energy cost of bringing water vapor to saturation in extremely arid climates (RH<20%) versus humid climates (RH=80%) can vary 50x due to a difference in the thermodynamic process utilized. In arid climates, the energy requirement to bring vapor to saturation is can be up to 18% of the latent heat of vaporization, and 93% of the Gibbs free energy.

6.3.5 Application of Renewable Energy Supplies for Atmospheric Water Capture

AWC is advantageous because it provides water off the centralized municipal water grid. It stands to reason then that an off-grid source of energy is desired to render AWC a completely decentralized technology. Renewable energy sources such as solar and wind can provide a range of power supply as a function of their size and capacity. A residential scale solar photovoltaic (PV) system or wind turbine can provide 10 kWh

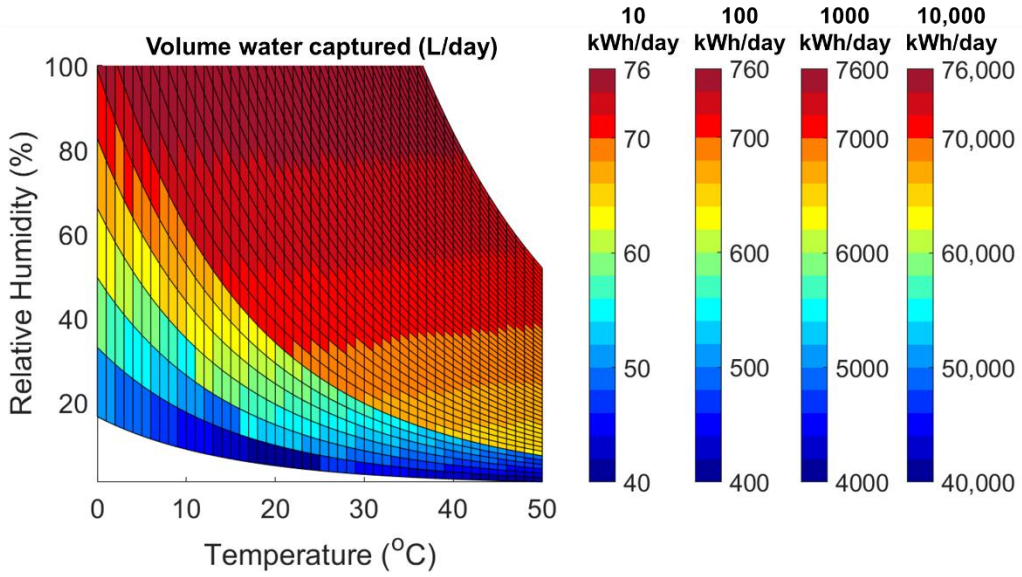

Figure 6-7 Volume of water captured from the atmosphere (L/day) as a function of temperature and relative humidity for variable power supplies (kWh/day listed above color bars), where energy required to saturate and condense water was calculated as the sum of work, heat and Gibbs Free energy.

power/day, enough energy to produce 40 – 76 L of water from the atmosphere at the thermodynamic limit (ΔG^o) as a function of region. Wind turbines at an industrial scale can range from small (100 kWh/day) and mid-size (1000 kWh/day) to large single units or wind farms (10,000 kWh/day). **Figure 6-7** shows AWC potential scales accordingly with the power supply. Solar PV power is a function of land area, PV panel wattage and efficiency. A large beverage manufacturing plant in Phoenix, AZ contains a 2900 kW solar array which produces an average of 15,000 kWh/day. Utilizing the entirety of this PV capacity can produce up to 114,000 L water/day at RH>80% and T>5ºC.

"NANO-BLOCKS": A PLAYFUL METHOD TO LEARN ABOUT NANOTECHNOLOGY-ENABLED WATER AND AIR TREATMENT

This chapter has been published as:

Mulchandani, A., Atkinson, A., Garcia-Segura, S., Westerhoff, P. "Nanoblocks": A playful method to learn about nanotechnology-enabled water and air treatment. *Journal of Chemical Education*, **2019**, *4*, 708-713.

7.1 Abstract

Research, patents, and start-up companies using nanotechnology are growing exponentially. The general public and young students who will be the next generation work force need to properly understand and get excited by nanotechnology to ensure its public support, acceptance, and advancement. Water and air have many pollutants that are invisible to the naked eye, and the concept of selectively removing the pollutants using nano-structured materials is difficult to convey. We developed a hands-on activity where pompoms, representing pollutants in water or air, "adsorb" to adhesive blocks, representing nano-structured adsorbents. Students compete with their choice of sorbent—one large block or 8 small "nano-blocks," both having the same unit volume—to see which sorbs/attaches more pompoms in the same period of time. Through this activity, students learn the nano-blocks have enhanced adsorption capacity due to higher surface area to volume ratio, and therefore the nano-blocks remove more pollutants (pompoms). This progressive and adjustable learning tool has been validated with multiple learner comprehension levels (preK-12, general public, and undergraduate) and has enabled discussions on advanced topics such as nano-scale capabilities, adsorption modeling, and new technologies to improve pollutant removal and degradation.

7.2 Graphical Abstract

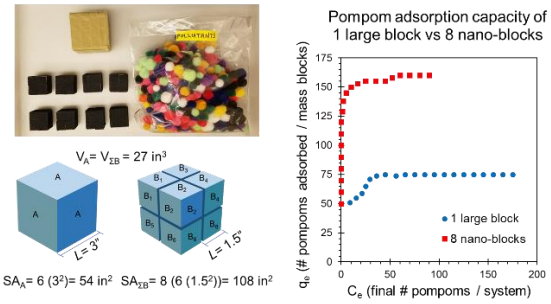

7.3 Keywords

Audience: General Public, Elementary / Middle School Science, First-Year Undergraduate / General

Domain: Demonstrations, Environmental Chemistry, Public Understanding / Outreach

Pedagogy: Hands-On Learnings / Manipulatives

Topic: Nanotechnology, Reactions

7.4 Introduction

Educating students and the public about nanoscale science, technology, and engineering is key to advancing the workforce, incentivizing technology development, and providing knowledge to make well-informed decisions related to technology acceptance. (Foley & Hersam, 2006) There is a need for educational materials to explain nanotechnology concepts in a simplistic manner to students ranging from elementary to undergraduate.

Surface area to volume ratio (SA:V) is a core concept that helps build understanding of novel properties and applications of nanoscale materials. (Blonder & Sakhnini, 2012) As the size of a particle decreases, its surface area (SA) and volume (V) non-linearly increase. Because nanoparticles (i.e., any material <100 nm in any one

dimension) are so small, they have very high SA:V ratios, which allow surface atoms and binding sites to interact with pollutants, enabling their removal or transformation from air or water. However, nanotechnology concepts are traditionally introduced with respect to size rather than volume or SA:V ratio: e.g., one nanometer is 100,000x smaller than the diameter of a strand of hair, or the ratio of a marble to the Earth is the same as the ratio of a nanoparticle to the marble.(National Nanotechnology Initiative, n.d.) These size comparisons are helpful, but they do not demonstrate *why* making something small results in unique properties.

To help conceptualize the benefits of nanotechnology, we developed a simple, cheap, and effective hands-on activity, adaptable to broad comprehension levels (i.e. K-12, general public, undergraduate). The goals of the activity and subsequent discussion are to i) understand that SA:V impacts sorption capacity; ii) introduce nanotechnology and nanoscale phenomena; iii) learn applications of nanotechnology for sorption of contaminants; and iv) demonstrate core concepts of adsorption isotherm modeling. The teaching method employs game-based learning and concept visualization. It also demonstrates simple mathematical models enhancing student comprehension of the critical nanotechnology concepts. (Blonder & Sakhnini, 2012) This activity and the subsequent discussion have been successfully performed and refined in more than 20 venues with over 1000 students (K-12 and undergraduate) over three years.

7.5 Nano-block Activity

7.5.1 Materials and Set-Up

The activity requires 1 large cube, 8 small cubes with unit length half that of the large cube, and pompoms **(Figure 7-1)**. The cubes are covered with hook-and-loop

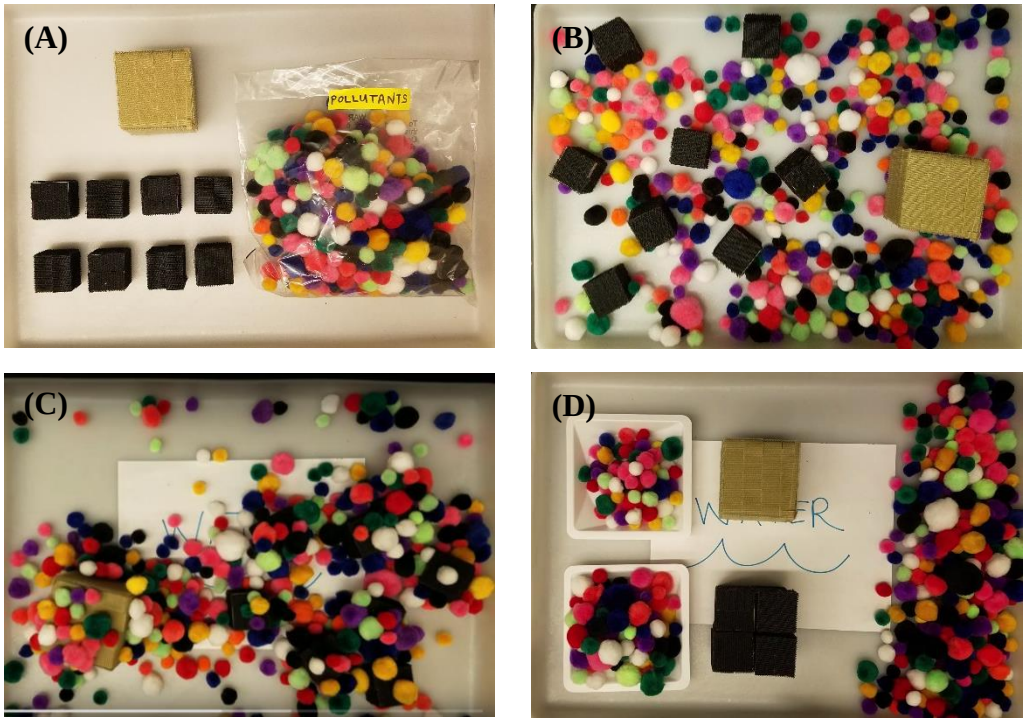

Figure 7-1 Activity setup. a) The activity requires 1 large and 8 small cubes, all covered with hook-and-loop fastener tape (adsorbents), pompoms (adsorbates/pollutants), and a large tray (system); b) 8 nano-blocks and 1 large block compete simultaneously for pompoms in the tray; c) The hook tape "adsorbs" the pollutants to the cubes; d) The 8 nano-blocks typically adsorb approximately twice the number of pompoms as the large block.

fastener tape. Detailed materials list and set-up information are provided in Supplemental Information, and a YouTube video that demonstrates this activity can be viewed online. (Mulchandani, Atkinson, Garcia-Segura, & Westerhoff, 2019)

7.5.2 Nano-blocks Demonstration

Begin the nano-blocks activity by stacking the eight small cubes, referred to as "nano-blocks," to form a large cube (B_1-B_8) as shown in **Figure 7-2**. Display the large nano-block cube next to the single large cube (A). Have the students observe that the two have the same size, volume, and exposed surface area. Disassemble the large nano-block into 8 pieces. Have the students hypothesize which set of blocks will attach more

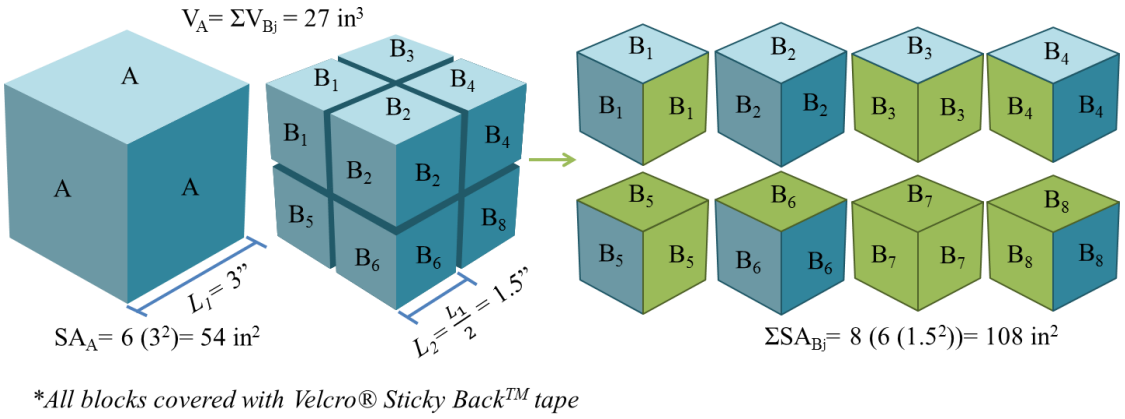

Figure 7-2 Nanoblocks description. Block A is a cube with unit lengths (L_1) of 3 inches. Blocks B_1-B_8 are cubes with L_2 of 1.5 inches. Both sets of blocks (A and B_1-B_8) have an equal total volume (V) of 27 in^3. Block A has six surfaces and total external surface area (SA) of 54 in^2. When separated, blocks B_1-B_8 each expose an additional three surfaces; newly revealed surfaces visible in this depiction are highlighted in green. By separating blocks B_1-B_8, the exposed surfaces double and thus the total SA also doubles to 108 in^2.

pompoms (1 large block or 8 nano-blocks collectively) in the system/tray. Answers will vary but may include "the small blocks, because they have more surface area," and "the large block, because it is bigger." Give one student the large block and another the eight nano-blocks, and have them compete to attach the most pompoms in 30 seconds. After time is called, have each student collect and count their attached pompoms.

7.6 Discussion

Discussions can be tailored based on learner level; mathematical concepts such as SA:V and adsorption isotherm modeling can be incorporated for higher grade and undergraduate students, while visualization is sufficient for lower grade students. Nanoscale concepts and sorption concepts and applications should be discussed with all audiences.

7.6.1 Surface Area to Volume Ratio

The 8 nano-blocks collectively should have adsorbed approximately 2x more pompoms than the single large block. The "pompom attachment capacity" of a block is directly proportional to its SA. When the large cube is split into 8 nano-blocks, total SA doubles while total unit V remains the same, as described in **Figure 7-2**. Students can use **Equations 1-4** to calculate SA, V, and SA:V of the large block and the nano-blocks, where L_i represents the unit length of each cube. If using the same size blocks as described in **Figure 7-2**, the SA, V, and SA:V are given in **Table 7-1**.

Table 7-1 Surface area, volume, and surface area to volume ratio calculations [a]

Characteristic	**1 large block**		**1 nano-block**		**8 nano-blocks**	
	Formula	If L_1 = 3in.	Formula	If L_2 = 1.5in.	Formula	If L_2 = 1.5in.
Surface Area	$6\ L_1{}^2$	54 in^2	$6\ L_2{}^2$	13.5 in^2	$8 * 6\ L_2{}^2$	108 in^2
Volume	$1\ L_1{}^3$	27 in^3	$1\ L_2{}^3$	3.375 in^3	$8 * 1\ L_2{}^3$	27 in^3
Surface Area to Volume Ratio	$\frac{6\ L_1^2}{L_1^3}$	2 in^{-1}	$\frac{6\ L_2^2}{L_2^3}$	4 in^{-1}	$\frac{(8\ *\ 6\ L_2^2)}{(8\ *\ L_2^3)}$	4 in^{-1}

[a] L_i = unit length

The calculations add mathematical evidence for the observed phenomena (i.e., that the volume of 1 large block and 8 nano-blocks collectively are the same, but the sum of the SAs and SA:V of the nano-blocks are double that of the large block).

7.6.2 Nanoscale Concepts

After performing the activity and comparing SA:V of the two sets of blocks, the concept of nanotechnology can be introduced. Ask students if they have previously heard the word "nano" or know what it means. Some will likely reply that it means "very small." Use **Figure 7-3** and **Equations 2, 4 and 5** to show how breaking the large block

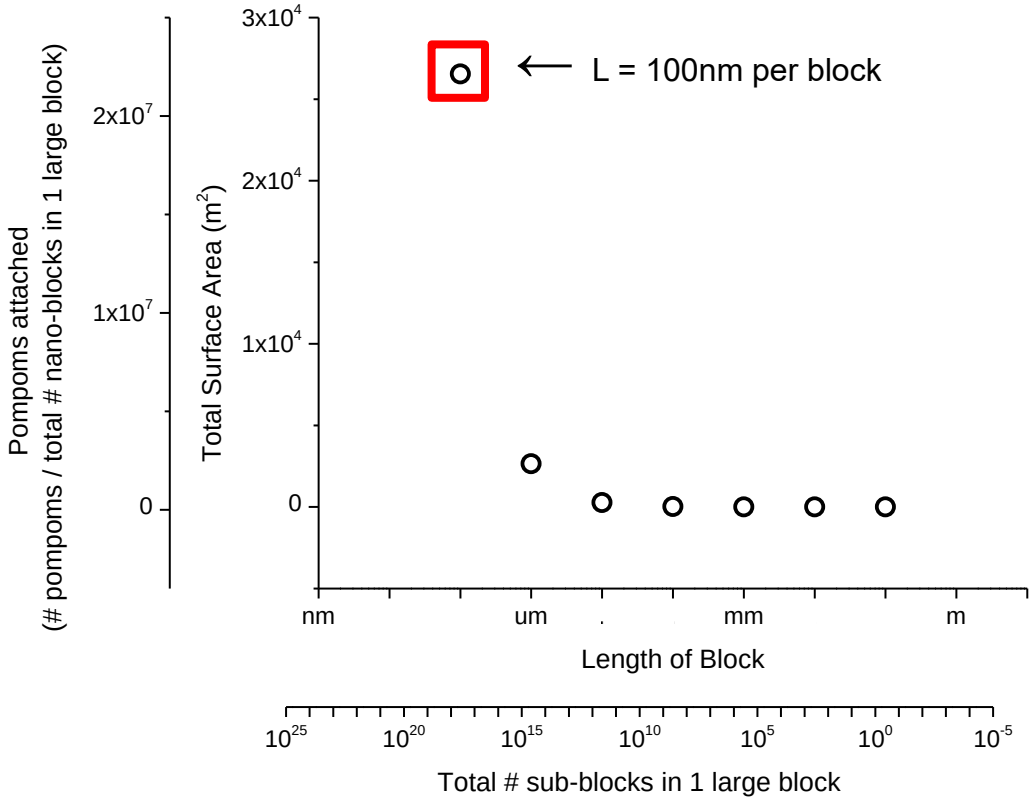

Figure 7-3 Length of nanoblock vs surface area and pompom sorption capacity. As 1 large block is segmented into blocks with unit length on the nanoscale, the number of blocks contained within the 1 large block, total surface area, and number of pompoms attached to all segmented blocks collectively increases. Values based on dimensions in Figure 2 and Table 1.

into smaller pieces (e.g., with unit lengths in the millimeter and micrometer size range) will increase the total number of blocks in a unit volume, total surface area, and total number of pompoms attached. It is important for instructors to emphasize to students that the nano-blocks are representative of the size, scale and SA:V ratio of nanomaterials, however a true nanomaterial is that with at least one dimension less than 100 nm. Breaking the large block into nano-sized pieces (L = 100 nm) would result in 450

quadrillion blocks ($4.5*10^{17}$) having a total surface area of 41 million in^2 ($4.1*10^7$) or 26,550 m^2, capable of adsorbing 23 million pompoms.

Nanoparticles can come in many shapes: cubes, spheres, rods, discs, and even stars. In all of these cases, the SA:V increases as particle size decreases, but SA (**Equation 1**) and V **Equation 3**) formulas vary based on shape.

7.6.3 Sorption Concepts and Applications

Adsorption is the physical or chemical attachment of an adsorbate (i.e., pollutant) in a fluid (i.e., water or air) to the surface of a solid substrate (i.e., adsorbent). In this activity, the pompoms are *adsorbates* and the blocks are *adsorbents.* Adsorption mechanisms can be classified as physical (e.g., non-specific binding, electrostatic attraction) or chemical (e.g., formation of chemical bond). Pompoms attaching to hook-and loop-fasteners is an example of physical adsorption and is easily reversible. To visualize chemical adsorption, imagine the pompoms secreting glue (i.e., forming a chemical bond) when attached to specific sites on the blocks. To remove the glue, a chemical solvent may be required, representing an additional stimulus required to break a chemical bond. In either adsorption mechanism, the SA:V of nano-sorbents increases potential surface sites available for attachment.

An example treatment process that uses adsorption is the removal of organic compounds from air or water using porous granular activated carbon (GAC). The nano-blocks can be used to demonstrate why newly-researched nanoscale carbonaceous materials (e.g., graphene, carbon nanotubes) adsorb $30 – 10^{34}$ times more organic pollutants compared to conventional GAC, which is 1000x larger. (Apul, Wang, Zhou, & Karanfil, 2013; Long & Yang, 2001)

7.6.4 Isotherms and Adsorption Process Modeling

For students with advanced understanding (e.g., undergraduate level), nano-blocks can also be used to teach core concepts of adsorption isotherm modeling. An adsorption isotherm is a relationship between the adsorbate and adsorbent in a control volume and describes how much of a pollutant can attach to adsorbent surfaces (i.e., capacity) at a specified constant temperature. (Duff, Ross, & Vaughan, 1988) The adsorbent capacity (q_e, # pompoms adsorbed per mass of blocks) is calculated from experimental data using **Equation 7**, where *V* is the volume of the system (1 tray), *m* is the mass of the adsorbent (students can weigh mass of blocks, but for simplicity mass is represented as "1 large block," where mass of "8 nano-blocks" = "1 large block"), C_i is the initial concentration of adsorbate (# pompoms initially placed per tray), and C_e is the equilibrium concentration of the adsorbate (# pompoms left per tray after adsorption). To simulate performing an adsorption isotherm experiment, have the large block and the nano-blocks "adsorb pompoms" separately. Use only same size pompoms for this activity to demonstrate sorption of a single pollutant. Vary the "pompom concentration" by repeating the activity for 10 rounds, adding more pompoms in each round. Example results are shown in **Table 7-2.**

Students will notice after a certain point that even with continued addition of pompoms, the blocks will have become covered, or saturated, with only one layer of pompoms and have no remaining attachment sites. This is an opportunity to introduce the concepts of maximum adsorption capacity (q_{max}) with **Equation 8** and monolayer vs multiple layer adsorption.

Table 7-2 Example calculations for nano-block adsorption isotherm activity [a]

C_i (initial #pompoms / system)	1 Large Block			8 Nano-blocks		
	C_e (final #pompoms /system)	q_e (#pompoms adsorbed /mass blocks)	C_e/q_e (mass blocks /system)	C_e (final # pompoms / system)	q_e (#pompoms adsorbed /mass blocks)	C_e/q_e (mass blocks /system)
50	0	50	0	0	50	0
60	9	51	0.176	0	60	0
70	15	55	0.273	0	70	0
80	21	59	0.356	0	80	0
90	25	65	0.385	0	90	0
100	29	71	0.408	0	100	0
110	36	74	0.486	0	110	0
120	45	75	0.600	0	120	0
130	56	74	0.757	1	129	0.008
140	65	75	0.867	2	138	0.014
150	75	75	1.000	5	145	0.034
160	85	75	1.133	10	150	0.067
170	95	75	1.267	17	153	0.111
180	105	75	1.400	25	155	0.161
190	115	75	1.533	35	155	0.226
200	125	75	1.667	45	155	0.290
210	135	75	1.800	52	158	0.329
220	145	75	1.933	60	160	0.375
230	155	75	2.067	70	160	0.438
240	165	75	2.200	80	160	0.500
250	175	75	2.333	90	160	0.563
Fit Langmuir Isotherm	$y = 0.013x + 0.04$ $1/q_{max} = 0.013$ $1/(q_{max}b)=0.04$ $q_{max} = 76.9$ $b = 0.3$ $q_e = (76.9 * 0.3 * C_e) / (1 + 0.3*C_e)$			$y = 0.006x + 0.002$ $1/q_{max} = 0.006$ $1/(q_{max}b)=0.002$ $q_{max} = 158.7$ $b = 3.3$ $q_e = (158.7 * 3.3 * C_e) / (1 + 3.3*C_e)$		

[a] Volume of system = "1 tray"; Mass of blocks = "1 large block"

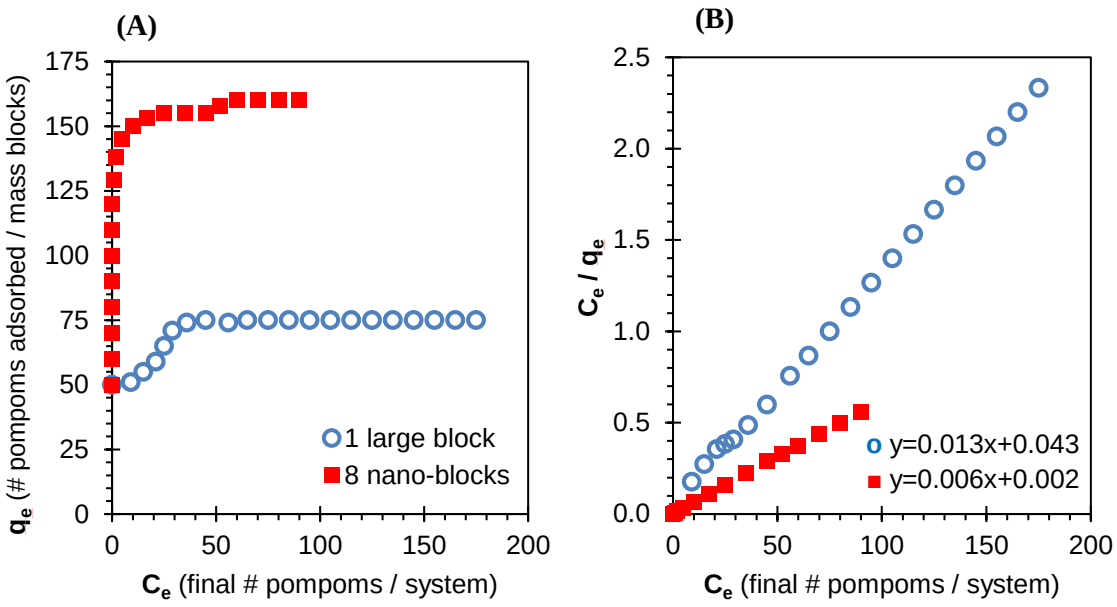

Figure 7-4 a) Adsorption isotherms for 1 large vs 8 nano-blocks, data from Table 2. b) Linearized Langmuir isotherm for 1 large vs 8 nano-blocks, using Equation 7. Volume of system = "1 tray"; Mass of blocks = "1 large block"

A visualization of multi-layer adsorption would be a second layer of pompoms sticking to the first layer that is attached to the block surface. For multi-layer adsorption, a Freundlich isotherm could be used (see Supplemental Information). (Skopp, 2009) However, because only a monolayer of pompoms occurs in our experiments, the Langmuir isotherm, defined by **Equation 9**, is a more appropriate model. (Martins & Nunes, 2015)

To determine b and q_{max}, plot the experimental data collected during the activity using the mathematically linearized expression of the Langmuir isotherm (**Equation 10)** as shown in **Figure 7-4b**, with C_e/q_e on the y-axis and C_e on the x-axis. Full derivation of linearization is provided in Supplemental Information. (Bird, 1933)

The slope ($1/q_{max}$) and y-intercept ($1/(q_{max}b)$) are used to calculate q_{max} and b to complete the Langmuir isotherm equation to fit the student experimental data in **Figure 7-4a**. Example results in **Table 7-2** show that higher SA:V of the nano-blocks compared to the large block leads to higher q_e, q_{max}, and b. This example further illustrates that the nano-blocks, as representatives of nanomaterials, are superior adsorbents when compared to their larger micro- or macro- counterparts. (Qu, Brame, Li, & Alvarez, 2012)

7.7 Conclusions

The nano-blocks activity using hook-and-loop tape-covered blocks to adsorb pompoms is novel, cheap, transportable, reusable, and widely applicable for K-12, undergraduate, and public education and outreach. This visually appealing, hands-on activity explains the importance of SA:V in adsorption processes and introduces applications of nanotechnology in engineering disciplines. Younger audiences doing the activity in an outreach setting reported understanding that "the smaller blocks attached more pompoms because they had more surfaces." Undergraduates used the adsorption isotherm activity as a visual and kinesthetic aid to grasp complex mathematical concepts. The nano-blocks activity can be applied beyond the examples portrayed above, to explain photo- and heterogeneous catalysis, partitioning between phases, and unique optical and electric properties that arise in the nanoscale.

7.8 Acknowledgements

This work was funded through the National Science Foundation Nanosystems Engineering Research Center on Nanotechnology-Enabled Water Treatment (EEC-1449500) and the Environmental Protection Agency STAR program (RD83558001). Laurel Passantino provided technical editing.

7.9 Equations

$$SA_{cube} = 6\ faces * [Length\ (L_i) * Width\ (L_i)] = \ 6\ L_i^2 \qquad [\text{in}^2] \text{ or } [\text{cm}^2] \tag{1}$$

$$\sum SA_{nanoblocks} = \#\ nanoblocks * 6\ L_i^2 \qquad [\text{in}^2] \text{ or } [\text{cm}^2] \tag{2}$$

$$V_{cube} = Length\ (L_i) * Width\ (L_i) * Height\ (L_i) = L_i^3 \qquad [\text{in}^3] \text{ or } [\text{cm}^3] \tag{3}$$

$$SA{:}V = \frac{SA}{V} \qquad [in^{-1}]\ or\ [cm^{-1}] \tag{4}$$

$$Total\ \#\ nanoblocks\ in\ unit\ volume = \left(\frac{L_A}{L_i}\right)^3 \tag{5}$$

$$Total\ \#pompoms\ attached\ to\ nanoblocks\ with\ L_i = \left(\frac{\sum SA_i}{SA_A}\right) *$$

$$\#\ pompoms\ attached\ to\ Block\ A \tag{6}$$

$$q_e = \frac{V(C_i - C_e)}{m} \tag{7}$$

$$q_{max} = \frac{maximum\ mass\ of\ adsorbate}{m} = \frac{maximum\ \#\ pompoms}{mass\ blocks}. \tag{8}$$

$$q_e = q_{max} * \frac{bC_e}{1 + bC_e} \tag{9}$$

where b is the Langmuir isotherm constant.

$$\frac{C_e}{q_e} = C_e\left(\frac{1}{q_{max}}\right) + \frac{1}{q_{max}b} \tag{10}$$

7.10 Supporting Information

7.10.1 Additional Resources for Instructors

Materials List:

Item	Quantity	Supplier
3 in. x 3 in. solid wood block OR 3 in. x 3 in. Styrofoam cube	1	Any craft store
1.5 in. x 1.5 in. solid wood block OR 1.5 in. x 1.5 in. Styrofoam cube	8	Any craft store
Creatology Pom Poms, ½ inch	10	Any craft store
Velcro® Brand Sticky Back™ Tape, 15 ft. x ¾ in.	2	Any craft store
6 Qt. Storage Tray	1	
1 Qt. Storage Tray	2	

Pre-Activity Setup:

Apply the hook (rough) side of hook-and-loop fastener tape to all surfaces of the nine cubes. The best approach is to apply two parallel ¾ in. x 1.5 in. strips on each face of the small cube and four parallel ¾ in. strips to each face of the large cube. Discard the loop (smooth) side of the fastener tape. Distribute the pompoms throughout the large tray. The completed setup is shown in **Figure 1**.

Video demonstration of activity:

https://bit.ly/nanoblocks-activity

Derivation of linearization of Langmuir isotherm:

$$q_e = q_{max} * \frac{bC_e}{1 + bC_e}$$

$$(1 + bC_e) = \frac{q_{max}\, bC_e}{q_e}$$

$$\frac{C_e}{q_e} = \frac{1 + bC_e}{q_{max} b}$$

$$\frac{C_e}{q_e} = \frac{C_e}{q_{max}} + \frac{1}{q_{max} b}$$

Freundlich isotherm equation:

$$q_e = k_F C_e^{\left(\frac{1}{n}\right)}$$

where K_F is the Freundlich adsorption capacity parameter and $1/n$ is the Freundlich adsorption intensity parameter.

Derivation of linearization of Freundlich isotherm:

$$q_e = k_F C_e^{\left(\frac{1}{n}\right)}$$

$$\log \frac{q_e}{k_F} = \frac{1}{n} \log C_e$$

$$\log q_e = \log k_F + \frac{1}{n} \log C_e$$

The Freundlich isotherm equation does not apply to the nano-blocks, as it represents multi-layer adsorption of the adsorbate to the adsorbent. However, the nano-blocks activity and discussion of the Langmuir isotherm is a great lead-in to discussing additional isotherm models.

7.10.2 Additional Resources for Students

"Nano-blocks" Undergraduate Student Handout

Activity Instructions:

1. Put 50 pompoms in an empty tray.

2. Use the large hook-tape covered block to attach as many pompoms as possible. Record the initial number of pompoms (C_i) and the final number of pompoms left in the tray that remain unattached to the block (C_e).

3. Detach the pompoms from the block. Add 10 more pompoms to the tray (total = 60), and perform step 2. Record your results.

4. Repeat steps 2 and 3, adding an additional 10 pompoms in each round, until the total number of pompoms equals 250.

5. Perform steps 1-4 with the 8 nano-blocks. Record your results.

Data analysis:

6. Calculate q_e (the number of pompoms adsorbed to the blocks):
   $$q_e = \frac{V(C_i - C_e)}{m}$$
   where V is the volume of the system (1 tray), m is the mass of the adsorbent (students can weigh mass of blocks, but for simplicity mass is represented as "1 large block," where mass of "8 nano-blocks" = "1 large block"), C_i is the initial concentration of adsorbate (# pompoms initially placed per pan), and C_e is the equilibrium concentration of the adsorbate (# pompoms left per pan after adsorption).

7. Calculate C_e/q_e

8. Graph #1: Plot C_e on the x-axis, and q_e on the y-axis. What do you observe about the graph?

9. Graph #2: Plot C_e/q_e on the y-axis and C_e on the x-axis. Obtain a linear trend line fit for the data. Use the mathematically linearized expression of the Langmuir isotherm to calculate q_{max} and b
   $$\frac{C_e}{q_e} = C_e\left(\frac{1}{q_{max}}\right) + \frac{1}{q_{max}b}$$

10. Write the complete Langmuir equation for the 1 large block and the 8 Nano-blocks.
    $$q_e = q_{max} * \frac{bC_e}{1 + bC_e}$$

	1 Large Block			8 Nano-blocks		
C_i (initial #pompoms / system)	C_e (final #pompoms /system)	q_e (#pompoms adsorbed /mass blocks)	C_e/q_e (mass blocks /system)	C_e (final # pompoms / system)	q_e (#pompoms adsorbed /mass blocks)	C_e/q_e (mass blocks /system)
50						
60						
70						
80						
90						
100						
110						
120						
130						
140						
150						
160						
170						
180						
190						
200						
210						
220						
230						
240						
250						
Fit Langmuir Isotherm	y = $1/q_{max}$ = $1/(q_{max}b)$ = q_{max} = b = q_e =			y = $1/q_{max}$ = $1/(q_{max}b)$ = q_{max} = b = q_e =		

SYNTHESIS

Limited access to clean water due to natural or municipal disasters, drought or contaminated wells is driving demand for point-of-use and humanitarian drinking water technologies. Currently, when liquid water sources (e.g. lakes, rivers, groundwater) are inaccessible or contaminated, communities rely upon bottled or transported water for weeks to months. Whereas centralized potable water costs <$0.001/L ($0.005/gal), bottled water costs >$0.32/L ($1.20/gal). There is significant economic space for technologies capable of providing the flexibility and safety of bottled water without the infrastructure required for municipal water. Atmospheric water capture (AWC) is a competitive technology that proves clean drinking water off the centralized water grid, does not require fixed physical infrastructure such as pipelines, and does not produce large waste streams associated with contaminant or salt removal from liquid water supplies. The atmosphere contains 12,900 km^3 of water, six times more than the volume stored in rivers. Its universal presence and accessibility provides opportunity for added resilience to water stressed communities. However, climate varies geospatially, and the impact of climate on AWC potential and energy requirement is not parameterized. In this dissertation, I aimed to define geographic and thermodynamic design boundary conditions for AWC and develop nanotechnology enabled AWC technologies to produce clean drinking water.

This work was guided by 4 research questions. My research philosophy to answer these research questions used a bottom up approach (**Figure 8-1**): I developed thermodynamic and geospatial models to compile knowledge from existing literature to create meaningful new conclusions and advise research direction. Operational envelopes

defined by the models led to development of niche technological solutions that solved specific challenges outlined during knowledge curation. These solutions were implemented at bench and pilot scale to prove technology application and verify models. Knowledge curation, technology development, and implementation steps each feed back to one another in the quest to overcome research barriers.

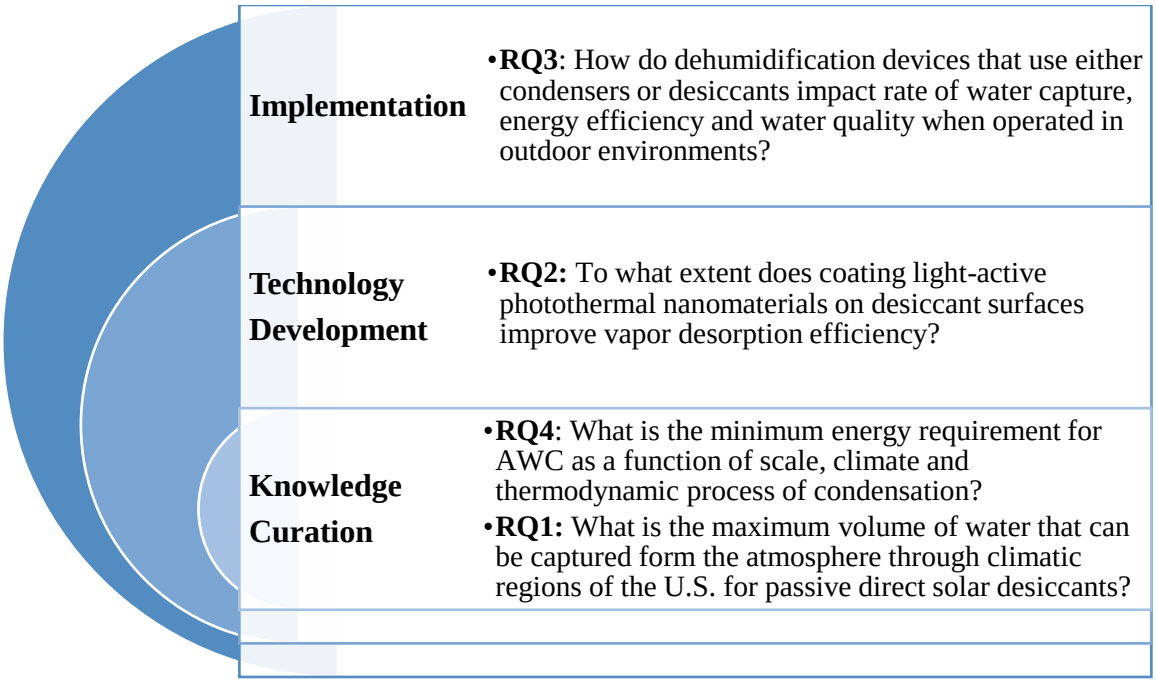

Figure 8-1 Bottom-up research philosophy used to guide and answer research questions posed in this dissertation.

8.1 Preliminary Knowledge Curation: AWC Potential is Influenced by Geospatial Climatic Factors and Material Selection

AWC has piqued interest from non-profit organizations and industries alike because it reduces reliance on liquid water reservoirs (e.g. lakes, rivers, groundwater). However, widespread application is limited because AWC production potential, energy requirement and best technology are all unknown. A literature review of AWC principles

and technologies showed two knowledge threads have stemmed over the last two decades from two separate groups: i) academic research and ii) the commercial sector. *Academic research* has focused on development of desiccant materials with high vapor sorption capacities for "passive AWC" – the desiccants are saturated with water vapor at night, and water vapor is desorbed and condensed during the day using solar thermal energy. Passive AWC systems have not been reported to produce more than 2 L water/day, but they operate completely off the electrical grid. Simultaneously, the *commercial sector* has pushed "active AWC" – compressor systems with refrigerants continuously harvest water vapor during all hours of the day and require electrical energy or gas. Small active AWC systems produce 7 L water/day, while larger units can produce up to 5000 L/day, with energy efficiencies ranging from 0.15 – 0.63 kWh/L in tested conditions (likely high relative humidity). Despite two decades of research, the academic sector knowledge curated from materials development has not transcended the technology development pipeline into commercial application. My initial goal was to determine maximum limit of AWC production potential from passive solar desiccant devices to determine where and how they could be implemented and whether they could be competitive with commercial devices.

I developed a geospatial climactic model for passive solar desiccant driven systems, where water vapor is adsorbed onto a desiccant bed at night, desorbed by solar heat during the day, and condensed. I first compiled materials property and water adsorption/desorption data from an array of materials science, chemistry, and environmental engineering journals. Upon closer look, it appeared that the vast majority of papers synthesized a new material, performed water adsorption isotherms, and

conjectured that the material could be used for AWC. Very few actually tested materials under relevant conditions, and none showed realistic desiccant performance data under multiple climatic conditions. Therefore, the goal of my models was twofold: i) determine the full range of solar-driven desiccant performance as a function of material and device properties, and ii) illustrate geospatial and climatic variation in AWC potential.

Modeling air flow through a 1 m^3 control volume over a 12 hour night where adsorption would occur, I found water vapor concentration varied geospatially and seasonally. **Figure 8-2a** shows water vapor availability varies from 160 L/m^2/day in the arid southwest to 815 L/m^2/day in the humid gulf coast of the United States in summer. Importantly, this map proves that there is an abundance of water vapor in the atmosphere in regions consider to be arid that could be utilized to supply water during a natural or municipal water disaster. **Figures 8-2b** and 8-**2c** show how material selection can impact the quantity of water captured from the air. MOF MIL101(Cr), a desiccant material with one of the highest maximum sorption capacities reported in literature, can produce up to 3 L/m^2/day if used in a humid region. However, in an arid region it produces 0.25 – 0.35 L/m^2/day, while a standard commercial silica gel desiccant can collect 0.8 – 1.2 L/m^2/day. Material selection needs to be climate specific, and rarely is there a one-size-fits-all solution. Turning the focus from adsorption potential to desorption potential, I calculated and mapped AWC potential as a function of the volume of water that could be

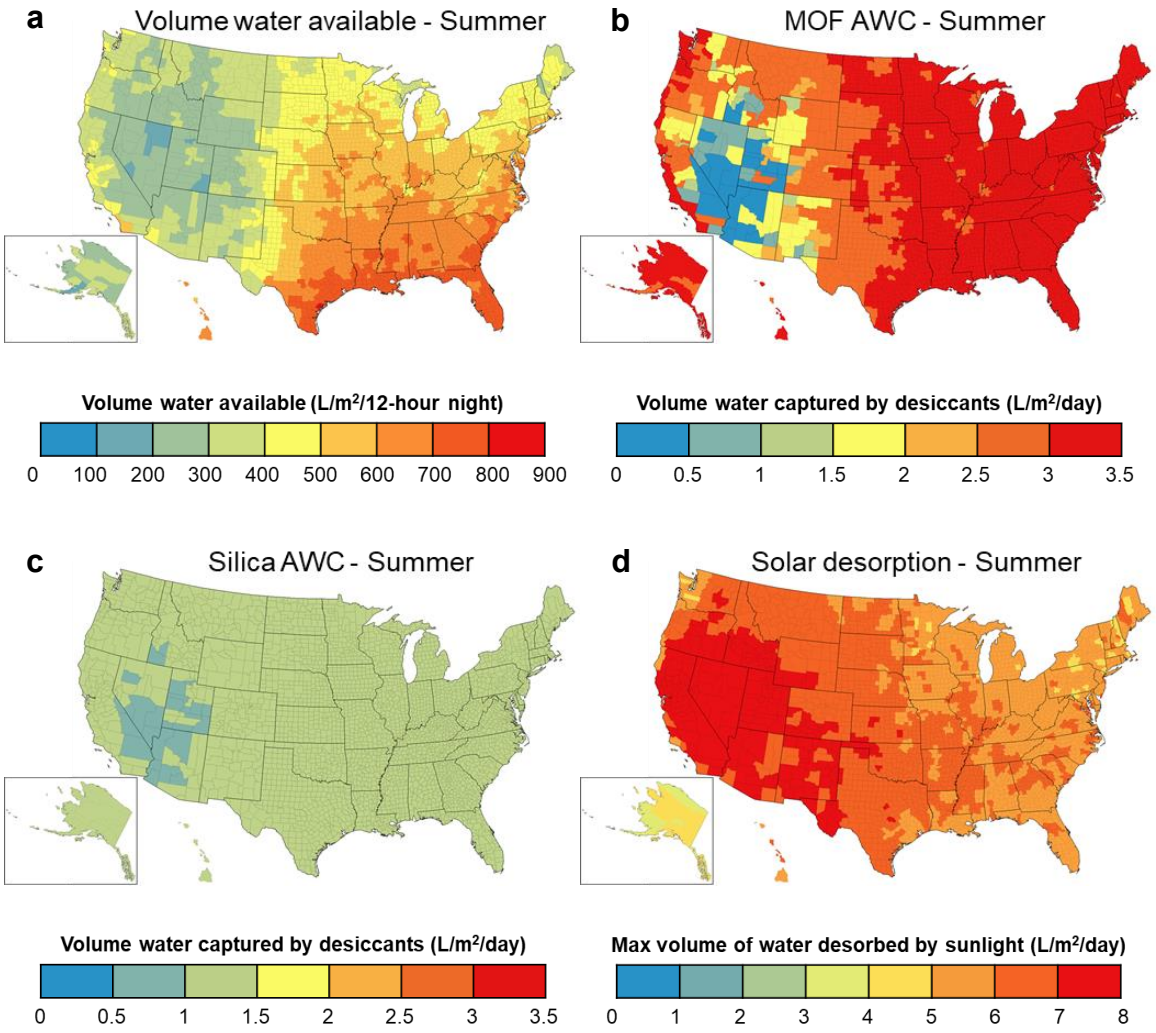

Figure 8-2 Volume of water captured from the atmosphere within a 1 m^3 control volume in summer (L/m^2/day). a) Upper boundary of volume of water available in the atmosphere passing through a 1 m^3 control volume over a 12-hour night. b) AWC potential of high surface area desiccant MOF MIL101(Cr). c) AWC potential of conventional commercial desiccant zeolite. d) Upper boundary of solar desiccant AWC, a function of solar energy available for desorption for E_{des} = 65 kJ/mol.

desorbed by solar energy, regardless of the material's adsorption capacity. **Figure 8-2d** shows significant variability in desorption potential, from 0 – 8 L/m^2/day. **Drawing conclusions from the four maps together, there is a significant opportunity space to**

develop materials for low RH water capture that are solar energy driven for application in the southwestern United States and similar climates worldwide.

8.2 Technology Development: Photothermal Nano-enabled Desiccants Maximize Performance of AWC Devices in Semi-Arid Regions

Motivated by the conclusions from RQ1, I set out to develop a solid desiccant that allowed for superior utilization of solar thermal energy and increased AWC production. I designed a nano-enabled desiccant which superheated under sunlight, increasing rate and overcoming activation energy of desorption. This allowed for a radical shift in operation of solar desiccant systems, from one cycle per day to performance of 10 or more adsorption/ desorption/ condensation cycles per day. This work furthers fundamental understanding of the correlation between light absorption and heat production properties of nanomaterials, and is the first to report performance of multiple solar desiccant AWC cycles per day (**Figure 8-3**). **Photothermal nano-enabled desiccants are uniquely tailored for optimal performance in low RH regions (RH = 40%) with abundant solar radiation and have production potential of 2.5 L/m^2/day over 11 cycles, 80% higher than predicted by the single cycle geospatial model.**

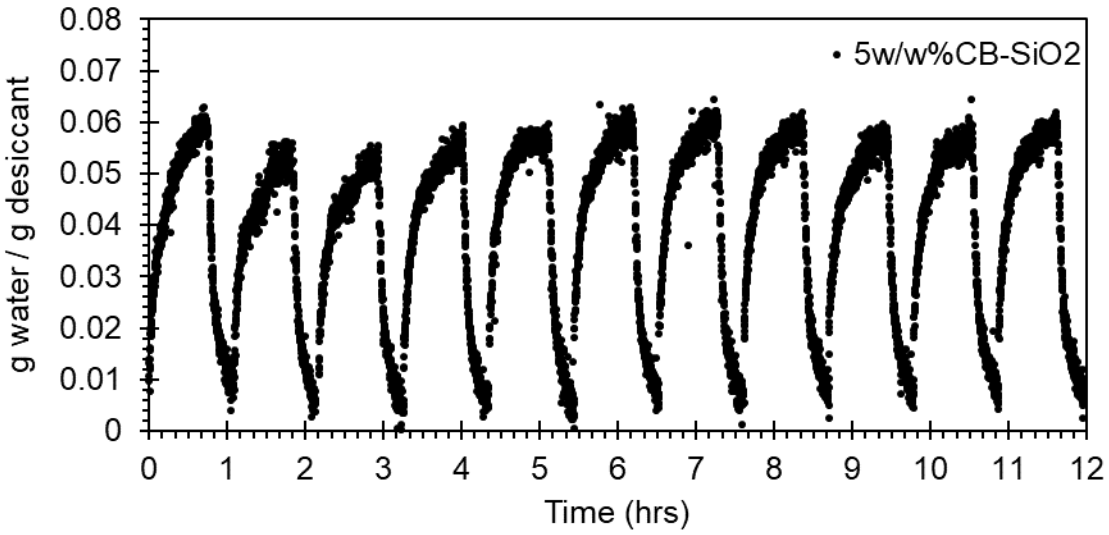

Figure 8-3 Experimental cycling of 5w/w% carbon black enabled silica gel desiccants between adsorption at 40% RH and desorption under simulated solar radiation.

8.3 Implementation: AWC Water Quality and Energy Efficiency are Influenced by Temporal Climatic Factors and AWC Device Selection

As ideal materials and technologies for AWC continue to be developed, it is important to determine how they will function in real outdoor conditions. Therefore, alongside model and material development, I ran a pilot-scale operation of commercial dehumidifiers outdoors for one year. The goal of this work was two-fold: i) Obtain temporal water quality data to discern what treatment trains would be required post water vapor condensation, and ii) Determine differences in water production potential and energy efficiency of two commercial sector AWC technologies – compressors and desiccants. Significant differences were found in production potential, energy, and water quality between the two systems. Compressor systems are most efficient for RH > 30% with energy factor 0.05 – 1.8 L/kWh as a function of RH and specific humidity. Desiccant systems, conversely, are ideal for RH < 30%, with energy factor 0.1 – 0.3

L/kWh. Desiccant system water quality is near distilled, with median conductivity 20µS/cm, turbidity < 0.5 NTU, and concentration of regulated metals >5x lower than maximum contaminant levels (MCL). Conversely, compressor systems can have turbidity 1 – 200 NTU, and Aluminum, Iron and Manganese concentrations above EPA MCLs year-around. Both desiccant and compressor systems have dissolved organic carbon concentration between 1-6 mg/L, with higher concentrations reported in summer months. Compressor systems can have DOC concentration up to 12 mg/L. **Minimal water treatment by carbon to remove organics and disinfection will be required for desiccant systems, while an additional filtration step will be required for compressor systems to remove particulate matter.**

Photothermal nano-enabled desiccants can be incorporated into desiccant dehumidifier configurations (**Figure 8-4**). Desiccants cycle between an adsorption zone exposed to ambient and a desorption zone exposed to solar radiation. Additional novel desiccant materials could be incorporated into a desiccant dehumidifier configuration to maximize water capture potential. High surface area desiccants such as MOFs can have 3-fold higher capacity compared to conventional zeolite desiccants if used in humid climates. This would bring desiccant systems on equal footing with compressor systems. This is particularly advantageous because desiccant systems have superior water quality to compressor systems and would require minimal treatment prior to use.

Figure 8-4 Electrical desiccant dehumidifier system with desiccant wheel containing 5w/w% carbon black enabled silica gel

8.4 Feedback Loop to Secondary Knowledge Creation: Thermodynamic Limit of AWC is a Function of Climate

Armed with knowledge of how geospatial climatic factors impact passive solar desiccant system water production yield and differences in water production yield and energy efficiency of compressor and desiccant dehumidification systems, I realized that the key limiting factor to advancement of atmospheric water capture technology is the need for knowledge curation on the thermodynamic limit of AWC and a determination of exactly which technology or thermodynamic process is ideal for a specified climatic zone. I created a thermodynamic model to calculate energy requirement to saturate water vapor as a function of relative humidity, temperature, and thermodynamic mode of condensation. A key conclusion is the energy requirement for saturation of water vapor to the phase change boundary in a humid climate (RH = 80%) is <0.4% of the latent heat of condensation and <2% of the Gibbs free energy between the liquid and vapor states. However, when RH <20%, the energy requirement to bring vapor to saturation is 50-fold

higher at 18% of the latent heat of vaporization, and 93% of the Gibbs free energy. (Figure 5) The latent heat of condensation (=44.1 kJ/mol) and Gibbs free energy (-8.6 kJ/mol) provide the upper and lower bounds for thermodynamic limit of water capture. If 100% of the heat released from condensation is recovered, AWC can reach the limit posed by Gibbs free energy.

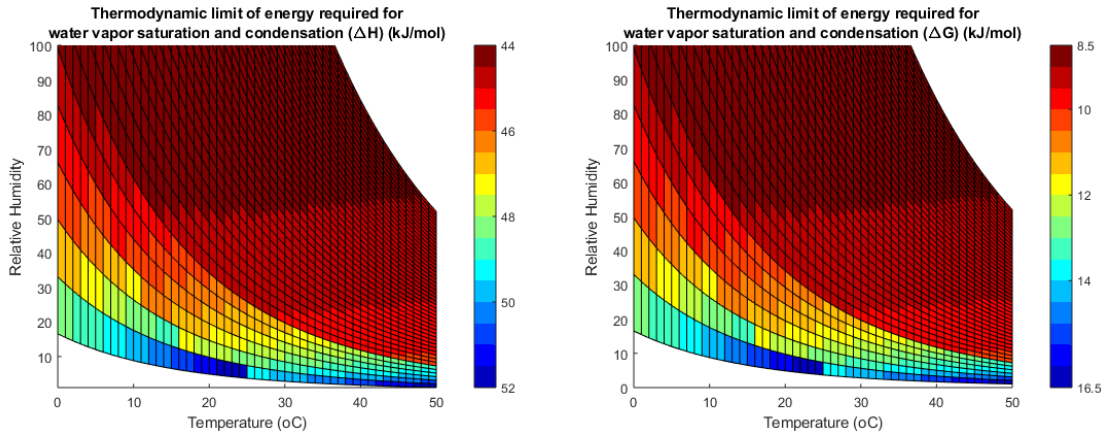

Figure 8-5 Thermodynamic limit of energy required for water vapor saturation and condensation as a function of temperature and relative humidity. a) Energy of water vapor saturation and latent heat of condensation (ΔH^o). b) Energy of water vapor saturation and Gibbs Free Energy (ΔG^o).

The thermodynamic model reconciles why desiccant technology should be utilized in arid climates. The energy required to saturate water vapor through an isobaric process is energy intensive. A desiccant can be used to concentrate vapor to near the saturation boundary such that only the energy for condensation need be applied. However, desiccants require heat energy for desorption as an additional energy input. Future research should be directed towards development of a closed loop system where heat energy from condensation is recovered and applied to desorb water vapor from the desiccant surface.

CONCLUSIONS AND FUTURE WORK

The overarching goal of this dissertation was to define geographic and thermodynamic design boundary conditions for AWC and develop nanotechnology enabled AWC technologies to produce clean drinking water. Below are conclusions from each research chapter and suggestions for future research directions.

9.1 Conclusions

Chapter 3: Geospatial climatic factors influence water production of solar desiccant-driven atmospheric water capture devices

Research Question: What is the maximum volume of water that can be captured form the atmosphere through climatic regions of the U.S. for passive direct solar desiccants?

Answer: The maximum volume of water that can be captured by passive direct solar desiccants varies 2-fold as a function of season, from 8.01 L/m^2/day in the summer, 7.10 L/m^2/day in the spring, 5.18 L/m^2/day in the fall and 4.70 L/m^2/day in the fall.

Significant conclusions

- Desiccant material selection for AWC needs to climate specific. For high humidity regions, desiccants with high specific surface area are key to maximizing AWC potential. Surface area larger than 560 m^2/g can produce >1 L/m^2/day, and when surface area is increased to 6000 m^2/g, AWC potential increases to 2.9L/m^2/day. In low humidity climates, desiccants must have both high specific surface area and Langmuir sorption constant (k_L) > 0.1.
- AWC as a function of available solar radiation for vapor desorption varies between 0.214 – 9 L/m^2/day as a function of geographic location and spring, with highest potential in spring and summer. In winter in high humidity climates, where adsorption

potential may be up to 8 L/m^2/day, desorption potential can be limited to 0 – 4 L/m^2/day. Therefore, choice of desiccant material properties and location of AWC operation must be an interplay, choosing a material with high surface area as well as operating in a location with enough solar irradiance to overcome activation energy and achieve complete desorption.

Chapter 4: Capacity of sunlight driven atmospheric water capture is enhanced by photothermal nanomaterial enabled desiccants

Research Question: To what extent does coating light-active photothermal nanomaterials on desiccant surfaces improve vapor desorption efficiency?

Answer: Coating silica gel desiccants with 5w/w% carbon black nanoparticles decreases time required for water vapor desorption 3-fold and allows for desorption of >90% of the adsorbed water vapor.

Significant conclusions

- 5 w/w% Carbon black nanoparticle enabled silica desiccants heat 2 times faster than the same surface loading of gold nanocubes and 4 times faster than gold nanorods. This is because carbon black absorbs light in the full solar spectrum and has a high efficiency of light absorption to heat conversion. Meanwhile, plasmonic gold nanoparticles absorb the majority of light at the surface plasmonic resonance wavelength and may have heat loss in the energy conversion from plasmonic resonance electron oscillation to heat.
- Photothermal nano-enabled desiccants are uniquely tailored for optimal performance in semi-arid regions (RH=40%) with abundant solar radiation and have production

potential of 2.5 L/m^2/day, 3 times more water than a conventional passive direct solar desiccant system.

- 5 w/w% nanoparticle enabled desiccants had 30-60% reduced water vapor adsorption capacity in comparison to bare silica gel desiccants. It is hypothesized this is due to 35-45% reduction in BET surface area from addition of 2.14 mmol 3-aminopropyltriethoxysilane (APTES) linker per gram silica gel. Nanoparticles were attached to the amine terminus of the APTES linker to ensure strong chemical attachment and limit nanoparticle leaching. However, this sustainability measure led to reduction in adsorption capacity of the nano-enabled desiccants compared to the bare silica gel desiccant. Future research should continue to optimize the APTES and nanoparticle loading to maximize both adsorption and desorption capacity.

Chapter 5: Benchmarking atmospheric water capture energy efficiency, production and water quality using dehumidifiers operated outdoors in Phoenix, AZ

Research Question: How do dehumidification devices that use either condensers or desiccants impact rate of water capture, energy efficiency and water quality when operated in outdoor environments?

Answer: Compressor systems are most efficient for RH > 30% with energy factor 0.05 – 1.8 L/kWh as a function of RH and specific humidity. Desiccant systems, conversely, are ideal for RH < 30%, with energy factor 0.1 – 0.3 L/kWh. Desiccant system water quality is near distilled, with median conductivity 20µS/cm, turbidity < 0.5 NTU, and concentration of regulated metals >5x lower than maximum contaminant levels (MCL). Conversely, compressor systems can have turbidity 1 – 200 NTU, and Aluminum, Iron and Manganese concentrations above EPA MCLs year-around.

Significant conclusions

- Choice of AWC technology and intended use of collected water will dictate the extent of water treatment needed. It is recommended that water captured from desiccant systems be treated by carbon to remove organics followed by disinfection, while water collected from compressor systems will require additional treatment by filtration to remove particulate matter.
- Water quality of AWC systems varies temporally. In Phoenix, AZ, dissolved organic carbon concentration increases 5-fold in the summer in comparison to fall, winter and spring.

Chapter 6: Thermodynamic boundaries guide selection of water vapor saturation process for atmospheric water capture

Research Question: What is the minimum energy requirement for AWC as a function of scale, climate and thermodynamic process of condensation?

Answer: energy requirement for saturation of water vapor to the phase change boundary in a humid climate (RH = 80%) is <0.4% of the latent heat of condensation (44.1 kJ/mol) and <2% of the Gibbs free energy (8.6 kJ/mol) between the liquid and vapor states. However, when RH <20%, the energy requirement to bring vapor to saturation is 50-fold higher at 18% of the latent heat of vaporization, and 93% of the Gibbs free energy.

Significant conclusions

- In regions where RH >40% and T>20^{o}C, cooling water vapor to dewpoint via an isobaric process or a coupled isochoric and isothermal process requires < 0.5 kJ/mol.
- A coupled isobaric and isothermal process is ideal for RH <30% and temperature 10-20^{o}C and requires 1.8-5.6 kJ/mol for vapor saturation.

- An isothermal process (mechanical compression) is most favorable at low temperature and high RH conditions and energy to saturate water vapor is < 1 kJ/mol.

Chapter 7: "Nano-blocks": A playful method to learn about nanotechnology-enabled water and air treatment

Objective: Develop and test a hands-on engineering education tool to effectively teach nanotechnology and sorption fundamentals and applications for water and air treatment.

Significant conclusions

- An activity consisting of Velcro-covered blocks (i.e. adsorbates) attach to pompoms (i.e. adsorbents) teaches students about the correlation between surface area to volume ratio and adsorption capacity. Mathematical modeling proves reducing size of blocks to the nano-scale can exponentially increase sorption capacity.
- Nanoblocks and pompoms can effectively be used in the undergraduate classroom to perform and model adsorption isotherms

9.2 Recommendations for Future Research

In order to enable widespread application of AWC, particularly for disaster relief, rural areas and the military, a "one size fits all" approach must be abandoned. Instead, AWC technologies must be region, climate and use-specific.

There is a significant opportunity to develop novel desiccant materials and desiccant-driven device configurations for operation in arid regions. It was determined that desiccant sorption capacity at low humidity is driven by the Langmuir sorption constant (k_L). Materials science and engineering research should be directed towards identifying what the driving material parameters are that enable large k_L. This may be desiccant surface hydroxyl groups, desiccant porosity, or desiccant hydrophilicity.

In humid regions, technologies which cool water vapor to dew point are ideal and energy efficient. Research should move towards reconciling the upper and lower bounds of the thermodynamic limit of water vapor condensation through heat recovery. Heat transfer modeling and study of heat transfer properties of refrigerants should be explored.

Finally, water captured from AWC systems must be treated prior to use as a drinking water source. As such, future research must explore ideal treatment trains as a function of time and technology. Water treatment will increase operation cost of AWC systems, which must be incorporated within estimates for application of renewable energy sources to ensure off-grid application.

REFERENCES

10 CFR Appendix X1 to Subpart B of Part 430 - Uniform Test Method for Measuring the Energy Consumption of Dehumidifiers (2017).

40 CFR 261. Identification and Listing of Hazardous Waste (2011).

60 FR 54764. (1995). Standards for the Use or Disposal of Sewage Sludge. *Federal Register Volume 60, Issue 206 (October 25, 1995)*, 54771–54792. Retrieved from http://www.gpo.gov/fdsys/pkg/FR-1995-10-25/html/95-25740.htm

Abualhamayel, H. I., & Gandhidasan, P. (1997). A method of obtaining fresh water from the humid atmosphere. *Desalination*, *113*(1), 51–63. https://doi.org/10.1016/S0011-9164(97)00114-8

Ahmed, M. H., Kattab, N. M., & Fouad, M. (2005). Evaluation and optimization of solar desiccant wheel performance. *Renewable Energy*, *30*(3), 305–325. https://doi.org/10.1016/j.renene.2004.04.010

Ahn, H., & Lee, C.-H. (2004). Effects of capillary condensation on adsorption and thermal desorption dynamics of water in zeolite 13X and layered beds. *Chemical Engineering Science*, *59*(13), 2727–2743. https://doi.org/10.1016/j.ces.2004.04.011

Akiyama, G., Matsuda, R., Sato, H., Hori, A., Takata, M., & Kitagawa, S. (2012). Effect of functional groups in MIL-101 on water sorption behavior. *Microporous and Mesoporous Materials*, *157*, 89–93. https://doi.org/10.1016/j.micromeso.2012.01.015

Ali, M. F., & Abbas, S. (2006). A review of methods for the demetallization of residual fuel oils. *Fuel Processing Technology*, *87*(7), 573–584. https://doi.org/10.1016/j.fuproc.2006.03.001

Alspach, B., & Juby, G. (2018). Cost-Effective ZLD Technology for Desalination Concentrate Management. *Journal - American Water Works Association*, *110*(1), 37–47. https://doi.org/10.5942/jawwa.2018.110.0005

American Society of Heating Refrigerating and Air-Conditioning Engineers. (2013). Sorbents and Desiccants. In *2013 ASHRAE Handbook: Fundamentals*.

American Society of Heating Refrigerating and Air-Conditioning Engineers. (2016a). Desiccant dehumidification and pressure-drying equipment. In *2016 ASHRAE Handbook - Heating, Ventilating, and Air-Conditioning Systems and Equipment*.

American Society of Heating Refrigerating and Air-Conditioning Engineers. (2016b). Mechanical dehumidifiers and related components. In *2016 ASHRAE Handbook - Heating, Ventilating, and Air-Conditioning Systems and Equipment*.

Anderson, R. T., & White, K. R. (2007). *7,272,947 B2*.

Andrews, H. G., Eccles, E. A., Schofield, W. C. E., & Badyal, J. P. S. (2011). Three-dimensional hierarchical structures for fog harvesting. *Langmuir*, *27*(7), 3798–3802. https://doi.org/10.1021/la2000014

Ang, B. T. W., Zhang, J., Lin, G. J., Wang, H., Lee, W. S. V., & Xue, J. M. (2019). Enhancing Water Harvesting through Cascading Effect. *ACS Applied Materials & Interfaces*. https://doi.org/10.1021/acsami.9b08460

Appels, L., Baeyens, J., Degrève, J., & Dewil, R. (2008). Principles and potential of the anaerobic digestion of waste-activated sludge. *Progress in Energy and Combustion Science*, *34*(6), 755–781. https://doi.org/10.1016/j.pecs.2008.06.002

Apul, O. G., Wang, Q., Zhou, Y., & Karanfil, T. (2013). Adsorption of aromatic organic contaminants by graphene nanosheets: Comparison with carbon nanotubes and activated carbon. *Water Research*, *47*(4), 1648–1654. https://doi.org/10.1016/j.watres.2012.12.031

Arienzo, M., Christen, E. W., Quayle, W., & Kumar, A. (2009). A review of the fate of potassium in the soil–plant system after land application of wastewaters. *Journal of Hazardous Materials*, *164*(2–3), 415–422. https://doi.org/10.1016/j.jhazmat.2008.08.095

Averitt, R. D., Westcott, S. L., & Halas, N. J. (1999). Linear optical properties of gold nanoshells. *Journal of the Optical Society of America B*, *16*(10), 1824. https://doi.org/10.1364/JOSAB.16.001824

Awad, M. M., Ramzy K, A., Hamed, A. M., & Bekheit, M. M. (2008). Theoretical and experimental investigation on the radial flow desiccant dehumidification bed. *Applied Thermal Engineering*, *28*(1), 75–85. https://doi.org/10.1016/j.applthermaleng.2006.12.018

Bagheri, F. (2018). Performance Investigation of Atmospheric Water Harvesting Systems. *Water Resources and Industry*. https://doi.org/10.1016/j.wri.2018.08.001

Bibby, K., & Peccia, J. (2013). Identification of viral pathogen diversity in sewage sludge by metagenome analysis. *Environmental Science & Technology*, *47*(4), 1945–1951. https://doi.org/10.1021/es305181x

Biller, P., & Ross, A. B. (2011). Potential yields and properties of oil from the hydrothermal liquefaction of microalgae with different biochemical content. *Bioresource Technology*, *102*(1), 215–225. https://doi.org/10.1016/j.biortech.2010.06.028

Bird, P. (1933). A derivation of Langmuir's adsorption isotherm. *Journal of Chemical Education*, *10*(4), 237. https://doi.org/10.1021/ed010p237

Bligh, E. G., & Dyer, W. J. (1959). A rapid method of total lipid extraction and purification. *Canadian Journal of Physiology and Pharmacology*, *37*(8), 911–917. https://doi.org/10.2307/2738252

Blöcher, C., Niewersch, C., & Melin, T. (2012). Phosphorus recovery from sewage sludge with a hybrid process of low pressure wet oxidation and nanofiltration. *Water Research*, *46*(6), 2009–2019. https://doi.org/10.1016/j.watres.2012.01.022

Blonder, R., & Sakhnini, S. (2012). Teaching two basic nanotechnology concepts in secondary school by using a variety of teaching methods. *Chem. Educ. Res. Pract.*, *13*(4), 500–516. https://doi.org/10.1039/C2RP20026K

Boocock, D. G. B., Konar, S. K., Leung, A., & Ly, L. D. (1992). Fuels and chemicals from sewage sludge: 1. The solvent extraction and composition of a lipid from a raw sewage sludge. *Fuel*, *71*(11), 1283–1289. https://doi.org/10.1016/0016-2361(92)90055-S

Boris, A. J., Napolitano, D. C., Herckes, P., Clements, A. L., & Collett, J. L. (2018). Fogs and air quality on the Southern California coast. *Aerosol and Air Quality Research*, *18*(1), 224–239. https://doi.org/10.4209/aaqr.2016.11.0522

Branton, P. J., Hall, P. G., Treguer, M., & Sing, K. S. W. (1995). Adsorption of Carbon Dioxide, Sulfur Dioxide and Water Vapour by MCMD41 , a Model Mesoporous Adsorbent. *J. Chem. Soc. Faraday Trans*, *91*(13), 2041–2043.

Bridle, T. R., & Pritchard, D. (2004). Energy and nutrient recovery from sewage sludge via pyrolysis. *Water Science and Technology : A Journal of the International Association on Water Pollution Research*, *50*(9), 169–175. Retrieved from http://www.researchgate.net/publication/8146909_Energy_and_nutrient_recovery_from_sewage_sludge_via_pyrolysis._Water_Sci_Technol

Bui, D. T., Kum Ja, M., Gordon, J. M., Ng, K. C., & Chua, K. J. (2017). A thermodynamic perspective to study energy performance of vacuum-based membrane dehumidification. *Energy*, *132*, 106–115. https://doi.org/10.1016/j.energy.2017.05.075

Burtch, N. C., Jasuja, H., & Walton, K. S. (2014). Water Stability and Adsorption in Metal − Organic Frameworks. *Chem. Rev.*, *114*(20), 10575–10612. https://doi.org/10.1021/cr5002589

Cadiau, A., Lee, J. S., Damasceno Borges, D., Fabry, P., Devic, T., Wharmby, M. T., … Serre, C. (2015). Design of Hydrophilic Metal Organic Framework Water Adsorbents for Heat Reallocation. *Advanced Materials*, *27*(32), 4775–4780. https://doi.org/10.1002/adma.201502418

Canivet, J., Fateeva, A., Guo, Y., Coasne, B., & Farrusseng, D. (2014). Water adsorption in MOFs: fundamentals and applications. *Chemical Society Reviews*, 5594–5617. https://doi.org/10.1039/c4cs00078a

Carmichael, C. (2020). ENERGY STAR Most Efficient Version 5.0 Dehumidifiers. Retrieved March 8, 2020, from https://data.energystar.gov/Active-Specifications/ENERGY-STAR-Most-Efficient-Version-5-0-Dehumidifie/cg3w-aeur

Chancerel, P., Meskers, C. E. M., Hageluken, C., & Rotter, V. S. (2009). Assessment of Precious Metal Flows During Preprocessing of Waste Electrical and Electronic Equipment. *Journal of Industrial Ecology*, *13*(5), 791–810. https://doi.org/10.1111/j.1530-9290.2009.00171.x

Chaudhry, Q., & Castle, L. (2011). Food applications of nanotechnologies: An overview of opportunities and challenges for developing countries. *Trends in Food Science & Technology*, *22*(11), 595–603. https://doi.org/10.1016/j.tifs.2011.01.001

Chen, B., Zhao, X., & Yang, Y. (2019). Superelastic Graphene Nanocomposite for High Cycle-Stability Water Capture–Release under Sunlight. *ACS Applied Materials & Interfaces*, acsami.9b02215. https://doi.org/10.1021/acsami.9b02215

Chen, D., Li, J., Zhao, J., Guo, J., Zhang, S., Sherazi, T. A., … Li, S. (2018). Bioinspired superhydrophilic-hydrophobic integrated surface with conical pattern-shape for self-driven fog collection. *Journal of Colloid and Interface Science*, *530*, 274–281. https://doi.org/10.1016/J.JCIS.2018.06.081

Chen, T., & Yan, B. (2012). Fixation and partitioning of heavy metals in slag after incineration of sewage sludge. *Waste Management (New York, N.Y.)*, *32*(5), 957–964. https://doi.org/10.1016/j.wasman.2011.12.003

Chiang, Y. C., Chen, C. H., Chiang, Y. C., & Chen, S. L. (2016). Circulating inclined fluidized beds with application for desiccant dehumidification systems. *Applied Energy*, *175*, 199–211. https://doi.org/10.1016/j.apenergy.2016.05.009

Cohen, A. P. (2003). Desiccants. In *Kirk-Othmer Encyclopedia of Chemical Technology*. Hoboken, NJ, USA: John Wiley & Sons, Inc. Retrieved from http://doi.wiley.com/10.1002/0471238961.0405190903150805.a01.pub2

Damania, R., Desbureaux, S., Hyland, M., Islam, A., Moore, S., Rodella, A.-S., … Zaveri, E. (2017). *Uncharted Waters: The New Economics of Water Scarcity and Variability*. *Uncharted Waters: The New Economics of Water Scarcity and Variability*. https://doi.org/10.1596/978-1-4648-1179-1

Darnall, D. W., Greene, B., Henzl, M. T., Hosea, J. M., McPherson, R. a, Sneddon, J., & Alexander, M. D. (1986). Selective recovery of gold and other metal ions from an algal biomass. *Environmental Science & Technology*, *20*(2), 206–208. https://doi.org/10.1021/es00144a018

Dawoud, B., & Aristov, Y. (2003). Experimental study on the kinetics of water vapor sorption on selective water sorbents, silica gel and alumina under typical operating conditions of sorption heat pumps. *International Journal of Heat and Mass Transfer*, *46*(2), 273–281. https://doi.org/10.1016/S0017-9310(02)00288-0

Debellefontaine, H., & Foussard, J. N. (2000). Wet air oxidation for the treatment of industrial wastes. Chemical aspects, reactor design and industrial applications in Europe. *Waste Management*, *20*(1), 15–25. https://doi.org/10.1016/S0956-053X(99)00306-2

Dong, H., Wang, N., Wang, L., Bai, H., Wu, J., Zheng, Y., … Jiang, L. (2012). Bioinspired electrospun knotted microfibers for fog harvesting. *ChemPhysChem*, *13*(5), 1153–1156. https://doi.org/10.1002/cphc.201100957

Dongare, P. D., Alabastri, A., Pedersen, S., Zodrow, K. R., Hogan, N. J., Neumann, O., … Halas, N. J. (2017). Nanophotonics-enabled solar membrane distillation for off-grid water purification. *Proceedings of the National Academy of Sciences of the United States of America*, *114*(27), 6936–6941. https://doi.org/10.1073/pnas.1701835114

Duff, D. G., Ross, S. M. C., & Vaughan, D. H. (1988). Adsorption from solution: An experiment to illustrate the Langmuir adsorption isotherm. *Journal of Chemical Education*, *65*(9), 815. https://doi.org/10.1021/ed065p815

Dufreche, S., Hernandez, R., French, T., Sparks, D., Zappi, M., & Alley, E. (2007). Extraction of Lipids from Municipal Wastewater Plant Microorganisms for Production of Biodiesel. *Journal of the American Oil Chemists' Society*, *84*(2), 181–187. https://doi.org/10.1007/s11746-006-1022-4

Energy Star. (n.d.). Dehumidifier Basics. Retrieved March 8, 2020, from https://www.energystar.gov/products/appliances/dehumidifiers/dehumidifier_basics

Energy Star. (2015). Energy Use in Wastewater Treatment Plants. Retrieved December 31, 2015, from https://www.energystar.gov/sites/default/files/tools/DataTrends_Wastewater_20150129.pdf

Engel, D. R., & Clasby, M. E. (1993). *5259203*.

EPA. (2011). *Planning for an Emergency Drinking Water Supply*. *Epa 600/R-11/054*. Retrieved from https://www.epa.gov/sites/production/files/2015-03/documents/planning_for_an_emergency_drinking_water_supply.pdf

Ervens, B., Wang, Y., Eagar, J., Leaitch, W. R., Macdonald, A. M., Valsaraj, K. T., & Herckes, P. (2013). Dissolved organic carbon (DOC) and select aldehydes in cloud and fog water: The role of the aqueous phase in impacting trace gas budgets. *Atmospheric Chemistry and Physics*, *13*(10), 5117–5135. https://doi.org/10.5194/acp-13-5117-2013

Fan, M., Panezai, H., Sun, J., Bai, S., & Wu, X. (2014). Thermal and kinetic performance of water desorption for N2 adsorption in Li-LSX zeolite. *Journal of Physical Chemistry C*, *118*(41), 23761–23767. https://doi.org/10.1021/jp5068236

FAO. (2012). Current world fertilizer trends and outlook to 2016. *Food and Agriculture Organization of the United Nations*.

Fathieh, F., Kalmutzki, M. J., Kapustin, E. A., Waller, P. J., Yang, J., & Yaghi, O. M. (2018). Practical water production from desert air. *Science Advances*, *4*(6), eaat3198. https://doi.org/10.1126/sciadv.aat3198

Feinberg, B. J., Ramon, G. Z., & Hoek, E. M. V. (2013). Thermodynamic analysis of osmotic energy recovery at a reverse osmosis desalination plant. *Environmental Science and Technology*, *47*(6), 2982–2989. https://doi.org/10.1021/es304224b

Ferreira, W., & Tieleman, H.-J. (2010). *US 2010/0266742 A1*.

Ferreira, W., & Tieleman, H.-J. (2014). *US 2014/0053580 A1*.

Folch, J., Lees, M., & Stanley, G. (1953). A simple method for the isolation and purification of total lipides from animal tissues. *Journal of Biological Chemistry*, *226*, 497–509.

Foley, E. T., & Hersam, M. C. (2006). Assessing the Need for Nanotechnology Education Reform in the United States. *Nanotechnology Law and Business*, *3*(4), 467–484.

Foster, T., Willetts, J., Lane, M., Thomson, P., Katuva, J., & Hope, R. (2018). Risk factors associated with rural water supply failure: A 30-year retrospective study of handpumps on the south coast of Kenya. *Science of the Total Environment*, *626*, 156–164. https://doi.org/10.1016/j.scitotenv.2017.12.302

Friesen, C. A., Friesen, G. H., Lorzel, H., & Goldberg, J. E. (2018). *US 2018/0043295 A1*.

Fumo, N., & Goswami, D. Y. (2002). Study of an aqueous lithium chloride desiccant system: air dehumidification and desiccant regeneration. *Solar Energy*, *72*(4), 351–361. https://doi.org/10.1016/S0038-092X(02)00013-0

Furukawa, H., Gándara, F., Zhang, Y.-B., Jiang, J., Queen, W. L., Hudson, M. R., & Yaghi, O. M. (2014). Water adsorption in porous metal-organic frameworks and related materials. *Journal of the American Chemical Society*, *136*(11), 4369–4381. https://doi.org/10.1021/ja500330a

Fytili, D., & Zabaniotou, A. (2008). Utilization of sewage sludge in EU application of old and new methods—A review. *Renewable and Sustainable Energy Reviews*, *12*(1), 116–140. https://doi.org/10.1016/j.rser.2006.05.014

Gad, H. ., Hamed, A. ., & El-Sharkawy, I. . (2001). Application of a solar desiccant/collector system for water recovery from atmospheric air. *Renewable Energy*, *22*(4), 541–556. https://doi.org/10.1016/S0960-1481(00)00112-9

Gao, Y., & Cranston, R. (2008). Recent Advances in Antimicrobial Treatments of Textiles. *Textile Research Journal*, *78*(1), 60–72. https://doi.org/10.1177/0040517507082332

Garrod, R. P., Harris, L. G., Schofield, W. C. E., McGettrick, J., Ward, L. J., Teare, D. O. H., & Badyal, J. P. S. (2007). Mimicking a Stenocara Beetle's Back for Microcondensation Using Plasmachemical Patterned Superhydrophobic−Superhydrophilic Surfaces. *Langmuir*, *23*(2), 689–693. https://doi.org/10.1021/la0610856

Ge, T. S., Li, Y., Wang, R. Z., & Dai, Y. J. (2008). A review of the mathematical models for predicting rotary desiccant wheel. *Renewable and Sustainable Energy Reviews*, *12*(6), 1485–1528. https://doi.org/10.1016/j.rser.2007.01.012

George, M. W. (2014). Gold. *US Geological Survey Minerals Yearbook*, (703), 66–67. https://doi.org/10.1126/science.1247727

Gido, B., Friedler, E., & Broday, D. M. (2016). Liquid-Desiccant Vapor Separation Reduces the Energy Requirements of Atmospheric Moisture Harvesting. *Environmental Science and Technology*, *50*(15), 8362–8367. https://doi.org/10.1021/acs.est.6b01280

Giusti, L. (2009). A review of waste management practices and their impact on human health. *Waste Management*, *29*(8), 2227–2239. https://doi.org/10.1016/j.wasman.2009.03.028

Golet, E. M., Strehler, A., Alder, A. C., & Giger, W. (2002). Determination of Fluoroquinolone Antibacterial Agents in Sewage Sludge and Sludge-Treated Soil Using Accelerated Solvent Extraction Followed by Solid-Phase Extraction. *Analytical Chemistry*, *74*(21), 5455–5462. https://doi.org/10.1021/ac025762m

Gottschalk, F., Sun, T., & Nowack, B. (2013). Environmental concentrations of engineered nanomaterials: review of modeling and analytical studies. *Environmental Pollution (Barking, Essex : 1987)*, *181*, 287–300. https://doi.org/10.1016/j.envpol.2013.06.003

Govorov, A. O., & Richardson, H. H. (2007). Generating heat with metal nanoparticles. *Nano Today*, *2*(1), 30–38. https://doi.org/10.1016/S1748-0132(07)70017-8

Hall, M. R., Tsang, S. C. E., Casey, S. P., Khan, M. A., & Yang, H. (2012). Synthesis, characterization and hygrothermal behaviour of mesoporous silica high-performance desiccants for relative humidity buffering in closed environments. *Acta Materialia*, *60*(1), 89–101. https://doi.org/10.1016/j.actamat.2011.09.016

Hamed, A. M. (2002). Theoretical and experimental study on the transient adsorption characteristics of a vertical packed porous bed. *Renewable Energy*, *27*(4), 525–541. https://doi.org/10.1016/S0960-1481(01)00112-4

Hamed, A. M., Abd El Rahman, W. R., & El-Eman, S. H. (2010). Experimental study of the transient adsorption/desorption characteristics of silica gel particles in fluidized bed. *Energy*, *35*(6), 2468–2483. https://doi.org/10.1016/j.energy.2010.02.042

Han, D., Meng, Z., Wu, D., Zhang, C., & Zhu, H. (2011). Thermal properties of carbon black aqueous nanofluids for solar absorption. *Nanoscale Research Letters*, *6*, 457. https://doi.org/10.1186/1556-276X-6-457

Hao, G.-P., Mondin, G., Zheng, Z., Biemelt, T., Klosz, S., Schubel, R., … Kaskel, S. (2015). Unusual Ultra-Hydrophilic, Porous Carbon Cuboids for Atmospheric-Water Capture. *Angewandte Chemie International Edition*, *54*(6), 1941–1945. https://doi.org/10.1002/anie.201409439

He, W. F., Xu, L. N., Han, D., Gao, L., Yue, C., & Pu, W. H. (2016). Thermodynamic investigation of waste heat driven desalination unit based on humidification dehumidification (HDH) processes. *Applied Thermal Engineering*, *100*, 315–324. https://doi.org/10.1016/j.applthermaleng.2016.02.047

Hecht, H. G. (1976). The Interpretation of Diffuse Reflectance Spectra. *J. Res. NBS A Phys. Ch.*, *80*(4), 567–583.

Heidari, A., Roshandel, R., & Vakiloroaya, V. (2019). An innovative solar assisted desiccant-based evaporative cooling system for co-production of water and cooling in hot and humid climates. *Energy Conversion and Management*, *185*(February), 396–409. https://doi.org/10.1016/j.enconman.2019.02.015

Henninger, S. K., Munz, G., Ratzsch, K., & Schossig, P. (2011). Cycle stability of sorption materials and composites for the use in heat pumps and cooling machines. *Renewable Energy*, *36*(11), 3043–3049. https://doi.org/10.1016/j.renene.2011.03.032

Herckes, P., Marcotte, A. R., Wang, Y., & Collett, J. L. (2015). Fog composition in the Central Valley of California over three decades. *Atmospheric Research*, *151*, 20–30. https://doi.org/10.1016/j.atmosres.2014.01.025

Herckes, Pierre, Lee, T., Trenary, L., Kang, G., Chang, H., & Collett, J. L. (2002). Organic matter in central California radiation fogs. *Environmental Science and Technology*, *36*(22), 4777–4782. https://doi.org/10.1021/es025889t

Herckes, Pierre, Valsaraj, K. T., & Collett, J. L. (2013). A review of observations of organic matter in fogs and clouds: Origin, processing and fate. *Atmospheric Research*, *132–133*, 434–449. https://doi.org/10.1016/j.atmosres.2013.06.005

Hii, K., Baroutian, S., Parthasarathy, R., Gapes, D. J., & Eshtiaghi, N. (2014). A review of wet air oxidation and Thermal Hydrolysis technologies in sludge treatment. *Bioresource Technology*, *155*, 289–299. https://doi.org/10.1016/j.biortech.2013.12.066

Hong, J., Hong, J., Otaki, M., & Jolliet, O. (2009). Environmental and economic life cycle assessment for sewage sludge treatment processes in Japan. *Waste Management*, *29*(2), 696–703. https://doi.org/10.1016/j.wasman.2008.03.026

Huston, R., Chan, Y. C., Gardner, T., Shaw, G., & Chapman, H. (2009). Characterisation of atmospheric deposition as a source of contaminants in urban rainwater tanks. *Water Research*, *43*(6), 1630–1640. https://doi.org/10.1016/j.watres.2008.12.045

Jain, S., & Bansal, P. K. (2007). Performance analysis of liquid desiccant dehumidification systems. *International Journal of Refrigeration*, *30*(5), 861–872. https://doi.org/10.1016/j.ijrefrig.2006.11.013

Jeremias, F., Khutia, A., Henninger, S. K., & Janiak, C. (2012). MIL-100(Al, Fe) as water adsorbents for heat transformation purposes - A promising application. *Journal of Materials Chemistry*, *22*(20), 10148–10151. https://doi.org/10.1039/c2jm15615f

Jeremias, F., Lozan, V., Henninger, S. K., & Janiak, C. (2013). Programming MOFs for water sorption: Amino-functionalized MIL-125 and UiO-66 for heat transformation and heat storage applications. *Dalton Transactions*, *42*(45), 15967–15973. https://doi.org/10.1039/c3dt51471d

Jia, C. X., Dai, Y. J., Wu, J. Y., & Wang, R. Z. (2006). Experimental comparison of two honeycombed desiccant wheels fabricated with silica gel and composite desiccant material. *Energy Conversion and Management*, *47*(15), 2523–2534. https://doi.org/10.1016/j.enconman.2005.10.034

Jiang, R., Cheng, S., Shao, L., Ruan, Q., & Wang, J. (2013). Mass-based photothermal comparison among gold nanocrystals, PbS nanocrystals, organic dyes, and carbon black. *Journal of Physical Chemistry C*, *117*(17), 8909–8915. https://doi.org/10.1021/jp400770x

Jones, E., Qadir, M., Vliet, M. T. H. Van, Smakhtin, V., & Kang, S. (2019). The state of desalination and brine production : A global outlook. *Science of the Total Environment*, *657*, 1343–1356. https://doi.org/10.1016/j.scitotenv.2018.12.076

Jones, S. B., Zhu, Y., Anderson, D. B., Hallen, R. T., Elliott, D. C., Schmidt, A. J., … Kinchin, C. (2014). *Process Design and Economics for the Conversion of Algal Biomass to Hydrocarbons: Whole Algae Hydrothermal Liquefaction and Upgrading*, *PNNL-23227*.

Ju, J., Bai, H., Zheng, Y., Zhao, T., Fang, R., & Jiang, L. (2012). A multi-structural and multi-functional integrated fog collection system in cactus. *Nature Communications*, *3*, 1247. https://doi.org/10.1038/ncomms2253

Kallenberger, P. A., & Fröba, M. (2018). Water harvesting from air with a hygroscopic salt in a hydrogel–derived matrix. *Communications Chemistry*, *1*(1), 28. https://doi.org/10.1038/s42004-018-0028-9

Khutia, A., Rammelberg, H. U., Schmidt, T., Henninger, S., & Janiak, C. (2013). Water Sorption Cycle Measurements on Functionalized MIL-101Cr for Heat Transformation Application. *Chemistry of Materials*, *25*(5), 790–798. https://doi.org/10.1021/cm304055k

Kim, H., Rao, S. R., Kapustin, E. A., Zhao, L., Yang, S., Yaghi, O. M., & Wang, E. N. (2018a). Adsorption-based atmospheric water harvesting device for arid climates. *Nature Communications*, *9*(1), 1–8. https://doi.org/10.1038/s41467-018-03162-7

Kim, H., Rao, S. R., Kapustin, E. A., Zhao, L., Yang, S., Yaghi, O. M., & Wang, E. N. (2018b). Adsorption-based atmospheric water harvesting device for arid climates. *Nature Communications*, *9*(1), 1–8. https://doi.org/10.1038/s41467-018-03162-7

Kim, H., Rao, S. R., Narayanan, S., Kapustin, E. A., Yang, S., Furukawa, H., … Wang, E. N. (2017). Response to Comment on "Water harvesting from air with metal-organic frameworks powered by natural sunlight." *Science*, *358*(6367), eaao3139. https://doi.org/10.1126/science.aao3139

Kim, H., Yang, S., Rao, S. R., Narayanan, S., Kapustin, E. A., Furukawa, H., … Wang, E. N. (2017). Water harvesting from air with metal-organic frameworks powered by natural sunlight. *Science*, *356*(6336), 430–434. https://doi.org/10.1126/science.aam8743

Kim, J. H., Lee, C. H., Kim, W. S., Lee, J. S., Kim, J. T., Suh, J. K., & Lee, J. M. (2003). Adsorption equilibria of CO2 on alumina, zeolite 13X, and a zeolite X/activated carbon composite. *Journal of Chemical and Engineering Data*, *48*(1), 137–141. https://doi.org/10.1021/je0201267

Kim, S.-I., Yoon, T.-U., Kim, M.-B., Lee, S.-J., Hwang, Y. K., Chang, J.-S., … Bae, Y.-S. (2016). Metal–organic frameworks with high working capacities and cyclic hydrothermal stabilities for fresh water production. *Chemical Engineering Journal*, *286*, 467–475. https://doi.org/10.1016/j.cej.2015.10.098

Kim, Y., & Parker, W. (2008). A technical and economic evaluation of the pyrolysis of sewage sludge for the production of bio-oil. *Bioresource Technology*, *99*(5), 1409–1416. https://doi.org/10.1016/j.biortech.2007.01.056

Kohavi, A., & Peretz, A. (2011). *US 2011/0048039 A1*.

Koronaki, I. P., Christodoulaki, R. I., Papaefthimiou, V. D., & Rogdakis, E. D. (2013). Thermodynamic analysis of a counter flow adiabatic dehumidifier with different liquid desiccant materials. *Applied Thermal Engineering*, *50*(1), 361–373. https://doi.org/10.1016/j.applthermaleng.2012.06.043

Kruger, O., Grabner, A., & Adam, C. (2014). Complete Survey of German Sewage Sludge Ash. *Environmental Science & Technology*, *48*, 11811–11818. https://doi.org/10.1021/es502766x

Küsgens, P., Rose, M., Senkovska, I., Fröde, H., Henschel, A., Siegle, S., & Kaskel, S. (2009). Characterization of metal-organic frameworks by water adsorption. *Microporous and Mesoporous Materials*, *120*(3), 325–330. https://doi.org/10.1016/j.micromeso.2008.11.020

La, D., Dai, Y. J., Li, Y., Wang, R. Z., & Ge, T. S. (2010). Technical development of rotary desiccant dehumidification and air conditioning: A review. *Renewable and Sustainable Energy Reviews*, *14*(1), 130–147. https://doi.org/10.1016/j.rser.2009.07.016

La, D., Li, Y., Dai, Y. J., Ge, T. S., & Wang, R. Z. (2012). Development of a novel rotary desiccant cooling cycle with isothermal dehumidification and regenerative evaporative cooling using thermodynamic analysis method. *Energy*, *44*(1), 778–791. https://doi.org/10.1016/j.energy.2012.05.016

Lalia, B. S., Anand, S., Varanasi, K. K., & Hashaikeh, R. (2013). Fog-harvesting potential of lubricant-impregnated electrospun nanomats. *Langmuir*, *29*(42), 13081–13088. https://doi.org/10.1021/la403021q

Landis, A. E., Miller, S. A., & Theis, T. L. (2007). Life cycle of the corn-soybean agroecosystem for biobased production. *Environmental Science and Technology*, *41*(4), 1457–1464. https://doi.org/10.1021/es0606125

Lapotin, A., Kim, H., Rao, S. R., & Wang, E. N. (2019a). Adsorption-Based Atmospheric Water Harvesting: Impact of Material and Component Properties on System-Level Performance. *Accounts of Chemical Research*, *52*, 1588–1597. research-article. https://doi.org/10.1021/acs.accounts.9b00062

Lapotin, A., Kim, H., Rao, S. R., & Wang, E. N. (2019b). Adsorption-Based Atmospheric Water Harvesting: Impact of Material and Component Properties on System-Level Performance. *Accounts of Chemical Research*, *52*, 1588–1597. https://doi.org/10.1021/acs.accounts.9b00062

Larsen, T. A., Hoffmann, S., Luthi, C., Truffer, B., & Maurer, M. (2016). Emerging solutions to the water challenges of an urbanizing world. *Science*, *352*(6288), 928–933. https://doi.org/10.1126/science.aad8641

LeBleu, T. L., & Forsberg, F. C. (1997). *5,669,221*.

Lee Bray, E. (2014). Aluminum. *US Geological Survey Minerals Yearbook*, *1*(703), 16–17.

Lee, Y.-C., Weng, L.-C., Tseng, P.-C., & Wang, C.-C. (2015). Effect of pressure on the moisture adsorption of silica gel and zeolite 13X adsorbents. *Heat and Mass Transfer*, *51*(3), 441–447. https://doi.org/10.1007/s00231-014-1442-x

Leng, L., Yuan, X., Huang, H., Jiang, H., Chen, X., & Zeng, G. (2014). The migration and transformation behavior of heavy metals during the liquefaction process of sewage sludge. *Bioresource Technology*, *167*, 144–150. https://doi.org/10.1016/j.biortech.2014.05.119

Leng, L., Yuan, X., Shao, J., Huang, H., Wang, H., Li, H., … Zeng, G. (2015). Study on demetalization of sewage sludge by sequential extraction before liquefaction for the production of cleaner bio-oil and bio-char. *Bioresource Technology*, *200*, 320–327. https://doi.org/10.1016/j.biortech.2015.10.040

Li, D., Huang, J., Han, G., & Guo, Z. (2018). A facile approach to achieve bioinspired PDMS@Fe3O4 fabric with switchable wettability for liquid transport and water collection. *Journal of Materials Chemistry A*. https://doi.org/10.1039/C8TA08993K

Li, R., Shi, Y., Alsaedi, M., Wu, M., Shi, L., & Wang, P. (2018). Hybrid Hydrogel with High Water Vapor Harvesting Capacity for Deployable Solar-Driven Atmospheric Water Generator. *Environmental Science and Technology*, *52*(19), 11367–11377. research-article. https://doi.org/10.1021/acs.est.8b02852

Li, R., Shi, Y., Shi, L., Alsaedi, M., & Wang, P. (2018). Harvesting Water from Air: Using Anhydrous Salt with Sunlight. *Environmental Science & Technology*, *52*(9), 5398–5406. https://doi.org/10.1021/acs.est.7b06373

Li, R., Shi, Y., Wu, M., Hong, S., & Wang, P. (2019). Improving atmospheric water production yield: Enabling multiple water harvesting cycles with nano sorbent. *Nano Energy*, (November), 104255. https://doi.org/10.1016/j.nanoen.2019.104255

Li, X., Li, Z., Xia, Q., & Xi, H. (2007). Effects of pore sizes of porous silica gels on desorption activation energy of water vapour. *Applied Thermal Engineering*, *27*(5), 869–876. https://doi.org/10.1016/j.applthermaleng.2006.09.010

Lin, J., Huang, S. M., Wang, R., & Chua, K. J. (2018). Thermodynamic analysis of a hybrid membrane liquid desiccant dehumidification and dew point evaporative cooling system. *Energy Conversion and Management*, *156*(October 2017), 440–458. https://doi.org/10.1016/j.enconman.2017.11.057

Lindberg, R. H., Wennberg, P., Johansson, M. I., Tysklind, M., & Andersson, B. a V. (2005). Screening of human antibiotic substances and determination of weekly mass flows in five sewage treatment plants in Sweden. *Environmental Science and Technology*, *39*(10), 3421–3429. https://doi.org/10.1021/es048143z

Linden, S., Kuhl, J., & Giessen, H. (2001). Controlling the interaction between light and gold nanoparticles: Selective suppression of extinction. *Physical Review Letters*, *86*(20), 4688–4691. https://doi.org/10.1103/PhysRevLett.86.4688

Loeb, S., Li, C., & Kim, J. H. (2018). Solar Photothermal Disinfection using Broadband-Light Absorbing Gold Nanoparticles and Carbon Black. *Environmental Science and Technology*, *52*(1), 205–213. https://doi.org/10.1021/acs.est.7b04442

Long, R. Q., & Yang, R. T. (2001). Carbon nanotubes as superior sorbent for dioxin removal. *Journal of the American Chemical Society*, *123*(9), 2058–2059. https://doi.org/10.1021/ja003830l

Lu, J., Ngo, C.-V., Singh, S. C., Yang, J., Xin, W., Yu, Z., & Guo, C. (2019). Bioinspired Hierarchical Surfaces Fabricated by Femtosecond Laser and Hydrothermal Method for Water Harvesting. *Langmuir*, acs.langmuir.8b04295. https://doi.org/10.1021/acs.langmuir.8b04295

Malik, F. T., Clement, R. M., Gethin, D. T., Krawszik, W., & Parker, A. R. (2014). Nature's moisture harvesters: A comparative review. *Bioinspiration and Biomimetics*, *9*(3). https://doi.org/10.1088/1748-3182/9/3/031002

Marchesan, S., & Prato, M. (2013). Nanomaterials for (Nano)medicine. *ACS Medicinal Chemistry Letters*, *4*(2), 147–149. https://doi.org/10.1021/ml3003742

Margulis, S. A. (2017). *Introduction to hydrology*. *Introduction to hydrology*. https://doi.org/10.1007/978-1-4612-4382-3_9

Marsden, J., & House, I. (2006). *The Chemistry of Gold Extraction* (2nd ed.).

Martin, V., & Goswami, D. . (1999). Heat and Mass Transfer in Packed Bed Liquid Desiccant Regenerators—An Experimental Investigatio. *Solar Energy and Energy Conservation*, *121*(3), 162–170. https://doi.org/10.1016/j.ijheatmasstransfer.2013.10.033

Martínez, J., & Carolina De Aguiar, A. (2014). Extraction of Triacylglycerols and Fatty Acids Using Supercritical Fluids -Review. *Current Analytical Chemistry*, *10*, 67–77. https://doi.org/1875-6727/14 $58.00+.00

Martins, A., & Nunes, N. (2015). Adsorption of a textile dye on commercial activated carbon: A simple experiment to explore the role of surface chemistry and ionic strength. *Journal of Chemical Education*, *92*(1), 143–147. https://doi.org/10.1021/ed500055v

Max, M. D. (2005). *US 6,945,063 B2*.

McClellan, K., & Halden, R. U. (2010). Pharmaceuticals and personal care products in archived U.S. biosolids from the 2001 EPA national sewage sludge survey. *Water Research*, *44*(2), 658–668. https://doi.org/10.1016/j.watres.2009.12.032

Mendez, C. B., Klenzendorf, J. B., Afshar, B. R., Simmons, M. T., Barrett, M. E., Kinney, K. A., & Kirisits, M. J. (2011). The effect of roofing material on the quality of harvested rainwater. *Water Research*, *45*(5), 2049–2059. https://doi.org/10.1016/j.watres.2010.12.015

Merritt, T. (2002). *6,343,479*.

Metcalf, & Eddy. (2013). *Wastewater Engineering: Treatment and Resource Recovery* (5th ed.). McGraw-Hill Education.

Miller, S. A., Landis, A. E., & Theis, T. L. (2006). Use of Monte Carlo analysis to characterize nitrogen fluxes in agroecosystems. *Environmental Science and Technology*, *40*(7), 2324–2332. https://doi.org/10.1021/es0518878

Misha, S., Mat, S., Ruslan, M. H., & Sopian, K. (2012). Review of solid/liquid desiccant in the drying applications and its regeneration methods. *Renewable and Sustainable Energy Reviews*, *16*(7), 4686–4707. https://doi.org/10.1016/j.rser.2012.04.041

Mock, J. J., Smith, D. R., & Schultz, S. (2003). Local refractive index dependence of plasmon resonance spectra from individual nanoparticles. *Nano Letters*, *3*(4), 485–491. https://doi.org/10.1021/nl0340475

Mohamed, M. H., William, G. E., & Fatouh, M. (2017). Solar energy utilization in water production from humid air. *Solar Energy*, *148*, 98–109. https://doi.org/10.1016/j.solener.2017.03.066

Mulchandani, A., Atkinson, A. J., Garcia-Segura, S., & Westerhoff, P. (2019). "Nanoblocks": A Playful Method To Learn about Nanotechnology-Enabled Water and Air Treatment. *Journal of Chemical Education*, acs.jchemed.8b00535. https://doi.org/10.1021/acs.jchemed.8b00535

National Nanotechnology Initiative. (n.d.). Size of the Nanoscale. Retrieved January 7, 2019, from https://www.nano.gov/nanotech-101/what/nano-size

National Renewable Energy Laboratory. (n.d.). National Solar Radiation Data Base 1991-2005 Update: Typical Meteorological Year 3. Retrieved December 19, 2019, from https://rredc.nrel.gov/solar/old_data/nsrdb/1991-2005/tmy3/

National Research Council. (2002). *Biosolids Applied to Land: Advancing Standards and Practices*. National Academy Press.

Neumann, O., Urban, A. S., Day, J., Lal, S., Nordlander, P., & Halas, N. J. (2013). Solar vapor generation enabled by nanoparticles. *ACS Nano, 7*(1), 42–49. https://doi.org/10.1021/nn304948h

Ng, K. C., Chua, H. T., Chung, C. Y., Loke, C. H., Kashiwagi, T., Akisawa, A., & Saha, B. B. (2001). Experimental investigation of the silica gel-water adsorption isotherm characteristics. *Applied Thermal Engineering*, *21*(16), 1631–1642. https://doi.org/10.1016/S1359-4311(01)00039-4

Nguyen, S. C., Zhang, Q., Manthiram, K., Ye, X., Lomont, J. P., Harris, C. B., … Alivisatos, A. P. (2016). Study of Heat Transfer Dynamics from Gold Nanorods to the Environment via Time-Resolved Infrared Spectroscopy. *ACS Nano*, *10*(2), 2144–2151. https://doi.org/10.1021/acsnano.5b06623

Öberg, V., & Goswami, D. Y. (1998). Experimental Study of the Heat and Mass Transfer in a Packed Bed Liquid Desiccant Air Dehumidifier. *Journal of Solar Energy Engineering*, *120*(4), 289. https://doi.org/10.1115/1.2888133

Park, K. C., Kim, P., Grinthal, A., He, N., Fox, D., Weaver, J. C., & Aizenberg, J. (2016). Condensation on slippery asymmetric bumps. *Nature*, *531*(7592), 78–82. https://doi.org/10.1038/nature16956

Park, Y. J., & Fray, D. J. (2009). Separation of zinc and nickel ions in a strong acid through liquid-liquid extraction. *Journal of Hazardous Materials*, *163*(1), 259–265. https://doi.org/10.1016/j.jhazmat.2008.06.085

Parker, A. R., & Lawrence, C. R. (2001). Water capture by a desert beetle. *Nature*, *414*(6859), 33–34. https://doi.org/10.1038/35102108

Pathak, A., Dastidar, M. G., & Sreekrishnan, T. R. (2009). Bioleaching of heavy metals from sewage sludge: a review. *Journal of Environmental Management*, *90*(8), 2343–2353. https://doi.org/10.1016/j.jenvman.2008.11.005

Peccia, J., & Westerhoff, P. (2015). We Should Expect More out of Our Sewage Sludge. *Environmental Science & Technology*, *49*(14), 8271–8276. https://doi.org/10.1021/acs.est.5b01931

Permyakova, A., Wang, S., Courbon, E., Nouar, F., Heymans, N., D'Ans, P., … Serre, C. (2017). Design of salt-metal organic framework composites for seasonal heat storage applications. *Journal of Materials Chemistry A*, *5*(25), 12889–12898. https://doi.org/10.1039/c7ta03069j

Pesaran, A. A., & Mills, A. F. (1987a). Moisture transport in silica gel packed beds—I.Theoretical study. *International Journal of Heat and Mass Transfer*, *30*(6), 1037–1049. https://doi.org/10.1016/0017-9310(87)90034-2

Pesaran, A. A., & Mills, A. F. (1987b). Moisture transport in silica gel packed beds—II. Experimental study. *International Journal of Heat and Mass Transfer*, *30*(6), 1051–1060. https://doi.org/10.1016/0017-9310(87)90035-4

Pfeifer, H., Freude, D., & Hunger, M. (1985). Nuclear magnetic resonance studies on the acidity of zeolites and related catalysts. *Zeolites*, *5*.

Pham, M., Schideman, L., Sharma, B. K., Zhang, Y., & Chen, W.-T. (2013). Effects of hydrothermal liquefaction on the fate of bioactive contaminants in manure and algal feedstocks. *Bioresource Technology*, *149*, 126–135. https://doi.org/10.1016/j.biortech.2013.08.131

Poindexter, F. (1994). *5301516*.

Qi, S., Hay, K. J., & Rood, M. J. (1998). Isotherm Equation for Water Vapor Adsorption onto Activated Carbon. *Journal of Environmental Engineering*, *124*(11), 1130–1134.

Qiu, J., & Wei, W. D. (2014). Surface Plasmon-Mediated Photothermal Chemistry. *The Journal of Physical Chemistry C*, *118*(36), 20735–20749. https://doi.org/10.1021/jp5042553

Qu, X., Brame, J., Li, Q., & Alvarez, P. J. J. (2012). Nanotechnology for a safe and sustainable water supply: Enabling integrated water teatment and reuse. *Accounts of Chemical Research*, *46*(3), 834–843. https://doi.org/10.1021/ar300029v

Radermacher, R. K., & Fawzi, H. (2006). *US 7.043.934 B2*.

Ramteke, S., Patel, K. S., Nayak, Y., & Jaiswal, N. K. (2015). Contamination of Heavy Metals and Nutrients in Sediment , Sludge and Sewage of India. *International Journal of Geosciences*, *6*, 1179–1192.

Redhead, P. A. (1962). Thermal desorption of gases. *Vacuum*, *12*(4), 203–211. https://doi.org/10.1016/0042-207X(62)90978-8

Reidy, J. J. (1992). *5106512*.

Richardson, H. H., Carlson, M. T., Tandler, P. J., Hernandez, P., & Govorov, A. O. (2009). Experimental and theoretical studies of light-to-heat conversion and collective heating effects in metal nanoparticle solution. *Nano Lett.*, *9*(3), 1139–1146. https://doi.org/10.1021/nl8036905.Experimental

Rieth, A. J., Yang, S., Wang, E. N., & Dincă, M. (2017). Record Atmospheric Fresh Water Capture and Heat Transfer with a Material Operating at the Water Uptake Reversibility Limit. *ACS Central Science*, *3*(6), 668–672. https://doi.org/10.1021/acscentsci.7b00186

Ritchey, J. G. (2008). *US 2008/0314062 A1*.

Rittmann, B. E., Mayer, B., Westerhoff, P., & Edwards, M. (2011). Capturing the lost phosphorus. *Chemosphere*, *84*(6), 846–853. https://doi.org/10.1016/j.chemosphere.2011.02.001

Roper, D. K., Ahn, W., & Hoepfner, M. (2007). Microscale Heat Transfer Transduced by Surface Plasmon Resonant Gold Nanoparticles. *The Journal of Physical Chemistry C*, *111*(9), 3636–3641. https://doi.org/10.1021/jp064341w

Saurat, M., & Bringezu, S. (2009). Platinum Group Metal Flows of Europe, Part II. *Journal of Industrial Ecology*, *13*(3), 406–421. https://doi.org/10.1111/j.1530-9290.2008.00106.x

Schoenecker, P. M., Carson, C. G., Jasuja, H., Flemming, C. J. J., & Walton, K. S. (2012). Effect of Water Adsorption on Retention of Structure and Surface Area of Metal–Organic Frameworks. *Industrial & Engineering Chemistry Research*, *51*(18), 6513–6519. https://doi.org/10.1021/ie202325p

Sedlak, R. (1991). *Phosphorous and Nitrogen Removal from Municipal Wastewater: Principles and Practice, Second Edition*. CRC Press.

Seo, Y. K., Yoon, J. W., Lee, J. S., Hwang, Y. K., Jun, C. H., Chang, J. S., … Férey, G. (2012). Energy-efficient dehumidification over hierachically porous metal-organic frameworks as advanced water adsorbents. *Advanced Materials*, *24*(6), 806–810. https://doi.org/10.1002/adma.201104084

Shammas, N. K., & Wang, L. K. (2007). Characteristics and Quantity of Biosolids. In L. K. Wang, N. K. Shammas, & Y.-T. Hung (Eds.), *Biosolids Treatment Processes*. The Humana Press Inc.

Shamuyarira, K. K., & Gumbo, J. R. (2014). Assessment of heavy metals in municipal sewage sludge: a case study of Limpopo province, South Africa. *International Journal of Environmental Research and Public Health*, *11*(3), 2569–2579. https://doi.org/10.3390/ijerph110302569

She, X., Yin, Y., & Zhang, X. (2014). Thermodynamic analysis of a novel energy-efficient refrigeration system subcooled by liquid desiccant dehumidification and evaporation. *Energy Conversion and Management*, *78*, 286–296. https://doi.org/10.1016/j.enconman.2013.10.057

Shiklomanov, I. A. (1992). World fresh water resources. In P. H. Gleick (Ed.), *Water in crisis: a guide to the world's fresh water resources* (pp. 13–24). New York: Oxford University Press.

Skopp, J. (2009). Derivation of the freundlich adsorption isotherm from kinetics. *Journal of Chemical Education*, *86*(11), 1341–1343. https://doi.org/10.1021/ed086p1341

Smithline, S. (2015). 2016 Processing Fees: Beverage Container Recycling. *CalRecycle*. Retrieved from http://www.calrecycle.ca.gov/BevContainer/Notices/2015/ProcessFee.htm

Smithsonian Institution. (1873). *Specific Gravities; Boiling and Melting Points; and Chemical Formula, Part 1*.

Song, R., Qin, Y., Suh, S., & Keller, A. A. (2017). Dynamic Model for the Stocks and Release Flows of Engineered Nanomaterials. *Environmental Science and Technology*, *51*(21), 12424–12433. https://doi.org/10.1021/acs.est.7b01907

Sönnichsen, C., Franzl, T., Wilk, T., von Plessen, G., Feldmann, J., Wilson, O., & Mulvaney, P. (2002). Drastic reduction of plasmon damping in gold nanorods. *Physical Review Letters*, *88*(7), 774021–774024. https://doi.org/10.1103/PhysRevLett.88.077402

Stratton, H., Fuchs, H., Chen, Y., Dunham, C., Ni, C. C., & Williams, A. (2017). Keeping Pace With Water and Wastewater Rates. *Journal - American Water Works Association*, *109*(10), E426–E439. https://doi.org/10.5942/jawwa.2017.109.0101

Tan, B., Luo, Y., Liang, X., Wang, S., Gao, X., Zhang, Z., & Fang, Y. (2019). Mixed-Solvothermal Synthesis of MIL-101(Cr) and Its Water Adsorption/Desorption Performance. *Industrial & Engineering Chemistry Research*, *58*(8), 2983–2990. https://doi.org/10.1021/acs.iecr.8b05243

Tashiro, Y., Kubo, M., Katsumi, Y., Meguro, T., & Komeya, K. (2004). Assessment of adsorption-desorption characteristics of adsorbents for adsorptive desiccant cooling system. *Journal of Materials Science*, *39*(4), 1315–1319. https://doi.org/10.1023/B:JMSC.0000013937.11959.6a

Thickett, S. C., Neto, C., & Harris, A. T. (2011). Biomimetic surface coatings for atmospheric water capture prepared by dewetting of polymer films. *Advanced Materials*, *23*(32), 3718–3722. https://doi.org/10.1002/adma.201100290

Thomas, E. A. (Ed.). (2016). *Broken Pumps and Promises: Incentivizing Impact in Environmental Health*. Springer.

U.S. EPA. (1994). *Land Application of Sewage Sludge: A Guide for Land Appliers on the Requirements of the Federal Standard for the Use or Disposal of Sewage Sludge, 40 CFR Part 503*. Washington, D.C. https://doi.org/EPA-831-B-93−002b

U.S. EPA. (2009). *Targeted National Sewage Sludge Survey Sampling and Analysis Technical Report*. https://doi.org/EPA-822-R-08-016

U.S. EPA. (2015). Sewage Sludge (Biosolids) Frequently Asked Questions. Retrieved December 28, 2015, from http://www.epa.gov/biosolids/frequently-asked-questions-about-biosolids

United States Environmental Protection Agency. (2016). Learn about Small Drinking Water Systems. Retrieved December 19, 2019, from https://www.epa.gov/dwcapacity/learn-about-small-drinking-water-systems

United States Environmental Protection Agency. (2019). Small Drinking Water Systems Research. Retrieved December 19, 2019, from https://www.epa.gov/water-research/small-drinking-water-systems-research

Valdez, P. J., Nelson, M. C., Wang, H. Y., Lin, X. N., & Savage, P. E. (2012). Hydrothermal liquefaction of Nannochloropsis sp.: Systematic study of process variables and analysis of the product fractions. *Biomass and Bioenergy*, *46*, 317–331. https://doi.org/10.1016/j.biombioe.2012.08.009

Vardon, D. R., Sharma, B. K., Scott, J., Yu, G., Wang, Z., Schideman, L., … Strathmann, T. J. (2011). Chemical properties of biocrude oil from the hydrothermal liquefaction of Spirulina algae, swine manure, and digested anaerobic sludge. *Bioresource Technology*, *102*(17), 8295–8303. https://doi.org/10.1016/j.biortech.2011.06.041

Venkatesan, A. K., & Halden, R. U. (2013a). National inventory of alkylphenol ethoxylate compounds in U.S. sewage sludges and chemical fate in outdoor soil mesocosms. *Environmental Pollution (Barking, Essex : 1987)*, *174*, 189–193. https://doi.org/10.1016/j.envpol.2012.11.012

Venkatesan, A. K., & Halden, R. U. (2013b). National inventory of perfluoroalkyl substances in archived U.S. biosolids from the 2001 EPA National Sewage Sludge Survey. *Journal of Hazardous Materials*, *252–253*, 413–418. https://doi.org/10.1016/j.jhazmat.2013.03.016

Venkatesan, A. K., & Halden, R. U. (2014). Brominated flame retardants in U.S. biosolids from the EPA national sewage sludge survey and chemical persistence in outdoor soil mesocosms. *Water Research*, *55*, 133–142. https://doi.org/10.1016/j.watres.2014.02.021

Vialle, C., Sablayrolles, C., Lovera, M., Jacob, S., Huau, M. C., & Montrejaud-Vignoles, M. (2011). Monitoring of water quality from roof runoff: Interpretation using multivariate analysis. *Water Research*, *45*(12), 3765–3775. https://doi.org/10.1016/j.watres.2011.04.029

Viau, E., Bibby, K., Paez-Rubio, T., & Peccia, J. (2011). Toward a consensus view on the infectious risks associated with land application of sewage sludge. *Environmental Science & Technology*, *45*(13), 5459–5469. https://doi.org/10.1021/es200566f

Wahlgren, R. V. (2001). Atmospheric water vapour processor designs for potable water production: a review. *Water Research*, *35*(1), 1–22. https://doi.org/10.1016/S0043-1354(00)00247-5

Wang, C., Luo, Y.-H., He, X.-T., Hong, D.-L., Wang, J.-Y., Chen, F.-H., … Sun, B.-W. (2019). Porous High-Valence Metal–Organic Framework Featuring Open Coordination Sites for Effective Water Adsorption. *Inorganic Chemistry*, *58*(5), 3058–3064. research-article. https://doi.org/10.1021/acs.inorgchem.8b03042

Wang, J. S., & Wai, C. M. (2005). Dissolution of Preciuos Metals in Supercritical Carbon Dioxide. *Ind. Eng. Chem. Res.*, *44*(4), 922–926. https://doi.org/10.1021/ie040198m

Wang, L., Li, N., & Zhao, B. (2010). Exergy performance and thermodynamic properties of the ideal liquid desiccant dehumidification system. *Energy and Buildings*, *42*(12), 2437–2444. https://doi.org/10.1016/j.enbuild.2010.08.022

Wang, P. (2018). Emerging investigator series: the rise of nano-enabled photothermal materials for water evaporation and clean water production by sunlight. *Environmental Science: Nano*, *5*(5), 1078–1089. https://doi.org/10.1039/C8EN00156A

Wang, S., Li, X., Zhao, Z., & Li, Z. (2015). Competitive Adsorption of Carbon Monoxide and Water Vapour on MIL-100(Fe) Prepared Using a Microwave Method. *Adsorption Science & Technology*, *33*(3), 279–296. https://doi.org/10.1260/0263-6174.33.3.279

Wang, T., Kim, J., & Whelton, A. J. (2019). Management of plastic bottle and filter waste during the large-scale Flint Michigan lead contaminated drinking water incident. *Resources, Conservation and Recycling*, *140*, 115–124. https://doi.org/10.1016/j.resconrec.2018.08.021

Wang, W., Wu, L., Li, Z., Fang, Y., Ding, J., & Xiao, J. (2013). An Overview of Adsorbents in the Rotary Desiccant Dehumidifier for Air Dehumidification. *Drying Technology*, *31*(12), 1334–1345. https://doi.org/10.1080/07373937.2013.792094

Weber, C. L., & Clavin, C. (2012). Life cycle carbon footprint of shale gas: Review of evidence and implications. *Environmental Science and Technology*, *46*(11), 5688–5695. https://doi.org/10.1021/es300375n

Wentzel, M. C., Comeau, Y., Ekama, G., van Loosdrecht, M. C., & Brdjanovic, D. (2008). Enchanced Biological Phosphorous Removal. In *Biological Wastewater Treatment: Principles, Modelling and Design*.

Westerhoff, P. K., Kiser, A., & Hristovski, K. (2013). Nanomaterial Removal and Transformation During Biological Wastewater Treatment. *Environmental Engineering Science*, *30*(3), 109–117. https://doi.org/10.1089/ees.2012.0340

Westerhoff, P., Lee, S., Yang, Y., Gordon, G. W., Hristovski, K., Halden, R. U., & Herckes, P. (2015). Characterization, recovery opportunities, and valuation of metals in municipal sludges from U.S. wastewater treatment plants nationwide. *Environmental Science & Technology*, 150127115347007. https://doi.org/10.1021/es505329q

William, G. E., Mohamed, M. H., & Fatouh, M. (2015). Desiccant system for water production from humid air using solar energy. *Energy*, *90*, 1707–1720. https://doi.org/10.1016/j.energy.2015.06.125

Williford, C., Chen, W.-Y., Wang, L. K., & Shammas, N. K. (2007). High Temperature Thermal Processes. In L. K. Wang, N. K. Shammas, & Y.-T. Hung (Eds.), *Biosolids Treatment Processes* (pp. 613–643). The Humana Press Inc.

Worley, M., & Yale, J. (2012). Biomass Gasification Technology Assessment Consolidated Report, (November). Retrieved from http://www.nrel.gov/docs/fy13osti/57085.pdf

Xian, S., Yu, Y., Xiao, J., Zhang, Z., Xia, Q., Wang, H., & Li, Z. (2015). Competitive adsorption of water vapor with VOCs dichloroethane, ethyl acetate and benzene on MIL-101(Cr) in humid atmosphere. *RSC Advances*, *5*(3), 1827–1834. https://doi.org/10.1039/C4RA10463C

Yan, J., Yu, Y., Ma, C., Xiao, J., Xia, Q., Li, Y., & Li, Z. (2015). Adsorption isotherms and kinetics of water vapor on novel adsorbents MIL-101(Cr)@GO with super-high capacity. *Applied Thermal Engineering*, *84*, 118–125. https://doi.org/10.1016/j.applthermaleng.2015.03.040

Yaziz, M. I., Gunting, H., Sapari, N., & Ghazali, A. W. (1989). Variations in rainwater quality from roof catchments. *Water Research*, *23*(6), 761–765. https://doi.org/10.1016/0043-1354(89)90211-X

Yin, K., Du, H., Dong, X., Wang, C., Duan, J.-A., & He, J. (2017). A simple way to achieve bioinspired hybrid wettability surface with micro/nanopatterns for efficient fog collection. *Nanoscale*, *9*(38), 14620–14626. https://doi.org/10.1039/c7nr05683d

Yip, N. Y., & Elimelech, M. (2012). Thermodynamic and energy efficiency analysis of power generation from natural salinity gradients by pressure retarded osmosis. *Environmental Science and Technology*, *46*(9), 5230–5239. https://doi.org/10.1021/es300060m

Yip, N. Y., Vermaas, D. A., Nijmeijer, K., & Elimelech, M. (2014). Thermodynamic, energy efficiency, and power density analysis of reverse electrodialysis power generation with natural salinity gradients. *Environmental Science and Technology*, *48*(9), 4925–4936. https://doi.org/10.1021/es5005413

Yuan, X., Huang, H., Zeng, G., Li, H., Wang, J., Zhou, C., … Liu, Z. (2011). Total concentrations and chemical speciation of heavy metals in liquefaction residues of sewage sludge. *Bioresource Technology*, *102*(5), 4104–4110. https://doi.org/10.1016/j.biortech.2010.12.055

Zaimes, G. G., Soratana, K., Harden, C. L., Landis, A. E., & Khanna, V. (2015). Biofuels via Fast Pyrolysis of Perennial Grasses: A Life Cycle Evaluation of Energy Consumption and Greenhouse Gas Emissions. *Environmental Science and Technology*, *49*(16), 10007–10018. https://doi.org/10.1021/acs.est.5b00129

Zakryk, J. M. (1997). *5,701,749*.

Zhang, F.-S., Yamasaki, S., & Kimura, K. (2001). Rare earth element content in various waste ashes and the potential risk to Japanese soils. *Environment International*, *27*(5), 393–398. https://doi.org/10.1016/S0160-4120(01)00097-6

Zhang, F.-S., Yamasaki, S., & Kimura, K. (2002). Waste ashes for use in agricultural production: II. Contents of minor and trace metals. *Science of The Total Environment*, *286*(1–3), 111–118. https://doi.org/10.1016/S0048-9697(01)00968-8

Zhang, F.-S., Yamasaki, S., & Nanzyo, M. (2002). Waste ashes for use in agricultural production: I. Liming effect, contents of plant nutrients and chemical characteristics of some metals. *Science of The Total Environment*, *284*(1–3), 215–225. https://doi.org/10.1016/S0048-9697(01)00887-7

Zhang, H., & Dreisinger, D. B. (2004). The recovery of gold from ammoniacal thiosulfate solutions containing copper using ion exchange resin columns. *Hydrometallurgy*, *72*(3–4), 225–234. https://doi.org/10.1016/S0304-386X(03)00183-X

Zhang, L. Z., Zhu, D. S., Deng, X. H., & Hua, B. (2005). Thermodynamic modeling of a novel air dehumidification system. *Energy and Buildings*, *37*(3), 279–286. https://doi.org/10.1016/j.enbuild.2004.06.019

Zhang, Lianbin, Wu, J., Hedhili, M. N., Yang, X., & Wang, P. (2015). Inkjet printing for direct micropatterning of a superhydrophobic surface: Toward biomimetic fog harvesting surfaces. *Journal of Materials Chemistry A, 3*(6), 2844–2852. https://doi.org/10.1039/c4ta05862c

Zhang, Linghong, Xu, C. (Charles), & Champagne, P. (2010). Overview of recent advances in thermo-chemical conversion of biomass. *Energy Conversion and Management, 51*(5), 969–982. https://doi.org/10.1016/j.enconman.2009.11.038

Zhang, S.-Y., Jensen, S., Tan, K., Wojtas, L., Roveto, M., Cure, J., … Zaworotko, M. J. (2018). Modulation of Water Vapor Sorption by a 4th Generation Metal-Organic Material with a Rigid Framework and Self-Switching Pores. *Journal of the American Chemical Society*, jacs.8b07290. https://doi.org/10.1021/jacs.8b07290

Zheng, X., Ge, T. S., & Wang, R. Z. (2014). Recent progress on desiccant materials for solid desiccant cooling systems. *Energy, 74*, 280–294. https://doi.org/10.1016/j.energy.2014.07.027

Zhou, X., Huang, W., Shi, J., Zhao, Z., Xia, Q., Li, Y., … Li, Z. (2014). A novel MOF/graphene oxide composite GrO@MIL-101 with high adsorption capacity for acetone. *Journal of Materials Chemistry A*, 4722–4730. https://doi.org/10.1039/C3TA15086K

Zuo, G., & Muhammed, M. (1990). Extraction of Gold and Silver by Thiourea-Based Reagents. *Separation Science and Technology*, *25*(13–15), 1785–1802. https://doi.org/10.1080/01496399008050424

APPENDIX A

RECOVERY OPPORTUNITIES FOR METALS AND ENERGY FROM SEWAGE SLUDGES

A RECOVERY OPPORTUNITIES FOR METALS AND ENERGY FROM SEWAGE SLUDGES

This appendix has been published as:

Mulchandani, A. and Westerhoff, P. Recovery opportunities for metals and energy from sewage sludges. *Bioresource Technology*, **2016**, *2015*, 215-226.

A-1 Abstract

Limitations on current wastewater treatment plant (WWTP) biological processes and solids disposal options present opportunities to implement novel technologies that convert WWTPs into resource recovery facilities. This review considered replacing or augmenting extensive dewatering, anaerobic digestion, and off-site disposal with new thermo-chemical and liquid extraction processes. These technologies may better recover energy and metals while inactivating pathogens and destroying organic pollutants. Because limited direct comparisons between different sludge types exist in the literature for hydrothermal liquefaction, this study augments the data with experimental findings. These experiments demonstrated 50% reduction in sludge mass, with 30% of liquefaction products converted to bio-oil and most metals sequestered within a small mass of solid bio-char residue. Finally, each technology's contribution to the three sustainability pillars is investigated. Although limiting hazardous materials reintroduction to the *environment* may increase *economic* cost of sludge treatment, it is balanced by cleaner environment and valuable resource benefits for *society*.

Keywords: wastewater, biosolids, biofuel, hydrothermal liquefaction

A-2 Introduction – Sewage Sludge Issues

Increasingly restrictive regulations for wastewater treatment prior to discharge coupled with the rising costs for sludge disposal pose two interrelated problems: (1) sludges loaded with contaminants may no longer be disposed in traditional ways, and (2) sludge treatment technologies, which have slowly evolved over the past 50 years to adapt to the changing regulations, have increased infrastructure and cost of treatment exponentially. Rather than continuing slow evolution of tweaking of sludge treatment, the authors believe there are existing technologies that provide a new approach to sludge treatment.

The history of sewage sludge treatment and disposal can be viewed as a game of playing catch-up with the regulations. In 1988, Congress passed the Ocean Dumping Ban Act, essentially mandating that all sewage sludge disposal be land-based. The Clean Water Act was amended in 1993 with Code of Federal Regulations Title 40 Part 503 to regulate the use and disposal of treated sewage sludges. (U.S. EPA, 1994) Land application of Class B sludges (i.e., treated sludges that still contain pathogens) on agricultural fields was encouraged under the idea that organics in the sludges would promote soil stabilization, enrich soils, and enhance crop growth. However, land application, by which 55% of sludge is disposed, continues to face setbacks ranging from public tolerance for odor to public health and environmental concerns stemming from presence of non-regulated metals and contaminants of emerging concern (CECs). Alternatives to land application include landfill disposal (30% of sludge) and incineration (15% of sludge). (Peccia & Westerhoff, 2015) Incineration poses human toxicity concerns associated with releasing heavy metals and particulates into the air. (Hong,

Hong, Otaki, & Jolliet, 2009) Thus, for treated sludges with high metal or CEC content, landfilling is increasingly the only remaining disposal method. These sludges are subject to municipal and hazardous waste landfill regulations set forth by the Resource Conservation and Recovery Act (RCRA). (40 CFR 261, 2011) Landfilling faces several drawbacks – specifically, space is limited due to the growing strain of urbanization, leading to increased cost of hauling to distant locations. Additionally, there is public distaste towards landfill odor, and environmental concerns regarding the release of greenhouse gases and the potential for groundwater contamination from the leachate. (Giusti, 2009)

Wastewater treatment technology has adapted to increasing regulations and concerns regarding the effects of disposal on aquatic life and water reuse applications. Activated sludge technology to reduce biological oxygen demand was first implemented in the mid-20th century. In the 1960s, chemical phosphorous precipitation was added, followed by biological treatment trains with nitrification, denitrification, and enhanced biological phosphorous removal (EBPR). These modifications produced higher quality effluents and increased viability for reuse; however, the biological processes also produce large volumes of low density (98% water) biological solids, chemicals, and inert particles associated with the lipid-rich bio-cellular materials. This ultimately results in a longer solids retention time (SRT) for sludge stabilization during anaerobic digestion, up to 30 days. These very long SRTs result in large reactor volumes with high capital costs and consequently only become economically viable for larger utilities (i.e., WWTPs that serve populations on the order of >100,000). (Peccia & Westerhoff, 2015)

Sewage solids treatments rely on sludge stabilization (e.g., alkaline lime stabilization, anaerobic digestion, aerobic digestion, and composting) to remove pathogens, pollutants, and odor. Anaerobic digestion has been used since the early 1900s and is one of the most popular sludge stabilization technologies. In the absence of oxygen, organic compounds and cells break down to produce biogas (65–70 vol% of methane, CH_4, 30–35 vol% CO_2). A 56–65.5% reduction in volatile suspended solids (VSS) occurs after a SRT between 15 and 30 days (depending on the operating temperature of the reactor). Aerobic digestion (i.e., in the presence of oxygen) can also stabilize sludges, but it does not allow for energy recovery, and the resulting sludge has poor dewaterability. Stabilized sludges are only 5–10 wt% dry solids and must be mechanically dewatered to 25–35 wt% dry solids using centrifuges and belt presses prior to disposal in order to reduce volume and mass for transportation. (Appels, Baeyens, Degrève, & Dewil, 2008; Metcalf & Eddy, 2013)

While biosolids may amend soil and provide plants with beneficial nutrients, they are only applied on <1% of the total agricultural land in the United States. (U.S. EPA, 2015) In Germany, only 2.6% of organic fertilizer is composed of sewage sludge. (Kruger, Grabner, & Adam, 2014) Soils are approaching their cumulative heavy metal loading rates (Table A-1), and the hauling distance required for land application is increasing. The authors argue that land application is merely a preferred sludge disposal alternative when compared to landfill or incineration, and there would be minimal agricultural loss if the total volume of solids produced was reduced and/or a separate, more beneficial use was found for them.

It is worthwhile to consider shifting the perspective of WWTPs from being waste treatment and disposal facilities to resource recovery facilities. Human-generated wastes consist of most everything used to nourish health and livelihood – metals, nutrients, organics, and more. Rather than disposing these items and investing time, money, and labor to produce and mine additional resources, society will benefit by seeking more sustainable practices that reuse and recycle these resources. The contents of sludges is a matter of perspective – metals, nutrients, and organics can be viewed as hindering waste disposal or as opportunities for resource recovery, recycling, and sustainability. The goal of this paper is to identify and evaluate alternate sewage sludge treatment trains to enable energy and metal recovery. Thermo-chemical processes and liquid solvents are explored for their potential to convert biomass into reusable forms while simultaneously destroying CECs without releasing harmful pollutants. Specifically, hydrothermal liquefaction (HTL), a thermal process adapted from the algae biofuel industry, is unique in that it can directly convert liquid biomass to energy in the form of bio-oil, thereby avoiding energy and costs associated with sludge dewatering. The technology occupies a minimal land footprint and operates 100 times faster than anaerobic digestion. The dry mass of the HTL product is half of the initial reactants, which will substantially reduce costs for hauling and disposing biosolids, and metals and nutrients are concentrated within this small remaining mass. As such, the remainder of this review identifies techniques adapted from the mining industry to extract these resources (metals and nutrients) for financial gain.

A-3 Sludge Composition and Recovery Potential

A-3.1 Metals

40 CFR Part 503 established ceiling concentrations for 10 metals in land-applied biosolids (As, Cd, Cu, Cr, Pb, Hg, Mo, Ni, Se, Zn). (U.S. EPA, 1994) However, Cr was removed from the list in 1995 because: (1) Cr appeared primarily in the less toxic, trivalent form rather than the toxic hexavalent form, and (2) field data did not show Cr toxicity to plants at the cumulative loading concentrations. (60 Federal Register 206, 1995) RCRA established limits on 8 metals in landfilled solid waste using the Toxicity Characteristic Leaching Potential (As, Ba, Cd, Cr, Pb, Hg, Se, Ag). (Table A-1) (40 CFR 261, 2011) There is a wealth of data for concentrations of these metals in sewage sludges in North America, Europe, and Asia. (Pathak, Dastidar, & Sreekrishnan, 2009) Less is known about non-regulated metals such as post-transition and precious metals (Au, Pt, Pd, Te, Bi, Sb, In) used in electronics and platinum group metals (Pt, Pd, Rh) used in chemical, petroleum, and glass industries, jewelry, dentistry, and car catalysts. (Chancerel, Meskers, Hageluken, & Rotter, 2009; Saurat & Bringezu, 2009) Recent breakthroughs in nanotechnology have led to metallic nanoparticles incorporated in foods (Ag, TiO_2, Si, Pt), textiles (Ag), and medicine (Au, Si). (Chaudhry & Castle, 2011; Gao & Cranston, 2008; Marchesan & Prato, 2013) WWTPs remove these nanoparticles effectively from the liquid effluent and accumulate them within sludges. (P. K. Westerhoff, Kiser, & Hristovski, 2013) Engineered nanomaterials may be detrimental to the environment if disposed on land, therefore identifying methods to limit their entrance into the environment is desirable. (Gottschalk, Sun, & Nowack, 2013)

The widespread use and emerging concern surrounding non-regulated metals led to the EPA surveying 28 metals (19 new metals – Al, Sb, Ba, Be, B, Ca, Cr, Co, Fe, Mg, Mn, P, Ag, Na, Tl, Sn, Ti, V, Y – in addition to 9 regulated by Part 503) in the 2006–2007 Targeted National Sewage Sludge Survey, which was intended to inform exposure and hazard assessments. (U.S. EPA, 2009) In a separate survey, sludges across the United States were analyzed for 58 regulated and non-regulated elements and were found to have heavy metals (Al, Ba, Cr, Fe, Mn, Sn, Ti) and precious metals (Ag, Au, Pd, Pt, Rh, Ru) in addition to Part 503 regulated metals. The metals all had enrichment factors above unity, indicating likely anthropogenic sources rather than dust or soil. (P. Westerhoff et al., 2015) Internationally, metal content of sludge ash post-incineration has also been evaluated. In Germany, Si, Ca, Fe, and Al were found in abundance, followed by Zn, Mn, Ba, Cu, Sr, Cr, Pb, and Zr. (Kruger et al., 2014) Rare earth element concentrations were calculated for sewage sludge ash in Japan and found to be enriched with Sm, Eu, Tb, Sc, and Gd and slightly enriched by La and Ce. (F.-S. Zhang, Yamasaki, & Kimura, 2001) Table A-2 compares metal concentrations in sewage sludge from the United States, India, and South Africa with sludge ash from Germany and Japan. For nearly all reported metals, incineration increases the metals concentration by up to one order of magnitude. This is likely because incineration reduces the dry mass of solids by more than 65%. (Williford, Chen, Wang, & Shammas, 2007)

Opportunities exist to recover metals from sludges because of the growing public and environmental threats associated with current methods of land disposal, landfill disposal, and incineration of sewage sludges. The metals recovery processes for sludges could be modeled after current recycling programs for glass, paper, and aluminum. In

2013, 1.95 million tons of Al were mined from ore in the United States, and 1.44 million tons were recovered from scrap. (Lee Bray, 2014) Using values presented in Table A-2, 336,000 tons of Al could be recovered globally from sludge, and 150,000 tons could be recovered within the United States (4.4% of total Al produced). For gold, a high commodity metal, mining from ore produced 2.77 million tons. (George, 2014) In comparison, extraction from global sludges can recover 18 tons of Au. The mass is <0.00065% of total Au mined, but it is valued at $20.5/ton of sludge (December 2015 price for pure gold $34,277.66/kg). Resource recovery calculations assume 1.2 billion people living in developed countries generate 30 million tons of sludge/year; the United States alone generates 8 million tons of sludge/year. (Kruger et al., 2014; National Research Council, 2002)

A-3.2 Nutrients

A-3.2.1. Phosphorous

An estimated 16% of the total mined phosphorous is digested by humans and relayed into the waste stream. Wastewater phosphorous concentration can be between 4 and 16 mg/L. (Rittmann, Mayer, Westerhoff, & Edwards, 2011) Half of this phosphorous integrates into the cellular biomass of sludges, while the other half discharges into waterways from the WWTPs. Phosphorous concentrations in wastewater effluent disposed to surface waters is limited to less than 2 mg/L across the United States to deter eutrophication. Common treatment processes to achieve these limits are chemical precipitation with iron and biological phosphorous removal. Both approaches accumulate phosphorous in sludges. Phosphorous bound to iron oxides is generally not bio-available to plants and is difficult to recover, but biologically sequestered phosphorous remains

bio-available and may be easier to recover upon cellular oxidation. EBPR processes, which stimulate growth of bacteria likely to uptake phosphorous, currently operate at full scale and enhance phosphorous removal compared against conventional activated sludge treatment processes. EBPR increases sludge phosphorous concentrations from 0.02 mg/mg VSS to 0.06–0.15 mg/mg VSS. This increased sludge phosphorus concentration coupled with the potential for land-applied treated sewage sludges to be subject to erosion and runoff can amplify phosphorus exposure in the environment. (Rittmann et al., 2011; Wentzel, Comeau, Ekama, van Loosdrecht, & Brdjanovic, 2008)

A-3.2.2. Nitrogen

Nitrogen enters the waste stream through proteins metabolized within the human body. In wastewater, nitrogen can be present as ammonia (40%), organic nitrogen (60%), or nitrate nitrogen (<1%). The influent total nitrogen concentration varies between 20 and 85 mg/L. Because ammonia can be toxic to aquatic life due to its oxygen consumption, nitrogen can be a nutrient to algae and cause eutrophication, and nitrate can cause blue-baby syndrome within infants, wastewater treatment processes must reduce concentration of nitrogenous compounds within the liquid waste effluent. Biological nitrification converts ammonia to nitrate, and the nitrifying bacteria settle through sedimentation, increasing the mass of sludge produced. Ultimately, 2.4–6.7% of the activated sludge dry mass consists of nitrogen (i.e., 24–67 g N/kg dry solids), and the remaining N is denitrified to become N_2 gas. (Sedlak, 1991; Shammas & Wang, 2007)

A-3.2.3. Potassium

Potassium is present in sewage sludges between 0.5–0.7% K_2O / weight of dry solids. (Shammas & Wang, 2007) Wastewater effluent leaving a WWTP has potassium

concentrations between 10 and 30 mg/L. Potassium applied to soil can increase the reserve of potassium bound to minerals within the soil and can be taken up by plants beneficially. There is, however, a risk of potassium leaching if applied excessively, but as there are no known adverse health or environmental risks, potassium regulatory limits generally do not exist. (Arienzo, Christen, Quayle, & Kumar, 2009)

A-3.2.4. Nutrient recovery potential

The 2016 forecast for global fertilizer nutrient demand is 45 million tons of phosphate (as P_2O_5), 116 million tons of nitrogen (as N), and 33 million tons of potassium (as K_2O). With 30 million tons of sludge generated globally annually, complete nutrient recovery and reuse from sludge can amount to 5% of phosphorus demand, 1.7% of nitrogen demand, and 0.64% of potassium demand. (FAO, 2012; Shammas & Wang, 2007)

A-3.3. Energy potential

The rising cost of energy and environmental pollution created by its production confirm the need for green, sustainable energy sources. Energy can be chemically or thermally bound with sludge. Anaerobically digested sewage sludge has a high storage of chemical energy, with carbon content of 67%, higher heating value of 32 MJ/kg. (Vardon et al., 2011) Temperature changes during sludge treatment create thermal energy, which can be collected as heat and reused within the treatment system. Anaerobic digestion produces 0.75–1.12 m^3 of gas (i.e. CH_4 and CO_2) per kg VSS destroyed, or 0.03–0.04 m^3/person/day. However, this energy produced by anaerobic treatment processes does not balance the total energy used by WWTPs (140–1400 KWh/person/day or 13–130 m^3/person/day). (Energy Star, 2015) Moreover, a 10–30 day SRT does not allow

anaerobic digestion to be an option at treatment plants with capacity less than 10 million gallons/day. (Metcalf & Eddy, 2013)

A-3.4. Organic pollutants and pathogens

The consolidation and concentration of pharmaceuticals, personal care products, and other CECs within wastewater solids is a significant cause for concern. Antibiotics are particularly scrutinized as they can increase the risk of antibiotic resistance through genetic mutation or gene transfer. Antibiotics and their metabolites enter sewage through feces, urine, or direct medication disposal and will ultimately enter the environment if not removed during sewage treatment. In particular, pharmaceuticals classified as fluoroquinolones, tetracyclines, and sulfonamides can be taken up by flora. (McClellan & Halden, 2010) A Swedish study (Lindberg et al., 2005) showed two fluoroquinolones, ciprofloxacin and norfloxacin, were present in all 10 samples collected from five different treatment plants at concentrations between 0.1 and 4.8 mg/kg (dry weight). The adsorption of these antibiotics to the sludge during treatment was 87%. (Lindberg, Wennberg, Johansson, Tysklind, & Andersson, 2005) Average concentrations for these fluoroquinolones in sludges in the United States were 6.8 mg/kg and 0.42 mg/kg for ciprofloxacin and norfloxacin, respectively. (Golet, Strehler, Alder, & Giger, 2002; McClellan & Halden, 2010) Other CECs found in sludges to date are brominated flame retardants (BFRs), perfluoroalkyl substances (PFAS), and alkylphenol ethoxylates (APEO). BFRs can persist in soil for at least 3 years, PFAS are resistant to biodegradation, and APEO metabolites have been shown to mimic hormones and can induce endocrine disruption within organisms exposed to the contaminant. These CECs are dangerous when released into the environment as their inability to completely

decompose can lead to spreading within soil, air, and water and can bioaccumulate in microbes and animals. (Venkatesan & Halden, 2013b, 2013a, 2014)

A wide variety of pathogens from human waste streams deposit within sewage sludges. Viruses are particularly challenging as their wide genotypic variety creates a plethora of shapes, sizes, infection potential, and fate and transport in the environment and human body. Recent metagenomic data from 12 sewage sludges sampled at 5 WWTPs across the United States identified 43 different forms of human viruses. In particular, the DNA viruses *Adenovirus, Herpesvirus,* and *Papillomavirus* were found in more than 90% of the samples, and the RNA viruses *Coronavirus, Klassevirus,* and *Rotavirus* were found in more than 80% of samples. (Bibby & Peccia, 2013) Bacteria found in class B sludges include fecal coliforms, *Escherichia coli*, *Enterococcus* spp., and *Clostridium* spp. When land-applying these sludges, the resulting aerosols subject humans to airborne exposure of pathogens. The inhalation risks for disaggregated and aggregated norovirus are 10^{-1} and 10^{-3} when standing 30 m away from the land application site. (Viau, Bibby, Paez-Rubio, & Peccia, 2011)

A-4 Recovery Treatment Processes

With the evolution of sludge treatment technologies constantly adapting to changing regulations, treatment cost has increased while efficiency has decreased. There is an immediate need for new technologies that will convert wastewater treatment plants to resource recovery centers. Guided by the three pillars of sustainability (economy, environment, and society), resource recovery creates economic opportunities, limits reintroduction of hazardous metals and CECs into the environment when solids are disposed, and potentially reduces public concerns related to odors emanating from

sludges or “not in my backyard” apprehension for siting incineration facilities. Instead, metals will be recycled for reuse and economic gain and CECs will be destroyed. Resource recovery technologies can be inspired by and adapted from fields outside of conventional treatment such as the algal biofuel, petroleum, and mining industries. This paper proposes several existing sludge treatment alternatives within the categories of thermal processes and liquid solvent application prior to precipitation or adsorption/extraction of the valuable products. Additionally, results are presented for bench-scale evaluations of HTL, a thermal treatment process. Table A-3 summarizes the thermal and liquid solvent processes discussed in this review for sludge treatment and resource recovery. The advantages and disadvantages are outlined in terms of energy use, cost, products, and feasibility for sludge application. Figure A-1 shows a likely alternate treatment train to conventional sludge treatment.

A-4.1. Thermal processes to lyse cells and release metals

Thermo-chemical processes such as liquefaction, pyrolysis, combustion, and gasification transform biomass organic and inorganic compounds into energy. These processes are more time efficient and have higher conversion efficiencies than biological processes such as anaerobic digestion. (Linghong Zhang, Xu, & Champagne, 2010) Thermal processes are evaluated and distinguished by their varying reaction conditions, energy input, use of dry or wet biomass, and value of product.

A-4.1.1 Hydrothermal liquefaction

HTL is an emerging technology used to extract biofuel from algae. While several thermal technologies (e.g., pyrolysis, combustion, gasification) require dry biomass to maximize energy recovery potential, HTL operates with 5–30% solids. The avoided

dewatering and drying costs significantly reduce energy use relative to pyrolysis and other conventional high temperature processes. HTL is all-encompassing, simultaneously achieving multiple sludge stabilization goals by increasing dewaterability, decreasing mass of the reaction product, and removing harmful pathogens and pollutants. Therefore, it is evaluated in depth for its potential to follow and even replace anaerobic digestion.

In HTL, liquid biomass reacts at a high temperature (250–350°C) and pressure (10–15 MPa), causing cells to lyse and proteins, lipids, and carbohydrates to break down into reactive molecules in the solvent (e.g., water, acetone, ethanol) and to repolymerize into oily compounds. (Linghong Zhang et al., 2010) The four products of HTL are bio-crude oil, a solid residue termed bio-char, an aqueous component containing water soluble compounds, and CO_2 gas. The biochemical composition of the biomass influences bio-oil yield and follows the trend lipids > proteins > carbohydrates. (Biller & Ross, 2011) HTL has been used to deactivate antibiotic resistant genes and remove bioactive compounds such as estrone, florfenicol, and ceftiofur in *Spirulina* algae and swine manure. (Pham, Schideman, Sharma, Zhang, & Chen, 2013)

HTL can be adapted for sewage sludges, which is a wet biomass medium similar to algae. Sludge that has been anaerobically digested and dewatered has 20–30% solids and is thus suitable for direct liquefaction. Return activated sludge (~2% solids) should be dried to achieve at least 5–30% solids prior to HTL. There are few reports of sewage sludge liquefaction to produce oil, and most have used a catalyst (NaOH) and/or liquefaction solvent (acetone, ethanol) to propel the reaction. (Leng et al., 2014; Yuan et al., 2011) Vardon et al. showed bio-oil yield of 9.4% from anaerobic sludge without a catalyst and using water as the solvent, while Leng et al. showed 45% bio-oil yield with

acetone and 40% with ethanol from dewatered sewage sludge. (Leng et al., 2014; Vardon et al., 2011)

Herein, the authors present data from their lab for application of HTL without a catalyst or solvent to both anaerobically digested sludge (ADS) and return activated sludge (RAS) at 20% solids. The liquefaction reaction was run for 30 minutes at 300°C and 10 MPa (see SI for details). HTL reduced the solids mass by 47% and 55% for ADS and RAS, respectively. In the remaining liquefaction product, 64% of ADS and 50% of RAS dry mass was in the bio-char, 32% and 41% in bio-oil, and the remainder in the water soluble aqueous byproduct. (Figure A-2) HTL efficiency can be compared to anaerobic digestion by calculating the loading rate. With a conservative estimate of 1 gram of solid reacting in a 300 mL vessel for 30 minutes, the equivalent loading rate is 160 kg/m^3/day, or 100 times more efficient than the anaerobic digestion solids loading rate of 1.6–4.8 kg VSS/m^3/day. (Metcalf & Eddy, 2013) This disparity and the relative similarity in HTL results between ADS and RAS shows HTL is viable to follow secondary treatment directly, thereby removing anaerobic digestion.

To study the effect of bacteria and organics transformation on metals migration within the liquefaction product, each sludge phase was microwave digested with 16 M nitric acid, 12 M hydrochloric acid, and 29 M hydrofluoric acid and analyzed for 58 elements using inductively coupled plasma mass spectrometry (ICP-MS) (see SI for details). Approximately 60–80% of each element concentrated within the bio-char fraction, the bio-oil fraction contained less than 7% of each metal, and the remaining percentage was unaccounted for within the pyrolyzed mass. Elsewhere, similar results were seen for Cr, Ni, Cu, Zn, Cd, and Pb undergoing liquefaction with acetone or

ethanol. (Leng et al., 2014, 2015) Figure A-3 shows concentrations of RCRA and 40 CFR Part 503 regulated metals from this work. Figure A-4 shows concentrations of all other metals present at concentrations higher than two times the detection limit of the ICP-MS. The authors hypothesize that significant volatilization is seen for arsenic due to biological formation of methylated arsenic species from organoarsenicals (arsenic ions reacted with carbon). The boiling points of these species vary between 128°C and 215°C, indicating that volatilization is possible at 300°C. (Smithsonian Institution, 1873) In separate work, phosphorous phase partitioning in algae was similar to this study's sludge experimental data; 80% of P in algae went to the aqueous phase after HTL at 250°C. Additionally, 75±9% of nitrogen distributed to the aqueous phase in the algae study. (Valdez, Nelson, Wang, Lin, & Savage, 2012)

Extracting individual metals from the bio-char may depend on the forms they are present in after stabilization and/or thermal processing. Several studies have utilized the European Commission's Community Bureau of Reference (BCR) extraction procedure to understand the chemical forms of metals in a complex matrix. Specifically, Yuan et al. determined that after liquefaction with acetone as the solvent and no catalyst, 35% of Cr, 50% of Zn and Ni, 60% of Cd, and 70% of Cu are in the "oxidizable phase" (i.e., bound to organic matter) while the remaining percentage is in the "residual phase" (i.e., not acid soluble, reducible, or oxidizable). (Yuan et al., 2011)

While only a small metals concentration enters the oil phase, it could cause concern with regards to oil purity and toxicity. However, when Leng et al. extracted metals from sewage sludges with a modified BCR method (0.1M acetic acid, 0.1M hydroxylammonium chloride, 30% hydrogen peroxide, and 1M ammonium acetate) prior

to liquefaction, bio-oil yield decreased by 20% and the oil's heating value also decreased. (Leng et al., 2015) Nevertheless, oil demetallization technologies can be adapted from the petroleum industry that will conserve oil volume and its properties. (Ali & Abbas, 2006)

Overall, HTL is 100x more efficient than anaerobic digestion with regards to loading rate, reduces biomass volume by half, produces energy in the form of bio-oil, and concentrates metals into bio-char fraction. To recover the metals for beneficial use, the metal-laden bio-char fraction must undergo further processing.

A-4.1.2. Incineration/Combustion

Several European and Asian countries incinerate sludges to reduce their final volume by up to 90%. Heating dewatered or dry sludge to higher than 760°C destroys organic pollutants and pathogens and converts the sludge to carbon dioxide, water, and ash. The potential release of toxic exhaust gases to the environment can be a significant problem; however, installing gas scrubbers at incineration plants has helped reduce emission of these byproducts. In the process of burning, metals concentrate and stabilize within the sludge ash, or slag. Depending on the temperature and reaction time, metal fixation to sludge ash can vary between 50 and 97%. (T. Chen & Yan, 2012)

Incineration is also used to recover energy from waste. Approximately 18% of the total heat input is recovered for sludge at 20% solids. This energy can be recycled into the system and used to dry sludge prior to incineration or used to produce electricity. (Williford et al., 2007) Co-incineration of biomass with coal or solid waste is a cost-effective technique to produce energy from multiple sources, but the process dilutes the density and value of metals in sludges that could potentially be extracted. (Linghong Zhang et al., 2010)

A-4.1.3. Chemical oxidation

Wet oxidation, also termed wet air oxidation and wet chemical oxidation (WCO), is a thermal process similar to incineration that oxidizes organics and inorganics remaining in anaerobically digested sludge using air or oxygen (T>150°C, P>1MPa). Oxidation creates hydroxyl and peroxide radicals that transform complex organics to low molecular weight carbon compounds and simultaneously destroy CECs and pathogens. WCO converts 99% of biomass to CO_2, H_2O, and non-hazardous byproducts, without producing hazardous byproducts such as nitrous oxides, sulfur oxides, dioxins, furans, and ash. Chemical oxygen demand is reduced by 15%. An additional advantage over incineration is its ability to operate using aqueous phase biomass, making it an ideal application for sewage sludge. (Fytili & Zabaniotou, 2008; Hii, Baroutian, Parthasarathy, Gapes, & Eshtiaghi, 2014) Oxidation can potentially leach metals from sludge and the HTL bio-char product. In the mining industry, refractory ores with a high carbon content require a pre-oxidation step to assist with releasing tightly bound metals. (Marsden & House, 2006) Given that sludge also has a high organic content and that 35–70% of metals are present in the oxidizable phase of the bio-char, oxidation can be used to liberate metal ions and colloids that may be firmly bound to the solids. (Figure A-1)

There is limited research testing the effect of WCO on resource recovery from sewage sludge. In a German study, oxidation was applied with nanofiltration to separate phosphorous and form phosphoric acid, resulting in 54% phosphorous recovery. Moreover, the volume of suspended solids was reduced by 75%. However, the process does not function if iron is being used at the plant for phosphorous removal. (Blöcher, Niewersch, & Melin, 2012)

A-4.2. Liquid extraction of critical elements

A-4.2.1. Conventional lipid extraction

High lipid content sludge can be subject to alternate energy extraction technologies in which extracted lipids are converted to biodiesel by the transesterification of fatty acid methyl ethers. Several classical solvent techniques have been proven for lipid extraction. The Folch method and Bligh and Dyer method both involve a mixture of chloroform and methanol as solvents. (Bligh & Dyer, 1959; Folch, Lees, & Stanley, 1953) The Soxhlet extraction technique, which can use chloroform, methanol, or toluene, has been successfully demonstrated on sewage sludges by extracting 12 wt% lipids. (Boocock, Konar, Leung, & Ly, 1992) These polar solvents target the polar heads of the phospholipid membranes in sludge microorganisms. (Dufreche et al., 2007) However, polyunsaturated fatty acids in sludges can undergo thermo-degradation under these extraction conditions, and these chemical solvents are highly toxic to human health and the environment. Therefore, green alternatives for lipid extraction must be identified and evaluated.

A-4.2.2. Super critical carbon dioxide for lipids and/or metal extraction

Super critical carbon dioxide ($scCO_2$) extraction has successfully extracted lipids from algae and sludges. Carbon dioxide at temperature and pressure above supercritical values ($T>31.1°C$, $P>7.38$ MPa) exhibits increased transport properties and ability to extract thermolabile compounds without degradation. (Martínez & Carolina De Aguiar, 2014) Super critical carbon dioxide extraction alone can yield 3.55 wt% oil from sewage sludge, and adding a polar co-solvent such as methanol can increase lipid yield to 13.56

wt%. However, although increasing polar solvent volume results in higher oil yield by weight, the transesterifiable material volume may decrease. (Dufreche et al., 2007)

In electronic waste application, $scCO_2$ dissolves precious metals (Au, Cu, Pd) when oxidized by HNO_3, followed by chelation with hexafluoroacetylacetone, to form CO_2 soluble metal β-diketonate complexes. These complexes are then reduced to their elemental state for pure element recovery, either by using supercritical fluid immersion deposition to form a thin film of metal on a silicon surface, adding a reducing agent (e.g., H_2, $NaBH_3CN$), or using a trap solution at ambient conditions. (J. S. Wang & Wai, 2005) While these techniques were developed for a different industry and waste, there is potential to adapt them for sewage sludges and other organic compounds.

A-4.2.3 Acids and green solvents for metal extraction

At neutral pH, metal ions are likely to be strongly bound to cell surfaces. Reducing the pH can desorb metals from cells and will facilitate metal recovery. Strong and weak acids (H_2SO_4, HNO_3, HCl) used in heap leaching processes can be applied to sludges and chars for complete recovery of metals, much like in acid digestion. Oxidizing agents such as nitric acid and hydrogen peroxide decompose complex organic material into carbon dioxide. In fact, the BCR sequential extraction procedure, which was used by Yuan et al. to identify speciation of metals after HTL, uses nitric acid, perchloric acid, and hydrogen peroxide in its final step to extract metals still bound to organics after the initial three extractions (acetic acid, hydroxylammonium chloride at pH 2, and hydrogen peroxide followed by ammonium acetate at pH 2). (Yuan et al., 2011) However, this process is likely to completely remove all organic content from char and produce acid waste that is difficult to dispose. Additionally, some metal ions, such as Au^{3+} and Ag^{+} do

not detach from cells in this acidic environment, and a ligand is required to chelate the metals. (Darnall et al., 1986)

Au and Ag are soft acids and have a tendency to be selective towards sulfur and nitrogen functional groups. While cyanide (CN^-) has been used universally to extract these precious metals from ore, it has toxic effects, and using it to treat sludges would not bode well for environmental and public health and safety. Alternate solvents that have potential for success but have not yet been tested on sewage sludges are thiourea and thiosulfate. Thiourea (CH_4N_2S) is a viable alternative ligand as it is nontoxic, has the ability to dissolve a wide array of metals, and behaves as a plant fertilizer in the environment. The ligand has both S and N atoms and can attract other metals that are soft acids such as Pt, Pd, and Cd. Thiosulfate ($S_2O_3^{2-}$), too, is a fertilizer and green alternative to cyanide, but has specificity towards Au, Ag, Zn, and Cu. (Marsden & House, 2006; Zuo & Muhammed, 1990)

A-4.3. Critical element recovery from liquid concentrate streams

Metals recovery from sewage sludges has not yet been explored within the literature beyond the acid digestions and extractions described in section 3.2.3. Acids are prone to generate hazardous waste that will increase, rather than decrease, waste treatment and disposal issues. In addition, application of acids will decrease the purity or "reusability" of the sludges or chars once the metals have been extracted. Instead, the following processes that have been successfully applied to other mediums such as ore and electronic waste are suggested for adaptation to sequester, concentrate, and recover elements from sewage sludge or any of its processed forms (e.g., post-liquefaction, post-oxidation).

Metals can be recovered from liquid chelating agents and solvents using ion-exchange resins, activated carbon, or precipitation. For example, Au in a thiosulfate solution can load onto a commercial, basic ion-exchange resin at pH 11. However, other metals in the solution such as Cu may compete for attachment. (H. Zhang & Dreisinger, 2004) Using this technology will add an additional step of separating various metals once they have adsorbed to the resin. Alternatively, a selective ion-exchange resin can be developed for individual element recovery.

Extraction of metals can also occur through precipitation. Two different metal ions in solution can be precipitated separately into nanoparticles through liquid-liquid extraction and separate from each other and the leaching solution. Subsequently, a reducing agent is applied to stabilize the particle. (Y. J. Park & Fray, 2009) These nanomaterials can be directly recycled into the nano-manufacturing industries.

While metals recovery is still under exploration, phosphorous recovery is being implemented at WWTPs. Phosphorous can be recovered as struvite ($MgNH_4PO_4 \cdot 6H_2O$) once its concentration reaches 100–200 mg/L in the presence of ammonium and magnesium ions. In the case of complete ammonium removal, potassium struvite could also form ($KMgPO_4 \cdot 6H_2O$). While struvite is actually a scalant that builds in pipes and near the anaerobic digester, it contains valuable nutrients that can be recycled as fertilizers. Struvite recovery efficiency from the waste stream is greater than 60%, and the process adaptation and implementation for commercial use has increased since the first full-scale tests in 2000. (Rittmann et al., 2011)

A-5 Sustainability Assessment

Because explicit cost comparisons are difficult to assess in the early stages of process development, processes are discussed herein using the triple bottom line framework of sustainable development (i.e., environment, economy, and society). New resource recovery centers can improve environmental quality by eliminating hauling of biosolids for land application, which will decrease carbon dioxide emissions and ensure hazardous materials are not reintroduced to the environment. Westerhoff et al. determined that for a community of 1 million people, metals in biosolids are valued up to $13 million per year. Extracting the 13 most valuable elements (Ag, Cu, Au, P, Fe, Pd, Mn, Zn, Ir, Al, Cd, Ti, Ga, and Cr) from sewage sludges could amount to a relative potential economic value of $280/ton of sludge produced. Nitrogen in sludges amounts to $24/ton of sludge, while phosphorous is valued at $7/ton of sludge. (Peccia & Westerhoff, 2015; P. Westerhoff et al., 2015) These extracted elements would return directly into society for reuse, ensuring minimization of waste and maximization of resources. Society pays to keep the environment clean by funding municipal solid waste programs, including recycling and reuse of glass, aluminum, and plastic. For example, a 2016 notice of beverage container recycling processing fees in California shows that recycling bimetal cost of $677.40/ton is an order of magnitude greater than the scrap value of $53.37 per ton. Glass had no monetary recycling value – it cost $99.97/ton to process, and in turn the scrap value paid to recyclers amounted to negative $1.10. (Smithline, 2015)

The current wastewater treatment cost (primary and secondary treatment, anaerobic digestion, and dewatering) is approximately $300/ton. This number can

skyrocket to $800/ton when the cost of hauling processed biosolids for land or landfill disposal and the energy cost of incineration, sludge treatment, and handling are considered. (Peccia & Westerhoff, 2015) Novel thermal processes and liquid solvent technologies described herein can eliminate the need for anaerobic digestion and significantly reduce capital costs for land. In terms of sludge loading, HTL is 100 times faster than anaerobic digestion (see section 3.1.1), thereby decreasing SRT for sludge stabilization, energy production, and resource concentration. Recovery will also contribute to decreased cost. These benefits outweigh initial capital costs for installation of new HTL and oil processing technologies (~$450 million for 440,000 tons/yr reactor) and further operation and maintenance (O&M) costs (~$60/ton, estimate adapted from algae biofuel analysis). (S. B. Jones et al., 2014) Ultimately, the goal of a new system is to be closer to net-neutral or even become net-positive in terms of energy use and costs endured in comparison to conventional systems.

A-6 Conclusions

Recent data shows metals (non-regulated transition, post-transition, and precious), nutrients, pathogens, and organic pollutants in sewage sludges. Alternative sludge treatments such as thermal processes and solvent application can be used to recover energy, metals, and nutrients. HTL showed 50% mass reduction, with 30–40% of the liquefaction product converting to oil, and metals sequestering within the bio-char residue. Transitioning to element recovery using the technologies outlined may evolve due to local sites' specific situations (e.g., phasing out land application). After pilot-scale technology demonstration, implementation is possible at large facilities where space limitations and public input reduces suitability for incineration.

A-7 Acknowledgements

This work is supported by the Arizona State University Fulton Schools of Engineering Deans Fellowship, Central Arizona Phoenix Long-Term Ecological Research (BCS-1026865), U.S. Environmental Protection Agency through the STAR program (RD83558001), and the National Science Foundation through the Nano-Enabled Water Treatment Technologies Nanosystems Engineering Research Center (EEC-1449500). We thank Drs. Kiril Hristovski and Pierre Herckes for their insight in data interpretation and Stan Klonowski for his assistance with hydrothermal liquefaction setup.

A-8 Tables and Figures

Table A-1
Metal concentrations and loading rates for land-applied and landfilled sewage sludges. Ceiling concentrations are the maximum allowable concentrations of metals in land-applied sludges. Cumulative pollutant loading rates are the maximum allowable concentrations of metals applied over the lifetime of a sludge disposal site. Regulatory levels are maximum concentrations of contaminants in municipal landfills obtained by the Toxicity Characteristic Leaching Procedure.

Pollutant	Ceiling Concentration (mg/kg) [a]	Cumulative Pollutant Loading Rate (kg/hectare, dry weight) [a]	Regulatory Level (mg/L) [b]
Arsenic	75	41	5
Barium			100
Cadmium	85	39	1
Chromium	3000	3000	5
Copper	4300	1500	
Lead	840	300	5
Mercury	57	17	0.2
Molybdenum	75	--	
Nickel	420	420	
Selenium	100	100	1
Silver			5
Zinc	7500	2800	

[a](U.S. EPA, 1994) [b] (40 CFR 261, 2011)

Table A-2
Concentrations of Elements in Sewage Sludges Globally (mg/kg)

Elements	USA #1[a] (biosolids)	USA #2[b] (biosolids)	Germany[c] (ash)	Japan[d] (ash)	India[e] (sludge)	South Africa[f] (sludge)
Li				23.7		
Be				0.9		
Na	2,937	952	6,000	17.6		
Mg	6,041.5	4,380	13,000	24.8		
Al	18,571	11,200	48,000	117	7,962	
Si			121,000			
P	20,966	18,750	79,000		375	
S			10,000		298	
Cl					95	
K	5,104		9,000	16.2	911	
Ca	32,656	27,550	105,000	100	81,166	
Sc	1.7		4.2	19.2		
Ti	827.5	87	4,000	401	770	
V	33.5	14	54	155	78	
Cr[2]	88	35	160	226	325	35.07-134.48
Mn	9,267.5	433	1,307	2	4,035	
Fe	19,989.5	16,300	95,000	39.8	267,975	
Co	6.6	4.6	20.7	90.6		
Ni[1]	36	24	74.8	213	15	18.89-51.43
Cu[1]	440.5	468	785	2,838	57	80.80-626.00
Zn[1]	740	803	2,534	3,276	211	303.83-1732
Ga	14.5		11.6	179		
As[1,2]	7.7	5.1	13.6		27	
Se[1,2]			2			
Rb	12			28.9		
Sr	270.5		493	434	86	
Y	5.7	3.8	9.2	16.5		
Zr			106	66.5		
Nb	6.1		11	11.7		
Mo[1]	12.5	11.2	20	19.2		
Ru	0.2					
Pd	0.3		0.109			
Ag[2]	35	14	9.1	13.8		0.22-21.93
Cd[1,2]	4.2	1.7	2.7	6.6		17.96-171.87
Sn	42	37	76.6	552		
Sb	3.3	1.6	12.4	54.8		

Cs	0.6			1.5		
Ba[2]	431	431	1,057	3295	515	
La	10.8		25.5	19.3		
Ce	18.5		42.8	35.4		
Pr	1.7		4.2	3.58		
Nd	6.8		15.6	13.7		
Sm	1.3		2.9	10.7		
Eu	0.3		0.6	1.65		
Gd	1.4		2.8	4.06		
Tb	0.1		0.4	0.8		
Dy	0.9		1.9	2.12		
Ho	0.2		0.4	0.43		
Er	0.5		1	1.08		
Tm	0.1		0.2	0.17		
Yb	0.5		1	1.13		
Lu	0.1		0.2	0.19		
Hf	0.7		3.2	3.8		
Ta			1.2	3.4		
W	1.2		41.1	11.8		
Re	0					
Ir	0					
Pt	0.1		0.108			
Au	0.6		0.9			
Tl	0.1			0.9		
Pb[1,2]	71.5	49	117	547	171	17.96-171.87
Bi				2.8		
Th	1.5	0.1	4.9	4.8		
U	2		4.9	1.9		

[a] Median of values reported in (Westerhoff et al., 2015), [b] U.S. EPA Targeted National Sewage Sludge Survey 50th percentile reported in (P. Westerhoff et al., 2015), [c] (Kruger et al., 2014), [d] (F.-S. Zhang et al., 2001; F.-S. Zhang, Yamasaki, & Kimura, 2002; F.-S. Zhang, Yamasaki, & Nanzyo, 2002), [e] (Ramteke, Patel, Nayak, & Jaiswal, 2015), [f] (Shamuyarira & Gumbo, 2014), [1]Regulated under Title 40 CFR Part 503 for land application, [2]Regulated under Title 40 CFR Part 261 for toxicity potential for landfill.

Table A-3
Comparison summary of advantages, disadvantages, and costs of various thermal and liquid solvent processes.

Conventional Sludge Stabilization Process		
Anaerobic digestion of RAS (Appels et al., 2008; Metcalf & Eddy, 2013)	Description	• No oxygen present; Organic compounds and cells break down to produce biogas (70% CH_4) • Loading capacity: 1.6-4.8 kg VSS/m^3/day
	Advantages	• VSS reduced by ~60%; produces CH_4 used for energy • Biological process, large energy input not required
	Disadvantages	• Solids retention time 15–30 days • Digesters have large land footprint • Solids must be dewatered prior to disposal
	Cost	• Capital: $426 million for 230,000 tons/yr digester; O&M: $10-50/ton
Thermal Processes to Lyse Cells and Release Metals		
Hydrothermal liquefaction of RAS/ADS (S. B. Jones et al., 2014; Pham et al., 2013; Vardon et al., 2011; Linghong Zhang et al., 2010)	Description	• T=250–300°C, P=10–15 MPa, N_2 gas • Loading capacity: 160 kg/m^3/day • Creates bio-oil (32–41 wt%), bio-char (50–64 wt%), water soluble compounds (4–9%) and CO_2 gas
	Advantages	• Mass reduced by 50%; produces bio-oil used for energy • Uses wet sludge, avoids associated dewatering costs • Deactivates antibiotic resistant genes; removes bioactive compounds
	Disadvantages	• Demonstration only at bench-scale • Metals and nutrients concentrated in bio-char fraction
	Cost	• Capital: $450 million for 440,000 tons/yr reactor; O&M: $60/ton
Pyrolysis of RAS/ADS (Bridle & Pritchard, 2004; Y. Kim & Parker, 2008)	Description	• T=275–900°C, N_2 gas • Sludge converted to oil, char, gas and reaction water
	Advantages	• Pilot scale tested and shown to reduce volume of waste produced • Deactivates antibiotic resistant genes; removes bioactive compounds
	Disadvantages	• Sludge must be pre-dried • Metals and nutrients concentrated in bio-char
	Cost	• Capital: $25 million for 25 tons/day; O&M: $50-200/dry ton
Combustion/ Incineration of RAS/ADS (Linghong Zhang et al., 2010)	Description	• Temperature and operational range is high (700–1400°C) • Oxidizes organics and inorganics
	Advantages	• 18% of heat input recovered as energy • Volume of waste reduced; organic pollutants and pathogens destroyed
	Disadvantages	• Metals concentrated in the ash/slag and gases require treatment prior to atmospheric discharge

		• Co-incineration with coal or food and yard waste can dilute metals concentration in the final product
	Cost	• Capital: $280 million for 300,000 tons/yr; O&M: $400/dry ton
Gasification of RAS/ADS (Worley & Yale, 2012; Linghong Zhang et al., 2010)	Description	• Carbonaceous biomass converted to combustible gasses (H_2, CO, CO_2, CH_4) in the presence of oxygen
	Advantages	• High thermal efficiency
	Disadvantages	• Small feed size • Potential for ash clinkering and bridging; high tar production
	Cost	• Capital: $70 million for 1000 tons/day
Oxidation of RAS/ADS or HTL product (Debellefontaine & Foussard, 2000; Hii et al., 2014)	Description	• T=150–330°C, P=1–22 MPa • Organics and inorganics oxidized, transformed to low molecular weight carbon compounds
	Advantages	• Destroys CECs and pathogens; no NOx, SOx, or ash byproduct • Metals in oxidizable phase can potentially be released
	Disadvantages	• Limited demonstration for resource recovery
	Cost	• Capital: $40 million for 7300 tons COD/yr; O&M: $460/dry ton
Liquid Extraction of Critical Elements		
Conventional lipid extraction from RAS (Boocock et al., 1992; Dufreche et al., 2007)	Description	• Polar solvents (e.g. chloroform, methanol, toluene) destroy cell phospholipid membrane to release lipids • Transesterification converts lipids to biodiesel
	Advantages	• 12 wt% lipids extracted by Soxhlet method
	Disadvantages	• Polyunsaturated fatty acids undergo degradation • Polar solvents used are toxic to environment
	Cost	• $3.11/gal oil, assuming 7% transesterification yield
Supercritical carbon dioxide extraction for lipids and/or metals (Dufreche et al., 2007; J. S. Wang & Wai, 2005)	Description	• T>31.1°C, P>7.38 MPa, CO_2 gas • Increased CO_2 transport properties helps extract thermolabile compounds
	Advantages	• 3.55 wt% oil extracted with $scCO_2$; 13.56 wt% oil extracted with $scCO_2$ + polar solvent (e.g. methanol) • $scCO_2$ + HNO_3 + hexafluoroacetylacetone dissolves precious metals; metals recovery exhibited for electronic waste
	Disadvantages	• Large volume of polar solvent decreases volume of transesterifiable material • Metals recovery from sludges not yet tested
	Cost	• Capital: $250 million for 250 tons/day; O&M: $3.11/gal oil, for 7% transesterification yield
Acids for metals extraction (Darnall et al., 1986; Yuan et al., 2011)	Description	• At low pH, metals can desorb from cells • Organic material is decomposed to CO_2
	Advantages	• Complete extraction of metals into solution
	Disadvantages	• Acid waste is difficult to dispose • Some metal ions (Au^{3+}, Ag^{+}) do not detach from cells
	Cost	• HNO_3, HCl: $40/L

Thiourea for metal extraction (Marsden & House, 2006; Zuo & Muhammed, 1990)	Description	• Sulfur and nitrogen functional groups can bind to soft metals (Au, Ag, Pt, Pd, Cd)
	Advantages	• Can extract Au, Ag, Pt, Pd, Cd; Complexes formed with Cu, Fe • Green alternative to cyanide
	Disadvantages	• Cu/Fe complexes are weaker than Au/Ag complexes • Metals recovery from sludges not yet tested
	Cost	• Two times higher than cyanide due to fast consumption and use of acids for pH control
Thiosulfate for metal extraction Marsden and House, 2006)	Description	• Sulfur functional group can bind to Au, Ag, Zn, Cu
	Advantages	• Can extract Au, Ag, Zn, Cu • Green alternative to cyanide
	Disadvantages	• Need oxidant (Cu^{2+}, Fe^{3+}) and oxidant stabilizer(HN_3) • Metals recovery from sludges not yet tested
	Cost	• $2.50–15.00/ton ore

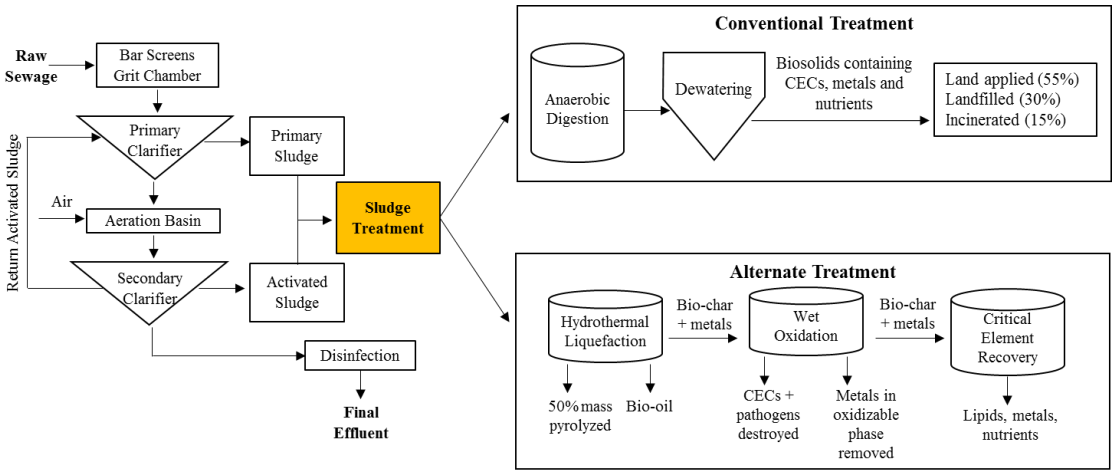

Figure A-1: Alternate treatment schematic outlined within this review compared to conventional treatment.

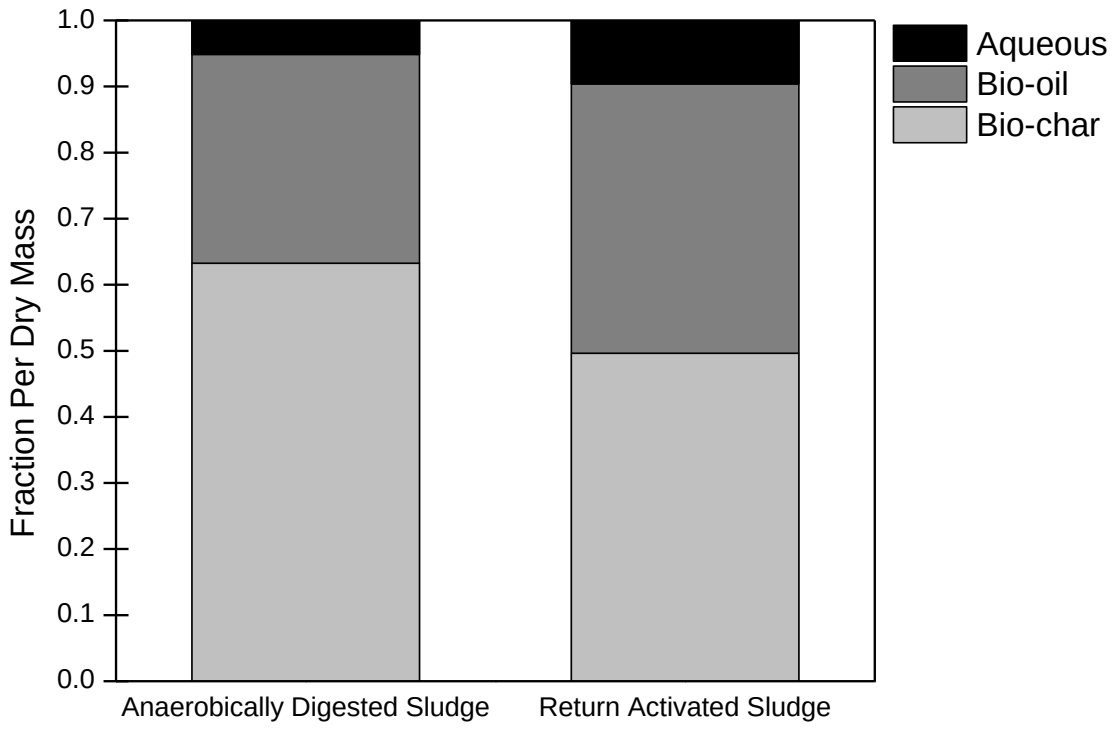

Figure A-2: Phase composition of 20g sewage sludge (20% solids) after hydrothermal liquefaction (300°C, 10 MPa, 30 minutes). The mass reduced by pyrolyzation was 47% and 55% for anaerobically digested sludge (ADS) and return activated sludge, respectively. Data for ADS based on the average of 4 replicates with 13% error.

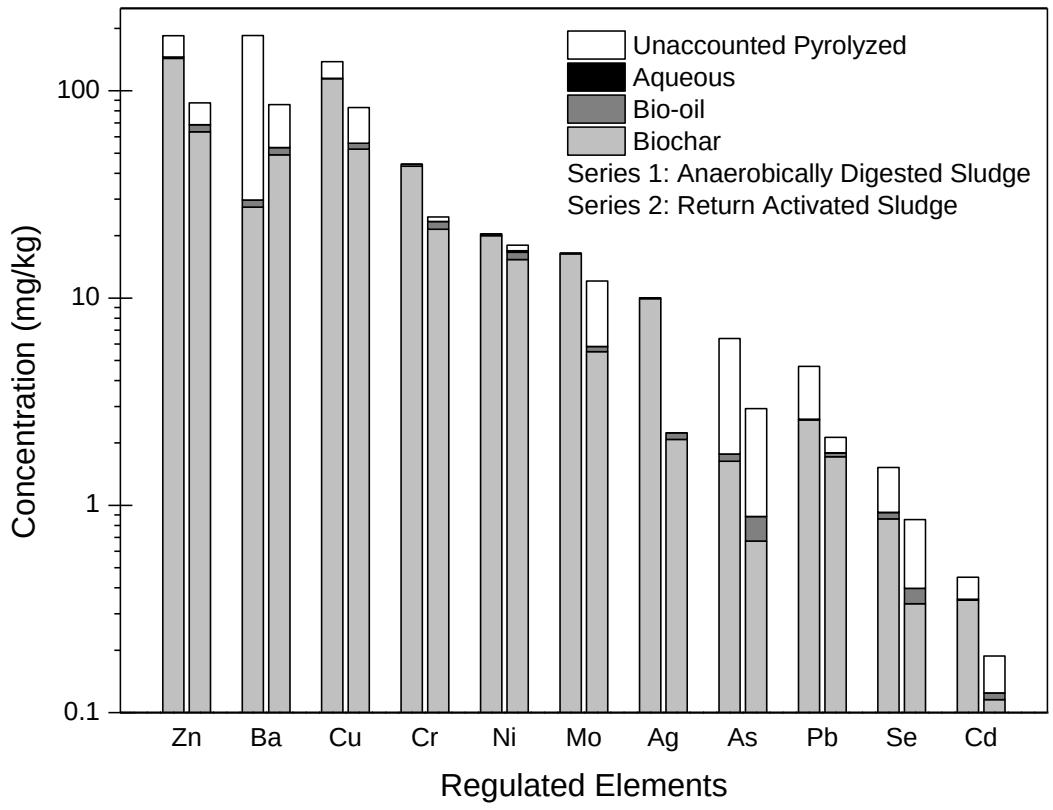

Figure A-3: Concentration of elements in each phase of sewage sludge after hydrothermal liquefaction of 20g sludges (20% solids). Elements are regulated by 40 CFR Part 503 and 40 CFR Part 261 (Resource Conservation and Recovery Act). Standard deviation for experimental replicates <20% of mean.

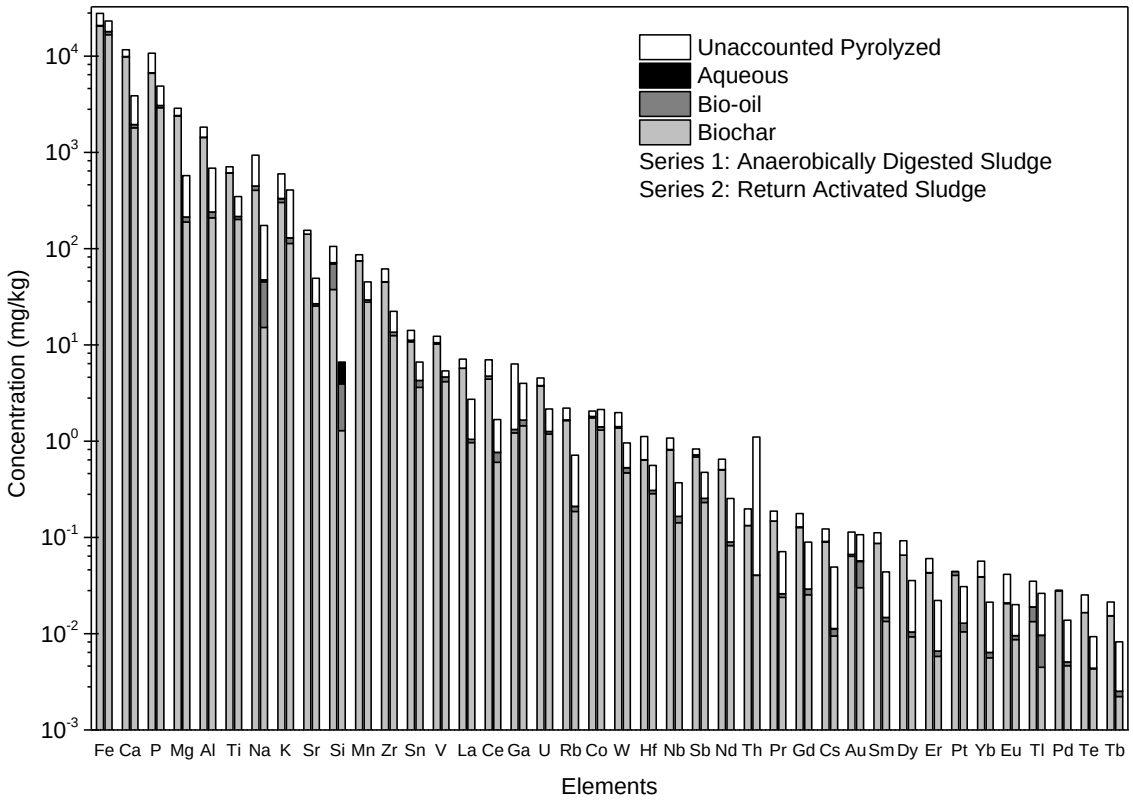

Figure A-4: Concentration of selected elements in each phase of sewage sludge after hydrothermal liquefaction of 20g sludges (20% solids). Standard deviation for experimental replicates <20%.